THE JOURNAL OF

PHYSICAL CHEMISTRY

AMERICAN CHEMICAL SOCIETY
1876-1976

THE JOURNAL OF
PHYSICAL CHEMISTRY

Published biweekly by the American Chemical Society at 20th and Northampton Sts., Easton, Pennsylvania 18042. Second class postage paid at Washington, D.C. and at additional mailing offices.

Editorial Information

Instructions for authors are printed in the first issue of each volume. Please conform to these instructions when submitting manuscripts.

Manuscripts for publication should be submitted to *The Journal of Physical Chemistry*, Department of Chemistry, University of Minnesota, Minneapolis, Minn. 55455. Correspondence regarding **accepted papers and proofs** should be directed to the Editorial Department at the ACS Easton address.

Page charges of $60.00 per page are assessed for papers published in this journal. Ability to pay does not affect acceptance or scheduling of papers.

Bulk reprints or photocopies of individual articles are available. For information write to Business Operations, Books and Journals Division at the ACS Washington address.

Requests for **permission to reprint** should be directed to Permissions, Books and Journals Division at the ACS Washington address. The American Chemical Society and its Editors assume no responsibility for the statements and opinions advanced by contributors.

Subscription and Business Information

1976 Subscription rates—including surface postage

	U.S.	PUAS	Canada, Foreign
Member	$24.00	$29.75	$30.25
Nonmember	96.00	101.75	102.25
Supplementary material	15.00	19.00	20.00

Air mail and air freight rates are available from Membership & Subscription Services, at the ACS Columbus address.

New and renewal subscriptions should be sent with payment to the Office of the Controller at the ACS Washington address. **Changes of address** must include both old and new addresses with ZIP code and a recent mailing label. Send all address changes to the ACS Columbus address. Please allow six weeks for change to become effective. **Claims** for missing numbers will not be allowed if loss was due to failure of notice of change of address to be received in the time specified; if claim is

dated (a) North America—more than 90 days beyond issue date, (b) all other foreign—more than 1 year beyond issue date; or if the reason given is "missing from files". Hard copy claims are handled at the ACS Columbus address.

Microfiche subscriptions are available at the same rates but are mailed first class to U.S. subscribers, air mail to the rest of the world. Direct all inquiries to Business Operations, Books and Journals Division, at the ACS Washington address or call (202) 872-4444. **Single issues** in hard copy and/or microfiche are available from Special Issues Sales at the ACS Washington address. Current year $4.75. Back issue rates available from Special Issues Sales. **Back volumes** are available in hard copy and/or microform. Write to Special Issues Sales at the ACS Washington address for further information. **Microfilm** editions of ACS periodical publications are available from volume 1 to the present. For further information, contact Special Issues Sales at the ACS Washington address. **Supplementary material** must be ordered directly from Business Operations, Books and Journals Division, at the ACS Washington address.

Microfiche	U.S.	PUAS, Canada	Other Foreign
Photocopy	$2.50	$3.00	$3.50
1–7 pages	4.00	5.50	7.00
8–20 pages	5.00	6.50	8.00

Orders over 20 pages are available only on microfiche, 4 × 6 in., 24X, negative, silver halide. Orders must state photocopy or microfiche if both are available. Full bibliographic citation including names of all authors and prepayment are required. Prices are subject to change.

Notice to Authors last printed in the issue of January 1, 1976

THE JOURNAL OF
PHYSICAL CHEMISTRY

29.คม.2519

■ Supplementary and/or miniprint material for this paper is available separately (consult the masthead page for ordering information); it will also appear following the paper in the microfilm edition of this journal.

* In papers with more than one author, the asterisk indicates the name of the author to whom inquiries about the paper should be addressed.

AUTHOR INDEX

Atomic Oxygen. VI. Isotope Effects in the Reactions of Deuterated 2-Methylpropenes with Oxygen (^{3}P) Atoms[1]

James J. Havel* and C. J. Hunt

Department of Chemistry, Rice University, Houston, Texas 77001 (Received August 25, 1975)

Publication costs assisted by the Petroleum Research Fund and the Robert A. Welch Foundation

The gas-phase reactions of ground state (triplet) oxygen atoms with 2-methylpropene-d_0, -1-d_1, and -1,1-d_2 have been studied. The oxygen atoms were generated by the mercury photosensitized decomposition of nitrous oxide. Vinylic deuterium substitution of the olefin increases the epoxide yield and decreases the yields of carbonyl products. The rate of O(^{3}P) addition to the olefin shows a small inverse secondary isotope effect. A primary isotope effect upon the relative migratory aptitudes of hydrogen vs. deuterium rearrangement in the formation of 2-methylpropanal was observed.

Introduction

In recent years, th study of the reactions of atomic oxygen has been greatly accelerated. This increased interest in the field has been prompted by a demand for more knowledge of the chemical mechanisms of three important phenomena: upper atmosphere chemistry,[2] photochemical air pollution,[3] and combustion.[4] The role of atomic oxygen in these three processes is still under investigation. The purpose of this work is to clarify by means of various deuterium isotope effects the mechanism of reaction of oxygen atoms with simple olefins.[5] Recently, applications of atomic oxygen reactions in the synthesis of new and useful organic compounds have been developed.[1,6]

Atomic oxygen in its ground (triplet) state is conveniently produced by the gas phase mercury photosensitized decomposition of nitrous oxide.[7]

$$Hg(^1S_0) + h\nu \xrightarrow{253.7 \text{ Å}} Hg(^3P_1)$$

$$Hg(^3P_1) + N_2O \rightarrow Hg(^1S_0) + N_2(^1\Sigma) + O(^3P)$$
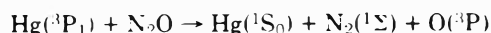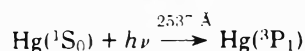
This technique has several advantages for the clean generation and reaction of oxygen atoms. First, the reaction is carried out in an easily constructed static system. Nitrous oxide does not react with simple organic molecules at ordinary temperatures and pressures. Also. nitrous oxide is inert to oxygen atoms and free radicals. The direct photolysis of nitrous oxide is negligible at the wavelengths emitted by low-pressure mercury lamps. Finally, the production of one molecule of nitrogen for every oxygen atom provides a built-in device for the determination of product yields. No external actinometer is necessary.

Cvetanovic has pioneered the field of atomic oxygen reactions.[5a] In his study of the reaction of 2-methylpropene with O(^{3}P), he reported three C_4H_8O products: 2,2-dimethyloxirane, 1 (54% relative yield); 2-methylpropanal, 2 (43%); and 2-butanone, 3 (3%).[8] Products of hydrogen abstraction or oxygen atom insertion into carbon–hydrogen bonds were not observed.

The proposed mechanism involves initial addition of O(^{3}P) to the double bond to form carbon–oxygen 1,3 biradicals, 4 and 5 (Scheme I). These biradicals form epoxide 1 by ring closure and carbonyl compounds 2 or 3 by 1,2 migration of a hydrogen atom or methyl radical. Assuming that the rates of ring closure of the two biradicals (k_3 and k_4) are approximately equal, then the large ratio of 2-methylpropanal to 2-butanone indicates that addition to carbon-1 of 2-methylpropene is faster than addition to carbon-2 (or $k_1 > k_2$). This result was to be expected. since biradical 4 possesses a tertiary carbon radical site, while biradical 5 has a primary carbon radical site.

Experimental Section

Materials. Commercial nitrous oxide and 2-methylpropene were purified by trap-to-trap distillation before reaction.

2-Methylpropene-1-d_1 was prepared in 70% yield by D_2O hydrolysis of the corresponding Grignard reagent.[9] The

Scheme I

TABLE I: Relative Product Yields from Reactions of Labeled 2-Methylpropenes with O(^{3}P)

Reactant	Relative product yield, %[a]			
	1	2	3	6
$Me_2C=CH_2$	51.4	45.3	2.9	0.4
$Me_2C=CHD$	55.3	41.6	2.7	0.4
$Me_2C=CD_2$	59.5	37.7	2.5	0.3

[a] Normalized yields of $C_4H_nD_{8-n}O$ products. Absolute yield = 68 to 74%. Absolute yield of CO $\leq$ 2%.
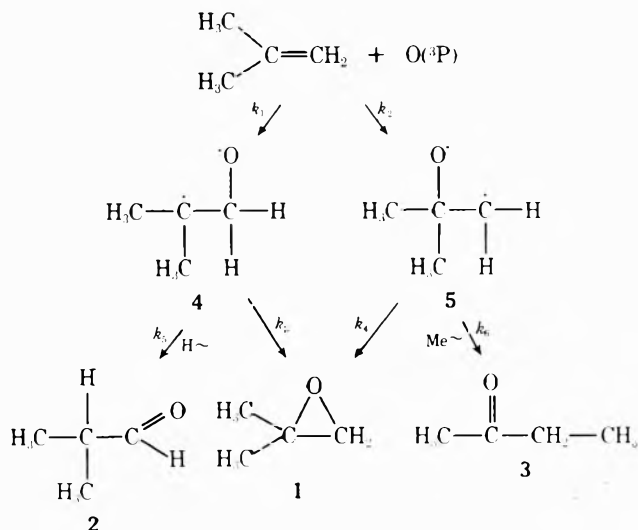
Grignard precursor, 1-bromo-2-methylpropene, was made by the method of Braude and Evans.[10]

2-Methylpropene-$1,1$-d_2 was prepared in poor yield (3%) from 1,1-dichloro-2-methylpropene[11] by the method of Craig and Fowler.[12] Labeled compounds were VPC purified before reaction.

Reaction Procedures. Oxygen (^{3}P) atoms were generated in the gas phase by the mercury photosensitized decomposition of nitrous oxide.[7] The general reaction technique has been described previously.[13]

In all of the reactions discussed below, the initial total pressure was 0.92 atm, and the reaction temperature was 25-29 °C. Two conditions were used to limit the reactions to primary processes. In order to minimize mercury photosensitized decomposition or rearrangement of the substrate, the ratio of nitrous oxide to olefin was 25:1. The reactions were stopped at less than 20% conversion of olefin in order to avoid reactions of O(^{3}P) with primary products.

Analyses. Reaction Products. Oxygenated products were analyzed by VPC on dinonylphthalate columns. Absolute yields of $C_4H_nD_{8-n}O$ products were determined by VPC after addition of a known volume of 1,2-dimethoxyethane as internal standard. Absolute yields of $C_4H_nD_{8-n}O$ products (based on nitrogen liberated by nitrous oxide decomposition) varied from 68 to 74%. The absolute yield of carbon monoxide never exceeded 2%.

Authentic samples of products 1, 2, and 3 were obtained commercially for comparison of spectra and VPC retention times. 2-Methoxypropene, 6, was prepared by the method of Newman and VanderZwan.[14] The relative molar VPC responses of these C_4H_8O materials varied by less than 1%, so no attempt was made to correct VPC areas in determining relative product yields.

Relative Reaction Rates. The relative rates of reaction of deuterated and undeuterated 2-methylpropenes were determined as described previously.[13] The total amounts of $C_4H_nD_{8-n}$ olefins before and after reaction were determined by both manometric and VPC analysis. The olefin mixtures were analyzed for isotopic content before and after reaction by mass spectrometry at an ionizing potential of 14 eV. The accuracy of these measurements was ±1% as determined with known gas mixtures.

Migratory Aptitude. The position of the deuterium in the 2-methylpropanal formed by the reaction of atomic

oxygen with 2-methylpropene-1-d_1 was determined by two methods: integration of the NMR spectrum and mass spectrometry at 70 eV (mass fragmentometry). The most accurate method involved comparison of the intensities of the CHO$^+$ and CDO$^+$ ions due to 2-methylpropanal-2-d_1 and 2-methylpropanal-1-d_1, respectively. To check for deuterium rearrangement before fragmentation, a sample of 2-methylpropanal-2-d_1 (**97% isotopic purity**) was prepared by six successive sodium deutroxide catalyzed isotopic exchanges between 2-methylpropanal-d_0 and excess D_2O. The mass spectrum of this material showed no detectable CDO$^+$. The accuracy of the mass fragmentometry method was ±4%, as determined by incremental addition of unlabeled 2-methylpropanal to a mixture of 2-methylpropanal-1-d_1 and -2-d_1.

Results and Discussion

Reaction Products. In reinvestigating the reaction of 2-methylpropene with O(^{3}P), we have found another C_4H_8O product, 2-methoxypropene, 6. Enol ethers have also been detected from the reactions of other acyclic olefins with oxygen atoms. For example, the reaction of 2,3-dimethyl-2-butene produces 2-methoxy-3-methyl-2-butene in 1.5% yield, relative to total recovered $C_6H_{12}O$ material.[15]

The formation of 2-methoxypropene in the 2-methylpropene reaction is most easily explained by rearrangement of a methyl group to the oxygen radical site of biradical 5. In atomic oxygen reactions, migrating alkyl groups are known to become at least partially detached from intermediates such as 5 during rearrangement.
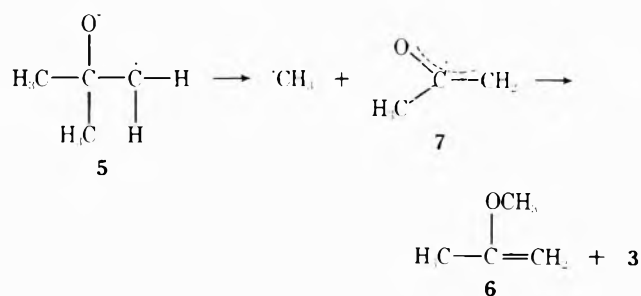
Cvetanovic has demonstrated that the separated methyl radicals can be scavanged by molecular oxygen before combination with radicals such as 7.[8]

The relative yields of products from the reactions of 2-methylpropene-d_0, -1-d_1, and -$1,1$-d_2 are summarized in Table I.

The analysis of these changes in relative product yield is complex because of the several competing reactions leading to products. However, certain trends are evident upon increased deuterium substitution of the double bond, namely, an increase in epoxide yield and a decrease in yield of carbonyl products. Some reasons for these trends will be discussed below.

Relative Reaction Rates. The effect of deuterium substitution on the rates of addition of various free radicals to olefins has been studied by several groups of workers.[16] Deuterium substitution produces an interesting inverse secondary isotope effect; that is, deuterium-substituted olefin reacts faster than protium-substituted olefin. The magnitude of this effect is a 2–4.5% rate increase per vinylic deuterium atom. We have found that the reaction of O(^{3}P) with labeled 2-methylpropenes shows a similar effect:

$$k_{\text{Me}_2\text{C}=\text{CHD}}/k_{\text{Me}_2\text{C}=\text{CH}_2} = 1.03 \pm 0.01$$

and

$$k_{\text{Me}_2\text{C}=\text{CD}_2}/k_{\text{Me}_2\text{C}=\text{CH}_2} = 1.05 \pm 0.01$$

The inverse isotope effect was originally attributed to changes in vibrational frequencies accompanying the sp^2 → sp^3 rehybridization at the carbon atom to which the free radical has added. More recent calculations by Strausz and Safarik[17] attribute the effect to the creation of new isotopically sensitive normal modes during the passage from reactant to transition state.

In either case, one would expect vinylic deuterium substitution to increase the rate of addition at carbon-1 of 2-methylpropene (k_1) relative to addition at carbon-2 (k_2). This expectation is confirmed by the decreased relative yields of 2-butanone (3) and 2-methoxypropene (6) with substitution of one or two deuteriums. However, the effect of isotopic substitution on the ratio k_1/k_2 is minor compared to isotope effects which arise later in the reaction sequence.

It should be noted that isotope effects on the orientation of oxygen atom addition have also been observed in the reactions of O(^{3}P) with *cis*- and *trans*-2-butene-2-d_1.[15] Examination of the labeling pattern of the 2-methylpropanal formed in these reactions[7] showed that addition to the deuterium-substituted carbon proceeded 1–3% faster than addition to the protium-substituted carbon.

Determination of isotope effects on relative reaction rates by the method described in the Experimental Section depends on the irreversibility of oxygen atom addition. This irreversibility was demonstrated in the addition of O(^{3}P) to *cis*-2-butene.[15] The unconsumed *cis*-2-butene recovered after reaction showed no trace of *trans*-2-butene. Some *trans*-2-butene would have been expected if the addition were reversible.
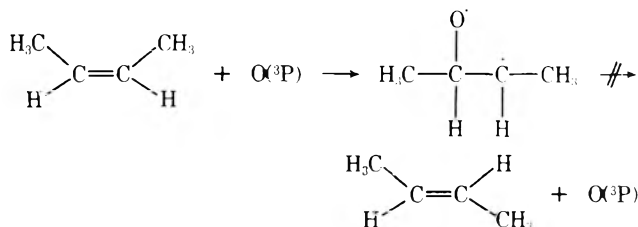
Migratory Aptitude. The reaction of O(^{3}P) with 2-methylpropene-*1*-d_1 provides an opportunity to directly determine the relative migratory aptitudes of hydrogen vs. deuterium from biradical 4d_1. The relative migratory aptitude is simply indicated by the ratio of 2-methylpropanal-*1*-d_1 to 2-methylpropanal-2-d_1.

4d
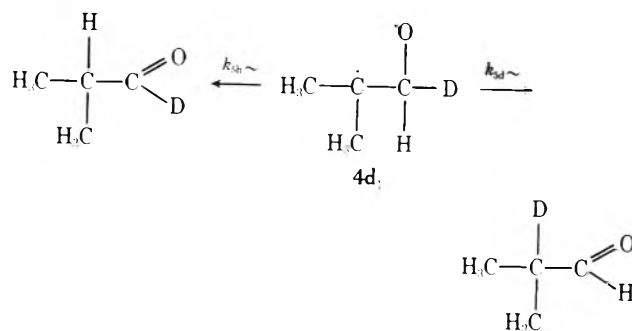
Analysis of the VPC-purified 2-methylpropanal from this reaction showed $k_{5h\sim}/k_{5d\sim} = 1.17 \pm 0.07$. Hydrogen rearranges faster than deuterium. Cvetanovic has shown[8] that a migrating hydrogen atom does not become detached from the molecule during rearrangement. The rearranging hydrogen atoms cannot be scavenged by molecular oxygen.

The slower rearrangement of deuterium is also reflected in the relative product yields of Table I. Deuterium substitution decreases the rate of aldehyde formation (k_5) without appreciably changing the competing rate of epoxide formation (k_3).

The closest literature analogy to the migratory aptitude isotope effect described above can be seen in the decomposition of 1-pyrazoline-*4*-d_1.[18] Thermolysis of this compound involves loss of nitrogen and formation of propene and cyclopropane.
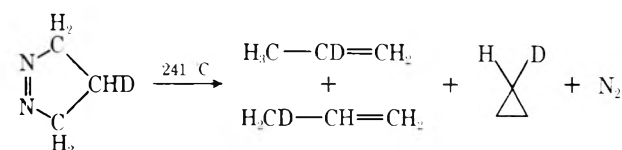
The relative migratory aptitude of the rearrangement leading to propene formation is $k_h/k_d = 1.50 \pm 0.08$. However, the pyrolysis of 1-pyrazolines probably does not involve triplet 1,3 biradical intermediates.[19]

References and Notes

(1) Part V: J. J. Havel and K. H. Chan, *J. Org. Chem.*, in press.
(2) (a) "Symposium on Aeronomy of the Stratosphere and Mesosphere", *Can. J. Chem.*, **52**, 1381–1634 (1974); (b) *Chem. Eng. News*, April 21, 1975, p 21.
(3) J. N. Pitts, Jr., and B. J. Finlayson, *Angew. Chem., Int. Edit. Engl.*, **14**, 1 (1975).
(4) (a) J. Minkoff and C. H. F. Tipper, "The Chemistry of Combustion Reactions", Butterworths, London, 1962; (b) R. S. Sheinson and F. N. Williams in "Combustion Institute, European Symposium, 1973", F. J. Weinberg, Ed., Academic Press, New York, N.Y., 1973, pp 707–711.
(5) (a) R. J. Cvetanovic, *Adv. Photochem.*, **1**, 115 (1963); (b) M. D. Scheer and R. Klein, *J. Phys. Chem.*, **73**, 597 (1969); (c) J. R. Kanofsky, D. Lucas, and D. Gutman, *Symp. (Int.) Combust.*, [*Proc.*], *14th, 1972*, 285–293 (1973).
(6) (a) J. J. Havel and K. H. Chan, *J. Org. Chem.*, **39**, 2439 (1974); (b) *J. Am. Chem. Soc.*, **97**, 5800 (1975).
(7) R. J. Cvetanovic, *J. Chem. Phys.*, **23**, 1203 (1955).
(8) R. J. Cvetanovic, *Can. J. Chem.*, **36**, 623 (1958).
(9) R. A. Caldwell, *J. Org. Chem.*, **35**, 1193 (1970).
(10) E. A. Braude and E. A. Evans, *J. Chem. Soc.*, 3334 (1955).
(11) R. S. Corley, S. G. Cohen, M. S. Simon, and W. T. Wolosinski, *J. Am.*

Chem. Soc., **78**, 2608 (1956).
(12) D. Craig and R. B. Fowler, *J. Org. Chem.*, **26**, 713 (1961).
(13) J. J. Havel, *J. Am. Chem. Soc.*, **96**, 530 (1974).
(14) M. S. Newman and M. C. VanderZwan, *J. Org. Chem.*, **38**, 2910 (1973).
(15) J. J. Havel, unpublished results.
(16) (a) Methyl radicals: M. Matsuoka and M. Szwarc, *J. Am. Chem. Soc.*, **83**, 1260 (1961); (b) hydrogen atoms: R. J. Cvetanovic, *Can. J. Chem.*,

40, 1037 (1962); (c) cyclopropyl radicals: A. P. Stefani, L. Y. Chuang, and H. E. Todd, *J. Am. Chem. Soc.*, **92**, 4168 (1970); (d) sulfur (^3P) atoms: O. P. Strausz, W. B. O'Callaghan, E. M. Lown, and H. E. Gunning, *ibid.*, **93**, 560 (1971).
(17) O. P. Strausz and I. Safarik, *J. Phys. Chem.*, **76**, 3613 (1972).
(18) B. H. Al-Sader and R. J. Crawford, *Can. J. Chem.*, **46**, 3301 (1968).
(19) R. J. Crawford and A. Mishra, *J. Am. Chem. Soc.*, **88**, 3963 (1966).

The Long-Lived Transient in the 2500–3500-Å Flash Photolysis of Gaseous Sulfur Dioxide

Jan W. Bottenheim and Jack G. Calvert*

Chemistry Department, The Ohio State University, Columbus, Ohio, 43210 (Received September 22, 1975)

The flash photolysis of pure SO_2, SO_2-Ar, SO_2-He, and SO_2-NO gaseous mixtures has been studied by kinetic spectroscopy. The transient absorbance of an unidentified species X formed in the flashed mixtures was followed by changes in the optical density at 3250 Å. Measurements of the initial changes in optical density and the lifetimes of the absorbing species have been made in a variety of experiments of varied reactant pressures and flash intensities. The results suggest that the rate-determining step in the formation of X involves an electronically excited singlet SO_2 molecule and a ground state SO_2 molecule. The decay of X is controlled by its rate of diffusion to the cell wall, as suggested in Hellner and Keller's previous work.[7] In the evaluation of the rate data attention was paid to the very large temperature rise which accompanies the flash photolysis of SO_2 mixtures. An alternative thermal equilibrium hypothesis for X generation, $SO_2 \rightleftharpoons X$, appears to fit some of the observations made here, but it is incompatible with others. Speculation on the chemical nature of X leads to the consideration of several alternatives: a "thermal" isomer of SO_2, S_2O, $(SO_2)_2$, and some seemingly less attractive species.

Introduction

The spectroscopy and the photochemistry of the simple triatomic molecule SO_2 within the first allowed absorption band still defies a complete and self-consistent description. Both spectroscopists[1] and photochemists[2] have been frustrated in attempts to resolve completely the interactions between the various singlet states ($^1B_1$, $^1A_2$) and triplet states ($^3B_1$, $^3A_2$, $^3B_2$) which are believed to be accessible to an SO_2 molecule excited within the first allowed absorption region (2400–3300 Å). Among the many unresolved problems in SO_2 photochemistry is the characterization of the long-lived transient species produced in the flash excitation of SO_2. A so-called continuum absorption is seen over all of the SO_2 absorption regions following the flash excitation of SO_2.[4-9] A similar continuum, which may or may not be related to that seen in the SO_2 flash experiments, has been found to preceed the appearance of product SO_2 in SO_2-forming thermal reactions such as the combustion of H_2S in O_2,[10] and the explosion of CS_2 with O_2,[11] as well as in the photolyses of H_2S, CS_2, and COS in O_2.[12] In flash photolysis studies it was observed that the continuum could be suppressed by addition of a large amount of thermalizing, unreactive gas such as nitrogen. As a consequence some workers have attributed the transient absorption to some thermal effect. Further evidence for this interpretation is seen in the absorption spectrum of SO_2 at elevated temperatures; here the normal SO_2 structure disappears as

a continuum grows in at increasing temperatures.[13-15] Furthermore the high-temperature infrared spectrum of SO_2 exhibits some new bands which increase with increasing temperature.[16] From the evidence at hand it is not possible to conclude unambiguously whether the transient absorption observed in the variety of both thermal and photochemical experiments has its origin in the same chemical species, although this conclusion seems to be accepted in much of the published literature on these systems.

Many hypotheses have been set forth as to the nature of the transient which is responsible for the continuum absorption in the variety of thermal and photochemical experiments. First it was reasoned by Myerson et al.[11] to have a structure S–O–O, and later it was given a less specific designation by Norrish and Oldershaw as a "thermal isomer" of SO_2.[4] Infrared spectral considerations of Giguère and Savoie[16] did not favor the S–O–O hypothesis. Hayes and Pfeiffer[3b] suggested from their LCAO–S CR–MO calculations on SO_2-like molecules that the transient may be a symmetrical form of SO_2 with a somewhat larger S–O bond distance and a O–S–O bond angle of 72°. Basco and Morse[6] had a very different interpretation; they studied the adiabatic flash photolysis of SO_2 and concluded that the appearance of the continuum absorption is the result of an optical illusion induced by temperature broadening of the $C(^1B_2)$–$X(^1A_1)$ and $A(^1B_1)$–$X(^1A_1)$ banded structure.

Recently the first kinetic study of the transient in SO_2 flash photolysis was performed by Hellner and Keller.[7]

They reported a most surprising result in terms of the then current hypotheses on the nature of the transient; the lifetime of the transient responsible for the continuum absorption increased with increase in pressure of the thermalizing gas and reached half-lives of about 1 s at 1 atm pressure. The rate of its disappearance was shown to be dependent on the rate of diffusion to the cell wall. Although temperature broadening of the SO_2 line structure must occur as Basco and Morse have reasoned, it seems highly improbable that the entire effect has this origin; one expects that added thermalizing gas would decrease the lifetime of the transient if this were the case, as a result of the increase in the rate of the thermallizing collisions. In explanation of their results Hellner and Keller suggested that the transient was a weak dimer of SO_2 which they proposed was formed by the interaction between two excited singlet molecules. However the kinetic studies upon which these conclusions were based involved some assumptions in data treatment which seem inappropriate to us. Although their flash experiments were carried out using pressures of pure SO_2 and SO_2 in added gas mixtures which extended up to 1 atm, the authors have assumed that the rate of light absorption in their photolysis cell was proportional to the SO_2 pressure. In view of the high extinction coefficient of SO_2 in the 2800-Å region and the diameter of their cell, the limiting form of Beer's law cannot apply. Furthermore their use of steady state expressions in analyzing the data, and the neglect of the effects of the large temperature rise which must have occurred in their studies, are not justified. In view of these problems in the data evaluation in the previous work, we initiated the present study to further delineate the mechanism of formation of the long-lived transient and the chemical nature of this species. Some interesting new features of the SO_2 flash photolysis system were observed and are reported here.

Experimental Section

The quartz reaction cell was 220 cm in length and 6.3 cm i.d. The monitoring light beam entered and exitted the cell through 1.5-in. quartz windows attached to stainless steel, O-ring fitted, end plates of the cell. The flash lamp which paralleled the cell was a 33 mm i.d. Vycor tube (cutoff, λ <2400 Å) which was filled with xenon (9 Torr) and oxygen (1 Torr). The cell and the flashlamp were light coupled with an aluminum reflector housing coated inside with white reflectance paint (Kodak 6080). The electrical energy dissipated through the flashlamp was generally 20 kJ, although this was varied in some runs over the range 12.5–22.5 kJ. The pulse width at half-maximum intensity was about 50 μs; the maximum intensity occurred at about 24 μs after initiation of the flash.

The continuum absorption was monitored in the first experiments with a controlled-delay spectroflash lamp and Hilger, quartz prism, plate spectrograph. Employed in the kinetic experiments was a xenon high-pressure continuous light source (Osram HBO 450 W), filtered with a 0.25-in. Pyrex plate and shuttered until just before the flash. After the analyzing beam passed through the cell it entered a Jarrell-Ash, 0.5-m grating monochromator, equipped with a 1P-21 (RCA) photomultiplier. In the latter case the wavelength chosen for monitoring was 3250 ± 2 Å so that our results would be directly comparable to those obtained in the previous kinetic work which was carried out at this wavelength.[7] The decay curve was recorded with a transient recorder (Biomation 610), digitized, and stored on paper tape for later treatment and/or displayed on an oscilloscope (Tektronix 561A) and the trace photographed.

The photolysis cell and flash lamp were connected to a conventional mercury-free vacuum system employing Teflon stopcocks. Pressures below 10 Torr were measured directly with a pressure transducer (Dynascience); this was used as null device in connection with a calibrated pressure gauge (Wallace and Tiernan) for the higher pressure range (10–100 Torr). When gas mixtures were prepared, uniform mixing of the components throughout the cell was ensured through the 30-min operation of a mechanical, glass, circulating pump, attached in series with the cell by means of a glass tubing loop connected through each of the endplates of the cell. The SO_2 reactant gas (Matheson and Co., anhydrous) was twice distilled from trap to trap with retension of only the middle boiling third of the sample. Argon gas (Airco, reagent grade) and helium (Matheson) were used without further purification. Nitric oxide (Matheson) was purified by distillation from silica gel at −131 to −196 °C.

Experimental Results and Discussion

The transient formed in the flash photolysis of SO_2 was followed by absorption spectroscopy in experiments designed to test the mechanism of its formation. Several of the observations of Hellner and Keller[7] are confirmed in this work, but some new and significant findings require some modification of the existing theories of the transient formation and decay mechanisms.

Observation of Two Transient Absorptions. Our initial plate spectrographic study of the spectral changes in flash photolyzed SO_2 confirmed the observations of many previous investigators:[4-9] a continuum absorption appears in the 2500–3300-Å region of the first allowed transition of SO_2. However in kinetic experiments in which the 3250-Å absorption was monitored, not one, but two first-order transient decays of different lifetime were observed. For an experiment in which P_{SO_2} = 0.80 Torr, an initial first-order decay was seen which had a lifetime of about 10 ms; the lifetime of this species increased in a regular fashion as P_{SO_2} was raised and was equal to 0.84 s in experiments at 31 Torr of SO_2; see the data of Table I. The decay time for this component was essentially unchanged when it was formed in successive flashes of the same sample. This is undoubtedly the transient absorption which was studied by Hellner and Keller,[7] and it is the one on which most of our attention will be focused. We will refer to the species responsible for this absorption as X. The second component (Y) in the absorption was evident in a long-lasting (∼1 s), low-intensity tail in the decay curve. The lifetime of Y changed somewhat erratically as the SO_2 pressure was increased. With successive flashes of the same sample of SO_2, the decay rate of Y seemed to increase, whereas its absorbance extrapolated to zero time decreased in a somewhat erratic fashion. The lifetimes of the two components X and Y appeared to merge at the higher pressures, and, of course, resolution of the two for these conditions was impossible. Because of the irreproducible character of the second component we have not been able to define its origin or its kinetics. It is possible that it is the result of an experimental artifact, or it may be related to the temperature broadening of the SO_2 structure in the viscinity of the 3250-Å region brought on by the absorption of light from the higher vibrational levels of the hot SO_2 molecules created in the adiabatic flash heating of the reactant; this was the previous suggestion of Basco and Morse[6] in explanation of the entire

TABLE I: Effect of SO$_2$ Pressure on the Lifetimes (τ) and the Initial Changes in Optical Densities (ΔOD^0) at 3250 Å for the Transient Formed in the Flash Photolysis of Gaseous SO$_2$ [a]

P_{SO_2}, Torr	τ, ms	ΔOD^0	kI_a [b]	T_{max}, K [c]
0.80	10.0	0.74	0.74	2119
1.05	12.7	0.97	0.95	2119
1.33	19.4	1.11	1.17	2097
1.55	23.1	1.24	1.33	2080
1.70	25.7	1.51	1.44	2069
2.00	26.8	1.68	1.69	2047
3.55	47.4	2.41	2.51	1938
5.00	64.2	3.00	3.07	1844
6.48	97.1	2.78	3.44	1756
8.00	125	2.78	3.66	1673
9.33	149	2.53	3.75	1606
15.8	316	1.42	3.38	1339
20.0	422	1.08	2.84	1209
24.6	614	0.57	2.71	1094
31.4	837	0.30	1.48	964

[a] Flash energy was 20 kJ; temperature cell at start, ~295 K. [b] This quantity is roughly proportional to the intensity of the light absorbed by SO$_2$ molecules at the center of the flash photolysis cell, near the position of optical density measurement; see the text for the calculation method. [c] Estimated maximum gas temperature in cell following the adiabatic flash photolysis of the SO$_2$; see the text for the calculation method.

transient absorption phenomenon. Another alternative is that an "apparent" absorption results from the creation of light scattering aerosol particles of H$_2$SO$_4$, formed on hydration of one of the initial products, SO$_3$. Absorption due to component Y is relatively low in most experiments, and it represents only a minor perturbation in the resolution of the kinetic behavior of the X species for the experiments at the lower SO$_2$ pressures. As a consequence we will base most of our interpretations on the results of these low-pressure experiments which allow a more definitive characterization of the kinetic parameters of X.

Dependence of the Initial Optical Density of the Transient X on the Intensity of the Light Absorbed by SO$_2$. A series of kinetic studies in pure SO$_2$ at varied pressures was made in which we determined the lifetime of the major transient species and its optical density at zero time after the flash. These data, summarized in Table I, provide new evidence of the mechanism of formation of the unknown X species.

It can be shown that the change in optical density at 3250 Å immediately following the flash (ΔOD^0) is related to the concentration of X by

$$\Delta OD^0 = (\epsilon_X - n\epsilon_{SO_2})[X]^0 l \qquad (1)$$

Here ϵ_X and ϵ_{SO_2} refer to the molar extinction coefficients of X and SO$_2$, respectively, at 3250 Å; l is the path length (220 cm); n is the number of SO$_2$ molecules which react to form a molecule of the transient X. The intensity of the flashlamp light (I_a, quanta l.$^{-1}$ flash^{-1}) of wavelength λ absorbed by SO$_2$ molecules in a volume element near the center of the cell (radius, a cm), the position of the optical density measurements, should be proportional to the product of the intensity of the flashlamp which is transmitted to this volume element, and the pressure of SO$_2$;

$$kI_{a\lambda} = (10^{-\epsilon\lambda[SO_2]a})P_{SO_2}^0 \qquad (2)$$

k is a proportionality constant which includes the recipro-

cal of the incident flash intensity. As a first approximation, we may assume an appropriate average value for ϵ and consider the flashlamp distribution to be a continuum of equal intensity per wavelength interval in the SO$_2$ absorption region (2400–3300 Å).[17] Then function 2 should be approximately proportional to the total number of light quanta absorbed by SO$_2$ per unit volume near the center line of the cylindrical cell. Following this procedure values of kI_a were calculated for different values of P_{SO_2} used in our experiments; these are shown in column 4 of Table I. Compare this quantity with the value of ΔOD^0 observed in these experiments (column 3, Table I). The two quantities are near equal to one another for experiments with $P_{SO_2} \leq 5$ Torr. The correspondence fails at high SO$_2$ pressures; kI_a values maximize at about 9 Torr while the ΔOD^0 values are a maximum at about 5 Torr. A quantitative treatment of the absorption data at high [SO$_2$] is impossible without a detailed knowledge of the complete absorption spectra of the transient X. However the high [SO$_2$] results can be rationalized well in a qualitative sense. One would anticipate that as the pressure of SO$_2$ is increased the concentration of the transient product X will increase significantly in that portion of the cell volume which extends from the cell wall to the center of the cell; this may act as an internal filter of increasing density as P_{SO_2} is increased, and penetration of the flashlamp radiation to the center of the cell will be attenuated more than predicted by the approximate relation 2. This potential complication should be unimportant for data at the lowest P_{SO_2} values, and these will give the most reliable indication of the dependence of ΔOD^0 on I_a. Thus the present data support the conclusion that ΔOD^0 is directly proportional to the first power of I_a.

Further experiments summarized in Table II show the effect of altered energy of the flash on the concentration of X formed initially. The flash energy was estimated from the energy stored in the condensors associated with the flash lamp ($CV^2/2$), and it should be approximately proportional to the number of photons of light emitted per flash at the higher charging voltages. At the lowest energy at which firing could be effected here (12 kJ), the fraction of the original stored energy which is dissipated to produce light is probably somewhat lower than that at the higher voltages since a complete discharge of the voltage stored in the condensors is not likely for these conditions. Thus only the highest four energy points were used in our analysis of the data of Table II. Plots of ln ΔOD^0 vs. ln (flash energy) were made (Figure 1), and the linear least-squares fit of these data give an estimate of the exponent m in the relation, ΔOD$^0 = \alpha I_a^m$. For the five series of runs shown in the order given in Table II, values of m are 0.94 ± 0.12 (2σ error limits); 0.98 ± 0.03; 1.54 ± 0.20; 1.46 ± 0.32; 0.69 ± 0.12 (0.90 ± 0.26, using all points). The weighted average of these estimates gives $m = 1.07 ± 0.16$. Both these data and those described previously from runs with varied pressures of SO$_2$ suggest that the concentration of the transient X which is present just after the flash is directly proportional to the absorbed light intensity. This result differs from that of Hellner and Keller[7] who reported $m = 2$ in their studies.

Effect of Added Gases on the Formation of X in SO$_2$ Flash Photolyses. The observed direct proportionality of the [X] with the intensity of the flashlamp light absorbed by SO$_2$ suggests that X may be formed in a reaction involving only one excited SO$_2$ molecule. The fact that this excited molecule is a singlet state of SO$_2$, as Hellner and Keller reported,[7] is confirmed here. The flash photolysis of a mix-

TABLE II: Effect of the Flash Energy on the Lifetimes (τ) and the Initial Optical Density Change (ΔOD^0) in the Flash Photolysis of SO$_2$ and SO$_2$-Ar Gaseous Mixtures^a

P, Torr		Flash energy,			
SO$_2$	Ar	kJ	τ, ms	ΔOD^0	T_{max}, K^b
1.5	4.0	12.5	28.9	0.46	980
		15.0	26.7	0.69	1108
		17.5	24.3	0.80	1235
		20.0	24.9	0.91	1361
		22.5	23.9	1.03	1486
2.0	4.53	12.5	28	0.49	1011
		15.0	29	0.87	1144
		17.5	24.8	0.99	1276
		20.0	24.7	1.16	1407
		22.5	23.5	1.26	1537
2.0	6.0	12.5	34.3	0.51	931
		15.0	33.3	0.79	1051
		17.5	31.3	1.06	1169
		20.0	31.3	1.26	1287
		22.5	30.8	1.49	1403
2.0	9.11	12.5	42.9	0.39	809
		15.0	41.7	0.63	907
		17.5	37.9	0.86	1004
		20.0	38.1	1.00	1100
		22.5	37.5	1.15	1196
10.1	0.0	12.0	c	1.19	1098
		14.0	c	1.53	1219
		16.0	c	1.72	1337
		18.0	c	1.88	1454
		22.0	c	2.09	1682

^{a} Temperature of the mixture in cell initially, 295 K. ^{b} Estimated maximum temperature in cell following the adiabatic flash photolysis of SO$_2$; see the text for the calculation method. ^{c} Not estimated.
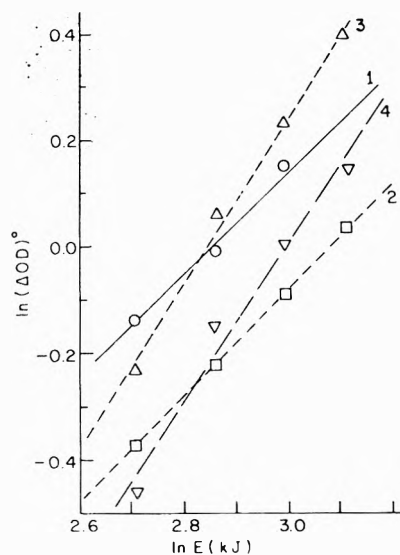
Figure 1. Test of the formation mechanism of the transient X; plot of the logarithm of the initial change in optical density at 3250 Å following the flash photolysis of SO$_2$-Ar and SO$_2$-He mixtures vs. the logarithm of the electrical energy ($CV^2/2$) used to create the flash; pressure of reactants (Torr): curve 1, Ar 4.53; SO$_2$ 2.0; curve 2, Ar 4.0, SO$_2$ 1.5; curve 3, Ar 6.0, SO$_2$ 2.0; curve 4, Ar 9.11, SO$_2$ 2.0.

ture of nitric oxide (1.0 Torr) and SO$_2$ (2.0 Torr) gave ΔOD^0 values only slightly depressed from those obtained in 2.0 Torr of pure SO$_2$, and there was no significant effect on τ. If one of the triplet states of SO$_2$ was responsible for X

TABLE III: Effect of Added Argon and Helium Gases on the Lifetimes (τ) and Initial Changes in Optical Density (ΔOD^0) at 3250 Å for the Transient in the Flash Photolysis of SO$_2$-Ar and SO$_2$-He Gas Mixtures^a

P_M, Torr	τ, ms	ΔOD^0	T_{max}, K^b
	M = Ar		
0.0	26.8	1.68	2047
4.0	27.9	1.38	1458
4.53	29.0	1.36	1407
6.0	31.3	1.26	1267
9.0	38.3	1.12	1106
9.11	38.2	1.00	1100
18.1	96.1	0.62	815
30.0	196	0.44	648
35.7	318	0.34	601
	M = He		
0.0	26.8	1.68	2047
2.5	8.4	1.53	1628
5.1	7.0	1.30	1357
10.4	8.2	0.94	1042
15.7	10.0	0.69	869
20.2	12.2	0.53	775

^{a} P_{SO_2} = 2.0 Torr; flash energy, 20 kJ; temperature of mixture initially, 295 K. ^{b} Estimated maximum gas temperature in the cell following the adiabatic flash photolysis of SO$_2$ in the gas mixture; see the text for the calculation method.

formation here, then essentially complete quenching of the absorbance of X would have been noted.

Further information on the nature of the kinetics of X formation can be gleamed from the flash experiments made using SO$_2$-Ar and SO$_2$-He mixtures. These are summarized in Table III. Note that ΔOD^0 decreases as the pressure of Ar or He is increased in mixtures containing 2 Torr of SO$_2$. The reciprocal of the ΔOD^0 values is seen to be a linear function of the pressure of added Ar (Figure 2) or He (Figure 3). The simplest kinetic mechanism which will account for this dependence is the following:

$$SO_2 + h\nu \ (\lambda \ 2500-3400 \ \text{Å}) \rightarrow \ ^1SO_2 \quad (3)$$

$$^1SO_2 + SO_2 \rightarrow X \ (+ \text{ other products}) \quad (4)$$

$$^1SO_2 + SO_2 \rightarrow \text{products other than X} \quad (5)$$

$$^1SO_2 + M \rightarrow SO_2 + M \quad (6)$$
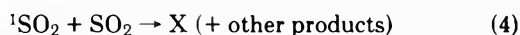
If this mechanism is operative then the following simple relation should hold:

$$\frac{1}{\Delta OD^0} = \frac{1}{kI_a}\left[\frac{k_4 + k_5}{k_4} + \frac{k_6}{k_4}\left(\frac{P_M}{P_{SO_2}}\right)\right] \quad (7)$$

We can test the mechanism in a more quantitative fashion using the linear least-squares parameters of the plots of Figures 2 and 3. In theory the (slope)/(intercept) ratio should equal $k_6/(k_4 + k_5)P_{SO_2}$. In Figure 2, the data for the SO$_2$-Ar mixtures give an intercept of 0.437 ± 0.057 and a slope of 0.0655 ± 0.032 Torr^{-1}. From these we estimate $k_6/(k_4 + k_5)$ = 0.30 ± 0.04. This is in good agreement with the ratio of excited singlet [SO$_2(^1B_1)$] quenching rate constants observed directly from SO$_2(^1B_1)$ lifetime measurements using laser excited SO$_2$-Ar mixtures: for experiments at 2662 Å, $k_6/(k_4 + k_5)$ = (1.1 ± 0.1) × 10^{10}/(3.8 ± 0.1) × 10^{10} = 0.29 ± 0.03; for 3130-Å excitation, $k_6/(k_4 + k_5)$ = (2.7 ± 0.2) × 10^{10}/(1.18 ± 0.03) × 10^{11} = 0.23 ± 0.02.[18]

From the intercept (0.496 ± 0.061) and slope (0.0638 ±
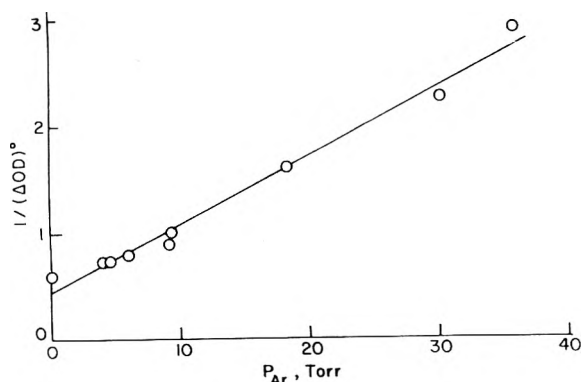
Figure 2. A further test of the formation mechanism of the transient X; plot of the pressure of argon vs. the reciprocal of the change in the optical density at 3250 Å observed in the flash photolysis of SO_2–Ar mixtures; P_{SO_2} = 2.0 Torr.
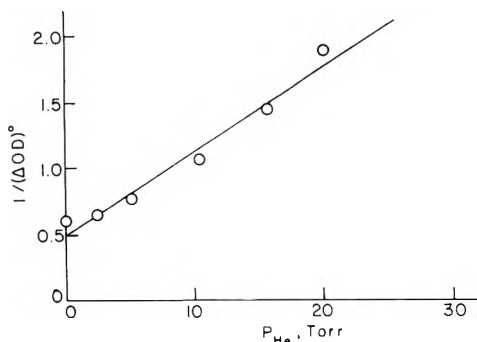
Figure 3. A further test of the formation mechanism of the transient X; plot of the pressure of helium vs. the change in optical density at 3250 Å observed in the flash photolysis of SO_2–He mixtures; P_{SO_2} = 2.0 Torr.

0.0053) of the plot of the data from the He–SO_2 data (Figure 3), we estimate $k_6/(k_4 + k_5)$ = 0.26 ± 0.04, where M in reaction 6 is now He. There are no direct lifetime data with which we can compare in this case. However the estimate is reasonable accord with Mettee's relative quenching rate constants obtained for these gases in steady state photolyses of SO_2–He and SO_2–Ar mixtures:[19] $k_6(He)/k_6(Ar) \simeq$ 0.65; thus $k_6(He)/(k_4 + k_5) \simeq 0.19$.

In summary we may conclude from the present work that the kinetics of formation of the transient X is consistent with the simple interaction of one electronically excited singlet SO_2 molecule and a ground state SO_2 molecule. This is not in accord with the conclusion of Hellner and Keller who suggest that X is derived from the interaction of two excited singlet SO_2 molecules.

Lifetime Data and the Mechanism of Removal of the Transient X. The present results on the lifetime of the transient X are consistent in most respects with the previous observations of Hellner and Keller who found the only significant loss of X was at the wall of the reaction vessel.[7] They suggested that the apparent first-order decay constant observed for disappearance of X should be described by

$$k = \frac{1}{\tau} = k_d \frac{1}{P} + k_1 + k_q P \qquad (8)$$

They estimated that the function k_d appropriate for the diffusion-controlled loss of species X from the centerline of the cylindrical cell would be given approximately by

$$k_d = \frac{(5.78)D(760)}{a^2} \qquad (9)$$

This should apply equally well for our conditions. Here D is the diffusion coefficient (cm^2 s^{-1}) of the gaseous mixture (at 760 Torr) and a is the radius of the cylindrical cell (cm).

Apparently one important factor related to the flash photolysis of SO_2 was not anticipated by Hellner and Keller, yet it must be taken into account in the testing for the diffusion mechanism for X decay in these flash systems: the temperature of the gaseous SO_2 mixtures immediately following the flash must rise well above room temperature as a result of the energy absorption by SO_2 and its dissipation in subsequent events. We have calculated the initial temperature rise expected in our runs, and these estimated maximum temperatures (T_{max}) are shown in each table. The method of calculation was straightforward. The number of quanta of light quanta absorbed by azomethane at low pressures was estimated from the nitrogen liberated: about 0.48% of the azomethane compound present was decomposed per flash (20 kJ), independent of the pressure of azomethane ($P_{Azo} <$ 5 Torr). Using this information and taking account of the differences in the absorption regions and extinctions of azomethane and SO_2, we estimated that the energy absorbed (Q, cal $l.^{-1}$ flash^{-1}) will be given approximately by

$$Q = 12.84[1 - 10^{-4.237 \times 10^{-2} P_{SO_2} (Torr)}] \frac{E}{22.5} \qquad (10)$$

Here E represents the energy (kJ) discharged through the flashlamp. Of course the magnitude of the temperature rise will depend upon the heat capacity of the gaseous mixture. We have used the heat capacities at constant volume (cal mol^{-1}, $(C_v)_{SO_2}$ = 9.908 + 1.089 × $10^{-3}T$ − 2.642 × $10^5/T^2$ and $(C_v)_{Ar,He}$ = 2.98, and set $Q = \int_{298}^{T} C_v \, dt$. The cubic equation in the unknown T which resulted after integration of this relation for the appropriate conditions of the given gaseous mixture was solved for the one significant root. The columns labeled T_{max} in Tables I–III show that the temperature rise expected in these experiments is truly significant, especially in experiments at low pressures of SO_2 where $T_{max} \simeq$ 2100 K. Such very high temperatures have been observed directly in similar unfiltered, flash-irradiated SO_2 by Basco and Morse.[6] For their flash system they estimated from the rotational line distribution of the transient SO molecule that the temperature following the flash was about 3000 K. Since the diffusion coefficient is a function of the temperature we must take this into account in our attempts to rationalize the lifetime data. A direct observation of the effect of temperature rise on the first-order decay constant for X can be seen from the lifetime data obtained in runs at varied flash energies in Table II. Note that in any given series of experiments with a mixture of fixed composition the lifetime of the transient decreases as the flash energy increases. It appears to us that a reasonable rationale for this is the increased rate of the diffusion of X which will occur as the temperature of the mixture is increased. A plot of the ln (τ_L/τ_i) vs. ln (T_i/T_L) shows that the temperature dependence of the τ_L/τ_i is approximately proportional to $(T_i/T_L)^{0.40 \pm 0.11}$; L and i subscripts refer to the quantities obtained in experiments at the lowest flash energy and the ith energy within a given series, respectively. This result is in reasonable accord with theoretical expectations; k_d/P should be approximately proportional to $T^{1/2}$ since the temperature dependence of D and hence that

of k_d will be approximately proportional to $T^{3/2}$ in this temperature range, and P is directly proportional to T.[20] Thus in testing the suitability of eq 8 and 9 to explain the $1/\tau$ dependence on P_{SO_2} (Table I), we have factored out the temperature dependence of the D/P term and plotted $1/\tau$ vs. $T^{0.40}/P_{SO_2}{}^0$ in Figure 4. The data follow the theoretically expected linear dependence rather well and the slope of this plot gives 3.65 ± 0.21 K$^{0.4}$ Torr^{-1} s^{-1}; $k_d(298$ K$) = 35.6$ Torr^{-1} s^{-1}; $D(298$ K, 1 atm$) = 0.081 \pm 0.005$ cm^2 s^{-1}. This checks reasonably well with the reported value of the self-diffusion coefficient for SO$_2$ (298 K, 1 atm): $D = 0.088$ cm^2 s^{-1}.[21]

A similar procedure was employed to take into account the effect of temperature on the lifetimes in the Ar–SO$_2$ and He–SO$_2$ mixtures. We have used the approximation that the diffusion coefficient of a mixture will be given by $D_{12} = n_1 D_{11} + n_2 D_{22}$ where n_i is the mole fraction and D_{ii} is the self-diffusion coefficient of the ith component. Combining this relation with eq 8 and 9, neglecting k_q and k_1 terms, and separating k_d/P temperature dependence as $T^{0.4}$, one expects in theory that a plot of $(P_{total})^2/\tau T^{0.4}$ vs. the pressure of the added gas (Ar or He) should be linear. The plots of the data for Ar–SO$_2$ mixtures and He–SO$_2$ mixtures given in Figure 5 are in qualitative accord with these expectations, although the data are much more scattered here than in the pure SO$_2$ experiments. We estimate from the slopes of these plots that the self-diffusion coefficients of Ar and He (298 K, 1 atm) are 0.21 ± 0.05 and 2.9 ± 0.4 cm^2 s^{-1}, respectively. Direct experimental values are 0.19 and 1.6 cm^2 s^{-1}, respectively.[21] The order of magnitude agreement seen here for the Ar–SO$_2$ and He–SO$_2$ data support the conclusion derived from the more precise pure SO$_2$ data: namely, the mechanism of X decay appears to be the diffusion-controlled loss of X at the cell wall.

Consideration of the Alternative Thermal Mechanism for Development of the Transient X. One may legitimately question whether the entire effect seen here might be the trivial result of purely thermal reactions which result from the very large temperature rise which develops in the gaseous mixture following the flash photolysis of SO$_2$ mixtures in our system. For example, reaction 11 can be important in

$$SO_2 + SO_2 \rightarrow SO_3 + SO \qquad (11)$$

the experiments with pure SO$_2$ mixtures at the lowest pressures where temperatures in excess of 2000 K are anticipated since $k_{11} \simeq 10^{12} e^{-70(\text{kcal/mol})/RT}$ M^{-1} s^{-1}.[22] In an experiment with 0.80 Torr of SO$_2$, we estimate that about 2.2×10^{-7} M SO$_2$ will have reacted by eq 11 during a 1-ms time period. Conceivably the transient X may be generated then from the thermal reactions of the initial products, SO and SO$_3$. It can be shown that this reaction rate dies quickly at the higher pressures, and it is not likely to be an important mechanism of X formation when temperatures near 1000 K are expected.

We might speculate, as others have done,[15] that X is a high-energy isomer of SO$_2$ formed following reaction 11 or by some other route, and it is in equilibrium with SO$_2$. If such a mechanism is assumed, only one molecule of SO$_2$ forms one molecule of X, and [X] $\ll$ [SO$_2$], then a plot of ln $(\Delta OD^0/P_{SO_2}{}^0)$ should be a linear function of $1/T$. If X were formed from two molecules of SO$_2$ than ln $[\Delta OD^0/(P_{SO_2}{}^0)^2 T]$ should be a linear function of $1/T$. Using the data of Table I plots of this sort have been constructed; see Figure 6. Indeed the data do follow well the expectations of the SO$_2 \rightleftarrows$ X equilibrium hypothesis. The slope of this plot
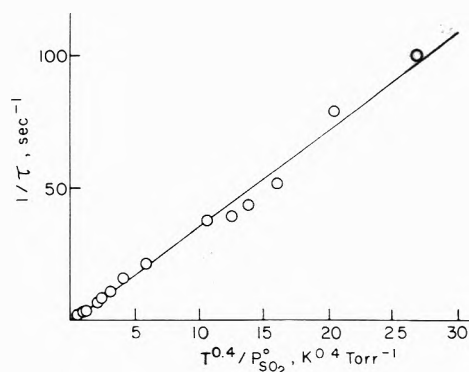
Figure 4. A test of the diffusion mechanism for loss of X at the cell wall; plot of the reciprocal of the lifetime of the transient X observed in the flash photolysis of pure SO$_2$ vs. $T^{0.4}/P_{SO_2}{}^0$.
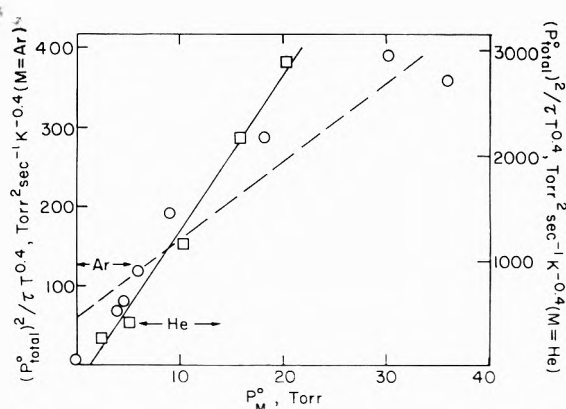
Figure 5. A further test of the diffusion mechanism for X loss at the cell wall; plot of $(P_{total}{}^0)^2/\tau T^{0.4}$ vs. the pressure of Ar or He; data are from the lifetime studies of the transient X formed in the flash photolysis of SO$_2$–Ar and SO$_2$–He mixtures; $P_{SO_2} = 2.0$ Torr.
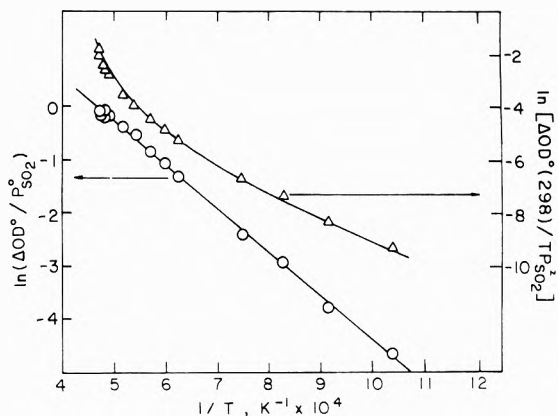
Figure 6. A test of the "thermal equilibrium" hypothesis for X formation; plot of ln $(\Delta OD^0/P_{SO_2}{}^0)$ and ln $[(\Delta OD^0)(298)/T(P_{SO_2}{}^0)^2]$ vs. $1/T$ for flash photolyses of pure SO$_2$ gas; ΔOD^0 is the change in optical density of the mixture at 3250 Å immediately after the flash.

gives an apparent ΔH for the hypothetical isomerization of 16.3 ± 0.4 kcal mol^{-1}. Although the fit of the data to this theory is gratifying, the value of ΔH found is about a factor of 4 larger than that observed in thermal studies of SO$_2$ by Brown and Burns.[15] When this seemingly realistic alternative mechanism for X formation is applied to the results from the SO$_2$–Ar and SO$_2$–He mixtures (Tables II and III), a very similar set of nearly linear relations between ln

$[\Delta OD^0/P_{SO_2}{}^0]$ and $1/T$ is seen; Figure 7. The apparent ΔH values (kcal mol^{-1}) in these cases are 3.4 ± 0.4 (series 1, Table II); 3.4 ± 0.2 (series 2); 5.2 ± 0.5 (series 3); 4.4 ± 0.3 (series 4); 2.8 ± 0.4 (series 5, Table II); 2.8 ± 0.2 (SO_2-Ar series, Table III); 2.9 ± 0.3 (SO_2-He series, Table III). These values afe very near those reported from thermal studies of SO_2 by Brown and Burns:[15] 4.1 ± 0.4 kcal mol^{-1}. There are, however, several features of the data which argue against acceptarce of the thermal hypothesis for X formation. First, the absolute magnitude of the ln ($\Delta OD^0/P_{SO_2}{}^0$) values are not constant with change in P_{SO_2}; in Figure 7 note the data for P_{SO_2} = 10.1 Torr (points marked by triangles) have much lower ordinate values than the experiments carried out with 2.0 and 1.5 Torr of SO_2. Secondly, the inconsistency in the magnitude of the slope of the plot for pure SO_2 in Figure 6 to those for SO_2-Ar and SO_2-He mixtures is unexpected in terms of the thermal equilibrium hypothesis. Both ΔOD^0 as well as the temperature rise in a given experiment are roughly proportional to the energy of the light absorbed by the system, so a qualitative correlation of ΔOD^0 with temperature is expected even with the operation of the photochemical reaction scheme outlined earlier. Although the relatively good correlations observed here support some aspects of the thermal equilibrium picture, its failure to account quantitatively for all of the observations rules out its acceptance as a realistic alternative to the photochemical formation mechanism for X.

Speculation on the Nature of the Transient X. Unfortunately the present work does not define the chemical nature of X. However it provides a new framework within which several possibilities may be considered. The experimental results obtained here require that X be formed following the rate-limiting interaction between an excited singlet SO_2 and a ground state SO_2 reactant. Among the many possible transients in the system which are logical products of this interaction are SO, SO_3, S_2O, SO_4, S, SO_2 (thermal isomer), and $(SO_2)_2$. The absorption characteristics of SO, SO_3, and S do not appear to be compatible with the 3250-Å absorption exhibited by X. On the other hand S_2O appears to be a reasonable candidate for X, since its extinction coefficient is at least a factor of 10–100 larger than that for SO_2,[23] and its absorption peaks seem by coincidence to occur just at the valleys of the SO_2 spectrum associated with the first allowed transition.[24] Presumably S_2O could form in the following sequence of reactions:

$$^1SO_2 + SO_2 \rightarrow SO_3 + SO \tag{12}$$

$$SO_3 + SO \rightarrow (SO_2)_2 \tag{13}$$

$$SO_3 + SO \rightarrow 2SO_2 \tag{14}$$

$$SO + SO \rightarrow SO_2 + S \tag{15}$$

$$S + SO \rightarrow S_2O \tag{16}$$
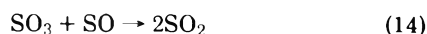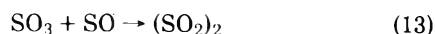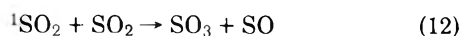
However the previous experiments of Norrish and Oldershaw[4] suggest that S_2O (then incorrectly designated as S_2O_2) is quite stable in flashed SO_2 mixtures. In view of the relatively short-lived nature of X, the attractiveness of S_2O as the X entity is diminished; certainly this possibility is not excluded but better lifetime information on S_2O samples is necessary to evaluate it properly.

X may be a transient weak dimer of SO_2, as originally suggested by Hellner and Keller.[7] Conceivably it could be formed as one of the products of the SO_3–SO reaction (eq 13) and live to encounter the wall where it may revert to $2SO_2$ molecules. The alternative formation of a transient
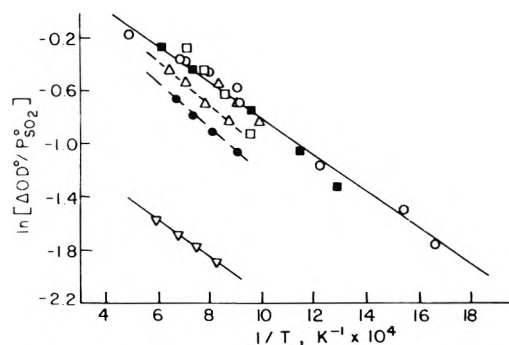
Figure 7. A further test of the "thermal equilibrium" hypothesis for X formation; plot of ln ($\Delta OD^0/P_{SO_2}{}^0$) vs. $1/T$ for flash photolyses of mixtures of SO_2-Ar, SO_2-He, and pure SO_2; the symbols $\triangle$, $\bullet$, $\square$, $\blacktriangle$, and ∇ refer to data from the sequence of runs in the order given in Table II; symbols O and ■ are from the SO_2-Ar and SO_2-He experiments, respectively, in Table III.

dimer through $^1SO_2$–$^1SO_2$ interactions, as Hellner and Keller concluded, has the incorrect kinetics to be compatible with X, and our computer simulations of the reactions which occur in this photolysis system show that the encounter rate of two $^1SO_2$ species is extremely low. Also one might imagine that a large fraction of the $^1SO_2$–$^1SO_2$ encounters would not give dimer but would lead to energy pooling in one molecule of SO_2, formirg $SO_2(^1B_2)$ and $SO_2(X,^1A_1)$; presumably the $SO_2(^1B_2)$ species would subsequently dissociate from a highly vibrationally excited level of this state.[25]

$$^1SO_2 + {}^1SO_2 \rightarrow SO_2(^1B_2) + SO_2(X,^1A_1) \tag{17}$$

$$SO_2(^1B_2) \rightarrow O(^3P) + SO(^3\Sigma) \tag{18}$$
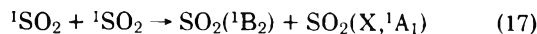
X in theory might be the illusive SO_4 species which has never been characterized but often suggested as an intermediate in SO_2 photochemical systems. The formation of SO_4 could occur by way of $O(^3P)$ atom attack on the product SO_3; this interaction in part gives SO_2 and O_2 as well:[26]

$$O(^3P) + SO_3 (+M) \rightarrow SO_4 (+M) \tag{19}$$

$$O(^3P) + SO_3 \rightarrow O_2 + SO_2 \tag{20}$$

Our computer simulations of the reaction system suggest that SO_4 formation is probably a relatively minor event in the flash photolysis of SO_2, so its consideration as X seems inappropriate. Also the transient designated as S_2O_7 in the experiments of Daubendiek and Calvert[25] should receive some attention here. It is thought to arise from the reaction $SO_4 + 2SO_2 \rightarrow S_3O_7$. However, its decay, $S_3O_7 \rightarrow 2SO_3 + SO_2$, is too slow to correlate with that observed for X (half-life, 300 s).

The "thermal isomer" hypothesis of Norrish and Oldershaw[4] remains a viable explanation of X. Conceivably the interaction between $^1SO_2$ and SO_2 which occurs in reaction 4 could result in the isomerization of an SO_2 molecule and the generation of the high-energy, highly bent form of SO_2 postulated by Hayes and Pfieffer[3b] and Chung.[3c]

Obviously several alternative explanations as to the chemical nature of X remain to be evaluated. It is apparent that the flash photolysis of SO_2 is a much more complicated system than had been pictured by the previous workers, and the characterization of the chemical nature of X remains an interesting challenge to photochemists.

References and Notes

(1) For examples of the recent spectroscopic studies of the first allowed transition in SO_2 and references to the earlier literature see: (a) J. C. Brand and R. Nanes, *J. Mol. Spectrosc.*, **46**, 194 (1973); (b) Y. Hamada and A. J. Meyer, *Can. J. Phys.*, **52**, 1443 (1974); (c) L. E. Brus and J. R. McDonald, *Chem. Phys. Lett.*, **21**, 283 (1973); (d) R. N. Dixon and M. Halle, *ibid.*, **22**, 450 (1973).

(2) For examples of the recent photochemical studies and references to the earlier literature see: (a) K. Chung, J. G. Calvert, and J. W. Bottenheim, *Int. J. Chem. Kinet.*, **7**, 161 (1975); (b) F. B. Wampler, A. Horowitz, and J. G. Calvert, *J. Am. Chem. Soc.*, **94**, 5523 (1972); (c) K. L. Demerjian and J. G. Calvert, *Int. J. Chem. Kinet.*, **7**, 45 (1975); (d) E. Cehelnik, C. W. Spicer, and J. Heicklen, *J. Am. Chem. Soc.*, **93**, 5371 (1971); (e) A. M. Fatta, E. Mathias, J. Heicklen, J. Stockburger, III, and S. Braslavsky, *J. Photochem.*, **2**, 119 (1973).

(3) For examples of the recent theoretical studies of the electronic states of SO_2 and references to the earlier literature see: (a) I. H. Hillier and V. R. Saunders, *Mol. Phys.*, **22**, 193 (1971); (b) T. F. Hayes and G. V. Pfeiffer, *J. Am. Chem. Soc.*, **90**, 4773 (1968); (c) K. Chung, "Experimental and Theoretical Study of Sulfur Dioxide", Ph.D. Thesis, The Ohio State University, Columbus, Ohio, 1974.

(4) R. G. W. Norrish and G. A. Oldershaw, *Proc. R. Soc. London, Ser. A*, **249**, 498 (1959).

(5) R. J. Donavan, D. Husain, and P. T. Jackson, *Trans. Faraday Soc.*, **65**, 2930 (1969).

(6) N. Basco and R. D. Morse, *Proc. R. Soc. London, Ser. A*, **321**, 129 (1971).

(7) C. Hellner and R. A. Keller, *J. Air Pollut. Control Assoc.*, **22**, 959 (1972).

(8) N. Basco and R. D. Morse, *Chem. Phys. Lett.*, **20**, 557 (1973).

(9) F. C. James, J. A. Kerr, and J. P. Simons, *Chem. Phys. Lett.*, **25**, 431 (1974).

(10) R. G. W. Norrish and A. P. Zeelenberg, *Proc. R. Soc. London, Ser. A*, **240**, 293 (1957).

(11) A. L. Myerson, F. R. Taylor, and P. L. Hanst, *J. Chem. Phys.*, **26**, 1309 (1957).

(12) J. J. McGarvey and W. D. McGrath, *Proc. R. Soc. London, Ser. A*, **278**, 490 (1964).

(13) L. Herman, J. Akriche, and H. Grenat, *J. Quant. Spectrosc. Radiat. Transfer*, **2**, 255 (1962).

(14) A. G. Gaydon, G. H. Kimbell, and H. B. Palmer, *Proc. R. Soc. London, Ser. A*, **267**, 461 (1963).

(15) J. Brown and G. Burns, *Can. J. Chem.*, **47**, 4291 (1969).

(16) P. A. Giguère and R. Savoie, *Can. J. Chem.*, **43**, 2357 (1965).

(17) (a) M. I. Christie and G. Porter, *Proc. R. Soc. London, Ser. A*, **212**, 398 (1952); (b) G. Wettermark, *Ark. Kemi*, **18**, 1 (1961).

(18) J. W. Bottenheim, H. W. Sidebottom, D. L. Thorsell, J. G. Calvert, and E. K. Damon, to be submitted for publication.

(19) H. D. Mettee, *J. Phys. Chem.*, **73**, 1071 (1969).

(20) T. R. Marrero and E. A. Mason, *J. Phys. Chem. Ref. Data*, **1**, 1 (1972).

(21) Landolt-Börnstein, "Transport Phenomena", 6th ed, Vol. II, Part 5, 1969.

(22) H. O. Olschewski, J. Troe, and H. G. Wagner, *Z. Phys. Chem. (Frankfurt am Main)*, **44**, 173 (1965).

(23) A. V. Jones, *J. Chem. Phys.*, **18**, 1263 (1950).

(24) E. D. Cehelnik, Ph.D. Thesis, Pennsylvania State University, University Park, Pa., 1971; we are grateful to Dr. Cehelnik for providing information on the S_2O spectrum.

(25) (a) M. H. Hui and S. A. Rice, *Chem. Phys. Lett.*, **17**, 474 (1972); (b) *ibid.*, **20**, 411 (1973).

(26) R. L. Daubendiek and J. G. Calvert, "A Photochemical Study Involving SO_2, O_2, SO_3, and O_3", presented at the 165th National Meeting of the American Chemical Soc., Dallas, Tx., April, 1973; to be submitted for publication.

Relative Rate Constants for Reaction of the Hydroxyl Radical with a Series of Alkanes, Alkenes, and Aromatic Hydrocarbons

Alan C. Lloyd, Karen R. Darnall, Arthur M. Winer, and James N. Pitts, Jr.*

Statewide Air Pollution Research Center, University of California, Riverside, California 92502 (Received October 21, 1975)

Publication costs assisted by the National Science Foundation-RANN and California Air Resources Board

The relative rates of disappearance in air at 305 ± 2 K of a set of 14 alkanes, alkenes, and aromatic hydrocarbons were measured in an environmental chamber under simulated atmospheric conditions. The observed rates of disappearance were used to derive relative rates of reaction with the hydroxyl radical (OH) on the previously validated basis that OH is the species dominantly responsible for the hydrocarbon disappearance under the experimental conditions employed. Absolute rate constants, obtained from the relative values by using the mean of the published rate constants for OH + n-butane (1.8×10^9 M^{-1} s^{-1}), are ($k \times 10^{-9}$ M^{-1} s^{-1}): isopentane, 2.0 ± 0.4; 2-methylpentane, 3.2 ± 0.6; 3-methylpentane, 4.3 ± 0.9; n-hexane, 3.8 ± 0.8; m-xylene, 12.9 ± 2.6; n-propylbenzene, 3.7 ± 0.8; isopropylbenzene, 3.7 ± 0.8; ethylbenzene, 4.8 ± 1.0; o-ethyltoluene, 8.2 ± 1.6; m-ethyltoluene, 11.7 ± 2.3; p-ethyltoluene, 7.8 ± 1.6; ethene, 5.2 ± 1.0; propene, 17.5 ± 3.5; cis-2-butene; 39.2 ± 8.0; 1,3-butadiene, 46.4 ± 9.3. In the case of seven of the compounds investigated these results are shown to be in good agreement with literature values reported for elementary rate constant determinations. For the remaining seven compounds no previous determinations have been made.

Introduction

The hydroxyl radical is well known to be an important species in the chemistry of combustion systems,[1,2] the stratosphere,[3-5] and the troposphere.[6-9] Recent direct determinations of its concentration in ambient air[10,11] have shown average daytime levels of about 5×10^6 molecule cm^{-3} in good agreement with predictions from computer models of the formation of photochemical air pollution.[6,12-14]

In order to develop satisfactory chemical mechanisms for modeling combustion and photooxidation systems includ-

ing urban airshed models,[15,16] kinetic data for the reactions of the OH radical with hydrocarbons, as well as various inorganic species, are necessary. Prior to 1970 relatively few absolute rate constants were available for OH reactions with organic species; however, since then a large number of determinations have been reported for alkanes[17-27] and alkenes.[21-23,28-36] Although aromatic compounds such as toluene, xylenes, propylbenzene, m-ethyltoluene, and 1,2,3- and 1,2,4-trimethylbenzenes are present in polluted ambient air,[37-39] only in the past few years have significant studies been reported on the reactions of the OH radical with some of these aromatics.[21,40-42] For example, recently we reported the use of an environmental chamber to obtain accurate relative rate constants for the gas phase reaction of hydroxyl radicals with a series of aromatic hydrocarbons using n-butane as the reference compound.[42] Although a number of other species are present in these experiments (i.e., O(^{3}P), HO$_2$, O$_3$, NO$_3$, etc.), with the exception of O$_3$ in the case of the alkenes, these species have been shown to make at most minor contributions to the observed disappearance of the hydrocarbons investigated. Thus, the rate constants determined in our previous study[42] are in good agreement with those determined subsequently in separate studies of the reactions of individual compounds with OH using a flash photolysis–resonance fluorescence technique.[40,41]

On the basis of this validation of the environmental chamber method, we have extended our investigation to include an additional six aromatic hydrocarbons, four alkanes, and four alkenes.

Experimental Section

Irradiations of the HC–NO$_x$–air system were carried out in an all-glass (Pyrex) chamber of approximately 6400-l. volume equipped with two externally mounted, diametrically opposed banks of Sylvania 40 BL fluorescent lamps.[43] Before each experiment the chamber was flushed for a minimum of 2 h at a rate of 12–15 scfm with a purified air stream.[44] The resulting matrix air contained less than ~1 × 10^{-9} M (100 ppb C) of nonmethane hydrocarbons. All reactants were injected into the chamber using 100-ml precision bore syringes and rapid mixing was obtained using Teflon-coated sonic pumps. During irradiation, the chamber temperature was maintained at 305 ± 2 K by passing chilled air between the chamber walls and the fluorescent lamp banks.

Hydrocarbon disappearance was measured by gas chromatography using the columns and techniques developed by Stephens and Burleson.[37,45] Ozone[46] was monitored by means of ultraviolet absorption (Dasibi Model 1003 analyzer), carbon monoxide by gas chromatography (Beckman 6800 Air Quality analyzer), and NO–NO$_2$–NO$_x$ by the chemiluminescent reaction of NO with ozone (TECO Model 14B).

The concentrations of the reactants ranged between 4.5 and 9.0 × 10^{-10} M (11–22 ppb in air) except for ethene, ethane, acetylene, and n-butane whose concentrations were 1.8, 3.7, 1.8, and 8.3 × 10^{-9} M (45, 92, 45, and 203 ppb in air), respectively. In addition low concentrations of carbonyl compounds (formaldehyde, acetaldehyde, and acetone) were present. Initial concentrations in the photolysis experiments were 27 × 10^{-9} M (2900 ppb C) of total nonmethane hydrocarbons, 1.75 × 10^{-9} M (0.43 ppm) of NO$_x$ (with an NO$_2$/NO$_x$ ratio of 0.12), 28.5 × 10^{-9} M (7 ppm) of CO, and 112.9 × 10^{-9} M (2775 ppb) of methane together

with water at 50% relative humidity. Four replicate experiments were carried out in which this mixture was irradiated for 3 h with continuous analysis of inorganic species and analysis of hydrocarbons every hour. The irradiation period was extended from 2 to 3 h compared with our earlier study in order to obtain additional data points. The light intensity, measured as the rate of NO$_2$ photolysis in nitrogen, k_1,[47] was approximately 0.26 min^{-1}. All data were corrected for losses due to sampling from the chamber (0.9–2.0%/h) by subtraction of the average dilution rate from the observed hydrocarbon disappearance rate. Although the HC/NO$_x$ ratio was chosen to delay the formation of ozone, after 3 h of irradiation the ozone concentration was 0.065 × 10^{-9} M (0.016 ppm) or less in three of the runs and 0.13 × 10^{-9} M (0.031 ppm) in the fourth (which had a higher initial formaldehyde concentration). A small correction for loss of hydrocarbon due to reaction with ozone was applied to the alkene disappearance rates.

Results

The rates of disappearance observed during a 3-h run for the seven aromatic hydrocarbons, four alkanes, and four alkenes are shown in Figures 1–3, respectively (n-butane is included as the reference compound in each figure). Table I gives the disappearance rates for these reactants (after application of the dilution correction and for alkenes, the ozone correction), relative to that for n-butane, based on data from the four separate experiments.

With the assumption that the OH radical is the species responsible for the hydrocarbon depletion during the 3-h irradiation, absolute rate constants were derived from the relative rates of disappearance using a value of 1.8 × 10^9 M^{-1} s^{-1} as the mean of the existing literature values for the reaction of OH with n-butane[21,23,24,27]

$$OH + n\text{-}C_4H_{10} \rightarrow H_2O + C_4H_9 \tag{1}$$
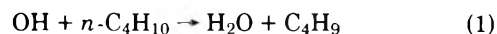
These results are shown in Table I and are compared with existing literature values whenever possible in Table II.

Discussion

As seen from Table II, the validation of the assumption that the OH radical is by far the major species depleting the hydrocarbons (during the first 2–3 h of reaction) has been provided by the good agreement observed between OH rate constants determined in our previous chamber study[42] for benzene, toluene, o-, m-, and p-xylenes, and the trimethylbenzenes with those determined in elementary reaction studies of each individual hydrocarbon.[40,41] The extent to which this assumption is valid is indicated by the results of computer modeling calculations[48] (shown in Figure 4) for an HC–NO$_x$ system of overall concentrations identical with that used in this study. In the computer simulation a propene and n-butane mixture was used as a surrogate for the complex hydrocarbon mixture employed in the experiment and the rate of attack on propene by OH, O$_3$, O(^{3}P), and HO$_2$ was calculated. The relative and total concentrations of propene and n-butane were chosen such that the overall hydrocarbon reactivity toward the OH radical would equal that predicted for the complex mixture. It is clear from Figure 4 that, although OH is the major attacking species in these experiments, the O$_3$ contribution to the disappearance rates of the alkenes increases with time of irradiation. In contrast the rates of reaction of O$_3$ with alkanes and aromatics are many orders of magnitude slower[50-52] than with alkenes[49,53] and no correction for
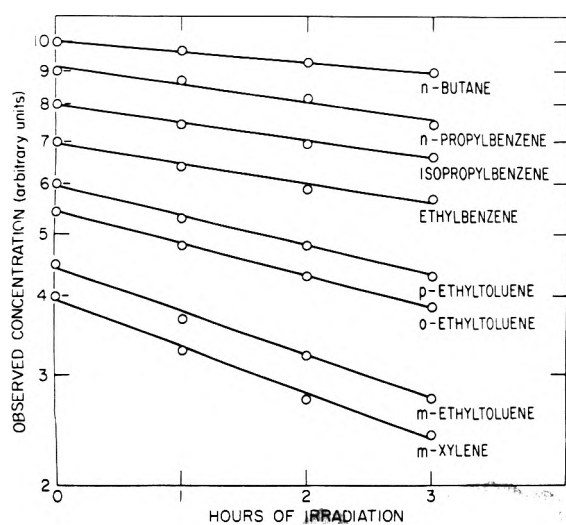
Figure 1. Logarithm of the aromatic hydrocarbon concentration during 3-h photolysis of HC–NO$_x$ mixture in air at 305 ± 2 K and 1 atm.
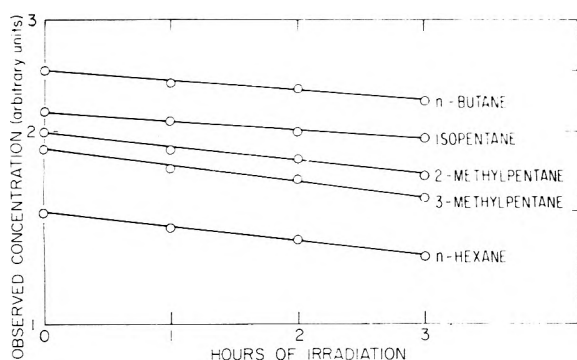
Figure 2. Logarithm of concentrations of alkanes during 3-h photolysis of HC–NO$_x$ mixture in air at 305 ± 2 K and 1 atm.
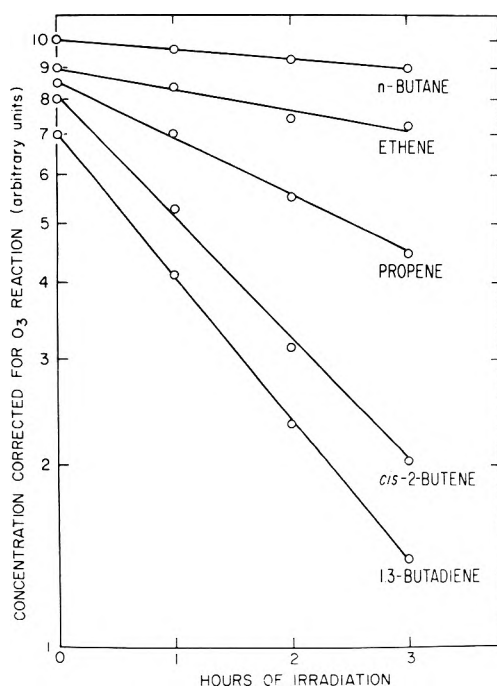
Figure 3. Logarithm of concentrations of alkenes during 3-h photolysis of HC–NO$_x$ mixture in air at 305 ± 2 K and 1 atm.

TABLE I: Rates of Disappearance and Rate Constants for Selected Alkanes, Alkenes, and Aromatic Hydrocarbons at 1 atm in Air at 305 ± 2 K

Compound	Relative rate of disappearance	$10^{-9}k,$[a] $M^{-1} s^{-1}$
n-Butane	1	1.8[b]
Isopentane	1.10	2.0 ± 0.4
2-Methylpentane	1.77	3.2 ± 0.6
3-Methylpentane	2.40	4.3 ± 0.9
n-Hexane	2.09	3.8 ± 0.8
m-Xylene	7.18	12.9 ± 2.6
n-Propylbenzene	2.07	3.7 ± 0.8
Isopropylbenzene	2.03	3.7 ± 0.8
Ethylbenzene	2.65	4.8 ± 1.0
o-Ethyltoluene	4.57	8.2 ± 1.6
m-Ethyltoluene	6.49	11.7 ± 2.3
p-Ethyltoluene	4.33	7.8 ± 1.6
Ethene	2.88	5.2 ± 1.0
Propene	9.70	17.5 ± 3.5
1,3-Butadiene	25.8	46.4 ± 9.3
cis-2-Butene	21.8	39.2 ± 8.0

[a] The indicated error limits are ±20% and are the estimated overall error limits. [b] Placed on an absolute basis using the mean of the literature values; ref 21, 23, 24, and 27.

TABLE II: Rate Constants, k, for OH Radical Reactions with n-Butane and Selected Alkane, Alkenes, and Aromatic Hydrocarbons at Room Temperature

Compound	$10^{-9}k$, $M^{-1} s^{-1}$ Environmental chamber studies[a,b]	Lit. values
Benzene	≤2.3[a]	0.74 ± 0.07[c]
		0.95 ± 0.07[d]
Toluene	2.5 ± 0.9[a]	3.47 ± 0.35[c]
		3.67 ± 0.24[d]
o-Xylene	7.7 ± 2.3[a]	9.18 ± 0.90,[c] 11[e]
m-Xylene	14 ± 1[a]	14.2 ± 1.4[c]
	12.9 ± 2.6[b]	11[e]
p-Xylene	7.4 ± 1.5[a]	7.32 ± 0.72,[c] 11[e]
1,2,3-Trimethylbenzene	14 ± 3[a]	15.8 ± 1.6[c]
1,2,4-Trimethylbenzene	20 ± 3[a]	20.1 ± 2.0[c]
1,3,5-Trimethylbenzene	31 ± 4[a]	28.3 ± 2.9[c]
Isopentane	2.0 ± 0.4[b]	2.7[f]
2-Methylpentane	3.2 ± 0.6[b]	3.4[f]
3-Methylpentane	4.3 ± 0.9[b]	3.4[f]
n-Hexane	3.8 ± 0.8[b]	2.9[f]
Ethene	5.2 ± 1.0[b]	5.7 ± 0.6[g]
		1.1,[h] 3.0,[i] 3.2 ± 0.4,[j]
		3.0,[k] 1.8 ± 0.6[l]
		1.0 ± 0.3,[m] 1.3 ± 0.1[n]
Propene	17.5 ± 3.5[b]	21.7 ± 2.4[g]
		10.2 ± 2.6[h]
		8.7 ± 1.3,[l] 15.1 ± 1.5,[o]
		9.6 ± 0.3,[p] 3.0 ± 1.0,[m]
		3.0 ± 0.6[n]
cis-2-Butene	39.2 ± 8.0[b]	36.7,[h] 32.3 ± 3.2,[o]
		25.7 ± 1.5[p]

[a] Reference 42. [b] From Table I. [c] Reference 40. [d] Reference 41. [e] Reference 21 for a mixture of xylene isomers. [f] Reference 24. [g] Reference 33. [h] References 30 and 21. [i] Reference 31. [j] Reference 36. [k] Reference 29. [l] Reference 28. [m] Reference 22. [n] Reference 32. [o] Reference 35. [p] Reference 34.
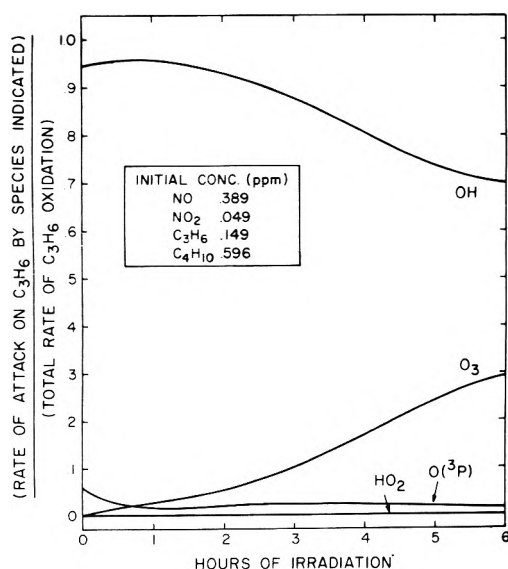
Figure 4. Predicted relative importance of several reactive intermediates during photooxidation of propene–*n*-butane mixture under simulated atmospheric conditions.

their reaction with ozone was necessary. For example, the rate constant for the reaction of ozone with toluene is about nine orders of magnitude lower than that for OH with toluene. During the initial hours of irradiation other species such as NO_3[55] and HO_2[56] may contribute slightly to hydrocarbon disappearance rates, especially for alkenes, but since their concentrations, and in some cases rate constants, are not known, correction was not possible.

Hydroxyl Radical Source in this System. The major sources of OH in our experimental system are probably the reactions[7,8,13,15]

$$NO + NO_2 + H_2O = 2HONO \qquad (2)$$

$$HONO + h\nu \ (290–410 \ nm) \rightarrow OH + NO \qquad (3)$$

$$HO_2 + NO \rightarrow OH + NO_2 \qquad (4)$$
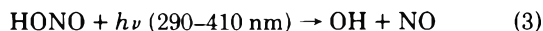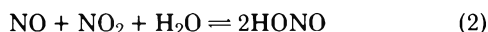
Nitrous acid has been observed in a chamber study of simulated atmospheres carried out in our laboratory[57] when a mixture of propene and nitrogen oxides in moist air was photolyzed, indicating that HONO can be formed in HC/NO_x systems under conditions similar to those employed in the present study (Nash[58] claims to have measured HONO in ambient air, at levels up to 11 ppb). Direct evidence for formation of OH radicals in environmental chambers has been provided recently by Niki, Weinstock, and coworkers.[11,54] Reaction 4, of major importance, provides a further source of the OH radical. HO_2 can be formed in air[56,59] by any mechanism producing H atoms or formyl radicals via the reactions

$$H + O_2 + M \rightarrow HO_2 + M \qquad (5)$$

$$HCO + O_2 \rightarrow HO_2 + CO \qquad (6)$$
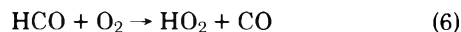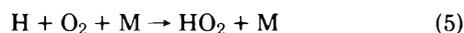
Thus any mechanism producing HO_2 in our system is also a means of furnishing OH radicals via reaction 4.

The concentration of OH radicals present during these experiments was calculated to be (1.5–2.0) × 10^6 molecules cm^{-3} using the observed rates of *m*-xylene disappearance (corrected for dilution) and the previously determined rate constant for OH + *m*-xylene.[40,42] These concentrations are

of the same order as those observed directly in ambient air[10,11] as discussed above.

Aromatic Hydrocarbons. Present results for the rate constant for the reaction of OH with *m*-xylene show good agreement with the previous study[42] carried out in our laboratory (Table II), indicating good reproducibility for this technique.

Rate constants for the reaction of OH with the propylbenzenes and ethyltoluenes have not been reported previously. However, the trend in rate constants for the reaction with *o*-, *m*-, and *p*-ethyltoluene is identical with that previously determined for the xylenes[40,42] which supports the concept that OH is an electrophilic species, since attack on the meta compound is favored.

Davis et al.[41] have studied the reaction of OH with benzene and toluene and from the observed pressure dependence of the reactions, conclude that addition occurs at least 50% of the time. In an environmental chamber study similar to that reported here, Schwartz et al.[60] tentatively identified a number of aerosol products such as phenols and aromatic nitro compounds from the photooxidation of toluene in the presence of nitrogen oxides. A mechanism was proposed assuming initial addition of OH to the aromatic ring. In the case of the more highly substituted aromatic compounds studied here, it may be possible that hydrogen abstraction from the side chain could possibly be as important as addition. This is supported by the fact that a log plot of the OH–aromatic hydrocarbon rate constants vs. the ionization potential of the hydrocarbon (which, for abstraction reactions, is expected to be linear) in this case did not yield a straight line.

Detailed product studies are required in order to obtain the quantitative data necessary to further elucidate the mechanism of OH attack on various aromatic hydrocarbons.

Alkanes. Greiner[24] has derived an empirical formula for calculating the rates of reaction of OH with alkanes based on his experimental results for the reaction of the OH radical with selected alkanes:

$$k = 6.15 \times 10^8 N_1 \exp(-1635/RT)$$
$$+ 14.1 \times 10^8 N_2 \exp(-850/RT)$$
$$+ 12.6 \times 10^8 N_3 \exp(+190/RT) \ M^{-1} \ s^{-1}$$

where N_1, N_2, and N_3 are the numbers of primary, secondary, and tertiary hydrogen atoms, respectively, in the alkane. We have used this equation to calculate the rate constants for isopentane, 2- and 3-methylpentane, and *n*-hexane. The calculated values are in quite good agreement with the experimental values. Although Greiner's formula predicts the same rate constants for the 2- and 3-methylpentanes, our study suggests that the latter is somewhat higher. Indeed this may be expected since the stability of the radical formed by the abstraction of the tertiary H atom from 3-methylpentane should be greater than that for the radical formed from similar attack in the 2-methylpentane case.

Alkenes. Unlike the alkanes and the aromatic compounds, alkenes react with ozone at a significant rate. Thus, in our experimental system, the small amounts of O_3 formed during the 3-h photolyses contributed to the alkene disappearance rates. From the measured concentrations of ozone and the published rate constants for the reaction of O_3 with the alkenes studied,[49,53,61–63] a correction was made to the alkene disappearance rates for loss due to reaction with ozone. This amounted to ~3% for ethene, ~7% for

propene, ~21% for cis-2-butene, and ~2% for 1,3-butadiene.

Our results for the reaction of OH with propene

$$OH + C_3H_6 \rightarrow products \tag{7}$$
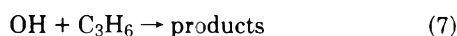
are within experimental error of a recent absolute determination of k_7 using flash photolysis–resonance fluorescence,[35] while the value of k_7 given in Table II for the result of Cox[33] incorporates a stoichiometry factor of 2 to 3. In parallel studies in this laboratory using flash photolysis–resonance fluorescence[35] no evidence was found within experimental error of a pressure effect for k_7 by varying the total pressure from 25 to 100 Torr of argon, but additional studies should be carried out, especially at lower pressures where such an effect would become evident, to see whether k_7 exhibits any pressure dependence.

The value of the rate constant obtained in this study for the reaction of OH with cis-2-butene, though somewhat high, is within experimental error of values previously reported from direct determinations.[21,34,35] In this case a significant (21%) correction for reaction with O_3 had to be applied to the data.

No previous determinations of absolute rate constants have been reported for the reaction of OH with 1,3-butadiene. However, the close agreement between our values for cis-2-butene and 1,3-butadiene is consistent with the work by Cvetanovic and Doyle[64] who showed that these two compounds reacted at similar rates with oxygen atoms.

The value obtained in this study for the rate constant of the reaction

$$OH + C_2H_4 \rightarrow products \tag{8}$$
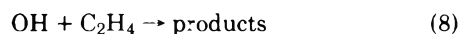
of 5.2×10^9 M^{-1} s^{-1} is about a factor of 2 higher than published values from low pressure (<300 Torr) studies.[21,22,28-32,36] The only other study to date carried out at atmospheric pressure is that recently reported by Cox,[33] in which OH was generated by photolyzing gaseous nitrous acid in nitrogen/oxygen mixtures (2:1) at 760 Torr and the effect of added alkenes on the photolysis of nitrous acid was studied. A rate constant $\alpha k_8 = (5.7 \pm 0.6) \times 10^9$ M^{-1} s^{-1} was obtained relative to a value of 9.0×10^7 M^{-1} s^{-1} for the reaction of OH with CO, where α is a stoichiometry factor. Cox suggests that α is between 2 and 3 based on published values for the direct determination of k_8. Davis et al.[36] have shown that the significant differences between low pressure measurements of reaction 8 can be rationalized by the fact that the reaction exhibits a pressure dependence over the region studied (3 to 300 Torr of He).

This pressure dependence is probably due to the initial formation of the adduct observed by Niki and coworkers.[21,30] Presumably this adduct becomes stabilized by collisional deactivation

$$OH + C_2H_4 \xrightarrow{M} \dot{C}H_2CH_2OH \tag{8a}$$

While it is possible that our determination of k_8 is higher than previous values due to the fact that species other than OH and O_3 are depleting the ethene, at least part of the discrepancy may be due to the difference in pressure regions studied. Figure 5 shows a plot of log k_8 vs. log P where P is the total pressure in the system for studies carried out using N_2, O_2, or N_2O as diluent gases. Studies carried out using less efficient third body gases such as He are not plotted since the present study is focused on ambient atmospheric conditions and third bodies such as N_2 or the
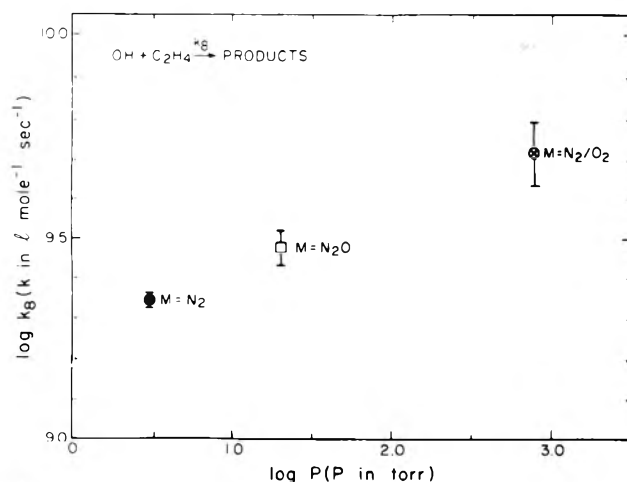
Figure 5. Variation with pressure of the rate constant k_8 for the reaction of OH with C_2H_4; M is "bath gas" in reaction 8: (●) Davis et al.;[36] (□) Smith and Zellner;[31] (⊗) this work.

equivalent. Thus, at 3 Torr of diluent gas, the results of Davis et al.[36] differ by a factor of 1.6 depending on whether N_2 or He is used as the diluent gas. Although our results for ethene are subject to some uncertainty, it appears possible that reaction 8 is not at the limiting high pressure kinetics region until the pressure exceeds 1 atm.

Conclusions

Relative rate constants have been determined for the reaction of OH with 14 hydrocarbons and these rate constants have been placed on an absolute basis using the literature values for the rate constant of OH + n-butane. No previous determinations have been reported in the case of seven of these compounds.

Our results indicate that the reaction of OH with ethene possibly does not obey second-order kinetics until pressures exceed 1 atm while for propene and the higher alkenes the reactions are second order at atmospheric pressure.

The comparatively high rates of reaction observed for the aromatic hydrocarbons have significant implications for the control of photochemical air pollution. This subject and the use of the present data in the formulation of a hydrocarbon reactivity scale has been treated in detail elsewhere.[65]

References and Notes

(1) R. R. Baker, R. R. Baldwin, and R. W. Walker, *Symp. (Int.) Combust. [Proc.]*, *13th*, 291 (1971).

(2) D. D. Drysdale and A. C. Lloyd, *Oxid. Combust. Rev.*, **4**, 157 (1970); W.

E. Wilson, Jr., *J. Phys. Chem. Ref. Data,* **1,** 535 (1972).

(3) H. S. Johnston, *Adv. Environ. Sci. Technol.,* **4,** 263 (1974).

(4) P. Crutzen, *Can. J. Chem.,* **52,** 1569 (1974).

(5) M. B. McElroy, S. C. Wofsy, J. E. Penner, and J. C. McConnell, *J. Atmos. Sci.,* **31,** 287 (1974).

(6) H. Levy, II, *Adv. Photochem.,* **9,** 369 (1974).

(7) K. L. Demerjian, J. A. Kerr, and J. G. Calvert, *Adv. Environ. Sci. Technol.,* **4,** 1 (1974).

(8) H. Niki, E. E. Daby, and B. Weinstock, *Adv. Chem. Ser.,* **No. 113,** 16 (1972).

(9) J. N. Pitts, Jr., and B. J. Finlayson, *Angew. Chem., Int. Edit. Engl.,* **14,** 1 (1975).

(10) C. C. Wang and L. I. Davis, Jr., *Phys. Rev. Lett.,* **32,** 349 (1974).

(11) C. C. Wang, L. I. Davis, Jr., C. H. Wu, S. Japar, H. Niki, and B. Weinstock, *Science,* **189,** 797 (1975).

(12) B. Weinstock and H. Niki, *Science,* **176,** 290 (1972).

(13) B. Weinstock and T. Y. Chang, *Tellus,* **26,** 108 (1974).

(14) J. G. Calvert and R. D. McQuigg, Proceedings of the Symposium on Chemical Kinetics Data for the Upper and Lower Atmosphere, Warrenton, Va., Sept. 15–18, 1974; *Int. J. Chem. Kinet.,* Symposium No. 1, 113 (1975).

(15) T. A. Hecht, J. H. Seinfeld, and M. C. Dodge, *Environ. Sci. Technol.,* **8,** 327 (1974).

(16) A. Q. Eschenroeder and J. R. Martinez, *Adv. Chem. Ser.,* **No. 113,** 101 (1972).

(17) D. D. Davis, S. Fischer, and R. Schiff, *J. Chem. Phys.,* **61,** 2213 (1974).

(18) R. Overend, G. Paraskevopoulos, and R. J. Cvetanovic, 11th Informal Conference on Photochemistry, Vanderbilt University, Tenn., June 1974.

(19) J. Margitan, F. Kaufman, and J. G. Anderson, *Geophys. Res. Lett.,* **1,** 80 (1974).

(20) S. Gordon and W. A. Mulac, Proceedings of the Symposium on Chemical Kinetics Data for the Lower and Upper Atmosphere, Warrenton, Va., Sept. 15–18, 1974; *Int. J. Chem. Kinet.,* Symposium No. 1, 289 (1975).

(21) E. D. Morris, Jr., and H. Niki, *J. Phys. Chem.,* **75,** 3640 (1971).

(22) J. N. Bradley, W. Hack, K. Hoyermann, and H. Gg. Wagner, *J. Chem. Soc., Faraday Trans. 1,* **69,** 1889 (1973).

(23) R. A. Gorse and D. H. Volman, *J. Photochem.,* **1,** 1 (1972); **3,** 115 (1974).

(24) N. R. Greiner, *J. Chem. Phys.,* **53,** 1070 (1970).

(25) N. R. Greiner, *J. Chem. Phys.,* **46,** 3389 (1967).

(26) J. Peeters and G. Mahnen, *Symp. (Int.) Combust. [Proc.], 14th,* 113 (1973).

(27) F. Stuhl, *Z. Naturforsch. A,* **28,** 1383 (1973).

(28) F. Stuhl, *Ber. Bunsenges. Phys. Chem.,* **77,** 674 (1973).

(29) N. R. Greiner, *J. Chem. Phys.,* **53,** 1284 (1970).

(30) E. D. Morris, Jr., D. H. Stedman, and H. Niki, *J. Am. Chem. Soc.,* **93,** 3570 (1971).

(31) I. W. M. Smith and R. Zellner, *J. Chem. Soc., Faraday Trans. 2,* **69,** 1617 (1973).

(32) A. V. Pastrana and R. W. Carr, Jr., *J. Phys. Chem.,* **79,** 765 (1975).

(33) R. A. Cox, Proceedings of the Symposium on Chemical Kinetics Data for the Lower and Upper Atmosphere, Warrenton, Va., Sept. 15–18, 1974; *Int. J. Chem. Kinet.,* Sypposium No. 1, 379 (1975).

(34) S. Fischer, R. Schiff, E. Machado, W. Bollinger, and D. D. Davis, 169th National Meeting of the American Chemical Society, Philadelphia, Pa., April 6–11, 1975.

(35) R. Atkinson and J. N. Pitts, Jr., *J. Chem. Phys.,* **63,** 3591 (1975).

(36) D. D. Davis, S. Fischer, R. Schiff, R. T. Watson, and W. Bollinger, *J. Chem. Phys.,* **63,** 1707 (1975).

(37) E. R. Stephens, "Hydrocarbons in Polluted Air", Summary Report, CRC Project CAPA-5-68, June 1973.

(38) A. P. Altshuller, S. L. Kopczynski, W. A. Lonneman, F. D. Sutterfield, and D. L. Watson, *Environ. Sci. Technol.,* **4,** 44 (1970).

(39) H. Mayrsohn, M. Kuremoto, J. H. Crabtree, T. D. Sothern, and S. H. Mano, "Atmospheric Hydrocarbon Concentrations", June–Sept., 1974, California Air Resources Board, April 1975.

(40) D. A. Hansen, R. Atkinson, and J. N. Pitts, Jr., *J. Phys. Chem.,* **79,** 1763 (1975).

(41) D. D. Davis, W. Bollinger, and S. Fischer, *J. Phys. Chem.,* **79,** 293 (1975).

(42) G. J. Doyle, A. C. Lloyd, K. R. Darnall, A. M. Winer, and J. N. Pitts, Jr., *Environ. Sci. Technol.,* **9,** 237 (1975).

(43) J. N. Pitts, Jr., P. J. Bekowies, G. J. Doyle, J. M. McAfee, and A. M. Winer, "An Environmental Chamber-Solar Simulator Facility for the Study of Atmospheric Photochemistry", to be submitted for publication.

(44) G. J. Doyle, P. J. Bekowies, A. M. Winer, and J. N. Pitts, Jr., "A Charcoal-Adsorption Air Purification System for Chamber Studies Investigating Atmospheric Photochemistry", *Environ. Sci. Technol.,* submitted for publication.

(45) E. R. Stephens and F. R. Burleson, *J. Air Pollut. Control Assoc.,* **17,** 147 (1967).

(46) Ozone measurement was based on calibration by the 2% neutral buffered KI method and was subsequently corrected from spectroscopic calibration data (see J. N. Pitts, Jr., J. M. McAfee, W. Long, and A. M. Winer, *Environ. Sci. Technol.,* in press).

(47) J. R. Holmes, R. J. O'Brien, J. H. Crabtree, T. A. Hecht, and J. H. Seinfeld, *Environ. Sci. Technol.,* **7,** 519 (1973).

(48) W. P. Carter, A. C. Lloyd, and J. N. Pitts, Jr., unpublished results.

(49) D. H. Stedman, C. H. Wu, and H. Niki, *J. Phys. Chem.,* **77,** 2511 (1973).

(50) D. H. Stedman and H. Niki, *Environ. Lett.,* **4,** 303 (1973).

(51) J. J. Bufalini and A. P. Altshuller, *Can. J. Chem.,* **45,** 2243 (1965).

(52) P. L. Hanst, E. R. Stephens, W. E. Scott, and R. C. Doerr, "Atmospheric Ozone-Olefin Reactions", The Franklin Institute, Philadelphia, Pa., 1958.

(53) S. M. Japar, C. H. Wu, and H. Niki, *J. Phys. Chem.,* **78,** 2318 (1974).

(54) H. Niki and B. Weinstock, Environmental Protection Agency Seminar, Washington, D.C., Feb., 1975.

(55) S. M. Japar and H. Niki, *J. Phys. Chem.,* **79,** 1629 (1975).

(56) A. C. Lloyd, *Int. J. Chem. Kinet.,* **VI,** 169 (1974).

(57) J. M. McAfee, J. N. Pitts, Jr., and A. M. Winer, "In-Situ Long-Path Infrared Spectroscopy of Photochemical Air Pollutants in an Environmental Chamber", presented at the Pacific Conference on Chemistry and Spectroscopy, San Francisco, Calif., Oct. 16–18, 1974.

(58) T. Nash, *Tellus,* **26,** 175 (1974).

(59) J. G. Calvert, J. A. Kerr, K. L. Demerjian, and R. D. McQuigg, *Science,* **175,** 751 (1972).

(60) W. E. Schwartz, P. W. Jones, C. J. Riggle, and D. F. Miller, "Chemical Characterization of Model Aerosols", EPA-650/3-74-011, Aug. 1974.

(61) F. S. Toby and S. Toby, Proceedings of the Symposium on Chemical Kinetics Data for the Upper and Lower Atmosphere, Warrenton, Va., Sept. 15–18, 1974; *Int. J. Chem. Kinet.,* Symposium No. 1, 197 (1975).

(62) K. H. Becker, U. Schurath, and H. Seitz, *Int. J. Chem. Kinet.,* **6,** 725 (1974).

(63) R. E. Huie and J. T. Herron, Proceedings of the Symposium on Chemical Kinetics Data for the Upper and Lower Atmosphere, Warrenton, Va., Sept. 15–18, 1974; *Int. J. Chem. Kinet.,* Symposium No. 1, 165 (1975).

(64) R. J. Cvetanovic and L. C. Doyle, *Can. J. Chem.,* **38,** 2187 (1960).

(65) K. R. Darnall, A. C. Lloyd, A. M. Winer, and J. N. Pitts, Jr., *Environ. Sci. Technol.,* in press.

Ion–Molecule Reactions of Substituted Cyclopropanes by Ion Cyclotron Resonance Spectroscopy

David A. Luippold[1a] and J. L. Beauchamp*[1b]

Arthur Amos Noyes Laboratory of Chemical Physics,[1c] California Institute of Technology, Pasadena, California 91125 (Received November 17, 1975)

The gas phase ion chemistry of cyclopropane and a variety of its monosubstituted derivatives ($c\text{-}C_3H_5X$, with X = H, Cl, NH_2, CN, OH, and $COCH_3$) has been investigated utilizing ion cyclotron resonance techniques. Reactions of ions with cyclopropane involve most prominently formation of a reaction intermediate from which loss of ethylene and to a lesser extent loss of methyl or ethyl radical occurs. The ion chemistry of substituted cyclopropanes is dominated entirely by the substituent and is markedly different from cyclopropane. In addition to the increased prominence of the protonated parent ion and its corresponding association products, loss of neutrals HX (e.g., HCl) from reaction intermediates becomes significant. Ion–molecule reaction rate constants are extracted and compared for the important reaction pathways of each of the cyclopropanes examined.

Introduction

The gas phase ion chemistry of small ring compounds, particularly of cyclopropanes, has been a subject of growing interest in recent years.[2-8] Such techniques as mass spectrometry,[2-5] gas phase radiolysis,[6] and ion cyclotron resonance spectroscopy (ICR)[7,8] have been used to study cyclopropane. In the present work the gas phase ion chemistry of cyclopropane and a variety of its monosubstituted derivatives ($c\text{-}C_3H_5X$ with X = H, Cl, NH_2, CN, OH, and $COCH_3$) has been investigated using ICR techniques. In addition to presenting the characteristic gas phase ion-molecule reaction sequences and providing absolute rate constants in substituted cyclopropanes, the present investigation probes the synergetic relationship between the reactivity of the cyclopropane ring system and its substituent. For comparison, the ion chemistry of the alkyl analogs of the six substituents considered here is already fairly well characterized in the literature. Interest in the cyclopropyl group as an unusual substituent dates from the original studies by Roberts and others of its effect on acid ionization and solvolytic reactivity of organic functional groups.[9]

Experimental Section

The techniques and instrumentation for ICR studies have been described elsewhere.[10-12] Where required, compounds were purified by gas chromatography. Chemicals were commercially available except for cyclopropyl chloride, supplied by Professor J. D. Roberts, and cyclopropanol, which was synthesized by treating ethyl magnesium bromide etherate with epichlorohydrin, followed by hydrolysis.[13] Noncondensable impurities were removed from all samples prior to use by freeze–pump–thaw cycles at liquid nitrogen temperatures. Rate constants were calculated from single resonance intensities using a program written by T. B. McMahon in these laboratories, as adapted from the analysis of Buttrill[14] and Marshall and Buttrill.[15]

Results

Cyclopropane. The reaction of ions with cyclopropane involve most prominently formation of a reaction complex from which loss of ethylene (reaction 1) and to a lesser ex-

tent loss of methyl or ethyl radical occurs (reactions 2 and 3).[2-8] At low electron energy (12 eV) only the parent ion

$$R^+ + c\text{-}C_3H_6 \left\{ \begin{array}{ll} \rightarrow RCH_2^+ + C_2H_4 & (1) \\ \rightarrow RC_2H_3^+ - CH_3 & (2) \\ \rightarrow RCH^+ + C_2H_5 & (3) \end{array} \right.$$
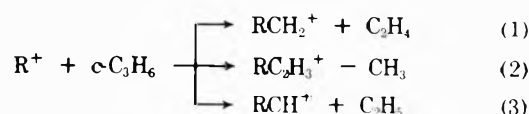
(97%) and the fragment $C_3H_5^+$ (3%) comprise the observed ions. As the pressure is increased (Figure 1), a complex sequence of reactions is observed. The major products resulting from reaction of the parent ion are $C_4H_7^+$, $C_4H_8^+$, and $C_5H_9^+$ formed in reactions 4–6, which exemplify the gener-

$$C_3H_6^+ + c\text{-}C_3H_6 \left\{ \begin{array}{lll} \overset{25\%}{\longrightarrow} & C_4H_7^+ + C_2H_5 & (4) \\ \overset{71\%}{\longrightarrow} & C_4H_8^+ + C_2H_4 & (5) \\ \overset{4\%}{\longrightarrow} & C_5H_9^+ + CH_3 & (6) \end{array} \right.$$
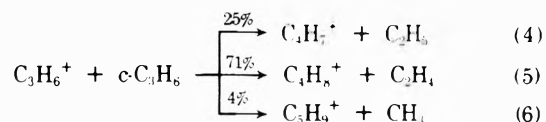
al processes 1–3. The major product ion $C_4H_8^+$ is the principle source of $C_5H_9^+$ and $C_6H_{11}^+$ evident at the highest pressures in Figure 1. Reactions 7 and 8 are again analo-

$$C_4H_8^+ + C_3H_6 \left\{ \begin{array}{ll} \rightarrow C_6H_{11}^+ + CH_3 & (7) \\ \rightarrow C_5H_9^+ + C_2H_5 & (8) \end{array} \right.$$
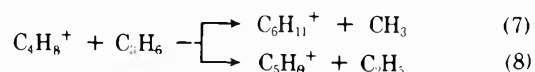
gous to processes 2 and 3. Whereas the odd electron species $C_4H_8^+$ is the principal product from the reaction of $C_3H_6^+$, the analogous process involving $C_4H_8^+$, which would lead to the formation of $C_5H_{10}^+$, is not observed to a significant extent.

At higher electron energies, fragment ions are observed which all react with cyclopropane, mainly in accordance with the general processes 1–3. For example, $C_3H_5^+$ reacts to form $C_4H_7^+$ (reaction 9) exclusively. An additional com-

$$C_3H_5^+ + c\text{-}C_3H_6 \longrightarrow C_4H_7^+ + C_2H_4 \quad (9)$$

plication occurs in that product distributions themselves vary with electron energy. For the purpose of the present study, the details of the myriad processes occurring at higher electron energy are not important and are not considered in detail. Trapped ion studies[12,16] indicate that the ions which remain at 10^{-5} Torr and long times in cyclopropane are even electron species for which especially stable structures can be imagined.
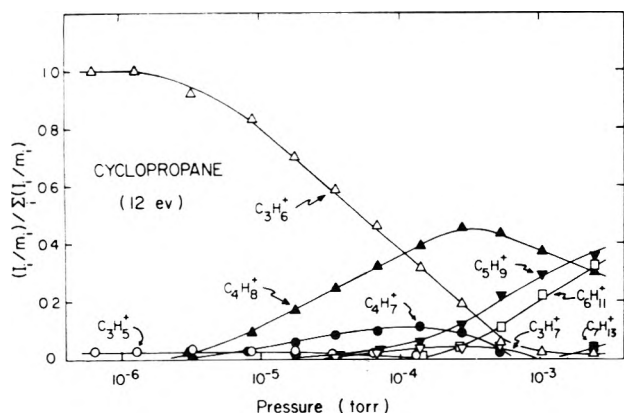
Figure 1. Variation of ion abundance with pressure in cyclopropane at 12 eV electron energy.

Figure 2. Variation of ion abundance with pressure in cyclopropyl chloride at 15 eV electron energy.

Figure 3. Variation of ion abundance with pressure in cyclopropyl cyanide at 13 eV electron energy.

Cyclopropyl Chloride. At 15 eV electron energy, the parent ion (48%) and $C_3H_5^+$ (35%) fragment ion are observed in abundance. The variation of ion concentrations with pressure is illustrated in Figure 2. Most apparent is the lack of reactivity of the parent molecular ion, whose abundance does not significantly decrease even at pressures up to 10^{-3} Torr. The fragment $C_3H_5^+$ does not show appreciable reactivity until reasonably high pressures (above 10^{-5} Torr). The decrease in the abundance of this species is accounted for by reactions 10 and 11, with the ratio of $C_6H_9^+$

$$C_3H_5^+ + c\text{-}C_3H_5Cl \longrightarrow \begin{cases} C_6H_9^+ + HCl & (10) \\ C_6H_7^+ + HCl + H_2 & (11) \end{cases}$$
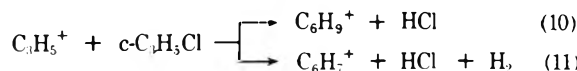
to $C_6H_7^+$ increasing with increasing pressure. This suggests that $C_6H_9^+$ formed in reaction 10 is vibrationally excited and further decomposes by loss of H_2 (reaction 11). At higher pressures, $C_6H_9^+$ is collisionally stabilized before H_2 elimination can occur. The protonated parent formed by proton transfer from minor fragments comprises less than 2% of the total ions at 15 eV electron energy. This product reacts rapidly to yield $(C_3H_5)_2Cl^+$ (reaction 12). In a 14:1

$$C_3H_5ClH^+ + c\text{-}C_3H_5Cl \longrightarrow (C_3H_5)_2Cl^+ + HCl \quad (12)$$

$$CD_5^+ + c\text{-}C_3H_5Cl \longrightarrow C_3H_5^+ + DCl + CD_4 \quad (13)$$

$$C_2D_5^+ + c\text{-}C_3H_5Cl \longrightarrow C_3H_5^+ + DCl + C_2D_4 \quad (14)$$

mixture of CD_4 and $c\text{-}C_3H_5Cl$, reactions 13 and 14 are observed to yield exclusively m/e 41 ($C_3H_5^+$) and not product ions which incorporate deuterium. This suggests that cyclopropyl chloride protonates exclusively on the halogen substituent and not on the ring.

Cyclopropyl Cyanide. Again the fragment ion $C_3H_5^+$ (67%) and the parent ion (33%) are observed in abundance at low electron energy. The variation of ion abundance with pressure shown in Figure 3 for an electron energy of 13 eV can be explained by the sequence of reactions 15–18. The

$$C_3H_5^+ + c\text{-}C_3H_5CN \longrightarrow C_3H_5CNH^+ + C_3H_4 \quad (15)$$

$$C_3H_5CN^+ + c\text{-}C_3H_5CN \longrightarrow \begin{cases} C_3H_6CNH^+ + C_4H_4N & (16) \\ C_5H_7N^+ + CH_2CHCN & (17) \end{cases}$$

$$C_3H_5CNH^+ + c\text{-}C_3H_5CN \longrightarrow (C_3H_5CN)_2H^+ \quad (18)$$
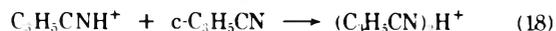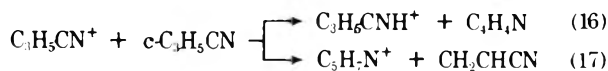
protonated parent ion formed in reactions 15 and 16 clusters to form the proton bound dimer (reaction 18).

Cyclopropylamine. Even at low electron energies the fragment ion corresponding to H atom loss dominates the
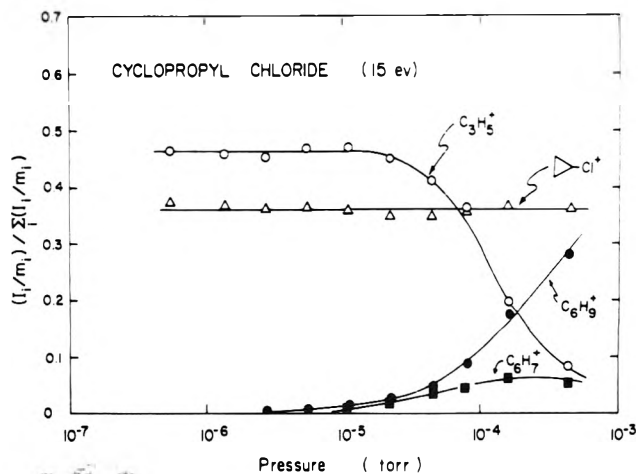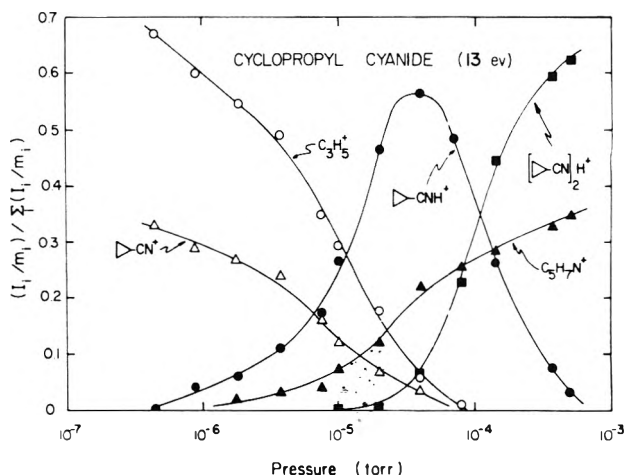
mass spectrum of cyclopropylamine. This species (67%), as well as a fragment ion at m/e 28 (8%, assumed to be protonated HCN), are observed along with the parent ion (17%) at 15 eV electron energy. The variation of ion abundance with pressure is shown in Figure 3. All three ionic species lead to formation of the protonated parent (reactions 19–21),

$$HCNH^+ + c\text{-}C_3H_5NH_2 \longrightarrow C_3H_5NH_3^+ + HCN \quad (19)$$

$$C_3H_6N^+ + c\text{-}C_3H_5NH_2 \longrightarrow C_3H_5NH_3^+ + C_3H_5N \quad (20)$$

$$C_3H_5NH_2^+ + c\text{-}C_3H_5NH_2 \longrightarrow C_3H_5NH_3^+ + C_3H_6N \quad (21)$$

$$C_3H_5NH_3^+ + c\text{-}C_3H_5NH_2 \longrightarrow [C_3H_5NH_2]_2H^+ \quad (22)$$
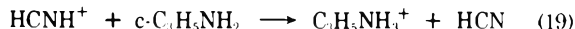
which in turn clusters to yield the proton bound dimer (reaction 22).

An ion corresponding to loss of NH_3 from the proton bound dimer is observed at high pressure. We could not eliminate the possibility that proton transfer to a trace impurity of dicyclopropylamine contributed to this species.

Methyl Cyclopropyl Ketone. The variation of ion abundance with pressure at an electron energy of 15 eV is shown in Figure 4 for methyl cyclopropyl ketone. Observed reactant ions include the two α-cleavage fragments CH_3CO^+ (21%) and $C_3H_5CO^+$ (42%) in addition to $C_3H_5^+$ (10%) and the parent ion (22%). Protonated methyl cyclopropyl ketone is formed by reactions 23 and 24 involving CH_3CO^+

TABLE I: Ion–Molecule Reaction Rates in Substituted Cyclopropanes

Species	Reaction	k^a
c-C_3H_6	$C_3H_6^+ + C_3H_6$ ⟶ $C_4H_7^+ + C_2H_5$	0.52
	$C_4H_8^+ + C_2H_4$	1.5
	$C_5H_9^+ + CH_3$	0.09
	$C_3H_5^+ + C_3H_6$ ⟶ $C_4H_7^+ + C_2H_4$	3.3
c-C_3H_5Cl	$C_3H_5^+ + C_3H_5Cl$ ⟶ $C_6H_9^+ + HCl$	0.78
	$C_6H_7^+ + HCl + H_2$	0.43
c-C_3H_5CN	$C_3H_5CN^+ + C_3H_5CN$ ⟶ $C_5H_7N^+ + CH_2CHCN$	9.0
	$C_3H_5CNH^+ + C_4H_4N$	8.8
	$C_3H_5^+ + C_3H_5CN$ ⟶ $C_3H_5CNH^+ + C_3H_4$	17.1
c-$C_3H_5NH_2$	$C_3H_5NH_2^+ + C_3H_5NH_2$ ⟶ $C_3H_5NH_3^+ + C_3H_6N$	1.9
	$C_3H_6N^+ + C_3H_5NH_2$ ⟶ $C_3H_5NH_3^+ + C_3H_5N$	1.3
	$HCNH^+ + C_3H_5NH_2$ ⟶ $C_3H_5NH_3^+ + HCN$	8.0
c-$C_3H_5COCH_3$	$C_3H_5COCH_3^+ + C_3H_5COCH_3$ ⟶ $C_3H_5COHCH_3^+ + C_5H_7O$	2.0
	$CH_3CO^+ + C_3H_5COCH_3$ ⟶ $C_3H_5COHCH_3^+ + CH_2CO$	7.1
	$C_3H_5^+ + C_3H_5COCH_3$ ⟶ $C_3H_5COHCH_3^+ + C_3H_4$	3.2
c-C_3H_6OH	$C_3H_5OH^+ + C_3H_5OH$ ⟶ $C_3H_5OH_2^+ + C_3H_5O$	1.5
	$C_3H_5O^+ + C_3H_5OH$ ⟶ $C_3H_5OH_2^+ + C_3H_4O$	2.0
	$HCO^+ + C_3H_5OH$ ⟶ $C_3H_5OH_2^+ + CO$	11.0

a Thermal rate constants for bimolecular processes in units 10^{-10} cm^3 molecule^{-1} s^{-1}. Estimated uncertainty ± 30%.

TABLE II: Ion–Molecule Reactions of Parent Ions in Substituted Methanes

Species	Reaction	k^a
CH_3Cl	$CH_3Cl^+ + CH_3Cl$ ⟶ $CH_3ClH^+ + CH_2Cl$	12.5
	$CH_3ClH^+ + CH_3Cl$ ⟶ $(CH_3)_2Cl^+ + HCl$	1.4
CH_3CN	$CH_3CN^+ + CH_3CN$ ⟶ $CH_3CNH^+ + CH_2CN$	20.9
	$CH_3CNH^+ + CH_3CN$ ⟶ $(CH_3CN)_2H^+$	
CH_3NH_2	$CH_3NH_2^+ + CH_3NH_2$ ⟶ $CH_3NH_3^+ + CH_4N$	19.8
	$CH_3NH_3^+ + CH_3NH_2$ ⟶ $(CH_3NH_2)_2H^+$	
$(CH_3)_2CO$	$(CH_3)_2CO^+ + (CH_3)_2CO$ ⟶ $(CH_3)_2COH^+ + C_2H_5O$	5.1
	$(CH_3)_2COCOCH_3^+ + CH_3$	1.4
	$(CH_3)_2COH^+ + (CH_3)_2CO$ ⟶ $[(CH_3)_2]H^+$	
CH_3OH	$CH_3OH^+ + CH_3OH$ ⟶ $CH_3OH_2^+ + CH_3O$	21.3
	$CH_3OH_2^+ + CH_3OH$ ⟶ $(CH_3)_2OH + H_2O$	1.0

a Thermal rate constant for bimolecular processes in units 10^{-10} cm^3 molecule^{-1} s^{-1}. Data taken from ref 17–21.

$$CH_3CO^+ + c\text{-}C_3H_5COCH_3 \longrightarrow C_3H_5COHCH_3^+ + CH_2CO \quad (23)$$

$$C_3H_5COCH_3^+ + c\text{-}C_3H_5COCH_3 \longrightarrow C_3H_5COHCH_3^+ + C_5H_7O \quad (24)$$

$$C_3H_5^+ + c\text{-}C_3H_5COCH_3 \longrightarrow C_3H_5COHCH_3^+ + C_3H_4 \quad (25)$$
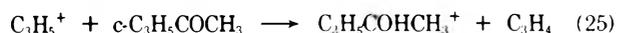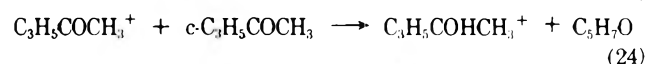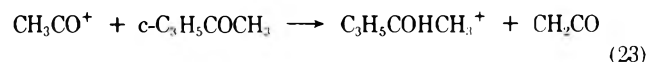
and the parent ion, and to a lesser extent by $C_3H_5^+$ (reaction 25). The remaining product ions are formed in the clustering reactions 26–28 of $C_3H_5CO^+$, $C_3H_5^+$, and the protonated parent ion with the neutral ketone.

$$C_3H_5CO^+ + c\text{-}C_3H_5COCH_3 \longrightarrow (C_3H_5CO^+)(C_3H_5COCH_3) \quad (26)$$

$$C_3H_5^+ + c\text{-}C_3H_5COCH_3 \longrightarrow (C_3H_5^+)(C_3H_5COCH_3) \quad (27)$$

$$C_3H_5COHCH_3^+ + c\text{-}C_3H_5COCH_3 \longrightarrow [C_3H_5COCH_3]_2H^+ \quad (28)$$
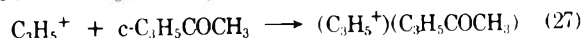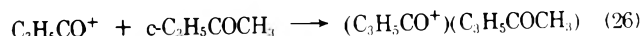
Cyclopropanol. At 15 eV electron energy the abundant ions are HCO^+ (12%), $C_3H_5OH^+$ (13%), and $C_3H_5O^+$ (64%). The variation of ion abundance with pressure (Figure 5) indicates a straightforward scheme of reactions in which all three primary ions react to form the protonated alcohol, which in turn clusters to form the proton bound dimer and trimer (reactions 29–33).

$$HCO^+ + c\text{-}C_3H_5OH \longrightarrow C_3H_5OH_2^+ + CO \quad (29)$$

$$C_3H_6O^+ + c\text{-}C_3H_5OH \longrightarrow C_3H_5OH_2^+ + C_3H_4O \quad (30)$$

$$C_3H_5OH^+ + c\text{-}C_3H_5OH \longrightarrow C_3H_5OH_2^+ + C_3H_5O \quad (31)$$
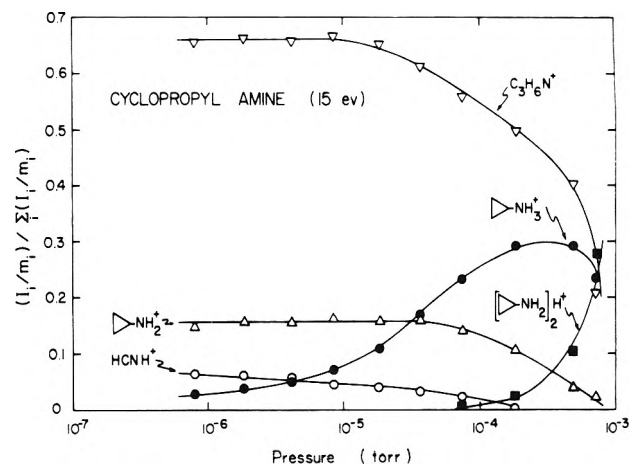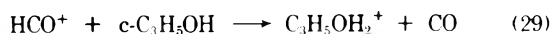
Figure 4. Variation of ion abundance with pressure in cyclopropyl amine at 15 eV electron energy.

$$C_3H_5OH_2^+ + c\text{-}C_3H_5OH \longrightarrow (C_3H_5OH)_2H^+ \quad (32)$$

$$(C_3H_5OH)_2H^+ + c\text{-}C_3H_5OH \longrightarrow (C_3H_5OH)_3H^+ \quad (33)$$

Rate Constants. In each system, rate constants were determined for bimolecular processes involving the abundant primary ions. These data are summarized in Table I. The uncertainty in the rate constants is estimated to be ±30%,
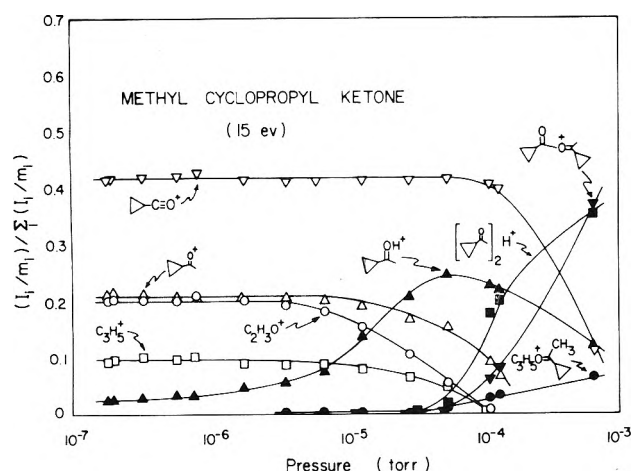
Figure 5. Variation of ion abundance with pressure in methyl cyclopropyl ketone at 15 eV electron energy.
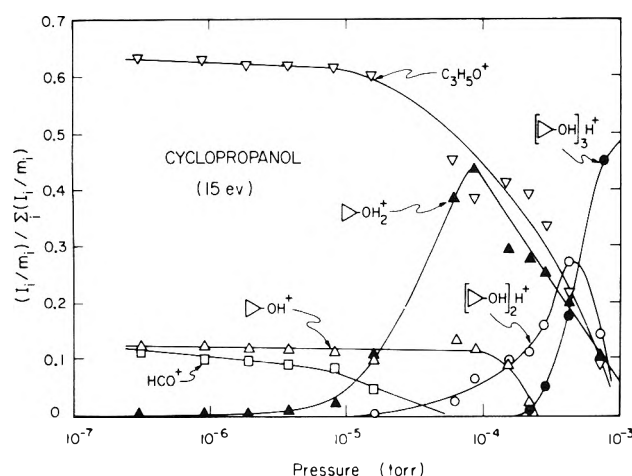
Figure 6. Variation of ion abundance with pressure in cyclopropanol at 15 eV electron energy.

due to uncertainties in pressure measurement and drift times.

Discussion

The gas phase ion chemistry of alkyl chlorides,[17] cyanides,[18] amines,[19] ketones,[20] and alcohols[21] has been investigated in detail for simple alkyl substituents and salient features are recorded in Table II for the methyl case. In all cases the parent ion reacts with the neutral species to generate protonated parent, which in turn reacts to yield either a proton bound dimer (association reaction) or an "onium" ion by loss of HX from the proton bound dimer. Only in the case of acetone is there a competing reaction channel of the parent ion (Table II). The reactions in Table II are characteristic of the substituents and are referred to as "substituentlike" reactions. They do not depend greatly on the nature of the alkyl group. With aliphatic alcohols the chemistry becomes somewhat more complex for larger alkyl substituents. In the case of isopropyl alcohol, for example, the dehydration reaction 34 is observed in addition to the expected processes 35 and 36.[21]

$$(CH_3)_2CHOH_2^+ \longrightarrow (CH_3)_2CHOH\cdots H^+\cdots OH_2 + C_3H_6 \quad (34)$$

$$+ \longrightarrow [(CH_3)_2CH]_2OH^+ + H_2O \quad (35)$$

$$(CH_3)_2CHOH \longrightarrow [(CH_3)_2CHOH]_2H^+ \quad (36)$$
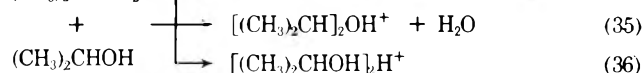
TABLE III: Ionization Potentials of Cyclopropyl and 2-Propyl Compounds

Substituent (X)	IP(c-C$_3$H$_5$X)^a	IP[(CH$_3$)$_2$CHX]^a
H	10.09	11.08
CN	10.37 ^{b,c}	11.43^c
Cl	10.10^d	10.78
OH	e	10.15
COCH$_3$	e	9.31
NH$_2$	6.70^b	8.72

^{a} First adiabatic ionization potential in eV. Except as noted, data are from J. L. Franklin, J. G. Dillard, H. M. Rosenstock, J. T. Herron, K. Draxl, and F. H. Field, *Natl. Stand. Ref. Data Ser., Natl. Bur. Stand.*, No. 26 (1969). ^{b} D. W. Turner, C. Baker, A. D. Baker, and C. R. Brundle, "Molecular Photoelectron Spectroscopy," Wiley-Interscience, London, 1970. ^{c} R. H. Staley, J. H. Kleckner, and J. L. Beauchamp, *J. Am. Chem. Soc.*, in press. ^{d} R. W. Kiser, "Introduction to Mass Spectrometry and Its Applications," Prentice-Hall, Englewood Cliffs, N.J., 1965, Appendix 4. ^{e} Not available.

It is evident that the observed ion–molecule reactions of the substituted cyclopropanes are largely dominated by the substituent. Only in the case of cyclopropyl cyanide is a "cyclopropanelike" reaction of the parent ion observed (process 17). There are several notable distinctions in the expected and observed reactivity, however, which deserve comment. The parent ion of cyclopropyl chloride is unreactive with the parent neutral and in particular does not react to form the protonated parent. The hydrogen affinity of an alkyl chloride radical ion (RCl$^+$–H homolytic bond dissociation energy) is 107 kcal/mol.[17] This is generally higher than C–H bond dissociation energies in alkanes, and formation of the protonated parent ion is an exothermic process. Although the C–H bond dissociation energy in cyclopropane is higher (101 ± 3 kcal/mol)[22] than normal secondary bonds (95 ± 2 kcal/mol),[22] it is unlikely that C–H bond energies in cyclopropyl chloride exceed 107 kcal/mol. If the failure of the cyclopropyl chloride molecular ion to form the protonated parent is to be attributed to the process being endothermic, then the radical cation must have some special stabilization which reduces the hydrogen affinity.[23] This might be due either to the lowest ionization process involving a ring orbital rather than a chlorine lone pair, or to a stabilizing interaction of the chlorine lone pair orbital with a ring orbital. The photoelectron spectrum of cyclopropyl chloride, which to our knowledge is not available, might provide some insight into this matter. The lowest adiabatic ionization potentials of substituted isopropyl and cyclopropyl compounds are compared in Table III and from the relative values the probable localization of the positive charge in the radical ion can be assessed. Cyclopropyl cyanide is the best candidate for appreciable charge localization on the ring, and indeed the "cyclopropanelike" reactivity may be directly related to this observation.

In the case of cyclopropanol it is interesting that the dehydration process analogous to reaction 34 is not observed. This is not surprising, however, since the enthalpy change of 38 kcal/mol estimated[24] for process 37 is substantially

$$c\text{-}C_3H_5OH \longrightarrow \text{(cyclopropane)} + H_2O \quad (37)$$
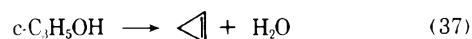
greater than in the case of isopropyl alcohol (12 kcal/mol).[21]

In the several instances where it is observed as an abundant fragment ion at low electron energies, C$_3$H$_5^+$ is ob-

served to react quite differently with substituted cyclopropanes than it does with cyclopropane (reaction 9). With cyclopropyl chloride a reaction intermediate is formed from which loss of HCl and H_2 occurs (reactions 10 and 11) in preference to ethylene. With the more basic compounds cyclopropyl cyanide (reaction 15) and methyl cyclopropyl ketone (reaction 25), the fragment $C_3H_5^+$ reacts by proton transfer. If $C_3H_5^+$ is assumed to have the structure of an allyl cation, then deprotonation to yield allene can occur with any acceptor whose proton affinity is greater than 188 kcal/mol.[25] This process is likely to be exothermic for all of the substituted cyclopropanes considered above with the exception of cyclopropyl chloride.[26]

A comparison of the ion–molecule reaction rates of the substituted cyclopropanes (Table I) to those for similarly substituted methyl compounds (Table II) suggests that the reactivity of the parent ions is somewhat reduced for the former. This may be due to greater charge delocalization in the ground states of the substituted cyclopropane molecular ions.

In summary it is evident in proceeding from cyclopropane to substituted cyclopropanes that the ion chemistry becomes dominated by the substituent, differing markedly from cyclopropane in the tendency to form the protonated parent ion and its various association and condensation products with the parent neutral. There is some indication that the cyclopropyl ring may stabilize an adjacent positive center in the radical ions, making certain processes less favorable. In comparison to acyclic analogues, differences in reactivity may largely be attributed to differences in thermochemistry of the reactions and the constraints imposed by the small strained ring system.

References and Notes

(1) (a) National Science Foundation Undergraduate Research Participant.

(b) Camile and Henry Dreyfus Teacher–Scholar, 1971–1976. (c) Contribution no. 5222 from the Arthur Amos Noyes Laboratory of Chemical Physics.

(2) A. A. Herod and A. G. Harrison, *J. Phys. Chem.*, **73**, 3189 (1969).

(3) A. G. Harrison and J. M. S. Tait, *Can. J. Chem.*, **40**, 1986 (1962).

(4) R. F. Pottie, A. J. Lorquet, and W. H. Hamill, *J. Am. Chem. Soc.*, **84**, 529 (1962).

(5) L. W. Sieck and J. H. Futrell, *J. Chem. Phys.*, **45**, 560 (1966).

(6) S. G. Lias, R. E. Rebbert, and P. Ausloos, *J. Am. Chem. Soc.*, **92**, 6430 (1970).

(7) A. A. Herod, A. G. Harrison, R. M. O'Malley, A. J. Ferrer-Correia, and K. R. Jennings, *J. Phys. Chem.*, **74**, 2720 (1970).

(8) M. T. Bowers, D. H. Aue, and D. D. Elleman, *J. Am. Chem. Soc.*, **94**, 4255 (1972).

(9) (a) X = OH, NH_2, Cl: J. D. Roberts and V. C. Chambers, *J. Am. Chem. Soc.*, **73**, 3176, 5030, 5034 (1951); (b) X = OH: V. C. Chambers, Ph.D. Thesis, Massachusetts Institute of Technology, 91950; (c) X = CN, Cl: M. T. Rogers and J. D. Roberts, *J. Am. Chem. Soc.*, **68**, 843 (1946); (d) X = $COCH_3$: M. T. Rogers, *ibid.*, **69**, 2544 (1947); (e) X = Cl: G. A. Olah and J. M. Bollinger, *ibid.*, **90**, 6082 (1968), and references therein; (f) X = $COCH_3$: D. G. Marsh and J. N. Pitts, *ibid.*, **93**, 326 (1971); D. G. Marsh, J. N. Pitts, K. Schaffner, and A. Tuinman, *ibid.*, **93**, 333 (1971).

(10) J. L. Beauchamp, *Annu. Rev. Phys. Chem.*, **22**, 527 (1971), and references therein.

(11) T. B. McMahon and J. L. Beauchamp, *Rev. Sci. Instrum.*, **42**, 1632 (1971).

(12) T. B. McMahon and J. L. Beauchamp, *Rev. Sci. Instrum.*, **43**, 509 (1972).

(13) L. Friedman and A. Shechter, *J. Am. Chem. Soc.*, **81**, 5512 (1959).

(14) S. E. Buttrill, *J. Chem. Phys.*, **50**, 4125 (1969).

(15) A. G. Marshall and S. E. Buttrill, *J. Chem. Phys.*, **52**, 2752 (1970).

(16) J. L. Beauchamp, unpublished results.

(17) J. L. Beauchamp, D. Holtz, S. D. Woodgate, and S. L. Patt, *J. Am. Chem. Soc.*, **94**, 2798 (1972).

(18) J. Vogt and J. L. Beauchamp, *J. Am. Chem. Soc.*, **97** 6682 (1975); S. K. Gupta, E. G. Jones, A. G. Harrison, and J. J. Myher, *Can. J. Chem.*, **45**, 3107 (1967); G. A. Gray, *J. Am. Chem. Soc.*, **90**, 6002 (1968).

(19) T. B. McMahon, Ph.D. Thesis, California Institute of Technology, 1973; E. G. Jones and A. G. Harrison, *Can. J. Chem.* **45**, 3119 (1967).

(20) A. S. Blair and A. G. Harrison, *Can. J. Chem.*, **51**, 703 (1973), and references therein.

(21) M. C. Caserio and J. L. Beauchamp, *J. Am. Chem. Soc.*, **94**, 2638 (1972).

(22) J. A. Kerr, *Chem. Rev.*, **66**, 465 (1966).

(23) For another interesting case where this effect is observed, see R. H. Staley and J. L. Beauchamp, *J. Am. Chem. Soc.*, **96**, 1604 (1974).

(24) S. W. Benson, F. R. Cruickshank, D. M. Golden, G. R. Hauger, H. E. O'Neal, and A. S. Rodgers, *Chem. Rev.*, **69**, 279 (1969).

(25) Calculated using thermochemical data given in S. E. Buttrill, A. D. Williamson, and P. LeBreton, *J. Chem. Phys.*, **62**, 1586 (1975).

(26) For representative data for proton affinities see J. L. Beauchamp in "Interactions between Ions and Molecules", P. Ausloos, Ed., Plenum Press, New York, N.Y., 1975, pp 413–444.

Bimolecular Interactions of Triplet Benzophenone in Aqueous Solution Studied by Energy Transfer to Biacetyl

G. Favaro* and G. Bufalini

Istituto di Chimica Fisica, Università di Perugia, I-06100 Perugia, Italy (Received March 24, 1975; Revised Manuscript Received November 26, 1975)

Triplet–triplet energy transfer from benzophenone to biacetyl in aqueous solution has been studied as a function of pH. Triplet lifetime of benzophenone has been obtained in the pH range 9.5 to 1.3 by quenching of benzophenone phosphorescence and/or biacetyl sensitized phosphorescence measurements. A reaction scheme has been proposed which implies self-quenching of the benzophenone triplet and reaction with H_3O^+ ions to give a short-lived triplet species ($\tau' \sim 4 \times 10^{-8}$ s). Assuming the diffusional value for the kinetic constant of the forward reaction, the rate constant of the back reaction, and then the equilibrium constant, have been determined.

Introduction

It is well known that benzophenone exhibits phosphorescence emission in fluid oxygen-free solutions at room temperature.[1-3] Particularly interesting is the phosphorescence behavior in aqueous solution, where the emission intensity decreases with decreasing pH[4,5] and is no longer detectable below pH 3.[4] At very high acid concentrations phosphorescence does appear again and has been assigned to the π,π^* triplet of the protonated benzophenone[4] ($pK = -5.7$,[6] $-6.09, -6.25$,[7] -4.74[8]).

The study of phosphorescence in water glassy solutions at 77 K permitted the observation of a blue shifted spectrum, which appears at intermediate acidities, between those at which the spectra of neutral benzophenone (B) and protonated benzophenone (BH$^+$) have been identified, in the same pH region, approximately, where the gap of the room temperature phosphorescence has been found. This emission was assigned to phosphorescence from a hydrogen-bonded complex with the hydroxonium ion.[9]

This paper presents the results of a further investigation into the behavior of triplet benzophenone in aqueous solution by the luminescence sensitization technique, which has been found a very useful tool in studying bimolecular interactions in the excited state for similar systems, in benzene.[10] The effect of pH on benzophenone's efficiency in sensitizing the phosphorescence of biacetyl has been studied. The results obtained indicate the occurrence of a change in the nature of the excited state with decreasing pH, as a consequence of a chemical reaction between B* and the solvent. A comparison with the low temperature results suggests that the same molecular species, which phosphoresces at intermediate acidities in rigid glasses, could also be responsible for the triplet behavior in solution.

In a recent paper by Rayner and Wyatt,[8] which appeared in the literature when this work was already at a very advanced stage, similar results have been obtained by laser flash photolysis experiments on benzophenone in aqueous solutions. While on one hand, the close agreement of some experimental data with those obtained in this laboratory, using a completely different method, supports the reliability of lifetime values obtained by energy transfer experiments, on the other hand, a different interpretation of the experimental data can be proposed. The decrease of the initial absorption intensities and lifetimes of the transients observed in laser flash experiments with decreasing pH has been explained as being due to the acid–base equilibrium in the triplet state.[8] The excited state is, in fact, more basic than the ground state, as shown also by the $pK(T_1)$ calculation by the Förster cycle (-0.4,[5] 0.6[8]). We believe that this interpretation is quite reasonable per se, but does not agree with the presence in rigid matrix of a phosphorescence which originates neither from B*, nor from BH^{+*},[9] in that very pH range where absorption and lifetime changes of the transients were observed and the drop of the emission intensity was found in fluid solution. In particular, as recognized by the authors[8] also, it is difficult to explain the emission gap in fluid solution, which has been tentatively attributed to a quenching effect on the BH^{+*} triplet by H_2O molecules.

These difficulties can be overcome if one assumes the presence of an excited triplet species different either from B*, or from BH^{+*}. The hypothesis of a hydrogen-bonded complex of benzophenone triplet with the hydroxonium ions, BH$_3$O^{+*}, previously proposed for similar systems,[11] also seems quite reasonable in this case.

Experimental Section

Benzophenone (Carlo Erba product) was recrystallized several times from water–ethanol. Biacetyl (Kock-Light Laboratories product) was distilled before using.

Britton buffer solutions were used from pH 9.5 to 2, at constant ionic strength, $\mu = 0.01$; HClO$_4$ solutions were used for higher acidities, down to pH 1.35. A Sargent PXB pH meter with a glass electrode was employed.

Phosphorescence spectra were recorded at room temperature (22 ± 2 °C) by a Hitachi-Perkin-Elmer MPF-3 fluorescence spectrophotometer, after having deaerated the samples by bubbling with pure nitrogen. The excitation was performed with 320-nm light, which is absorbed almost exclusively by the benzophenone donor (B). Both sensitized biacetyl (Q) phosphorescence and benzophenone phosphorescence quenching were followed simultaneously in the pH range 9.5 to 4, as shown, e.g., in Figure 1, at pH 7.4. Below pH 4, only measurements of sensitized biacetyl
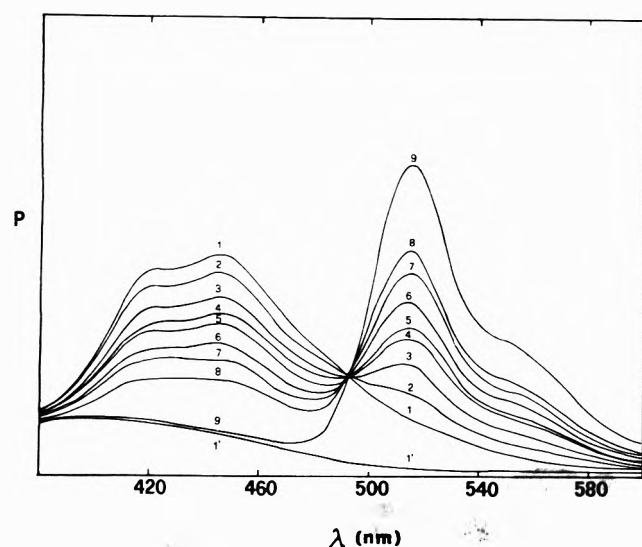
Figure 1. Simultaneous quenching of benzophenone phosphorescence (left-hand side) and sensitization of biacetyl phosphorescence (right-hand side) in aqueous solution at pH 7.4, [B] = 2.4 × 10^{-4} M. [Q] increases from 0 to 1.8 × 10^{-5} M on going from spectrum 1 to 9; 1' refers to the background of the solvent.

TABLE I: Experimental Values of the Benzophenone Triplet Lifetime at pH 7.4, Obtained from Acceptor Sensitization (τ_{expt})$_s$ and Donor Quenching (τ_{expt})$_q$ Measurements at Various Donor Concentrations

[B], 10^{-5} M	(τ_{expt})$_s$, 10^{-5} s	(τ_{expt})$_q$, 10^{-5} s
20.4	2.5	3.0
9.9	5.5	3.8
8.3	7.0	6.4
5.9	6.8	5.8
3.7	9.5	9.8
2.2	12.7	14.0

TABLE II: Triplet Lifetime at Infinite Dilution (τ_∞) and Self-Quenching Constant (k_B) of Benzophenone in Aqueous Solutions as a Function of pH

pH	τ_∞, 10^{-5} s	k_B, 10^8 M^{-1} s^{-1}	pH	τ_∞, 10^{-5} s
9.5	25.5	2.0	3.05	0.29
7.4	21.5	1.6	2.84	0.19
7.1	22.0	1.6	2.4	0.071
5.4	14	1.1	1.99	0.022
4.0	2.8		1.7	0.018
3.55	0.96		1.35	0.0098

phosphorescence were carried out, due to the intensity drop of benzophenone emission with decreasing pH.

The acceptor concentration ranged from 7 × 10^{-4} to 2 × 10^{-6} M, for the experiments at pH ≥ 4, and from 8 × 10^{-3} to 2 × 10^{-4} M, for those at lower pH values. This increase in the acceptor concentration was necessary in order to observe the sensitized emission, since the triplet lifetime of the donor decreases with decreasing pH. At each pH value, several runs (five–eight) were performed using decreasing donor concentrations, in the range 3 × 10^{-4} to 2 × 10^{-5} M, up to about 0.01 of absorbance at the irradiation wavelength; this may be considered the limiting absorbance value to obtain reliable sensitized phosphorescence measurements under our experimental conditions.

The sensitized phosphorescence intensities of biacetyl (Q) were read at 514 nm (the phosphorescence maximum in water) and corrected for the background due to the solvent and, where necessary, for the long wavelength tail of the benzophenone emission (see Figure 1). These intensities (P) were found to fit the Stern–Volmer equation

$$P^{-1} = K \left(1 + \frac{1}{k_t \tau_{expt}[Q]} \right) \tag{1}$$

in the whole pH interval explored. K is constant in each experimental run. From the linear plots P^{-1} vs. $[Q]^{-1}$, the experimental triplet lifetime (τ_{expt}) of B was obtained, assuming for the bimolecular rate constant of the B to Q energy transfer process, the value directly obtained in water by Almgren[12] for this donor–acceptor pair (k_t = 1.2 × 10^9 M^{-1} s^{-1}). It corresponds to the diffusional value, somewhat reduced to account for the partial reaction of biacetyl with water, giving a product which is a less effective quencher than biacetyl itself.

The quenching intensity ratios (P_0'/P') for B, read at 447 nm and corrected only for the solvent background (Q does not emit in this wavelength region), fitted the Stern–Volmer equation well:

$$P_0'/P' = 1 + k_t \tau_{expt}[Q] \tag{2}$$

from which the τ_{expt} value was obtained.

In the pH region 4 to 9, where both types of measure-

ments were feasible, the agreement in τ_{expt} values obtained by the two methods was within 15%, as shown, e.g., in Table I for the measurements carried out at pH 7.4. In each experimental run, the intensity data (seven to ten points for each Stern–Volmer plot), treated by the least-squares method, gave correlation coefficients not lower than 0.995.

Results and Discussion

The experimental lifetime of benzophenone triplet was found to decrease with decreasing pH and with increasing concentration of benzophenone itself, at the highest pH values, as shown in Tables I and II. Taking into account the dependence of τ_{expt} on donor concentration and pH, Scheme I has been assumed for the deactivation of benzo-

Scheme I
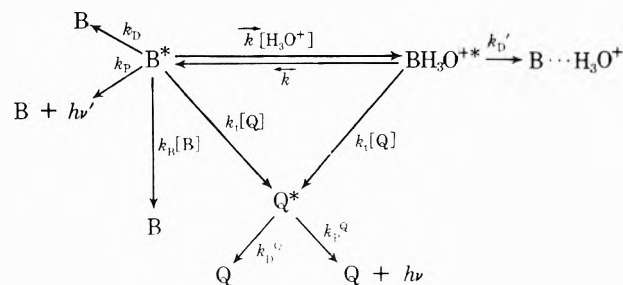
phenone triplet (B*) in the presence of biacetyl acceptor (Q). In this mechanism, the occurrence of the reaction of excited B* with the hydroxonium ions is assumed to give the excited complex BH_3O^{+*}: however, the same scheme should hold for an acid–base reaction also. Neither self-quenching, nor phosphorescence were included for the species produced in acidic medium, since they were not experimentally observed. From straightforward steady-state kinetics, applied to Scheme I, the following expressions were derived for the sensitized acceptor phosphorescence (P):

$$P^{-1} = K\{(1 + \vec{k}\tau' + k_t\tau'[Q])(1 + \vec{k}\tau[H_3O^+] +$$
$$k_t\tau[Q] + k_B\tau[B]) - \vec{k}\vec{k}\tau\tau'[H_3O^+]\}/\{k_t\tau[Q] \times$$
$$(1 + \vec{k}\tau' + k_t\tau'[Q] + \vec{k}\tau'[H_3O^+])\} \quad (3)$$

and for the quenching of the donor phosphorescence (P'):

$$P_0'/P' = \{(1 + \vec{k}\tau')/(1 + \vec{k}\tau' + k_t\tau'[Q])\} \times$$
$$\{(1 + \vec{k}\tau' + k_t\tau'[Q])(1 + k_B\tau[B] + k_t\tau[Q] + \vec{k}\tau[H_3O^+]) -$$
$$\vec{k}\vec{k}\tau\tau'[H_3O^+]\}/\{(1 + \vec{k}\tau')(1 + k_B\tau[B]) + \vec{k}\tau[H_3O^+]\} \quad (4)$$

where $\tau' = 1/k_D'$ refers to the triplet lifetime of the excited complex and $\tau = 1/(k_D + k_P)$ refers to the triplet lifetime of B*. The constant K is the same as in the experimental eq 1 and includes the benzophenone triplet yield, biacetyl triplet lifetime, the rate of light absorption, and an instrumental factor. These equations can be easily rearranged in the form:

$$P^{-1} = K\left\{1 + \frac{1}{k_t\tau[Q]}\left[\frac{1 + \vec{k}\tau' + k_t\tau'[Q] + \vec{k}\tau[H_3O^+]}{1 + \vec{k}\tau' + k_t\tau'[Q] + \vec{k}\tau'[H_3O^+]} + \right.\right.$$
$$\left.\left. k_B\tau[B]\frac{1 + \vec{k}\tau' + k_t\tau'[Q]}{1 + \vec{k}\tau' + k_t\tau'[Q] + \vec{k}\tau'[H_3O^+]}\right]\right\} \quad (3')$$

and

$$P_0'/P' = \{(1 + \vec{k}\tau')/(1 + \vec{k}\tau' + k_t\tau'[Q])\} \times$$
$$\{1 + [k_t\tau[Q](1 + \vec{k}\tau' + k_B\tau'[B] + k_t\tau'[Q] + \vec{k}\tau'[H_3O^+]) +$$
$$k_t\tau'[Q]]/[(1 + \vec{k}\tau')(1 + k_B\tau[B]) + \vec{k}\tau[H_3O^+]]\} \quad (4')$$

In view of the great complexity of these equations compared with the experimental ones (eq 1 and 2), also considering the very good linearity of the Stern–Volmer plots and the unitary intercept of P_0'/P' vs. [Q] diagrams, some approximations must hold good. First of all, square terms, $[Q]^2$, which would give some deviation from the linearity of the plots, must be negligible in the whole pH interval explored. Secondly, considering that differences of three orders of magnitude were found in lifetime between alkaline and acidic solutions, τ' is negligible relative to τ and the terms where τ' is multiplied by a kinetic constant and a concentration term (such as [Q] and [B], which are lower than 10^{-3} M) are negligible relative to unity. On the other hand, the product of τ' for a kinetic constant can be comparable with unity and therefore it cannot be neglected a priori. Thus, the experimental lifetime (eq 1 and 2) can be expressed from eq 3' and 4' as

$$\tau_{expt} = \frac{\tau(1 + \vec{k}\tau' + \vec{k}\tau'[H_3O^+])}{(1 + \vec{k}\tau')(1 + k_B\tau[B] + \vec{k}\tau[H_3O^+])} \quad (5)$$

The agreement in the two types of determinations, in the pH region where both were possible (pH >4), was very good. In the pH range 9.5 to 7.1, when the contribution of the forward reaction ($\vec{k}[H_3O^+]$) is negligible, the expression for τ_{expt}, rearranged in the reciprocal form, to evidence better the concentration dependence, becomes

$$\tau_{expt}^{-1} = \tau^{-1} + k_B[B] \quad (6)$$

This equation allowed us to obtain the triplet lifetime at infinite dilution (τ_∞) and the self-quenching constant (k_B). The results are reported in Table II. The limiting value in alkaline solution, averaged from those at pH 9.5, 7.4, and 7.1, can be assumed as the triplet lifetime of B* ($\tau = [2.3 \pm 0.2] \times 10^{-4}$ s) in aqueous solution. This value is in very good agreement with the triplet deactivation constant obtained by Ledger and Porter,[4] who measured directly the phosphorescence duration in water ($k_D = [5.0 \pm 1] \times 10^3$

s^{-1}). The self-quenching constant, $k_B = (1.7 \pm 0.2) \times 10^8$ M^{-1} s^{-1}, obtained from the slopes of the plots $1/\tau_{expt}$ against benzophenone concentration and averaged between the highest pH's, is similar to that reported by these authors ($[1.8 \pm 0.4] \times 10^8$ M^{-1} s^{-1}).

By decreasing the pH, the terms containing $\vec{k}[H_3O^+]$ are no longer negligible, while it becomes difficult to measure k_B, since the decrease in lifetime reduces the probability of encounter between triplet state molecules and ground state molecules. On the other hand, the concentration of benzophenone cannot be increased due to its low solubility. Therefore, at low pH (≤ 4), τ_∞ values, reported in Table II, were not extrapolated but obtained averaging the results of at least five runs, since the concentration dependent term is negligible.

From the general eq 5, setting [B] = 0, the reciprocal of τ_∞ values in Table II corresponds to

$$\frac{1}{\tau_\infty} = \frac{1 + \vec{k}\tau' + \vec{k}\tau[H_3O^+]}{\tau(1 + \vec{k}\tau' + \vec{k}\tau'[H_3O^+])} \quad (7)$$

which gives, by adding and subtracting $\vec{k}\tau'[H_3O^+]$ to the numerator and neglecting τ' in the difference $\tau - \tau'$

$$\frac{1}{\tau_\infty} = \frac{1}{\tau} + \frac{\vec{k}[H_3O^+]}{1 + \vec{k}\tau' + \vec{k}\tau'[H_3O^+]} \quad (8)$$

where the terms containing $[H_3O^+]$ may or may not be neglected, depending on the pH range of measurement. As stated already, $1/\tau_\infty$ approaches $1/\tau$, the decay constant of B*, at low $[H_3O^+]$, and $1/\tau'$,[13] the decay constant of BH_3O^{+*}, at high acidities. This is as expected. This equation requires that a plot of $1/\tau_\infty$ against $[H_3O^+]$ should be a convex curve with initial slope $\vec{k}/(1 + \vec{k}\tau')$ and intercept $1/\tau$, approaching a horizontal asymptote of $1/\tau'$ value at high acidities. Because of the difficulty of obtaining reliable measurements of the lifetime at very low pH values, the asymptotic value was not reached, but the convexity was observed below pH 2. On the hypothesis of a simple quenching of B* by the hydrogen ions,[4] a straight line should be obtained plotting $1/\tau_\infty$ vs. $[H_3O^+]$.

Equation 8 can be rearranged in the following form, suitable to extrapolate τ':

$$\frac{\tau\tau_\infty}{\tau - \tau_\infty} = \tau' + \frac{1 + \vec{k}\tau'}{\vec{k}[H_3O^+]} \quad (9)$$

The result of plotting the left-hand-side of eq 9 against $[H_3O^+]^{-1}$ is shown in Figure 2. The triplet lifetime of BH_3O^{+*}, obtained from the intercept, was $\tau' \sim 4 \times 10^{-8}$ s. It should be noted that the small value of the intercept will mean that the obtained lifetime will be subject to a very great uncertainty. Therefore, the extrapolated value only gives the order of magnitude of τ'. Since eq 9 gives the best accuracy at the lowest pH values (when τ_∞ approaches τ, $\tau - \tau_\infty$ is affected by a very high imprecision) and eq 8 gives a linear plot of τ_∞^{-1} vs. $[H_3O^+]$ at the highest pH values, both equations were checked to cover the entire pH interval. The values obtained from the slopes of the diagrams

$$(1 + \vec{k}\tau')/\vec{k} = 2.7 \times 10^{-9} \text{ M s} \quad (10)$$

from eq 9 in the pH range 1.35–4.0, and

$$\vec{k}/(1 + \vec{k}\tau') = 3.6 \times 10^8 \text{ M}^{-1} \text{ s}^{-1} \quad (11)$$

from eq 8 in the pH range 2.4–7.4 matched very well. The equilibrium constant for the dissociation reaction in the excited state $K^* = \vec{k}/\vec{k}$ should be obtained solving eq 10 (or
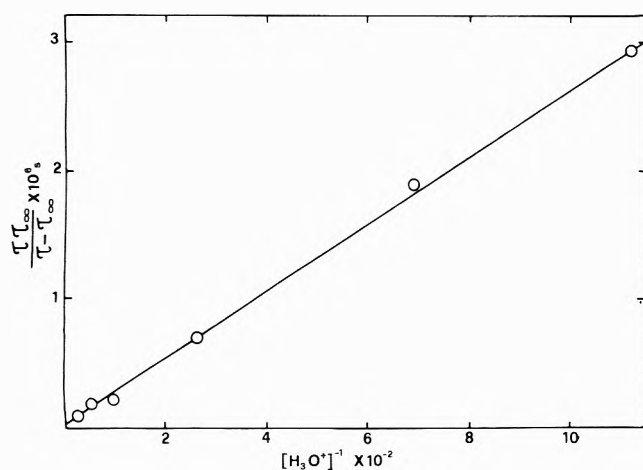
Figure 2. Lifetime data of benzophenone in aqueous solution, pH 1.35 to 3.05, treated according to eq 9.

Figure 3. Plot of the intensity ratio against $[H_3O^+]$, according to eq 12, for benzophenone phosphorescence in aqueous solution.

11) for $\bar{k}$ and $\bar{k}$. Since these equations do not permit obtaining the rate constants separately, the diffusional value $(6 \times 10^9 \ M^{-1} \ s^{-1})$ can be assumed for the forward reaction rate, as was experimentally found or proposed in other, similar cases.[14,15] Inserting this $\bar{k}$ value and $\tau' = 4 \times 10^{-8}$ s in eq 10 and 11, the following constants were derived: $\bar{k} = 3.8_6 \times 10^8 \ s^{-1}$; $K^* = 6.4 \times 10^{-2}$; $pK^* = 1.19$. These values are consistent with the approximations previously stated on the basis of the experimental results.

Since benzophenone shows phosphorescence emission in fluid solution, these results can be checked by an independent method which does not require the presence of any energy acceptor. Were it possible to follow phosphorescence of both reacting and produced species as a function of pH, $\bar{k}$ and $\bar{k}$ could be determined separately.[15,16] The equation

$$\frac{I^0}{I} = 1 + \frac{\bar{k}\tau_{expt}}{1 + \bar{k}\tau'} [H_3O^+] \qquad (12)$$

relating the relative quantum yield of fluorescence to pH for the protonation of a weak base,[17] can be applied in the present case following benzophenone phosphorescence as a function of pH. I^0/I is the intensity ratio (approximated to the quantum yield ratio) of the phosphorescence emission at 445 nm of a solution where 100% of B* exists and that of solutions where B* has partially reacted with the hydroxonium ions. The experimental results, plotted in Figure 3, give a straight line with slope

$$\frac{\bar{k}\tau_{expt}}{1 + \bar{k}\tau'} = 2.4 \times 10^4 \ M^{-1} \qquad (13)$$

The lifetime τ_{expt} of B* can be easily calculated by eq 6, making allowance for the self-quenching at the experimental benzophenone concentration $(7.6 \times 10^{-5} \ M)$:

$$\tau_{expt} = (2.3 \times 10^{-4})/(1 + 2.3 \times 10^{-4} \times 1.7 \times 10^8 \times$$
$$7.6 \times 10^{-5}) = 5.8 \times 10^{-5} \ s$$

Insertion of the τ_{expt} value in eq 16 yields

$$\frac{\bar{k}}{1 + \bar{k}\tau'} = 4.1 \times 10^8 \ M^{-1} \ s^{-1}$$

This value can be considered to be in very good agreement with that obtained by the energy transfer technique (eq 11), since the rate constant k is only slightly lower $(3.4 \times 10^8 \ s^{-1})$, but the pK^* results almost the same (1.2_5), as ex-

pected. Nevertheless, we believe that the method of phosphorescence sensitization leads, in general, to more reliable results, since it can be applied in a larger pH range and, moreover, it is much more sensitive, permitting work with very low donor concentrations. In fact, the directly excited phosphorescence of benzophenone can scarcely be detected below pH 3, where the percentage of equilibrated form should be about 10^{-2}, while there are about 40% of B* molecules which have reacted with hydroxonium ions at the lowest pH (1.35) examined by the sensitization technique. Thus, the reliability of the kinetic relationships could be verified in the presence of high complex (or acid) concentrations. Were it not possible to realize this, there might be some doubt as to whether a reaction or a simple quenching process were occurring in the excited state.
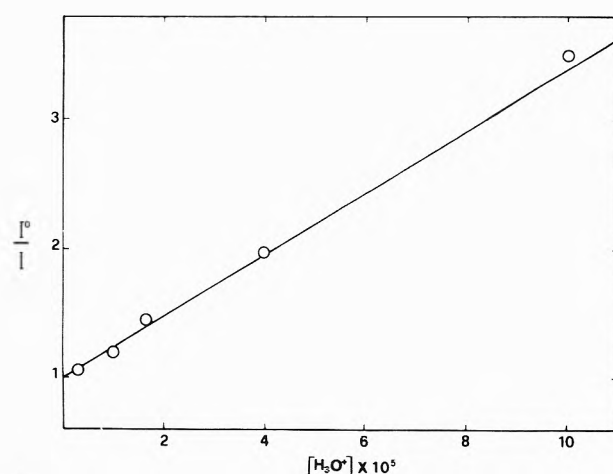
A comparison of our results with those of Rayner and Wyatt[8] shows very good agreement in the lifetimes measured at low pH, as shown in Figure 4, while the discrepancies found above pH 4 can easily be explained, since the lifetimes measured by these workers were affected by the self-quenching process $([B] = 2 \times 10^{-4} \ M)$, while those of this work were extrapolated at infinite dilution. The agreement also holds good for the pK^* $(1.5)^8$ and the triplet lifetime of the species which is produced in acidic medium $(6.2 \times 18^{-8} \ s)$.[8]

However, the results obtained from phosphorescence measurements at low temperature suggest a possible alternative to the interpretation proposed by these authors as regards the reaction responsible for the lowering of phosphorescence intensity and sensitizing capability of benzophenone with decreasing pH. Phosphorescence emission at 77 K from aqueous matrices in the acidity interval pH 3 to H_0 −4 was clearly different, as regards lifetime, near edge position and structure, either from that in neutral glasses (typical n,π* transition of the free carbonyl), or from emission at very high acidities (70% $HClO_4$ or 96% H_2SO_4) where protonation of the carbonyl occurs in the ground state. Low temperature experiments seem to indicate the formation of a definite complex between benzophenone and solvent, most probably a hydrogen-bonded complex of the carbonyl with the hydroxonium ions.[9] It can be thought that the same species which appears in rigid glasses at intermediate acidities may also play an important role in fluid solutions. It should not be surprising that the hypothesized excited complex is a more short-lived species than
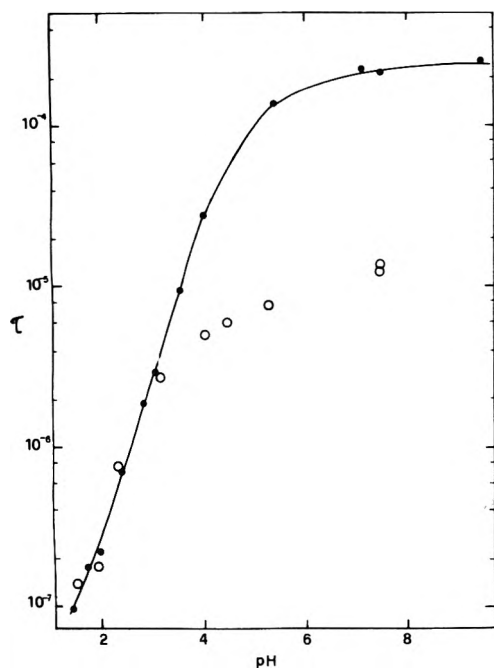
Figure 4. Effect of pH on triplet lifetime of benzophenone in aqueous solution: filled points, this work; circles, from ref 8.

the free carbonyl excited molecule in fluid solution and a more long-lived one in rigid matrix, since, probably, the highly solvated polar complex undergoes a very fast deactivation through the vibrational modes of the solvent.

The calculation of $pK(T_1)$ (where $K(T_1)$ is the dissociation constant of the protonated benzophenone triplet) could give some information on the reaction which occurs in the excited state. We estimated $pK(T_1)$ as -1 to -2.8 (2.5 to 4 pK units lower than the experimental pK^*), de-

pending on the literature value assumed for the ground state pK,[6-8] by the Förster cycle from spectroscopically measured energy levels ($\bar{\nu}_B = 23\,450$ cm^{-1} and $\bar{\nu}_{BH^+} = 21\,800$ cm^{-1}). The difference from the $pK(T_1)$ value calculated by Rayner and Wyatt ($pK(T_1) = 0.6$)[8] depends on the fact that these workers used ethanol matrices to get 0–0 frequencies for the calculation, while in the present work these figures were obtained from phosphorescence spectra in ice. However, the uncertainties in the 0–0 frequency determinations as well as in the acidity scale used in measuring the ground state pK, do not allow us to exclude the occurrence of acid–base reaction, in spite of the large difference in $pK(T_1)$ and experimental pK^*.

References and Notes

(1) H. L. Backstrom and K. SANDROS= *Acta Chem. Scand.*, **14**, 48 (1960).
(2) W. D. K. Clark, A. D. Litt, and C. Steel, *J. Am. Chem. Soc.*, **91**, 5413 (1969).
(3) C. A. Parker and T. A. Joyce, *Trans. Faraday Soc.*, **65**, 2823 (1969).
(4) M. B. Ledger and G. Porter, *J. Chem. Soc., Faraday Trans. 1*, **68**, 539 (1972).
(5) J. F. Ireland and P. A. H. Wyatt, *J. Chem. Soc., Faraday Trans. 1*, **69**, 161 (1973).
(6) T. G. Bonner and J. Phillips, *J. Chem. Soc. B*, 650 (1966).
(7) A. Fischer, B. A. Grigor, J. Packer, and J. Vaughan, *J. Am. Chem. Soc.*, **83**, 4208 (1961).
(8) D. M. Rayner and P. A. H. Wyatt, *J. Chem. Soc., Faraday Trans. 1*, **70**, 945 (1974).
(9) G. Favaro, *Chem. Phys. Lett.*, **31**, 87 (1975).
(10) G. Favaro, *Chem. Phys. Lett.*, **23**, 592 (1973).
(11) P. R. Callis and R. W. Wilson, *Chem. Phys. Lett.*, **13**, 417 (1972).
(12) M. Almgren, *Mol. Photochem.*, **4**, 213 (1972).
(13) Really, from eq 8, one finds $1/\tau_\infty = (1/\tau) + (1/\tau')$, at high acidity values, depending on the approximation previously introduced $\tau - \tau' \simeq \tau$. The complete equation gives exactly $1/\tau_\infty = 1/\tau'$, at high acidities.
(14) N. Lasser and J. Feitelson, *J. Phys. Chem.*, **77**, 1011 (1973).
(15) A. R. Watkins, *Z. Phys. Chem. (Frankfurt am Main)*, **75**, 327 (1971).
(16) A. R. Watkins, *J. Chem. Soc., Faraday Trans. 1*, **68**, 28 (1972).
(17) A. Weller, *Prog. React. Kinet.*, **1**, 187 (1961).

Enthalpies of Dilution of Strong Polyelectrolyte Solutions. Comparisons with the Cell and Line Charge Theories

G. E. Boyd* and D. P. Wilson

Department of Chemistry, University of Georgia, Athens, Georgia 30602 (Received August 11, 1975)

Publication costs assisted by the University of Georgia

A sensitive, isothermal titration microcalorimeter was used in the measurement of the enthalpies of dilution, ΔH_D, of several strong polyelectrolytes in aqueous solutions at 298.15 K. The sodium salts of atactic poly(styrenesulfonic acid), NaPSS, of varying molecular weight, of poly(ethylenesulfonic acid), NaPES and of poly(3-methacryloyloxypropane-1-sulfonic acid), NaPMOS, were employed in dilutions from 0.2 to ca. 3×10^{-4} monomolar concentration. The NaPSS and the NaPMOS preparations gave ΔH_D values in agreement with predictions of electrostatic theory based on the cell model for dilution from initial concentration below $m_i = 3.1 \times 10^{-2}$ monomolar, using the "structural value" for the charge density parameter, $\xi = 2.828$. The limiting slope for the change in ΔH_D with $\log m$ predicted by the infinite line-charge model also appeared to be approached by the NaPSS and NaPMOS solutions at high dilutions. The anomalously low ΔH_D values observed with the NaPES solutions could be brought into agreement with the cell model only if an empirical ξ greater than twice the magnitude of the "structural value" was assumed. Alternatively, the small dilution enthalpies of NaPES can be attributed to complex formation between the counterions (i.e., Na^+) and the sulfonate groups attached to the chain backbone.

The recent development of sensitive microcalorimeters for the measurement of the heat changes which occur in small volumes of viscous aqueous solutions of macromolecular solutes promises to be of importance in the determination of the thermodynamic properties of these hitherto infrequently examined systems. The property changes accompanying the dilution of synthetic, strong polyelectrolyte and biopolyelectrolyte solutions are of particular interest because of the availability of quantitative electrostatic theories[1-4] based on molecular models of cylindrical symmetry which yield predictions with which experimental results may be compared. A sensitive test of the theory is afforded by measurements of the enthalpies of dilution, particularly at small concentrations of polyelectrolyte where a limiting behavior is predicted which is analogous to the prediction made by the Debye–Hückel theory of simple electrolyte solutions.

The sodium salts of three polyvinylsulfonic acids were employed in our enthalpy of dilution (ΔH_D) measurements: (a) poly(styrenesulfonic acid) of two molecular weights; (b) poly(ethylenesulfonic acid); and, (c) poly(3-methacryloyloxypropane-1-sulfonic acid) to investigate a possible molecular weight dependence of ΔH_D; to determine the effect, if any, of the distance of the sulfonate group from the polyelectrolyte chain backbone; and, whether or not the nature of the substitution of the sulfonate group to the chain backbone affects the magnitude of ΔH_D.

Measurements of the concentration dependence of the enthalpies of dilution of poly(styrenesulfonic acid), of its alkali metal and several of its alkaline earth salts, have been reported previously.[5-6] In these investigations a large double compartment, Dewar-type solution calorimeter was employed which gave results which appear to agree well with theory. The thermal effects were quite small, however, and, because systematic errors may be introduced in the calorimetry of polyelectrolyte solutions as a result of their appreciable viscosity, it seemed that confirmatory determi-

nations with a radically different type of calorimeter would be worthwhile.

Experimental Section

Materials. Sodium poly(styrenesulfonate) (NaPSS) preparations NC 1557 and NC 1585 with viscosity molecular weights of $40\,000 \pm 2\,000$ and $450\,000 \pm 20\,000$, respectively, were obtained through the courtesy of the Dow Chemical Co., Midland, Mich. These para-substituted salts were purified by dialysis of their aqueous solutions in a hollow-fiber dialysis cell, concentrated with a rotary evaporator and pure, dry, colorless powdered solids were obtained by vacuum freeze drying. Their equivalent weights, determined by acidimetric weight titration of the poly(sulfonic acid) produced from them by cation exchange, were 207.4 $\pm$ 0.5 and 206.5 $\pm$ 0.3, respectively, indicating a degree of substitution close to 100%. Ultraviolet absorption spectra were measured with a Cary Model 16 recording spectrophotometer to establish the purity of the preparations.[7] The changes in their optical density at 261.5 nm as a function of NaCl concentration showed them to be hyperchromic from which the atactic character of the polymer chain was inferred following the recent report of Aylward.[8]

The sodium poly(ethylenesulfonate) (NaPES) used was a pure compound received from Professor U. P. Strauss of Rutgers University who has described its preparation and purification.[9] The viscosity average molecular weight estimated by him was ca. 100 000. Attempts by us to measure the ultraviolet absorption of dilute aqueous solutions of NaPES were unsuccessful; very little absorption could be detected down to 200 nm in agreement with Eisenberg and Mohan.[10]

Small quantities of pure sodium poly(3-methacryloyloxypropane-1-sulfonate), NaPMOS, were kindly given to us by Dr. J. S. Tan of the Eastman Kodak Co., Rochester, N.Y., who has described its preparation and purification elsewhere.[11] Its weight average molecular weight, $\bar{M}_w$, has

been reported as ca. 530 000. No absorption either in the ultraviolet or visible by dilute aqueous solutions of NaP-MOS was detected.

Calorimetry. An isothermal titration microcalorimeter of recent design[12] capable of detecting and measuring heat effects as small as a few millicalories was employed. (1 cal = 4.1840 J.) The major components of the system included a 90-l. water bath controlled to $\pm 3 \times 10^{-4}$ °C, a stainless steel reaction vessel, and an isothermal control circuit utilizing constant Peltier thermoelectric cooling and variable Joule heating controlled by a thermistor in an ac Wheatstone bridge. The calorimeter was tested periodically by measuring the heats of dilution of aqueous sodium chloride solutions (i.e., <0.1 m). Measurements with aqueous polyelectrolyte solutions were performed by diluting 2.5-ml volumes (made up by weight to known initial concentrations) into 25 ml of pure water, or, of polyelectrolyte solution, initially in the reaction cell. This calorimeter system is well suited for the measurement of the thermal effects shown by small samples, such as when compounds difficult to prepare and purify in larger than fractional gram amounts are examined (viz. synthetic polyelectrolytes, biopolyelectrolytes, etc.).

In the operation of an isothermal calorimeter not only does the temperature of the reaction cell remain constant at all times, but the temperature differential between the reaction vessel and the surrounding bath does not change so that heat losses between the cell and its environment are constant. Under ideal conditions during the intervals before and after the reaction period (i.e., lead and trail periods) the only undetermined heat inputs are those caused by stirring and by resistive heating of the control and monitor thermistors. When titrant is added to the calorimeter, however, the lead and trail positions will no longer be identical because of changes in the stirring energy and in the thermistor self-heating consequent to the increase in cell volume ("geometric effect") and to changes in the viscosity of the solution in the cell ("viscosity effect"). If the viscosity change is only 1–2% the base line shift will be small and its increase will be linear with the titrant volume, or with the time for a constant volumetric addition rate.

Aqueous strong polyelectrolyte solutions in the absence of salts are unusual in that they show exceptionally large viscosities which vary rapidly with concentration especially at high dilution. Thus, the relative viscosity, η/η_0, of a typical solution at $c = 10^{-4}$ is 1.062, while at $c = 10^{-2}$ monomolar the value of increases to 2.233. These values may be compared with those for 1.0 M sodium chloride and 20 wt % aqueous sucrose solutions where $\eta/\eta_0 = 1.096$ and 1.904, respectively. Clearly, the dilution of pure aqueous polyelectrolyte solutions will be attended by substantial viscosity, and hence, heat of stirring changes. Large shifts between the lead and trail positions in isothermal calorimetry therefore are observed, and the change in general will not be linear with time, nor with the volume of polyelectrolyte added. Numerous experiments have shown, however, that when the rate of addition was sufficiently small the shift of the baseline depended only on the final concentration, m_f, in the reaction cell. A plot of the observed shift vs. m_f was employed to construct the baseline required to correct the heats of dilution for the changing geometry and viscosity of the solution in the reaction cell as polyelectrolyte was added. The baseline in some cases was strongly nonlinear, and the correction amounted to as much as 30% of the total heat evolved as, for example, when a 0.12 m NaPSS solu-

tion was added to pure water to give a final concentration, $m_f = 9.1 \times 10^{-3}$. The empirical baseline shift vs. m_f plots used to estimate the baseline corrections to be applied to the observed heat effects on dilution were constructed for each polyelectrolyte preparation of differing molecular weight by determining the shift associated with each progressive dilution of its aqueous solutions to various m_f values starting with the most concentrated solution.

Results and Discussion

The measurement of what may be termed "intermediate" enthalpies of dilution of the sodium salts of several poly(vinylsulfonic acids) are presented in Figure 1 where the scale of the abscissa is expressed as the logarithm of the initial (monomolal) concentration, m_i. The enthalpy changes, ΔH_D, in calories per monomole are relative to a final concentration of 3.2×10^{-4} m because of the logarithmic concentration dependence of ΔH_D at high dilutions which is predicted by theory. The Fuoss–Lifson–Katchalsky cell model for strong polyelectrolyte solutions leads to an equation[5] for the electrostatic contribution to the enthalpy change, $\Delta H_e(m_1 \rightarrow m_2)$, defined as the change which accompanies dilution from m_1 to m_2 calculated per monomole of solute. The observed dilution enthalpy, $\Delta H_D(m_1 \rightarrow m_2)$, is related to the electrostatic contribution by

$$\Delta H_D(m_1 \rightarrow m_2) = \Delta H^\circ(m_1 \rightarrow m_2) + \Delta H_e(m_1 \rightarrow m_2) \quad (1)$$

where $\Delta H_D (m_1 \rightarrow m_2)$ is the enthalpy of dilution of the polyelectrolyte solution in a hypothetical reference state in which all the ions are discharged. It will be assumed in the equations which follow that ΔH° is always negligibly small relative to ΔH_e. The electrostatic enthalpy, H_e, of the polyelectrolyte solution is related to the electrostatic internal energy, E_e, by

$$H_e = E_e + \frac{z_p RT}{2z_c \xi}\left[1 - \beta^2 - \frac{2\xi e^{2\gamma}}{(e^{2\gamma} - 1)} \right] \frac{T}{V}\left(\frac{\partial V}{\partial T}\right)_p \quad (2)$$

where

$$E_e = \left(\frac{z_p RT}{z_c \xi}\right) u(1 + d \ln D/d \ln T) \quad (3a)$$

with

$$u = (1 + \beta^2)\gamma + \ln\left[\frac{(1 - \xi)^2 - \beta^2}{1 - \beta^2} \right] + \xi \quad (3b)$$

In eq 3 z_p is the charge carried by the ionic group on the polyion, z_c, is the charge on the counterion, and d ln D/d ln $T = -1.372$ while R and T have their usual meanings. The charge density parameter, ξ, is defined by

$$\xi = z_p z_c e_0^2/DbkT \quad (4)$$

where e_0 is the elementary charge, D, the macroscopic dielectric constant of the solvent, k, the Boltzmann constant, and b, the distance between neighboring charges on the polyion in its configuration of maximum extension. The concentration parameter, γ, is defined by

$$\gamma = 0.5 \ln (1000/\pi a^2 b N_A) - 0.5 \ln c \quad (5)$$

where a is the radius of the cylindrical polyion, N_A, the Avogadro number, and c, the monomolar concentration. The constant β in eq 2 and 3b is related to the charge density and concentration parameters by the transcendental equation
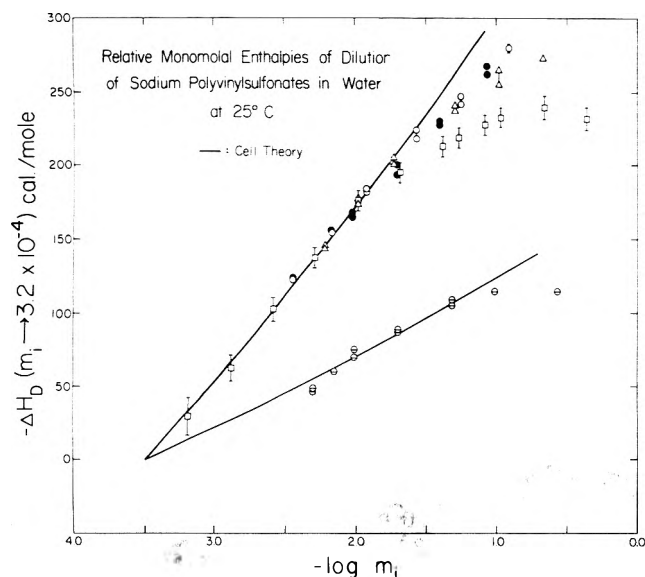
Figure 1. Relative monomolar enthalpies of dilution of sodium poly-(vinylsulfonates) in water at 25°C: △, NaPSS, mol wt = 40 000; □, NaPSS, mol wt = 200 000 (Dolar); ○, NaPSS, mol wt = 450 000; ●, NaPMOS, mol wt = 530 000; ⊖, NaPES, mol wt = 100 000. Solid curves computed with eq 2 and b = 2.52 (upper) and 1.00 Å (lower), respectively.

$$\xi = (1 - \beta^2)/[1 + \beta \coth (\beta\gamma)] \tag{6a}$$

The value of ξ for the vinylic polysulfonates employed in Figure 1 was the structural value, ξ = 2.828, which was obtained with eq 4 for $z_p = z_c = 1$, T = 298.15 K, D = 78.54, and b = 2.523 Å. For values of $\xi > 1$ the constant β is imaginary and eq 6a becomes

$$\xi = (1 + |\beta|^2)/[1 + |\beta| \cot (|\beta|\gamma)] \tag{6b}$$

In eq 2 and 3b also, β^2 must be replaced by $|\beta|^2$ and a change in sign when $\xi > 1$.

In the limit of high dilution when the concentration becomes vanishingly small, eq 6 requires that the constant β also approach zero; eq 2a then takes on the limiting form which is given also by the infinite line charge theory[4]

$$\lim_{c \to 0} \frac{d\Delta H_D}{d \ln c} = -\frac{z_p R T}{2 z_c \xi} (1 + d \ln D/d \ln T) \tag{7}$$

The enthalpy of dilution values in Figure 1, which include those published by Skerjanc and Dolar,[5] appear to agree well over a wide range in concentration with the curve computed from eq 2 with a high-speed computer. The experimental precision of the ΔH_D values is indicated by vertical bars or by duplicate points at constant $-\log m_i$. Below $-\log m_i$ = 1.8 (i.e., m_i = 1.85 × 10^{-2}) with NaPSS there is no dependence on molecular weight. All of the data taken with sodium poly(styrenesulfonate) suggests that the limiting slope predicted by the infinite line charge model (eq 7) is approached at concentrations below ca. 3 × 10^{-3} m (Figure 2).

Interestingly, the measurements taken with the NaPMOS solutions (Figure 1) appear to agree well with eq 2 whereas the ΔH_D values for the NaPES solutions depart widely from both the cell and line charge theories. The behavior of this latter polyelectrolyte is quite similar to that of aqueous solutions of sodium poly(acrylate), NaPA, which recently also have been found[13] to show much smaller enthalpies of dilution than those estimated from eq 2 assuming the "structural value" of ξ = 2.828.
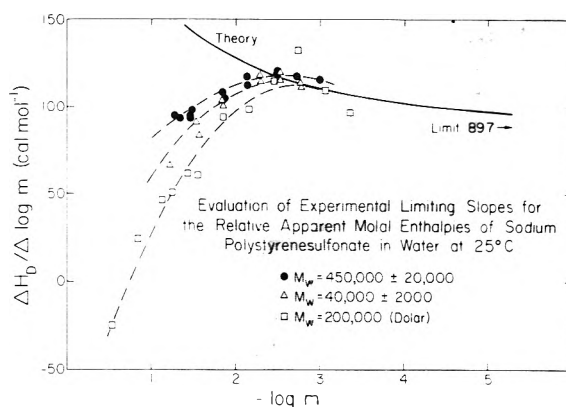
Figure 2. Evaluation of experimental limiting slopes for the relative apparent monomolar enthalpies of dilution of NaPSS in water at 25°C: infinite line-charge theory limit = 89.7 cal monomole^{-1}.

The enthalpy of dilution values observed with sodium polyacrylate solutions have been accounted for by Skerjanc[13] who has followed Katchalsky and coworkers[14] in using an empirical, or "effective", value of the charge density parameter, ξ_{eff}, to fit the data. The ratio, ξ_{eff}/ξ_{struct}, between the empirical and the structural value, eq 4, of ξ is always greater than or equal to unity, and appears to be proportional to the extent of coiling of the macroion. The ratio of ξ_{eff} to ξ_{struct} for highly charged vinylic polymers is close to 2.0 using osmotic coefficient data. If ξ_{eff} = 5.66 is used in eq 2 the estimated concentration dependence of ΔH_D on $-\log m$ for NaPA is found to agree with experiment for concentrations between m = 0.1 and 0.0094 monomolar. There are difficulties with the foregoing proposed explanation in addition to the fact that a value of ξ_{eff} = 5.66 would require excessive polyion coiling. Other measurements, such as those of ionic and mean ionic activity coefficients, Donnan distributions, etc. are consistent with the structural value of ξ = 2.83. Thus, it would seem that the cause of the failure of eq 2 and 7 with $\xi = \xi_{struct}$ to describe the concentration dependence of ΔH_D for NaPA and NaPES solutions (Figure 1) should be looked for elsewhere.

Several properties of NaPSS, NaPES, and NaPA solutions support the hypothesis that the counterions (i.e., Na$^+$) are the most strongly bound to the PES$^-$ polyion. The sequences of the osmotic coefficients[7,15] and of the sodium ion activity coefficients[6] are NaPSS > NaPA > NaPES. Further, the volume increase on forming NaPSS, NaPA, and NaPES in dilute aqueous media from their respective tetramethylammonium salts have been reported[17] as 1.2, 4.1, and 4.7 ml per equivalent of total cation present. If, as these results suggest, substantial solvation changes occur in the formation of NaPES and NaPA the calorimetric measurements would be expected to show deviations from the electrostatic theory. The relatively smaller ΔV for NaPSS can be attributed to difference from NaPES in the spacing of the sulfonate groups making the cooperation of adjacent groups in the binding of Na$^+$ ion more difficult for the PSS$^-$ polyion. Thus, NaPSS is more suitable for studying long-range electrostatic forces with minimum interference from short-range interactions, and it is not surprising that the enthalpies of dilution of NaPSS follow the predictions of electrostatic theory.

The conclusions from recent light scattering and intrinsic viscosity determinations with NaPMOS, NaPSS, NaPA,

and NaPES solutions,[18] which show the latter polyelectrolyte to be the most flexible of the group, are not inconsistent with the occurrence of the strongest binding of Na^+ ion by it: sodium ions shield the negative charges on the PES^- polyion efficiently, and hence reduce the sulfonate group repulsions to the greatest extent.

The virtually identical concentration dependence of ΔH_D (Figure 1) found with NaPSS and NaPMOS is of interest in that dilute solutions of both polyelectrolytes obey the predictions of electrostatic theory. Both polyanions have bulky sidechains and their sulfonate groups are approximately equidistant from the chain backbone, although there are differences in their hydrophobic characters and molecular rigidities. Both polyelectrolytes are well extended in the absence of salt because of the mutual repulsion of their sulfonate groups, but, because of its flexible, hydrated sidechain, these groups in NaPMOS may be approached more readily by counterions. The extent of Na^+ ion binding in NaPMOS, therefore, is larger than in NaPSS. However, in both polyelectrolytes there is little or no short-range interaction with the Na^+ ion.

References and Notes

(1) R. M. Fuoss, A. Katchalsky, and S. L. Lifson, *Proc. Nat. Acad. Sci.*, **37**, 579 (1951).
(2) S. Lifson and A. Katchalsky, *J. Polym. Sci.*, **13**, 43 (1954).
(3) T. Alfrey, P. W. Berg, and H. Morawetz, *J. Polym. Sci.*, **7**, 543 (1951).
(4) G. S. Manning, *J. Chem. Phys.*, **51**, 924 (1969).
(5) J. Skerjanc, D. Dolar, and D. Leskovsek, *Z. Phys. Chem. (Frankfurt am Main)*, **56**, 207, 218 (1967); **70**, 31 (1970).
(6) J. Skerjanc, S. Hocervar, and D. Dolar, *Z. Phys. Chem. (Frankfurt am Main)*, **86**, 311 (1973).
(7) G. E. Boyd, "Polyelectrolytes", Vol. I., E. Sélègny, Ed., D. Reidel Publishing Co., Dordrecht, Holland, 1974, pp 135–155.
(8) N. N. Aylward, *J. Polym. Sci., Polym. Chem. Ed.*, **13**, 373 (1975).
(9) J. Hen and U. P. Strauss, *J. Phys. Chem.*, **78**, 1013 (1974).
(10) H. Eisenberg and G. R. Mohan, *J. Phys. Chem.*, **63**, 671 (1959).
(11) J. S. Tan and S. P. Gasper, *J. Polym. Sci., Phys. Ed.*, **12**, 1785 (1974).
(12) J. J. Christensen, J. W. Gardner, D. J. Eatough, and R. M. Izatt, *Rev. Sci. Instrum.*, **44**, 481 (1973).
(13) J. Skerjanc, *Biophys. Chem.*, **1**, 376 (1974).
(14) A. Katchalsky, Z. Alexandrowicz, and O. Kedem, "Chemical Physics of Ionic Solutions", B. E. Conway and R. G. Barradas, Ed., Wiley, New York, N.Y., 1966, pp 295 ff.
(15) N. Ise and K. Asai, *J. Phys. Chem.*, **72**, 1366 (1968).
(16) R. W. Armstrong and U. P. Strauss, *Encycl. Polym. Sci. Technol.*, **10**, 781–861 (1969); see p 811, Figure 12.
(17) U. P. Strauss and Y. P. Leung, *J. Am. Chem. Soc.*, **87**, 1475 (1965).
(18) J. S. Tan and S. P. Gasper, *J. Polym. Sci., Polym. Phys. Ed.*, **13** [9], 1705 (1975).

Enthalpies of Mixing of Polyelectrolytes with Simple Aqueous Electrolyte Solutions

G. E. Boyd,* David P. Wilson,

Department of Chemistry, University of Georgia, Athens, Georgia 30602

and Gerald S. Manning

School of Chemistry, Rutgers University, New Brunswick, New Jersey 08901 (Received September 19, 1975)

Publication costs assisted by the University of Georgia

The enthalpy changes on mixing dilute aqueous solutions of atactic sodium poly(styrenesulfonate), NaPSS, and sodium chloride were measured at 298.15 K with a sensitive isothermal microcalorimeter. The addition of salt to a NaPSS solution in general was accompanied by the absorption of heat, while the addition of polyelectrolyte to a salt solution became less exothermic with increasing NaCl concentration. The observed mixing enthalpies departed widely from values predicted on the basis of the "additivity rule" (i.e., no interaction between salt and polyelectrolyte), but, when they were corrected for the heat of dilution of the salt, they agreed well over a wide composition range with predictions from the infinite line charge theory.

Introduction

The fundamental assumption that the addition of simple salt to an aqueous polyelectrolyte solution does not significantly alter the immediate ionic atmosphere around the polyions has been the starting point for a number of investigations of the properties of such mixtures. If the foregoing hypothesis accurately describes the structure of electrolyte–polyelectrolyte mixtures it may be expected that the separate contributions of the added salt and of the polyion with its counterions to a given thermodynamic property of a mixture will be distinguishable and independent of each other. Additivity of several properties related to the excess free energy of salt–polyelectrolyte mixtures (viz. osmotic and activity coefficients, Donnan distributions, etc.) have

been reported and discussed most notably by Katchalsky and his co-workers.[1-3]

The empirical nature of the "additivity rule" derived from observations on colligative properties is now recognized, and, in fact, strict additivity has been shown not to be obeyed when precise measurements are available.[4-6] Furthermore, results from the infinite line charge theory of polyelectrolytes[7,8] which is based on a different model suggest that the assumption that the salt does not interact with the polyions cannot be correct. On the other hand, good approximations to the measured properties of mixtures can be inferred from additivity, and thus the "rule" may have useful applications to systems of biological interest or of industrial importance.

Measurements of the enthalpies of mixing of a uni-univalent salt with an aqueous strong polyelectrolyte solution with a common cation were undertaken in this research to determine if a simple mixture rule might hold. For example, if additivity were obeyed the heat of mixing of polyelectrolyte and salt would be given by the sum of the heats of dilution of each to the final volume of the mixed solution. It was anticipated that the thermal effects would be small by analogy with the known mixing enthalpies for uni-univalent electrolytes with one another. A sensitive isothermal titration microcalorimeter therefore was employed.

Experimental Section

Sodium poly(styrenesulfonate), NaPSS, with a viscosity molecular weight of 40 000 ± 2 000, obtained through the courtesy of the Dow Chemical Co., Midland, Mich., was employed. The preparation (NC 1557) was purified and isolated as a colorless solid following an already described procedure.[5] Solutions of accurately known concentration were prepared by weight dilution of a stock solution with ultrapure water (specific conductance $<0.2 \times 10^{-6}$ ohm^{-1} cm^{-1}) taken from a Milli-Q2 system (Millipore Corp., Bedford, Mass.). Stock solutions were made up by weight from pure, solid NaPSS vacuum dried at 60 °C for 24 h. These solutions were contained in tightly stoppered Teflon (FEP) bottles and stored at 6 °C until needed for dilutions. Aqueous sodium chloride solutions were prepared by weight dilution of a saturated NaCl stock solution maintained at 25.00 °C for which $m = 6.144 \pm 0.001$.

An isothermal titration microcalorimeter described elsewhere[9] was employed to measure the thermal effects which were generally less than 10 mcal on mixing salt and polyelectrolyte. The mixing reactions were conducted by delivering either salt or polyelectrolyte solution of predetermined concentration to 25.00 ml of polyelectrolyte or salt solution, respectively, initially held in a ca. 30-ml stainless steel calorimeter reaction vessel. The titrant was delivered by a 2.5-ml capacity ultraprecision digital micrometer syringe (Roger Gilmont Instruments, Inc.), and its volume could be estimated to ±0.0001 ml. The temperature differential between the titrant and titrate was initially adjusted to be less than 10^{-4} °C.

Base-line corrections to the total heat effect were required, as in our earlier work[10] with strong polyelectrolyte solutions, because of changes in the viscosity of the cell solution on mixing. The addition of dilute NaCl solutions to NaPSS usually gave a substantial decrease, while the addition of polyelectrolyte usually gave a small increase in the viscosity[11] of the solution in the reaction cell. Empirical base-line correction curves were required for each mixing reaction. These curves were constructed following a previously described procedure.[10]

Corrections (0.1–0.4 mcal) also were made for the difference in temperature between the titrant and the thermally equilibrated reaction cell solution, and for a constant, small heat absorption (ca. 0.4 mcal) by the titrant solution as it passed through the stainless steel cover plate which closed the reaction vessel. Data were taken by recording the unbalanced, rectified ac output from a Wheatstone bridge on a 10-in. strip-chart recorder (Hewlett-Packard 7101B) operated at a chart speed of 1 in./min. The area between the curve traced during the reaction period and the empirically constructed base line connecting the end of the lead and the beginning of the trail periods was estimated with a compensating polar planimeter and converted to millicalo-

ries using a factor derived from electrical calibration. Background fluctuations in the calorimeter caused by stirring, thermistor heating, etc. limited the sensitivity of the heat measurements to about 0.1 mcal. The precision of the 28 measurements reported was ±0.4 mcal while the uncertainties in the derived enthalpies plotted in Figure 1 varied between ±1.0 and ±10.0 cal equiv^{-1} depending on the number of millimonomoles of NaPSS in the mixing process. Periodic checks on the performance of the calorimeter system were made by measuring the heat of dilution of pure, 0.1000 m aqueous sodium chloride solution to a final concentration such that ca. 10 mcal of heat was evolved. The small quantities of titrant involved in the mixing experiments seems noteworthy; when polyelectrolyte was added to dilute NaCl solutions amounts of only 0.2–2.5 μmol of NaPSS were employed.

Results and Discussion

The mixing reaction taking place in the isothermal calorimeter cell may be formulated as

$$x \text{ ml NaPSS}(m_p^i) + y \text{ ml NaCl } (m_s^i) \rightarrow$$
$$(x + y) \text{ ml (NaCl + NaPSS)}(m_p^f; m_s^f) \quad (1)$$
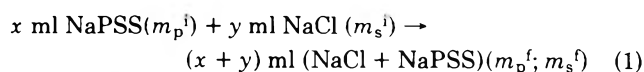
where m_p^i and m_p^f, and m_s^i and m_s^f are the initial and final polyelectrolyte and salt concentrations, respectively. The values used for x and y were 2.5 ± 0.2 ml of NaPSS or NaCl and 25.0 ± 0.5 ml of NaCl or NaPSS, respectively.

Estimates of the enthalpy change in eq 1 may be derived either from the cell[1] or from the infinite line charge theories[7,8] of polyelectrolyte solutions. Both theories are electrostatic in nature involving point ions and specific interaction is assumed to be absent. A treatment based on the line charge theory appears to be easier to develop although the result is restricted to dilute mixtures because the electrostatic potential governing the uncondensed mobile ions in the system is based on the Debye–Hückel approximation. The formula to be developed, therefore, is a limiting law strictly valid only at extreme dilution. The excess Helmholtz free energy of a solution of volume, V, containing polyelectrolyte in equivalent concentration, n_e, is given by[7]

$$F^E/VkT = -\xi n_e \ln \kappa \quad (2)$$

where ξ is the polyelectrolyte charge density parameter defined by

$$\xi = z_p z_c e_0^2 / DbkT \quad (3)$$

and κ is the Debye screening factor which, when two kinds of mobile, singly charged ions (i.e., counterions and coions) are present, is given by

$$\kappa = (4\pi e_0^2/DkT)(n_e + 2n_s) \quad (\xi < 1) \quad (4)$$

In eq 3 and 4, z_p is the charge carried by the ionic group on the polyion; z_c the counterion charge; e_0, the elementary charge; D, the macroscopic dielectric constant of the solvent; b, the distance between the neighboring charges on the polyion in its configuration of maximum extension; and n_s the concentration of uniunivalent salt added to the polyelectrolyte solution. The other symbols have their usual meaning.

The excess Helmholtz free energy of eq 2 may be replaced by the excess Gibbs free energy, G^E, to a good approximation. Application of the Gibbs–Helmholtz equation to G^E leads directly to an expression for the enthalpy of
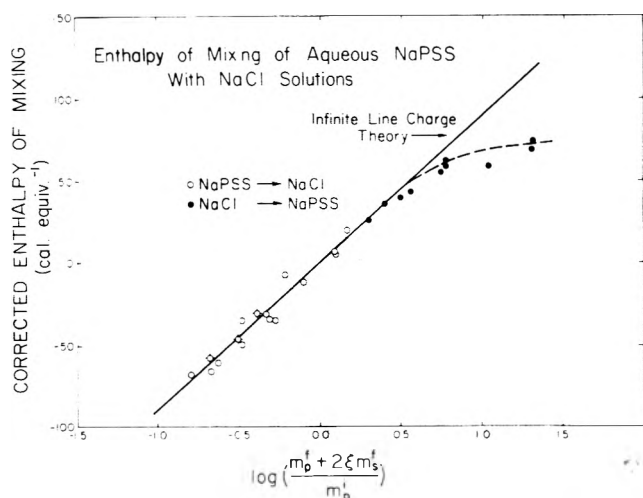
Figure 1. Enthalpy changes on mixing aqueous sodium poly(styrenesulfonate) with sodium chloride solution at 25 °C. (The initial concentration of NaPSS for the points designated by ⧫ was 0.20 m which is above the range of validity of eq 7. Accordingly, a small, additional correction to the enthalpy of mixing was made for the enthalpy of dilution of 0.20 m NaPSS which was taken from Figure 1, ref 10.)

mixing, $\Delta H_M = Q_M/n_p$, when $\xi < 1$ and n_p is the number of monomoles of NaPSS:

$$Q_M = -\frac{n_p R T \xi}{2}\left(1 + \frac{d \ln D}{d \ln T}\right)\ln\left(\frac{m_p^f + 2m_s^f}{m_p^i}\right) \quad (5a)$$

When $\xi > 1$ eq 5a becomes

$$Q_M = -\frac{n_p R T}{2}\xi^{-1}\left(1 + \frac{d \ln D}{d \ln T}\right)\ln\left(\frac{\xi^{-1}m_p^f + 2m_s^f}{\xi^{-1}m_p^i}\right)$$

$$(5b)$$

The theory on which eq 5 is based is valid only at limiting, small concentrations so that a comparison of measured Q_M values with it for the mixing of solutions of finite although small concentration involves some approximation. Note that in the limit, $n_p \to 0$, and Q_M becomes vanishingly small. In actuality, Q_M should tend to $Q_D(\text{NaCl})$ where the latter refers to the process

$$x \text{ ml } H_2O + y \text{ ml } NaCl(m_s^i) \to (x + y) \text{ ml } NaCl(m_s^f)$$

$$(6)$$
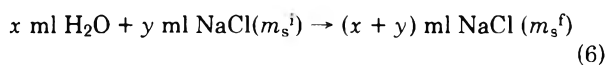
Conversely, when the number of moles of salt involved in mixing becomes vanishingly small ($n_s \to 0$) the value of Q_M in eq 5b approaches the limiting value for the heat of dilution of n_p moles of polyelectrolyte from m_p^i to m_p^f:

$$Q_D(\text{NaPSS}) = -\frac{1}{2}n_p R T \xi^{-1}\left(1 + \frac{d \ln D}{d \ln T}\right)\ln (m_p^f/m_p^i)$$

$$(7)$$

The straight line shown in Figure 1 is a plot of eq 5b expressed as $\Delta H_M = Q_M/n_p$, while the points shown are the experimentally measured enthalpies of mixing per monomole of polyelectrolyte corrected for the enthalpy of dilution of the sodium chloride solution from a concentration of m_s^i to m_s^f. This empirical approach forces an agreement between theory and experiment at $n_p = 0$. Values for $\Delta H_D(\text{NaCl})$ needed to correct the observed mixing enthalpies were estimated from a large plot constructed from a collation[12] of the best available data on the enthalpies of dilution of aqueous sodium chloride solutions.

The data in Figure 1 appear to be in agreement with eq 5b assuming $\xi = 2.828$ over a surprisingly wide range, and they serve to bring out a number of features of this relationship. The addition of even a small amount of salt, holding the ratio, m_p^f/m_p^i, constant, significantly reduces the heat evolved on mixing. The addition of salt to a solution in which the polyelectrolyte concentration is held constant (i.e., $m_p^f = m_p^i$) is accompanied by absorption of heat. For relatively large additions of salt eq 5b is no longer obeyed, and the mixing enthalpy rapidly becomes less than predicted and appears to approach a constant, positive value.

It is clear almost beyond question that the enthalpy change on mixing is not given by the additivity rule. If additivity were obeyed, in all cases heat would have been evolved on mixing, whereas in our measurements heat was absorbed whenever NaCl was added to NaPSS solution, and also in three cases when NaPSS was added to salt. The quantitative agreement of the corrected mixing enthalpy changes with those predicted by the infinite line charge theory appears to give strong support to the model on which the latter is based, namely, the assumptions of ion condensation and of the interaction of added salt with the Debye–Hückel atmosphere of the uncondensed counterions of the polyelectrolyte.

References and Notes

(1) A. Katchalsky, *Pure Appl. Chem.*, **26**, 371 (1971).
(2) Z. Alexandrowicz, *J. Polym. Sci.*, **56**, 97 (1962).
(3) Z. Alexandrowicz and A. Katchalsky, *J. Polym. Sci., Part A*, **1**, 3231 (1963).
(4) J. W. Lyons and L. Kotin, *J. Am. Chem. Soc.*, **87**, 1781 (1965).
(5) G. E. Boyd, "Polyelectrolytes", Vol. I, E. Sélégny, Ed., D. Reidel Publishing Co., Dordrecht, Holland, 1974, pp 135–155.
(6) T. J. Podlas and P. Ander, *Macromolecules*, **3**, 154 (1970).
(7) G. S. Manning, *J. Chem. Phys.*, **51**, 924, 934 (1969).
(8) G. S. Manning, "Polyelectrolytes", Vol. I, E. Sélégny, Ed., D. Reidel Publishing Co., Dordrecht, Holland, 1974, p 9–37.
(9) J. J. Christensen, J. W. Gardner, D. J. Eatough, and R. M. Izatt, *Rev. Sci. Instrum.*, **44**, 481 (1973).
(10) G. E. Boyd and D. P. Wilson, *J. Phys. Chem.*, in press.
(11) J. A. V. Butler, A. B. Robins, and K. V. Shooter, *Proc. R. Soc. London, Ser. A*, **241**, 299 (1951).
(12) V. B. Parker, *Natl. Stand. Ref. Data Ser., Natl. Bur. Stand.*, **No. 2** (1965).

Solvation Effects on the Thermodynamics of Hydrogen Bonded Systems. II

J. N. Spencer,* Judy R. Sweigart, Michael E. Brown, Ronald L. Bensing, Thomas L. Hassinger, William Kelly, Donna L. Housel, and G. William Reisinger : Solvation Effects on the Thermodynamics of Hydrogen Bonded Systems. II

Department of Chemistry, Lebanon Valley College, Annville, Pennsylvania 17003 (Received October 20, 1975)

Thermodynamic functions for the hydrogen bonded complexes of phenol and guaiacol with pyridine in cyclohexane, CCl_4, carbon disulfide, benzene, 1,2-dichloroethane, and chloroform solvents have been determined by monitoring the hydroxyl stretching frequency at about 3 μ. The differences in the thermodynamic data between phenol–pyridine and guaiacol–pyridine complexes are interpreted in terms of a specific interaction of the free phenol hydroxyl with solvent. For 1,2-dichloroethane and chloroform, specific interactions with pyridine also lead to significant solvation effects. No evidence is found for the pyridine–carbon tetrachloride or pyridine–benzene interaction postulated by ESP theory.

Introduction

Solvation effects on hydrogen bonded systems have long been recognized as being of considerable significance but only recently have systematic studies of these effects been carried out. Of the various models used in an attempt to correlate solvation effects, probably the one due to Drago et al.[1-3] has been most thoroughly studied. Central to Drago's approach is the elimination of solvation contributions of the reaction species. In several cases the elimination of solvation procedure (ESP) has been shown by Drago to be generally valid.[1,3] However, certain hydrogen bonded systems do not fit the ESP model and specific solvation contributions have to be inferred. For 1,2-dichloroethane solvent, a lack of agreement was found between experiment and model and various factors were suggested as possible reasons for the failure of the model in this solvent.[3]

In order to interpret the discrepancies found between experiment and the ESP model in carbon tetrachloride solvent with pyridine as the proton acceptor and alcohols as the donors, it was necessary to ascribe a specific interaction to pyridine with carbon tetrachloride.[3] The calorimeteric work of Morcom and Travers[4] was first used to suggest a 0.3 kcal mol^{-1} interaction between pyridine and carbon tetrachloride. The interaction enthalpy was later raised to 0.5 kcal mol^{-1}[5] and presently in order to fit ESP theory the interaction is considered to be 0.9 kcal mol^{-1}.[1] Sherry and Purcell[6] argue that the pyridine–carbon tetrachloride interaction enthalpy is 1.7 kcal mol^{-1} and further suggest a comparable energy of 2 kcal mol^{-1} for the disruption of associated pyridine molecules. The pyridine interaction has also been extended to aromatic solvents, in which the pyridine–solvent interaction is considered to be 0.9 kcal mol^{-1}.[1,3]

Others disagree as to the nature of the interactions in carbon tetrachloride solvent. Gramstad et al.[7,8] consider that proton solvation of the alcohol by carbon tetrachloride is responsible for the differences in the enthalpy of hydrogen bonding in cyclohexane and carbon tetrachloride. Duer and Bertrand[9] ascribe hydrogen bonding of phenol to carbon tetrachloride. Arnett et al.[10,11] have ignored the proposed pyridine–carbon tetrachloride interaction, claiming it to be significant because phenol–pyridine formation enthalpies are the same in carbon tetrachloride and pyridine solvents. As noted above, Sherry and Purcell argue

that this similarity is due to the closeness of the dissociation enthalpies for pyridine–pyridine interactions and pyridine–carbon tetrachloride interactions but this would require a much higher interaction energy than ESP theory allows. The hydroxy–carbon tetrachloride interaction is also supported by Fletcher.[12,13] Because the pyridine–carbon tetrachloride interaction is crucial to ESP theory and because carbon tetrachloride is the most commonly used solvent for near-ir studies, it is of considerable importance to resolve the questions concerning solvation effects in carbon tetrachloride.

The present investigation makes use of phenol and guaiacol, two proton donating species which should provide evidence for either the pyridine–CCl$_4$ or phenol–CCl$_4$ interaction. Because the proton of guaiacol is intramolecularly hydrogen bonded, differences in the trends of the thermodynamic data observed for guaiacol complexes in different solvents cannot be ascribed to hydroxyl bonding to the solvent. Therefore, if pyridine interacts with CCl$_4$ and aromatic solvents, the enthalpy change for the formation of the guaiacol–pyridine complex should be different when cyclohexane is the solvent as compared to CCl$_4$ or aromatic solvents. If solvation effects in phenol–CCl$_4$ systems are due to phenol hydroxyl–CCl$_4$ interactions, no such effects should be observed when guaiacol is the proton donor. If the solvents 1,2-dichloroethane and chloroform, there is direct evidence[14] for a weak pyridine–solvent interaction and the pyridine–chloroform complex has been reported by several investigators.[15] These interactions should be reflected in the thermodynamic properties of these complexes and a further comparison with carbon tetrachloride and benzene solvents is possible.

Experimental Section

Experimental details, methods of calculation, and purification of the phenols and solvents have been previously reported.[16,17] Fisher certified ACS grade pyridine was distilled under nitrogen atmosphere from barium oxide.

Absorption data were obtained in 2-mm pathlength cells and are given in Table I. The data for the bonded absorption in cyclohexane, benzene, and 1,2-dichloroethane solvents cannot be considered highly reliable due to excessive solvent absorption and the broadness of the bands. The frequencies reported in these solvents were reproducible

TABLE I: Frequency Data[a] for the Hydrogen Bonded Complexes of Phenol and Guaiacol with Pyridine

Solvent	Nonbonded frequency		Bonded frequency		$\Delta \nu$	
	Phenol	Guaiacol	Phenol	Guaiacol	Phenol	Guaiacol[b]
Cyclohexane	3615	3561	3207	3217	408	398
CCl₄	3609	3557	3143	3177	466	432
CS₂	3599	3551	3138	3136	461	463
Benzene	3561	3544	3221	3225	340	336
1,2-Dichloro-ethane	3565	3534	3200	3206	365	359
Chloroform	3596	3544	3159	3163	437	433

[a] All data in cm⁻¹. [b] The frequency shift for guaiacol is taken relative to the nonbonded frequency of phenol in the same solvent.

TABLE II: Thermodynamic Data for the Complexes of Phenol and Guaiacol with Pyridine and Me₂SO

Solvent	$K_{20°C}$		$-\Delta H$, kcal mol⁻¹		$-\Delta S$, cal deg⁻¹ mol⁻¹		$-\Delta H$,[a] kcal mol⁻¹	
	Phenol	Guaiacol	Phenol	Guaiacol	Phenol	Guaiacol	Phenol	Guaiacol
Cyclohexane	157.7	2.71	7.27 ± 0.34	3.13 ± 0.07	14.8	8.7	8.96 ± 0.25	3.77 ± 0.37
CS₂	84.1	2.67	5.97 ± 0.41	3.74 ± 0.13	11.5	10.8	7.08 ± 0.24	4.50 ± 0.05
CCl₄	58.3	1.44	5.70 ± 0.29	3.04 ± 0.33	11.4	9.78	6.33 ± 0.07	3.04 ± 0.14
Benzene	24.8	1.72	5.03 ± 0.32	4.11 ± 0.08	10.8	13.9	5.14 ± 0.12	3.88 ± 0.06
1,2-Dichloroethane	18.2	2.10	5.55 ± 0.15	3.12 ± 0.28	13.2	9.2	6.07 ± 0.14	3.43 ± 0.09
Chloroform	22.1	1.40	5.10 ± 0.12	2.53 ± 0.30	11.2	7.3	3.12 ± 0.03	2.09 ± 0.18

[a] Data from ref 16 for the complexes of phenol and guaiacol with Me₂SO. In all systems the error reported is the error in the least-squares slope of a plot of ln k vs. T^{-1}. The equilibrium constants are reproducible to about ±10%.

when 2-mm cells were used but were smaller than the values obtained in 1-cm cells.

The solutions for analysis were about 0.002 M in the phenols and 0.1 M in pyridine. The temperature range was from 10 to 40 °C.

Results and Discussion

Thermodynamic data for the pyridine complexes with phenol and guaiacol are given in Table II. Enthalpy data for the phenol and guaiacol complexes with Me₂SO[16] are also given in Table II for comparison and subsequent use. These data show that the enthalpy change and equilibrium constant for the formation of phenol complexes with pyridine or Me₂SO vary from solvent to solvent. Most commonly, the reason advanced for the variation of ΔH with solvent for alcohol systems is that the hydroxyl interacts in varying degrees with the different solvents.[7-9] Comparison of data shows ΔH for the formation of the phenol complexes with pyridine is consistent with that for the phenol–Me₂SO complexes. The OH···π interaction between phenol and benzene is well established[15] and there seems little doubt that at least part of the more endothermic character of the reaction in this solvent is accounted for by hydroxyl-solvent interaction. Specific interactions by Me₂SO and pyridine with 1,2-dichloroethane and chloroform have been reported[14,15] and are responsible for the slightly lower enthalpy change in these two solvents relative to the more "inert" solvents, cyclohexane, carbon disulfide, and carbon tetrachloride.

When phenol is replaced by guaiacol as the proton donor, the variation in the thermodynamic properties of the pyridine complexes in the different solvents is slight. The variation in ΔH for the phenol complexes with pyri-

dine as contrasted with the relative insensitivity of ΔH to solvent for the guaiacol complexes provides strong support for a phenol–solvent interaction and in as far as ΔH is affected these interactions are dominant. If pyridine–solvent interactions were strong, ΔH for the guaiacol complexes would show greater differences in the various solvents. In particular, if pyridine interacts strongly with CCl₄ and benzene, ΔH in these solvents would be expected to be less than in cyclohexane provided other solvation effects are not large in comparison.

The enthalpy changes for the pyridine complexes with guaiacol in 1,2-dichloroethane and chloroform are somewhat lower than those in other solvents and show that for the solvents in which direct evidence of a pyridine–solvent interaction is known,[14,15] the effect is apparent in the enthalpy data. Pyridine should interact more strongly with chloroform than with 1,2-dichloroethane and this is shown by the slightly lower enthalpy change for the guaiacol–pyridine complex in chloroform. It can be concluded that the pyridine–chloroform interaction is stronger than the pyridine–1,2-dichloroethane interaction and that the Me₂SO–chloroform interaction is greater than the Me₂SO–1,2-dichloroethane interaction. It may also be seen from a comparison of enthalpy data that Me₂SO interacts more strongly with chloroform than does pyridine.

Enthalpy changes for elimination reactions in various solvents are given in Table III. According to ESP theory,[1-3] in the absence of strong specific interactions with the solvent, all the enthalpy changes given in this table for a given acid and base should be identical. For the first set of six reactions involving phenol, Me₂SO, and pyridine there is no apparent trend and if ESP theory is followed, variations in ΔH must be attributed to specific interactions with the sol-

TABLE III: Enthalpy Changes for Elimination Reactions in Various Solvents

Solvent	Reaction AB' + B = AB + B'	ΔH, kcal mol^{-1}
Cyclohexane	Phenol·Me$_2$SO + Pyridine = Phenol·Pyridine + Me$_2$SO	+1.69 ± 0.59
CCl$_4$		+0.63 ± 0.36
Benzene		+0.11 ± 0.44
CS$_2$		+1.11 ± 0.65
1,2-Dichloroethane		+0.52 ± 0.29
Chloroform		−1.98 ± 0.15
Cyclohexane	Guaiacol·Me$_2$SO + Pyridine = Guaiacol·Pyridine + Me$_2$SO	+0.95 ± 0.48
CCl$_4$		+0.20 ± 0.25
Benzene		+0.96 ± 0.14
CS$_2$		+1.23 ± 0.17
1,2-Dichloroethane		+0.99 ± 0.32
Chloroform		−0.13 ± 0.39
Cyclohexane	Phenol·Pyridine + Guaiacol = Guaiacol·Pyridine + Phenol	+4.45 ± 0.45
CCl$_4$		+2.86 ± 0.40
Benzene		+2.11 ± 0.40
CS$_2$		+2.70 ± 0.53
1,2-Dichloroethane		+3.11 ± 0.38
Chloroform		+2.88 ± 0.33
Cyclohexane	Phenol·Me$_2$SO + Guaiacol = Guaiacol·Me$_2$SO + Phenol	+5.19 ± 0.62
CCl$_4$		+3.29 ± 0.21
Benzene		+1.26 ± 0.18
CS$_2$		+2.58 ± 0.29
1,2-Dichloroethane		+2.64 ± 0.23
Chloroform		+1.03 ± 0.21

vent. The interaction of Me$_2$SO and pyridine with 1,2-dichloroethane and chloroform[14] is known but there is no evidence for specific interactions of Me$_2$SO with the other solvents.[2] According to Drago et al.[1-3] ΔH for the pyridine complexes in the solvents CCl$_4$ and benzene should be "corrected" for the pyridine interaction by subtracting 0.9 kcal mol^{-1} from ΔH found for the elimination reactions in these solvents. The enthalpy change should then be close to that in cyclohexane and CS$_2$. This procedure results in even poorer agreement between the enthalpy changes in these solvents. Similar results are obtained with the system guaiacol, Me$_2$SO, and pyridine. Because this procedure has worked well for Drago, data obtained by other investigators were treated according to ESP theory.

Data taken from Sherry and Purcell,[6] Gramstad,[18] Lamberts,[19] and Purcell et al.[20] were subjected to elimination procedures and the results are given in Table IV. All elimination reactions involve pyridine which according to ESP theory should undergo a specific interaction with CCl$_4$ but not with cyclohexane, hexane, or carbon disulfide. The CCl$_4$–pyridine interaction should be evident in the enthalpy change for the elimination reactions between the pairs of solvents. However the data of Sherry and Purcell and that of Arnett et al. give almost identical enthalpy changes in the pairs of solvents listed and a correction of −0.9 kcal mol^{-1} makes the difference between the enthalpy changes larger for all solvent pairs. The close agreement of the enthalpy data for all solvent pairs for these data may be interpreted in terms of ESP theory as support for the absence of a pyridine–CCl$_4$ interaction.

Also given in Table III are reactions for phenol, guaiacol, Me$_2$SO, and for phenol, guaiacol, and pyridine for which the uncomplexed base has been eliminated. These reactions remove the consideration of Me$_2$SO and pyridine interactions with the solvents and because all the species with the exception of phenol are hydrogen bonded any

TABLE IV: Elimination Reactions Involving Pyridine

Solvent	Reaction[a]	ΔH	Ref
CCl$_4$	TEA·HFIP + PY = HFIP·PY + TEA	+1.6	20
C$_6$H$_{14}$		+1.7	
CCl$_4$	TFE·γ-C + PY = TFE·PY + γ-C	+0.85	6
C$_6$H$_{14}$		+0.98	
CCl$_4$	HFIP·γ-C + PY = HFIP·PY + γ-C	+1.27	6
C$_6$H$_{14}$		+1.37	
CCl$_4$	THF·P + PY = PY·P + THF	−1.6	19
C$_6$H$_{12}$		−1.3	
CCl$_4$	TBA·P + PY = PY·P + TBA	−0.1	18
CS$_2$		+0.4	

[a] TEA = triethylamine, HFIP = 1,1,1,3,3,3-hexafluoro-2-propanol, PY = pyridine, TFE = 2,2,2-trifluoroethanol, γ-C = γ-collidine, THF = tetrahydrofuran, P = phenol, TBA = tributylamine.

variation in ΔH for these elimination reactions should be largely determined by the solvation of phenol in the various solvents. If phenol does not undergo specific interaction with the solvent, or give rise to unusual solvation effects, the enthalpy changes for these elimination reactions should be the same in all solvents. The variations actually found in ΔH are most reasonably attributed to phenol–solvent interaction. Calorimetric data for the heat of solution of phenol in cyclohexane, carbon tetrachloride, and benzene have been reported as +7.625,[9] +6.27,[10] and +4.72[10] kcal mol^{-1}, respectively. The trend in ΔH for the elimination reactions follows the trend in increasing solvation of phenol as given by these heats of solution.

References and Notes

(1) R. M. Guidry and R. S. Drago, J. Phys. Chem., 78, 454 (1974).
(2) R. S. Drago, M. S. Nozari, and G. C. Vogel, J. Am. Chem. Soc., 94, 90 (1972).
(3) M. S. Nozari and R. S. Drago, J. Am. Chem. Soc., 94, 6877 (1972).
(4) K. W. Morcom and D. N. Travers, Trans. Faraday Soc., 62, 2063 (1966).
(5) W. Partenheimer, T. D. Epley, and R. S. Drago, J. Am. Chem. Soc., 90, 3886 (1968).
(6) A. D. Sherry and K. F. Purcell, J. Am. Chem. Soc., 92, 6386 (1970).
(7) T. Gramstad and O. Mundheim, Spectrochim. Acta, Part A, 28, 1405 (1972).
(8) T. Gramstad and W. J. Fuglevik, Acta Chem. Scand., 16, 6 (1962).
(9) W. C. Duer and G. L. Bertrand, J. Am. Chem. Soc., 92, 2587 (1970).
(10) E. M. Arnett, L. Joris, E. Mitchell, T. S. S. R. Murty, T. M. Gorrie, and P. v. R. Schleyer, J. Am. Chem. Soc., 92, 2365 (1970).
(11) E. M. Arnett, E. J. Mitchell, and T. S. S. R. Murty, J. Am. Chem. Soc., 96, 3875 (1974).
(12) A. N. Fletcher and C. A. Heller, J. Phys. Chem., 71, 3742 (1967).
(13) A. N. Fletcher, J. Phys. Chem., 73, 2217 (1969).
(14) A. Allerhand and P. v. R. Schleyer, J. Am. Chem. Soc., 85, 1715 (1963).
(15) M. D. Joesten and L. J. Schaad, "Hydrogen Bonding", Marcel Dekker, New York, N.Y., 1974, p 366.
(16) J. N. Spencer, R. S. Harner, and C. D. Penturelli, J. Phys. Chem., 79, 2488 (1975).
(17) J. N. Spencer, R. A. Heckman, R. S. Harner, S. L. Shoop, and K. S. Robertson, J. Phys. Chem., 77, 3103 (1973).
(18) T. Gramstad, Acta Chem. Scand., 16, 807 (1962).
(19) L. Lamberts, Z. Phys. Chem. (Frankfurt Am Main), 73, 159 (1970).
(20) K. F. Purcell, J. A. Stikeleather, and S. D. Brunk, J. Am. Chem. Soc., 91, 4019 (1969).

Activity Coefficients of Alkyl Acetates in Concentrated Electrolyte Solutions

R. F. Cross*[1] and P. T. McTigue

The activity coefficients of methyl acetate (MeOAc), ethyl acetate (EtOAc), n-propyl acetate (n-PrOAc), n-butyl acetate (n-BuOAc), and n-pentyl acetate (n-PeOAc) have been measured at 25 °C in concentrated aqueous solutions of electrolytes using the distribution technique. The salts used were LiCl, NaCl, KCl, CsCl, KF, KBr, $NaNO_3$, and $NaClO_4$. In general, the results obtained are as might be expected. A mechanistic explanation is given of the trends observed and unexpected features in the data are explained with the aid of some assumptions regarding the nature of ionic hydration. The apparent molar volumes of MeOAc have also been determined over the full range of molalities for each of the salts used in the activity coefficient determinations. These measurements are then used in conjunction with thermodynamic data for the salt solutions (from the literature) to calculate the MeOAc activity coefficients according to the expanded McDevit and Long equations developed in an earlier publication. Similar, but less accurate calculations have also been done for the activity coefficients of the larger esters. In these cases, apparent molar volumes were determined only in water. The calculations are found to have mixed success.

Introduction

The dependence of rates of reaction upon substrate activity coefficients was enshrined in transition state theory in the early 1930's. Since that time, innumerable investigations have utilized this theory, the activity coefficients of a wide range of substrates (mostly nonelectrolytes) having been measured in an equally diverse range of media, aqueous salt solutions being a common medium in which solvent effects have been examined. It is therefore not surprising that chemists have endeavored to calculate the activity coefficients of nonelectrolytes in aqueous salt solutions.[2-8]

In aqueous solutions, however, a problem arises due to the hydrogen-bonded networks which extend throughout the solution, such that the concept of localized solute–solvent interaction is often probably inappropriate, as is the assumption of pairwise additivity of interaction of species.[9] While a quantitative description of the properties of aqueous solutions may eventually be derived using the statistical mechanics of hard-sphere fluids as a basis, this seems only likely to occur by detailed reference to the unique structure of the water molecule.[10] To date, "scaled particle theory" calculations have been based upon the Pierotti ap-

proach[11] in which the specific nature of water is only implicitly taken with account through the use of the experimental densities and coefficients of thermal expansion compressibility. More detailed analyses of this approach, questions its direct applicability to water solutions[10,12] and the calculations of activity coefficients of nonelectrolytes in salt solutions have had varied success.[7,8,13-16] One of these attempts has concerned polar nonelectrolytes. Wilcox and Schrier[15] calculated the limiting salting coefficients (k_s) for small aliphatic alcohols in aqueous solutions of the sodium halides. Agreement between theory and experiment was generally good, notwithstanding the above.

An alternate approach is that of McDevit and Long.

The McDevit and Long (McDL) approach to calculating k_s[5] has recently been extended to enable the calculation of activity coefficients of nonelectrolytes in concentrated solutions of electrolytes.[17] The equations developed there were found to give excellent agreement with experiment for most of the nonpolar nonelectrolyte systems considered. In this paper the new equations are applied to the solutions of polar nonelectrolytes. Altshuller and Everson[18] have previously applied the McDL approach in the case of polar nonelectrolytes, but only to the calculation of k_s and with-

out quantitative correction for the distance of closest approach of nonelectrolyte and ion.

Theory

The molal coefficients for the partition of a nonelectrolyte (n) between an organic and an aqueous phase are given by

$$D = (m_{n,org}\gamma_{n,org})/(m_{n,aq}\gamma_{n,aq})$$

Hence for identical molalities of nonelectrolyte in organic phases in equilibrium with water (w) and with a salt solution (s), the relative molal activity coefficient of the nonelectrolyte is

$$\gamma_n(= \gamma_{n,s}/\gamma_{n,w}) = D_s/D_w$$

After conversion to the molal scale, the corrected equation developed in ref 17 is

$$\lim_{n_n \to 0} (\log \gamma_n) = \frac{V_n C_s(V_s - \phi_s)}{2.303RT\beta}\left[1 - \right.$$

$$\left. \frac{C_s}{2}(V_s - \phi_s)\right]\frac{\bar{r}_h}{\bar{r}_h + r_n} - \log(1 + 2 \times 10^{-3}m_s M_s) \quad (1)$$

γ_n = the relative molal activity coefficient of the nonelectrolyte, n; V_n = molar volume of nonelectrolyte; C_s = molar concentration of salt; V_s = molar volume of liquid salt extrapolated to the temperature of solution (the intrinsic volume); ϕ_s = apparent molar volume of salt in m_s molal salt solution; β = isothermal compressibility of an m_s molal salt solution; m_s = molality of salt; M_s = molecular weight of salt; r_n = distance of closest approach to the nonelectrolyte molecule; $\bar{r}_h$ = distance of closest approach to the average "solvated" [19] ion present in solution.

It is evident from eq 1 that once the salt solution parameters have been fixed, the application of these expressions to a variety of nonelectrolytes requires only knowledge of V_n and r_n. As these equations are only functions of bulk observable properties of solution and do not depend upon an assumed model of solvent structure or solute–solvent interactions, eq 1 provides a relatively quick and painless method of calculating nonelectrolyte activity coefficients in salt solution.

Experimental Section

The KF, cyclohexane, and esters were laboratory reagent grade. All other chemicals were analytical reagent grade.

The esters were purified according to Vogel[21] and stored over vacuum-dried Linde 3-4A molecular sieves, under argon, in 2–3 cm³ quantities sealed in glass ampoules. Cyclohexane was distilled once at the accepted boiling point.[22] As the $NaClO_4$ was invariably wet, its solutions were made up approximately by weight and then accurately determined by evaporation to dryness. The other salts were dried at 400 °C ($NaNO_3$, 250 °C) for 4 h, with occasional stirring. Anhydrous Na_2CO_3 was dried at 270–290 °C, with occasional mixing, and then cooled and stored under vacuum. HCl was standardized vs. the Na_2CO_3 according to Kolthoff and Sandell,[23] the HCl being used to standardize the NaOH solutions employed.

Partition solutions were made up by weight (keeping $m_{n,aq}$ well under 0.1 m), thermostatted at 25.00 ± 0.05 °C, and shaken for 30–60 s every 0.5 h for about 5 h and then left to stand overnight. Variation in this procedure did not lead to different distribution coefficients. We assumed this to indicate the attainment of equilibrium. The less dense

organic phase was removed by suction with a water pump, an aliquot of the aqueous phase run into a not-greater-than-50%-excess of NaOH solution, covered with an inert atmosphere, stoppered in an airtight fashion, shaken, and left overnight. An automatic titrator (Radiometer) was then used to determine the excess NaOH with standard HCl. It was not found necessary to employ an inert atmosphere during titration.

The apparent molar volumes of the esters were determined at the ambient temperature of an internal room, the temperature of which varied only by tenths of a degree over the period of 1 h. To ensure thermal equilibrium was attained, all glassware and the prepared solutions were stored in the closed room overnight. Weighings were made on a five-place automatic Mettler H 20 T balance. The balance was carefully checked with standard weights and the density bottles handled only with insulated tongs. With care, weighings were reproducible within ±3 × 10⁻⁵ g.

Results and Discussion

The distribution coefficients for esters between water and cyclohexane (D_w) were sometimes found to vary a little from batch to batch of cyclohexane. Fortunately, the activity coefficients did not vary provided that D_w and D_s were determined from the same batch of cyclohexane. The variation of D_w with molality of ester in the cyclohexane phase was determined for each of the esters other than n-BuOAc.[24] For the smaller esters, D_w is small enough for $m_{n,org}$ to vary quite appreciably between aqueous solutions when a fixed volume of the ester is partitioned, whereas for n-BuOAc, D_w is large enough such that $m_{n,org}$ varies by only 0.8% from water to the most strongly salting-out solution. For n-PeOAc, the solubility is so low that it was not possible to add the ester to the partition mixture both rapidly and quantitatively. Consequently, the variation of D_w with $m_{n,org}$ had again to be determined for n-PeOAc.

The activity coefficient data (γ_n) are given in Table I.

Extensive measurements of γ_n for the n-alkyl acetates in concentrated salt solutions have previously been made only in the case of EtOAc and determinations of γ_n using the distribution technique have only once been reported (Philip and Bramley[25,26]). Inspection of Figure 1 shows good agreement between the determinations of γ_n for EtOAc in NaCl solutions according to the distribution technique: Philip and Bramley[25] (20 °C), this work (25 °C). If the temperature dependence of γ_n as determined by Altshuller and Everson[18] by solubility measurements can be taken to be qualitatively correct, agreement between the work of Philip and Bramley and the work presented in this paper is excellent. For the other salt solutions employed by Philip and Bramley (LiCl, NaCl, and $NaNO_3$) the agreement between studies is identical. So too are the solubility determinations of γ_n[18,27,28] quite different to the distribution determinations of γ_n in each case. Long and McDevit[29] have pointed out the dangers of the solubility technique due to the possible dissolution of water to differing extents in the supposedly pure reference phase, with the consequential change in activity of the solute in its reference phase. The possibility of medium effects in the aqueous phase also arises where the nonelectrolyte solubility is too large. With solute concentrations greater than about 0.2 M, self-interaction can be detected.[28] As the solubility of EtOAc in water lies somewhere between 0.801 and 0.835 m[18,27,28,30] and the solubility of water has been reported to be approximately 0.35 m in EtOAc,[27] it seems apparent that the use of

TABLE I: Activity Coefficients of the Alkyl Acetates in Aqueous Salt Solutions at 25 °C

LiCl molality, m	0.944	1.85	2.83	3.90	5.13	5.79	6.85
MeOAc	1.205	1.39	1.58	1.81_5	1.91	2.16	2.14
EtOAc	1.26	1.618	2.00	2.28	2.78_5	2.98	3.33
n-PrOAc	1.36	1.77	2.54	3.10_5	3.54	3.77	4.80
n-BuOAc	1.60	1.93	2.76	3.78	5.11	5.87	7.21
n-PeOAc	1.56	2.34	3.16	6.28	9.44		

LiCl molality, m	0.911	1.885	2.89	3.93	5.02
n-PrOAc	1.33	1.933	2.46	3.04	3.51

NaCl molality, m	1.02	2.11	3.21	4.38	5.34	5.62	5.98	6.11	6.18
MeOAc	1.335	1.560	2.13	2.80		3.63			3.60
EtOAc	1.44	2.13	2.94	4.33	6.09	6.60	6.92	7.54	
n-PrOAc	1.639	2.49	3.88	5.81		8.96			10.90
n-BuOAc	1.78	2.77	4.42	7.26	10.5	12.53		12.32	17.86
n-PeOAc	1.78	2.88	4.85	8.92	11.1			12.41	

KCl molality, m	0.820	1.686	2.59	3.55	4.20	4.57	4.74	4.79
MeOAc	1.115	1.26	1.41	2.07	2.20			2.46
EtOAc	1.383	1.72	2.25	2.93	3.60			4.04
n-PrOAc	1.41	1.93	2.61	3.35	4.71	4.98		5.27
n-BuOAc	1.63	2.01	2.99	4.50		6.44		7.07
n-PeOAc	1.38	2.06	3.72	5.84	7.56		10.63	

CsCl molality, m	0.840	1.80	2.82	3.83	5.16	6.50
MeOAc	1.266	1.364	1.59	1.86	2.16	2.77
EtOAc	1.21	1.63	2.05	2.64	3.45	4.22
n-PrOAc	1.34	1.91	2.30	3.19	4.32	5.72
n-BuOAc	1.44	1.67	2.33	3.27	4.33	6.73
n-PeOAc	1.36	1.90	2.37	3.12	5.64	7.90

KF molality, m	0.969	1.951	2.995	4.062	5.216	6.222
MeOAc	1.48	2.73	4.30	5.46	8.35	9.76
EtOAc	1.84_5	3.18	5.87	9.62		
n-PrOAc	1.98	3.64	6.73	11.0		
n-BuOAc	1.98	3.52	5.00	7.23	9.42	

KBr molality, m	0.625	1.279	1.964	2.681	3.439	4.132
MeOAc	0.98	1.12	1.18_5	1.34	1.49	1.63
EtOAc	1.11	1.29	1.48	1.79	1.99	2.32
n-PrOAc	1.16	1.37	1.54	1.88	2.15	2.78
n-BuOAc	1.26	1.41	1.79	2.02	2.49	3.03
n-PeOAc	1.37_5	1.80	2.32	3.22	4.36	5.47

$NaNO_3$ molality, m	1.03	2.13	3.31	4.58	5.98	7.00
MeOAc	1.09_5	1.21	1.36	1.65	2.02	2.18
EtOAc	1.18	1.42	1.82	2.27	2.98	3.42
n-PrOAc	1.18		2.05	2.71	3.63	4.44
n-BuOAc	1.23	1.59	2.12	2.95	4.39	5.41
n-PeOAc	1.41	2.05	2.98	5.19	7.50	9.35

$NaClO_4$ molality, m	0.78	1.81	2.84	3.96	5.20	6.56
MeOAc	0.913	0.89	0.95	0.97	1.016	0.953
EtOAc	0.99	1.02	1.08	1.14	1.23_5	1.45
n-PrOAc	1.00	1.05	1.16	1.34	1.61	1.83
n-BuOAc	1.06	1.20	1.28	1.53	1.80	2.36
n-PeOAc	1.24	1.65	2.29	3.32	4.01	

the solubility method for the determination of EtOAc activity coefficients is not valid.

Application of eq 1 requires selection of intrinsic volume data (V_s). Several sets of these data are given in Table II. Generally the order of V_s is the same for each set of data, although for each of KF and LiCl there is one inconsistent value. The data of line 2 have been taken as a reference,

with V_s for $NaNO_3$ and $NaClO_4$ taken from line 4 to complete the set. The data of line 2 do not contain any anomalous values of V_s and were derived by Scott[31] according to his concept of the critical disruptive state in which further expansion of a crystal leads to a breakdown of the characteristic lattice structure and replacement by the more mobile fluid state. A distinction is therefore drawn between V_s
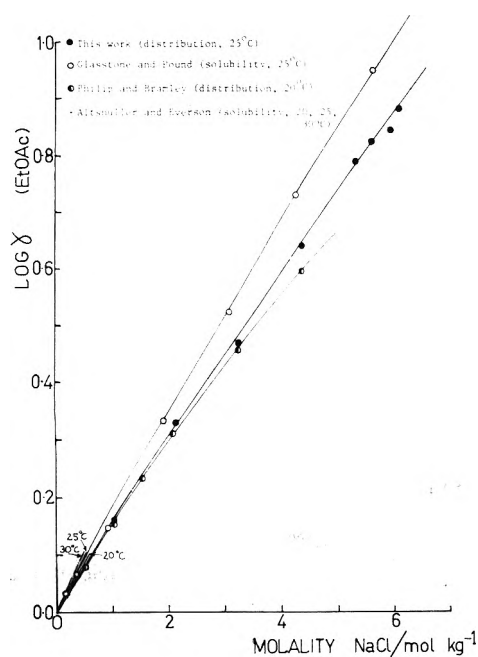
Figure 1. Log γ for ethyl acetate in NaCl solutions. The originators of the measurements, the technique used, and the temperature are indicated in the key (inset). The lines marked 20, 25, and 30 °C are due to Altshuller and Everson.

derived from the true CsCl structure (48.0 cm³ mol⁻¹) and V_s derived from the hypothetical rock salt structure (47.2 cm³ mol⁻¹). Comparison of CsCl V_s values with the other V_s in each series shows the CsCl values to be consistent with the value of 47.2 cm³ mol⁻¹ which was derived from the incorrect crystal structure of the salt. $V_s = 48.0$ cm³ mol⁻¹ has been chosen as the reference value of V_s for CsCl. The set of reference values have been plotted vs. themselves in Figure 2 and the abscissa positions labeled with the salt. The other sets of V_s have then been plotted against these reference points on the abscissa and lines of best fit drawn for each series. To be consistent with the V_s values found appropriate in ref 17, Scott's alternate estimates of V_s (line 6 of Table I) have been selected other than for CsCl. In this case, a value 50.0 cm³ mol⁻¹ taken from the line of best fit to Scott's data (□). Similarly, V_s values for KF (25.7 cm³ mol⁻¹), NaNO₃ (37.8 cm³ mol⁻¹), and NaClO₄ (50.8 cm³ mol⁻¹) have been taken from the same line of best fit.

Table III shows the sources of apparent molar volumes of the salts and of compressibilities, densities, and heat capacities of the salt solutions. Where possible (LiCl, NaCl, KCl, and KBr), Gibson's isothermal compressibility data[34] have been used. As his data were found to be internally consistent and generally in excellent agreement with other sources, NaNO₃ and CsCl isothermal compressibility data have been obtained from Gibson on the basis of additivity. For KF and NaClO₄ solutions there are only adiabatic compressibility data available at 20 °C. These have been converted to isothermal compressibilities at 20 °C according to the relationship given in ref 35. β appears to vary very little, if at all, with temperature.[36,37]

Limiting apparent molar volumes of the esters (ϕ_v^∞) have been used for V_n in calculations of log γ_n according to eq 1. Figure 3 shows the variation of ϕ_v^∞ for MeOAc in the solutions of each of the salts. In the case of the larger esters, this dependence was not determined. However, in order to carry out approximate calculations for the esters

other than MeOAc, ϕ_v^∞ was determined for EtOAc, n-PrOAc, and n-BuOAc in pure water. A value of ϕ_v^∞ was obtained for n-PeOAc by extrapolation of the linear variation of ϕ_v^∞ (for the three previous homologues) as a function of the carbon number of the side chain. Table IV gives these data. As a slightly better approximation to the likely true ϕ_v^∞ for the larger esters, we have used the quantity ϕ_v^∞(MeOAc, salt solution) $\times$ ϕ_v^∞(ester, H₂O)/ϕ_v^∞(MeOAc, H₂O) for the calculation of log γ_n in the case of the larger esters. We therefore assume the same manner of variation in ϕ_v^∞ with salt concentration for the larger esters, as is observed for MeOAc.

r_n values, the distance of closest approach to the nonelectrolyte, have been calculated from

$$\phi_v^\infty = \tfrac{4}{3}\pi r_n^3 \qquad (2)$$

r_h were calculated from the individual radii of hydrated ions, as determined from density measurements and tabulated in ref 6. (See ref 17 and 20.) The NO₃⁻ and ClO₄⁻ ions have been assumed to be unsolvated. Values of 2.03 and 2.27 Å respectively are taken from Hindman.[45]

The values of log γ_n calculated from eq 1 for MeOAc are shown in Figure 4, along with the experimental data. As the experimental procedure had been found to achieve equilibrium, the scatter in the data must be due to errors in analysis. The overall salting orders are generally similar, although with some inversions. For the K⁺ salts the anion salting orders are identical, F⁻ > Cl⁻ > Br⁻, as are the anion salting orders for the Na⁺ salts, Cl⁻ > NO₃⁻ > ClO₄⁻. The salting in of MeOAc by NaClO₄ is predicted, although at high molalities of NaClO₄ there is poor quantitative agreement. In the case of the cations, the observed salting orders is Na⁺ > K⁺ > Cs⁺ > Li⁺, whereas the predicted order is Na⁺ > Li⁺ > K⁺ ≫ Cs⁺.

Quantitative agreement between eq 1 and experiment is excellent for MeOAc in KF, NaCl, and LiCl solutions. In KCl solutions, the calculated line passes through the experimental points at low salt concentrations but is quite divergent from those experimental points determined in the presence of larger salt concentrations. It seems apparent that these two groups of experimental points are incompatible. Reference to Figure 5 (and Figures 5M and 6M)[24] indicates that the correct cation salting orders for the smaller n-alkyl acetates is Na⁺ > K⁺ > Cs⁺, Li⁺ and that the lower lying experimental log γ_n points are in error. This is consistent with the order of salt effects generally expected for polar nonelectrolytes which do not have pronounced acidic or basic tendencies.[29] Furthermore, inspection of Figure 6 also tends to lead to the same conclusion. The log γ_n plots calculated from eq 1 for the higher homologues are all appreciably lower lying than the experimental data, which in these cases are not badly scattered as for MeOAc. This indicates that the chosen value of the intrinsic volume (V_s) of KCl is too low. A more appropriate choice of V_s that would approximate better to the experimental data for the larger esters, would also approximate to the higher lying log γ_n values determined for MeOAc in the more concentrated solutions of KCl.

Figure 7 shows the effect of increasing nonelectrolyte size (V_n) upon the calculated and experimental log γ_n values for a salt (NaCl) in the presence of which the variation of log γ_n was correctly predicted for MeOAc. From eq 1 it is clear that log γ_n increases with the volume occupied by the nonelectrolyte and in the case of nonpolar nonelectrolytes in a series of salt solutions, experimental determi-

TABLE II: Intrinsic Volumes of Salts (cm^3 mol^{-1})

KF	NaCl	KCl	LiCl	CsCl	KBr	NaNO$_3$	NaClO$_4$	Symbol[a]	Ref
	28.9	36.9	26.1	46.7[b]	41.7[b]	36.9[b]		x	5[c]
24.0	26.9	36.3	25.3	48.0	41.3			●	31
				47.2					
26.5	27.5	37.0	22.5	47.0	42.0	36.0	49.0		32
21.7	30.4	37.1	27.5	47.9	43.8		60.1	+	33
	29.1	38.4	26.5	49.0	43.0			□	31

[a] See Figure 6. [b] Obtained assuming additive effects of individual ions. [c] From dP_e/dC_s data of Gibson (see ref 5). P_e is the "effective pressure" as defined by Gibson.
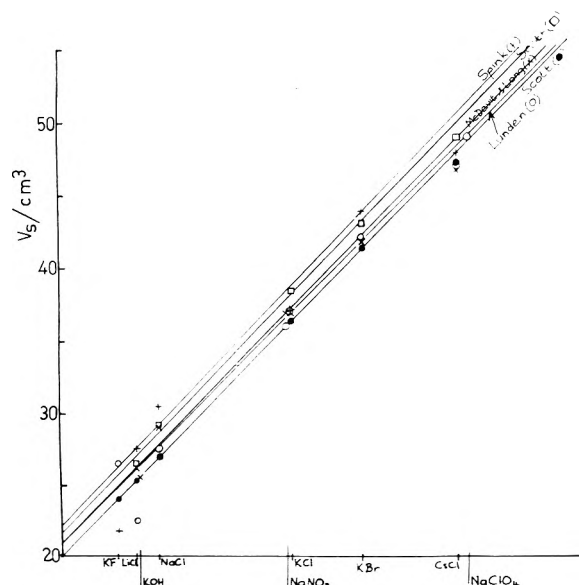
Figure 2. Plots of the intrinsic volume (V_s) of salts according to several sources (see text).

nation of the Setchenow salting constants (k_s) has indicated an approximately correct sensitivity of the McDevit and Long theory to molecular size.[46,47] The same may be said of the relative values of the experimental and calculated log γ_n in Figures 7 (NaCl), 8M[24] (LiCl), and 9M[24] (KF). That the quantitative prediction of the variation of log γ_n with increasing nonelectrolyte size is far from perfect, will in part be due to the assumed variation in ϕ_v^∞ for the larger esters. It is impossible to guess whether this factor will account for the entire discrepancy between calculated and determined values of log γ_n in all cases, but in solutions of KF, where ϕ_v^∞ varies by almost 10% over the range from 0 to 6 M KF even for MeOAc, quite large variations in ϕ_v^∞ may well occur for the larger esters.

It is particularly gratifying that the same NaCl solution data (especially V_s) have been able to give rise to equally good estimates of the variation of the activity coefficients of a polar nonelectrolyte (MeOAc) and a nonpolar nonelectrolyte (benzene[17]) over a range of concentrated salt solutions. As suggested in ref 17, it seems possible that eq 1 may be capable of predicting the activity coefficients of a wide range of electrolytes once an appropriate value of V_s has been found. All that is required for a new nonelectrolyte is accurate V_n and r_n data. In its given form, eq 1 could not be expected to satisfactorily predict the activity coefficients of strongly polar nonelectrolytes capable of competing with water to solvate the electrolyte ion. Crystallographic radii of the ions would then have to be used to determine the factor correcting for the nonzero distance of closest approach of the nonelectrolyte and ions.

Given the considerable range of V_s values (Table I) and the sensitivity of eq 1 to V_s, it is not surprising that less accurate prediction of γ_n is achieved for the electrolytes exhibiting weaker salting effects. $V_s - \phi_s$ is typically about 6 cm^3 mol^{-1} in these instances, compared to V_s and ϕ_s about 40 cm^3 mol^{-1}. An uncertainty of 1 cm^3 in V_s is 17% of $V_s - \phi_s$ and may be up to a difference of 0.1 in log γ_n. This order of magnitude of uncertainty in V_s is sufficient to account for the discrepancy between eq 1 and experiment for NaNO$_3$ and NaClO$_4$ but not in the cases of CsCl and KBr.

The possible general utility of eq 1 lies in its relative simplicity of format. To this end we have determined a set of V_s values which fit the experimental data for MeOAc. They are listed in Table V. The intermediate quantities required for a rapid calculation of log γ according to eq 1 using the V_s of Table V are given in Table 1M.[24] Figures 4, 5, 5M, 6M, and 7M show plots of γ_n as a function of salt molality for the eight salts, for MeOAc, EeOAc, n-PrOAc, n-BuOAc, and n-PeOAc, respectively. As mentioned earlier in connection with MeOAc, the salting out orders of the electrolytes, and of the cations and anions individually, are as expected for the lower homologues.[29] Increasing size of the hydrocarbon segment can be seen to lead to generally higher activity coefficients. This aspect can be more readily ascertained from Figure 6, which shows γ_n for each of the nonelectrolytes in KCl solutions. Consideration of the effect of increasing size upon the activity coefficients of nonpolar nonelectrolytes in solutions of small ion salts[7,47] would lead us to expect this feature also. Mechanistically, an explanation can be given in the framework of Bockris et al.[4] As the ion–dipole and dipole–dipole forces involving the polar part of the esters will be approximately constant for the series of esters in solutions of a particular salt, (i) the electrostatic repulsion of the hydrocarbon segment, (ii) the attractive interactions of the induced dipole in the hydrocarbon segment with ions and water dipoles, and (iii) dispersion forces will be the factors which affect the change in γ_n with size of the ester. As the hydrocarbon segments of the esters are relatively small and saturated, the polarizability of these groups, and hence (ii), will be small. Similarly, (iii) will generally be small, especially in view of the short range of dispersion forces and the "solvation"[20] of the ions in question. The effect of increasing size is thus expected to be compatible with a predominant, increasing electrostatic repulsion, as is observed.

The implication of this analysis is that for any single ester there will be a gradation from strong salting out, by electrolytes containing the smaller ions with the higher charge densities, to weak salting out (or salting in) by electrolytes comprised of larger ions. Even on the basis of crystallographic ionic radii, the cationic and anionic salting orders are in accord with this view, Li$^+$ being the exception. A more realistic evaluation of salting orders requires look-

TABLE III: Literature Sources of Auxiliary Data

Salt	LiCl	NaCl	KCl	KBr	CsCl	NaNO$_3$	KF	NaClO$_4$
ϕ_s		← 38,39 →		38	38,40	41,42	38,43	42
β			← 34 →				← 32,36,44 →	
ρ							41,43	41,42
C_p							43	42

TABLE IV: Limiting Apparent Molar Volumes (ϕ_v^∞) and the Average Deviation from the Mean for the n-Alkyl Acetates in Water

Ester	ϕ_v^∞, cm^3	No. of measure- ments	Temp, °C
MeOAc	71.8 ± 0.2	7	19.1
EtOAc	88.0 ± 0.1	7	18.5
n-PrOAc	103.8 ± 0.3	9	18.2
n-BuOAc	119 ± 1	10	18.6
n-PeOAc	(135 ± 2)^a		(~18.5)

^{a} Obtained by extrapolation of the linear variation of ϕ_v^∞ with ester size. $\phi_v^\infty = (56.0 + 15.8n) \pm 0.1$, where n is the number of carbon atoms in the side chain and 0.1 is the standard deviation.
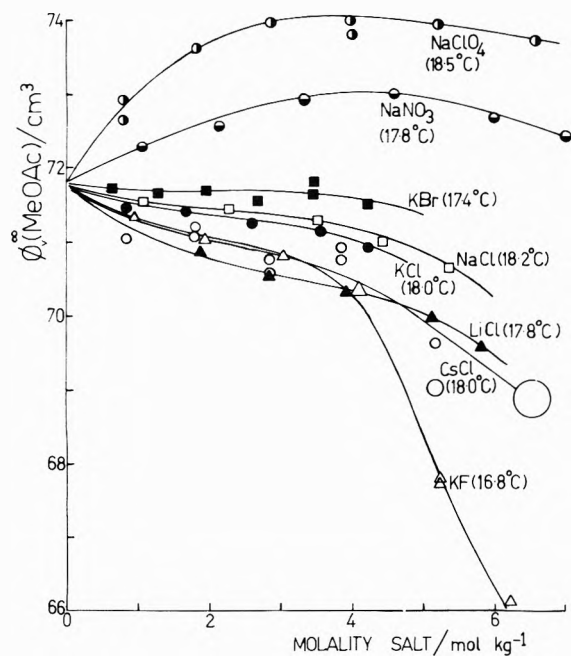
Figure 3. Limiting apparent molal volumes (ϕ_v^∞) of methyl acetate in salt solutions.

Figure 4. Plots of log γ_n vs. the molality of added electrolyte. The numbered lines were calculated using eq 1 and the points are the experimental data: KF (1, ▲); NaCl (2, ●); LiCl (3, O); KCl (4, △); NaNO$_3$ (5, ◒); KBr (6, ■); CsCl (7, □); NaClO$_4$ (8, ◐).
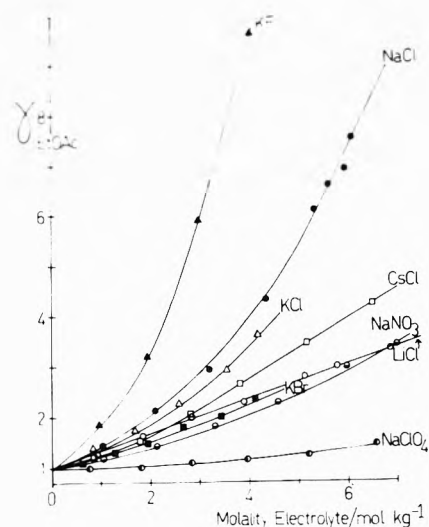
Figure 5. The effects of salts on the activity coefficient of ethyl acetate.

ing at ionic hydration. As Bonner has pointed out, salting out is but one of many solution phenomena which peak at either Na$^+$ or K$^+$.[48] A distinction has to be made between the strength of bonds between ions and their nearest neighbor water molecules (strength of hydration) and the extent of hydration, whether this later quantity is measured in terms of a solvation number or a coordination number. Relative to the larger alkali metal cations, the decrease in cationic size is a disproportionately large percentage between Na$^+$ and Li$^+$, so that the Li$^+$ to nearest neighbor water bonds must be disproportionately strong, the nearest neighbor water molecules must be polarized particularly strongly, the second layer of water molecules unexpectedly firmly held, and so on out into the solution *further* than for the larger cations. The net result is a greater shielding of

the Li$^+$ charge, leading to a lowering of the electrostatic repulsion of nonpolar molecules or segments.

One of the unexpected features of the data is the change in the relative salting effect of Li$^+$ on the larger esters. From a slightly downward turning curve for MeOAc, the γ_n plots change to linear for EtOAc and n-PrOAc to upward curving plots for the n-Bu and n-Pe esters (see Figure 8M[24]). As the molality of LiCl increases from 2 to 4 to 6, the number of water molecules present in solution per mole of salt decreases from 28 to 14 to 9, the shielding of the small Li$^+$ probably decreases and a resultant increase in electrostatic repulsion of the hydrocarbon segment of the

TABLE V: V_s Values Fitting Methyl Acetate Experimental Activity Coefficient Data

Salt	KF	NaCl	KCl	LiCl	CsCl	KBr	NaNO$_3$	NaClO$_4$
V_s, cm^3 mol^{-1}	25.9	29.1	39.7	26.7	55.6	46.3	39.2	53.0
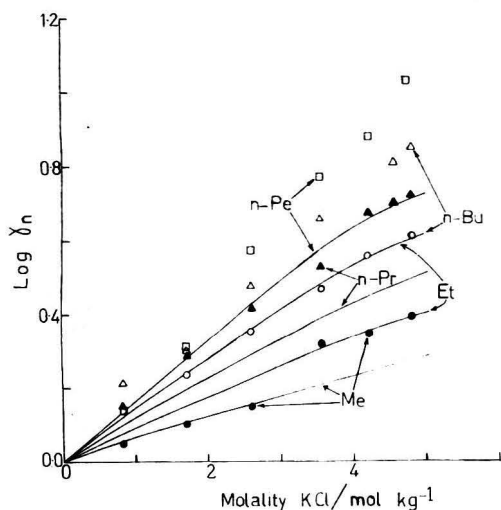
Figure 6. Calculated (lines) and experimental (points) values of log γ_n for methyl acetate (Me), ethyl acetate (Et), n-propyl acetate (n-Pr), n-butyl acetate (n-Bu), and n-pentyl acetate (n-Pe) in KCl solutions.
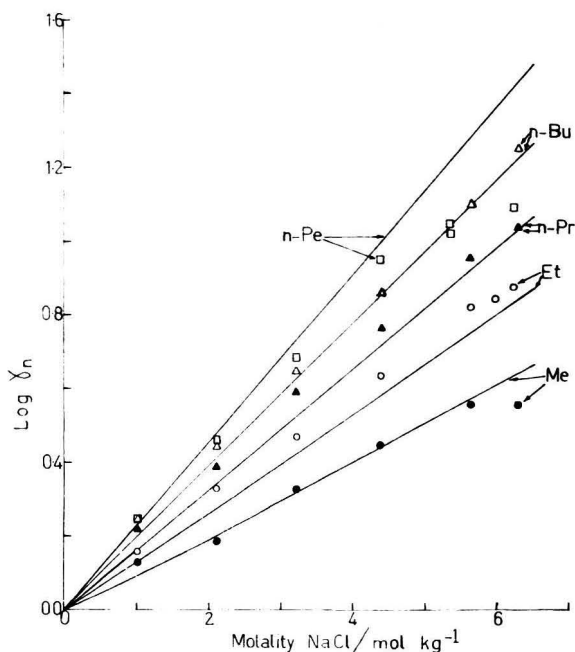
Figure 7. Calculated (lines) and experimental (points) values of log γ_n for methyl acetate (Me), ethyl acetate (Et), n-propyl acetate (n-Pr), n-butyl acetate (n-Bu), and n-pentyl acetate (n-Pe) in NaCl solutions.

ester occurs. While an increase in the ion dipole (and other lesser attractive forces) may offset the increased electrostatic repulsion between Li$^+$ and the smaller esters, as the Li$^+$ concentration increases, for the higher homologues, the larger electrostatic repulsion at any given molality of salt would give rise to heightened salting out.

The other surprising aspect of the results concerns the inverted orders of salting out for some of the higher esters over parts of the concentration ranges in NaCl (Figure 7)

and KF (Figure 9M[24])[49] solutions and the very small increase in γ_n between n-BuOAc and n-PeOAc in CsCl solutions. These may be dispersion force effects. If we assume that F$^-$ is the larger of the isoelectronic pair of ions F$^-$ and Na$^+$, and that F$^-$ therefore binds waters of hydration less strongly,[51] then relative to KCl the stronger salting out by F$^-$ than by Na$^+$ may be equated with greater electrostatic repulsion of the esters by F$^-$, due to less effective shielding of its charge. This less effective shielding of the F$^-$ ion would allow more ready access of the esters to the ion which, combined with the larger polarizability of F$^-$, would give rise to appreciably stronger attractive dispersion forces with the larger esters and may explain the more striking salt reversal observed in KF solutions than NaCl solutions.

It is interesting to note (Figure 10M[24]) that the activity coefficients of t-BuOAc[54] are very similar to those of n-BuOAc.

As with some other writers,[55] we have avoided resorting to the comfort of arguments based upon the structure of water, etc.; not because we feel that the presence of extended hydrogen bond networks in aqueous solutions may be denied, but rather that much specious material may have already been written on this account,[56] and further, that it is difficult to decide how relevant a Némethy and Scheraga picture of water[57] is in concentrated electrolyte solutions where 15 molecules of water is an average per pair of ions present. After solvation of the ions, and perhaps further coordination, there are few water molecules left.

References and Notes

(1) On study leave at the Department of Industrial Chemistry, Brunel University, Kingston Lane, Uxbridge, Middlesex UB8 3PH England (during 1976). Permanent address: Department of Chemistry, Swinburne College of Technology, John Street, Hawthorn, Victoria, Australia 3122.
(2) P. Debye and J. McAulay, *Phys. Z.*, **26**, 22 (1925).
(3) P. Debye, *Z. Phys. Chem.*, **130**, 56 (1927).
(4) J. O'M. Bockris, J. Bowler-Reed, and J. A. Kitchener, *Trans. Faraday Soc.*, **47**, 184 (1951).
(5) W. F. McDevit and F. A. Long, *J. Am. Chem. Soc.*, **74**, 1773 (1952).
(6) B. E. Conway, J. E. Desnoyers, and A. C. Smith, *Phil. Trans. R. Soc. London, Ser. A*, **256** (1074), 389 (1964).
(7) S. K. Shoor and K. E. Gubbins, *J. Phys. Chem.*, **73**, 498 (1969).
(8) E. W. Tiepel and K. E. Gubbins, *Ind. Eng. Chem., Fundam.*, **12**, 18 (1973).
(9) H. S. Frank, *Z. Phys. Chem. (Leipzig)*, **228**, 364 (1965).
(10) F. H. Stillinger, *J. Solution Chem.*, **2**, 141 (1973).
(11) R. A. Pierotti, *J. Phys. Chem.*, **69**, 281 (1965).
(12) A. Ben-Naim and H. L. Friedman, *J. Phys. Chem.*, **71**, 448 (1967).
(13) M. Lucas, *Bull. Soc. Chim. Fr.*, 2994 (1969).
(14) W. L. Masterton and T. P. Lee, *J. Phys. Chem.*, **74**, 1776 (1970).
(15) F. L. Wilcox and E. E. Schrier, *J. Phys. Chem.*, **75**, 3757 (1971).
(16) Y. L. Tien, M. Y. Schrier, and E. E. Schrier, *J. Phys. Chem.*, **78**, 165 (1974).
(17) R. F. Cross, *J. Phys. Chem.*, **79**, 1822 (1975).
(18) A. P. Altshuller and H. E. Everson, *J. Am. Chem. Soc.*, **75**, 4823 (1953).
(19) Solvation here is used in the sense of Bockris and Saluja in ref 20.

(20) J. O'M. Bockris and P. P. S. Saluja, *J. Phys. Chem.*, **76**, 2298 (1972).
(21) A. I. Vogel, "A Textbook of Practical Organic Chemistry", Longmans, Green and Co., London, 1948.
(22) "Handbook of Chemistry and Physics", 48th ed, The Chemical Rubber Co., Cleveland, Ohio, 1967–1968.
(23) I. M. Kolthoff and E. B. Sandell, "Textbook of Quantitative Inorganic Analysis", 3rd ed, MacMillan, New York, N.Y., 1952.
(24) See paragraph at end of text regarding supplementary material.
(25) J. C. Philip and A. Bramley, *J. Chem. Soc.*, **107**, 377 (1915).
(26) J. C. Philip and A. Bramley, *J. Chem. Soc.*, **107**, 1831 (1915).
(27) S. Glasstone and A. Pound, *J. Chem. Soc.*, **127**, 2660 (1925).
(28) S. Glasstone, D. A. Dimond, and E. C. Jones, *J. Chem. Soc.*, **129**, 2935 (1926).
(29) F. A. Long and W. F. McDevit, *Chem. Rev.*, **51**, 119 (1952).
(30) N. Schlessinger and W. Kubasowa, *Z. Phys. Chem. A*, **142**, 25 (1929).
(31) A. F. Scott, *J. Phys. Chem.*, **35**, 3379 (1931).
(32) B. Lunden, *Z. Phys. Chem. (Leipzig)*, **192**, 345 (1943).
(33) C. H. Spink, Ph.D. Thesis, Pennsylvania State University, University Park, Pa., 1962.
(34) R. E. Gibson, *J. Am. Chem. Soc.*, **57**, 284 (1935).
(35) D. S. Allam and W. H. Lee, *J. Chem. Soc. A*, 5 (1966).
(36) Yu. S. Manucharov, I. G. Mikhailov, and V. A. Shutilov, *Vestn. Leningr. Univ., Ser. Fiz. Khim.*, **19** (16), No. 3, 65 (1964).
(37) E. B. Freyer, *J. Am. Chem. Soc.*, **53**, 1313 (1931).
(38) W. Geffcken, *Z. Phys. Chem. A*, **155**, 1 (1931).
(39) F. Vaslow, *J. Phys. Chem.*, **70**, 2286 (1966).
(40) M. S. Stakhanova and V. A. Vasilev, *Russ. J. Phys. Chem.*, **37**, 839 (1963).
(41) "International Critical Tables of Numerical Data. Physics, Chemistry and Technology", 1st ed, McGraw-Hill, New York, N.Y., 1929.
(42) Yu. A. Epikhin and M. S. Stakhanova, *Russ. J. Phys. Chem.*, **41**, 1157 (1967).
(43) Yu. A. Epikhin, M. S. Stakhanova, and M. Kh. Karapet'yants, *Russ. J. Phys. Chem.*, **40**, 201 (1966).
(44) A. Passynski, *Acta Physicochim. URSS*, **8**, 385 (1938).
(45) J. C. Hindman, *J. Chem. Phys.*, **36**, 1000 (1962).
(46) M. A. Paul, *J. Am. Chem. Soc.*, **74**, 5724 (1952).
(47) N. C. Deno and C. H. Spink, *J. Phys. Chem.*, **67**, 1347 (1963).
(48) O. D. Bonner, *Rec. Chem. Prog.*, **32**, 1 (1971).
(49) n-PeOAc is sufficiently insoluble in aqueous solutions that the excess of standard base added to the aliquots of the aqueous phase for analysis was of about the same magnitude as the concentration of HF in the concentrated KF solutions.[50] Hence unequivocal determinations were not possible.
(50) "Stability Constants", *Chem. Soc., Spec. Publ.*, No. 17 (1964).
(51) (a) There is some doubt as to whether the F⁻ ion is larger than the Na⁺ ion.[52] (b) The relative strengths of cationic and anionic binding of water is also unresolved although some authors[45,53] feel that cationic bonding is stronger.
(52) J. E. Desnoyers and C. Jolicoeur in "Modern Aspects of Electrochemistry", Vol. 5, J. O'M. Bockris and B. E. Conway, Ed., Plenum Press, New York, N.Y., 1969.
(53) G. Engel and H. G. Hertz, *Ber. Bunsenges. Phys. Chem.*, **72**, 808 (1968).
(54) P. T. McTigue and A. R. Watkins, *Aust. J. Chem.*, **18**, 1943 (1965).
(55) J. E. Prue, A. J. Reed, and G. Romeo, *Trans. Faraday Soc.*, **67**, 420 (1971).
(56) A. Holtzer and M. F. Everson, *J. Phys. Chem.*, **73**, 26 (1969).
(57) G. Nemethy and H. A. Scheraga, *J. Chem. Phys.*, **36**, 3382 (1962).

Refractometric Determination of Stability Constants

Lajos Barcza

Institute of Inorganic and Analytical Chemistry, L. Eotvos University, 1443 Budapest, Hungary (Received September 22, 1975)

The theoretical and practical possibilities of refractometry have been discussed in view of the determination of equilibrium constants. The method developed is very quick and simple (if some requirements are fulfilled) and applicable to the determination of a (rather low) stability constants range which cannot be investigated easily by any other methods. The method has been demonstrated on an extensively studied system (on the formation of $HgCl_3^-$ and $HgCl_4^{2-}$ species) and the measured and computed results are practically the same as the results determined by other methods.

Introduction

It is well known that the phenomenon of refraction is connected after all to the polarizability of electron clouds. As the latter is changed by the formation of complex compounds,[1] it can be supposed that refractometry is a very good tool for investigating complex equilibria.

In the literature, several papers can be found (partly summarized in ref 1–4) using refractometry for the investigation of formation stoichiometries, but only two deal with the problem of the determination of stability constants.[5,6] The method used for finding stoichiometric ratios has been, first of all, the method of continuous variation, which can often give inconsistent results.[7] Its quantitative solution had been used by Japanese authors[5] and by Giles and his co-workers, together with the solute excess method[6] known and criticized in spectrophotometry a long time.

The main point of the criticisms against the application of refractometry in physical–chemical research is that no general relation is known for the connection between the refractive index (or its square or molar refraction, etc.) and the concentration.[2,8] However, this fact only strengthens the first assumption; it means that refraction is influenced also by weak, secondary, and long distance interactions and these can be investigated by refractometry, too, only the experimental and computing techniques must be chosen and controlled very carefully.

Chemical Background

In analytical chemistry, the empirical relationship for some relatively diluted solutions are used and proved[3,9] very often:

$$n = n_0 + kc \tag{1}$$

where n is the refractive index measured; n_0 is that of the solvent; k is an empirical factor; c is the concentration of the solute expressed in volume or weight percent, or even in molarity. The k refractive factors or increments are fairly constant up to 0.5 M and often higher (1–2 M) concentrations in most aqueous and nonaqueous solutions having either electrolytes or nonelectrolytes as solutes.

However, there are some inconsistencies, because it can be pointed out[3] (even theoretically) that the refractive indices are additive, first of all, when the concentrations are expressed in molar volumes or at least in concentration units related to the volume. In eq 1, the concentration of the solute as molarity is given in such a scale, but the concentration of the solvent seems to be constant. In concentration range mentioned, it cannot be true, that is, the constant k must be an apparent constant.

When the concentration of the solvent is expressed also in molarity, eq 1 can be rewritten as

$$n = n_0^* c_0 + n_1^* c_1 \qquad (2)$$

where c_1 is the concentration of the solute; c_0 is that of the solvent, both expressed in molarity; and n_i^* can be considered (as the molar absorbance coefficient) as the molar refractive coefficient.

There is no difficulty in finding the connection between eq 1 and 2, only some requirements must be postulated. (i) The kind of interactions between the molecules of the solvent and solute must not be changed in the concentration range investigated; that is, a solvation factor f_1^s must be constant. (ii) The structure of the solvent is not influenced. (iii) There is no change in the degree of the dissociation or association of the solute. (iv) The density of the solution ought to be varied nearly linearly by the concentration as

$$d = d_0 + f_1^d c_1 \qquad (3)$$

where d and d_0 are the densities of the solution and the pure solvent; f_1^d is a constant. (Equation 3 is equivalent to eq 1 not only formally but theoretically, too. It means that its validity depends also on requirements (i)–(iii).) It is essential, that eq 3 must be valid within ±0.1% for the concentration range under investigation, which is fairly true for most solutions up to 0.5 M (even to 1–2 M) concentrations.

These requirements can be substituted into eq 2 and it can be rewritten as

$$n = \frac{n_0^* 1000 d_0}{M_0} +$$
$$c_1 \left(n_1^* + \frac{n_0^*}{M_0}(1000 f_1^d - M_1) - n_0^* f_1^s \right) \qquad (4)$$

where M_i is the molecular weight.

It can be easily seen that the first part of the right-hand side is really equal to the refractive index of the pure solvent; and the multiplier of c_1 defines exactly the meaning and the validity range of the so-called refractive increment k, or better, that of the apparent molar refractive coefficient (n_i^M, see eq 7). Its value can be measured for different simple substances easily:

$$n_1^M = (n - n_0)/c_1 \qquad (5)$$

The refractive index of a multicomponent solution can be characterized by a set of such equations, in the general form, as

$$n = n_0 + \Sigma n_i^M c_i \qquad (6)$$

where the definition of the apparent molar refractive coefficients is

$$n_i^M = n_i^* - n_0^* f_i^s + \frac{n_0^*}{M_0}(1000 f_i^d - M_i) \qquad (7)$$

The equilibria can be followed and the equilibrium con-

stants can be computed using eq 6. First of all, the apparent molar refractive coefficients have to be determined (and controlled) for every reactants separately. When they react, the refractive indices measured in their mixtures cannot be described by the type of eq 6 composed simply as a set of eq 5 measured separately. The differences between the measured and calculated values are directly caused by new species having new and different apparent molar refractive coefficient(s). Using the principle of electroneutrality (as is usual in coordination chemistry) and a computer, the real eq 6 can be solved for the stability constant(s) by a rather simple iteration procedure. (The computing is really so simple, that no details are necessary and can be managed in most of cases even by desk computer. Some practical problems will be discussed later.)

Although there are similarities between the molar absorbance and refractive coefficients, a typical difference is that all of the components are refractometrically active. The interactions can be detected by refractometry when the apparent molar refractive coefficients of reactants and products differ on a measurable scale. Sometimes these differences are large enough for the detecting of rather weak complexes (such as the formation of a complex between propionic aldehyde and dimethylformamide[10]), but there is the possibility that the apparent molar refractive coefficient of the product is nearly the sum of those of the reactants. In these cases no interactions can be detected, although rather stable complexes have been found in the system by other methods.[11] This phenomenon seems to connect with substances forming strong hydrogen bridges with the solvent when the further interaction is of the same type.

It follows that the lack of measurable change in refractive indices is no proof against the formation of complex compounds.[4]

Another difference between the molar absorbance and refractive coefficients is that the latter is valid only for a rather narrow concentration range since it can be determined in relatively concentrated solutions. However, the possibilities can be extended (first of all for aqueous solutions) using a rather high constant ionic strength. The structure of the solvent, the conditions of the solvation, and roughly the density, too, would be practically influenced and kept constant by the inert electrolyte; eq 5 would be valid in more concentrated solutions of different species and thermodynamic constants could be directly calculated from the measured data.

An Experimental Example

Although both of the quantitative methods mentioned[5,6] dealt with the investigation of hydrogen bridged complexes, the ability of the present method is not demonstrated on a similar system (in spite of fact that it is very favorable for such ones, too), but on a more complicated still better known system. The equilibria between mercury(II) chloride and chloride ions

$$HgCl_2 + Cl^- = HgCl_3^- \qquad (8)$$
$$K_3 = [HgCl_3^-]/[HgCl_2][Cl^-]$$

and

$$HgCl_2 + 2Cl^- = HgCl_4^{2-} \qquad (9)$$
$$K_3 K_4 = [HgCl_4^{2-}]/[HgCl_2][Cl^-]^2$$
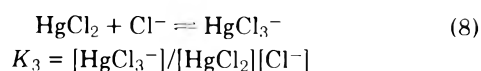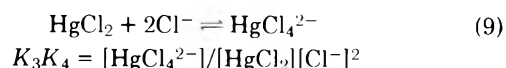
had been investigated by several methods and several au-
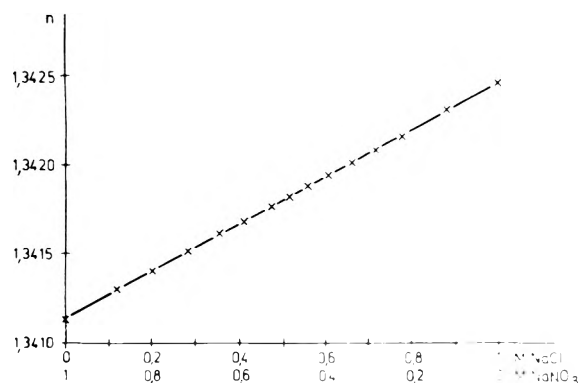
Figure 1. Refractive indices of solutions containing 1.000 M Na^+, a M Cl^-, and $1.000 - a$ M NO_3^- (solid line, calculated values using the computed apparent molar refractive coefficients).
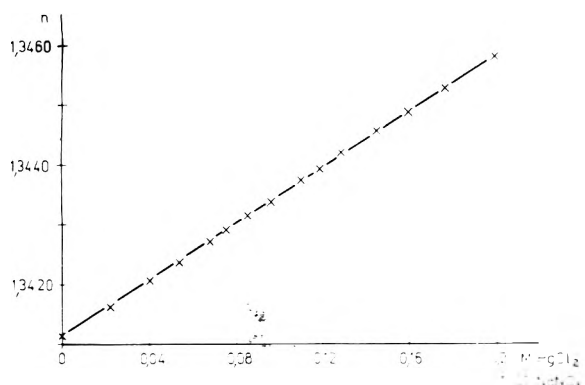
Figure 2. Refractive indices of $HgCl_2$ solutions in 1.000 M $NaNO_3$ (solid line, calculated values using the computed apparent molar refractive coefficients).

Figure 3. Refractive indices of $HgCl_2$ solutions in 1.000 M NaCl (broken line, tangent of first points for calculating of approximate $n^M_{HgCl_4^{2-}}$ value; solid line, calculated one using the computed n^M and K values).

Figure 4. Refractive indices of 0.2000 M $HgCl_2$ solutions containing 1.000 M Na^+, a M Cl^-, and $1.000 - a$ M NO_3^- (solid line, calculated values using the computed constants).

thors;[12] the values of the equilibrium constants measured (in 0.5–3 M $Na(ClO_4)$, at 25 °C) are very consistent to each other (log K_3 = 0.75–0.95; log K_3K_4 = 1.85–2.13). These equilibria have been reinvestigated by the present method in 1 M $Na(NO_3)$ and at 25 °C.

All of the reagents were of highest purity and the following stock solutions were prepared at 25.00 °C: 1.000 M $NaNO_3$, 1.000 M NaCl, 0.2000 M $HgCl_2$ in 1.000 M $NaNO_3$, 0.2000 M $HgCl_2$ in 1.000 M NaCl.

During the investigations, one of the solutions was pipetted into an exactly thermostated vessel (the temperature variation did not exceed the limit of ±0.05 °C) and its refractive index was measured several times with a Zeiss type dipping refractometer. Then a small volume of the second solution (also measured accurately and exactly thermostated at 25.00 °C) was mixed with the solution in the vessel and the refractive index was measured again after some minutes. This procedure was repeated several times, as the whole procedure and its inverse.

In the first series, sodium nitrate was mixed with sodium chloride. It means that the sodium concentration was kept constant (1.000 M), while the nitrate was decreased from 1.000 M and the chloride was increased to 1.000 M concentration. As can be seen in Figure 1, the n vs. c relation is linear; both $n^M_{NaNO_3}$ and n^M_{NaCl} can be directly calculated using eq 6.

In the second step, a series of $HgCl_2$ solutions in 1.000 M $NaNO_3$ was produced and measured in a similar way (Figure 2). Mercury(II) chloride does not dissociate or hydro-

lyze to a degree[12] measurable by refractometry, so its apparent molar refractive coefficient can be calculated, too.

In spite of that, there are no linear relations when NaCl and $HgCl_2$–NaCl (chloride concentration constant, Figure 3) or $HgCl_2$–$NaNO_3$ and $HgCl_2$–NaCl (mercuric chloride concentration constant, Figure 4) solutions are mixed. These results can be explained if the new species formed have different n^M values and parallel with their formation the concentrations of mercury(II) and chloride ions (see eq 8–9) decreased. An approximate $n^M_{HgCl_4^{2-}}$ value can be calculated from the slope of the first part of the curve on Figure 3 and a less accurate $n^M_{HgCl_3^-}$ value can be supposed as a mean value of $n^M_{HgCl_4^{2-}}$ and $n^M_{HgCl_2}$. These data are the initial ones in the iterative computer calculation and will be refined in the successive steps together with the stability constants seeking the best fit.

For the iterations, eq 5, 6, 8, and 9 and the equations of mass balance

$$[HgCl_2]_T = [HgCl_2] + [HgCl_3^-] + [HgCl_4^{2-}] \qquad (10)$$

$$[Cl^-]_T = [Cl^-] + [HgCl_3^-] + 2[HgCl_4^{2-}] \qquad (11)$$

were used. The guessed pairs of K_3 and K_4 values were 10–10, 5–20, and 20–5 (and without any results 10–0 and 0–100). The best fit was always found in a few cycles with the values K_3 = 7.83 ± 0.09 or log K_3 = 0.894 and K_3K_4 = 106.5 ± 0.6 or log K_3K_4 = 2.025.

Discussion

The figures and the final results show that the recent refractometric method gives identical results with other methods. (Further examples for its application will be published later.)

The conditions of the method are also demonstrated. (i) The type of species formed in system under investigation must be known or at least precisely guessed and then proved by calculations similar to other methods. e.g., to potentiometry. (ii) The linearity of eq 5 must be proved separately for all of the reactants. (iii) To increase accuracy, a number of different concentrations must be made and measured at constant temperature.

However, the method developed is very advantageous, because (i) it is very simple and quick; (ii) less stable complexes of different type can be investigated for which we do not have too many or simple methods; (iii) even the stabili-

ty constants of hydrogen bridged complexes can be measured in aqueous solutions, also.

References and Notes

(1) S. S. Batsanov. "Refractometry," Consultants Bureau, New York, N.Y., 1961.
(2) B. W. Joffe, *Jen. Rev.*, **17**, 170 (1972).
(3) B. V. Ioffe, "Refr. met. khim." (Izd. Khim.), Leningrad, 1974.
(4) G. C. Pimentel and A. L. McClellan, "The Hydrogen Bond," W. H. Freeman, San Francisco, Calif., 1960. p 55.
(5) Z. Yoshida and E. Osawa, *Bull. Chem. Soc. Jpn.*, **38**, 140 (1965).
(6) C. H. Giles, J. Gallangher, A. McIntosh, and S. N. Nakhwa. *J. Soc. Dyers Colour* **88**, 360 (1972).
(7) M. M. Jones and K. K. Innes. *J. Phys. Chem.*, **62**, 1005 (1958).
(8) B. V. Ioffe, *Usp. Khim.*, **29**, 137 (1960).
(9) S. Z. Lewin and N. Bauer, "Treatise on Analytical Chemistry," Part I, Vol. 6, I. M. Kolthoff and Ph. J. Elving, Ed., Interscience, New York, N.Y., 1965. p 3895.
(10) F. M. Arshid, C. H., Giles, and S. K. Jain, *J. Chem. Soc.*, 559 (1956).
(11) H. Fritzsche, *Z. Chem.*, **6**, 39 (1966).
(12) L. G. Sillén and A. E. Martell, Ed., "Stability Constants," The Chemical Society, London, 1964 and 1971.

Melting Point of Crystallites in Dilute Solutions of Polymers. Poly(vinyl Chloride) in Tetrahydrofuran

Jørgen Lyngaae-Jørgensen

Instituttet for Kemiindustri, The Technical University of Denmark, Bygning 227, Lyngby, Denmark   (Received July 31, 1975)

A model is derived which permits the prediction of the melting point of crystallites in dilute polymer solutions based on the melting point of crystallites in the pure polymer, the molecular weight, and the interaction parameter. The model prediction is in accordance with experimental data for poly(vinyl chloride) in tetrahydrofuran. Furthermore, an expression for the chemical potential of repetition units in the range between the theory for extremely dilute solutions and the Flory–Huggins theory for solutions with uniform segment distribution has been shown to be a reasonable approximation.

Introduction

The fact that poly(vinyl chloride), PVC, molecules form aggregates in dilute solutions was realized by Doty[1] in 1947. Since then extensive investigations of the phenomenon have shown that aggregates can be formed in all known solvents[2] but in greater amounts in poor solvents.[2,3] Hengstenberg[1] concluded that the aggregates were held together by crystallites.

In accordance with Hengstenberg's work, it is found that the amount of aggregates is a function of the degree of crystallinity, temperature, solvent power, and solvent concentration.[5-15] The rate of recrystallization in dilute solutions depends on the tacticity of the sample,[7] but is normally a very slow process at high dilution and low degree of tacticity.[7,10,11] The aggregates found in dilute solutions of tetrahydrofuran (THF) are built of a number of single molecules bound together by a crystalline nucleus.[16]

The characterization of PVC molecules by light scattering etc. presupposes a solution consisting of single molecules. The purpose of this work was therefore to develop and experimentally verify a model for the prediction of the

melting point of crystallites in dilute solutions as a function of the melting point of the crystallites in pure PVC, the solvent concentration, and the solvent power. The model was tested with tetrahydrofuran since it is a solvent often used in characterization work.

Theoretical

An expression is sought for solutions of PVC molecules in the concentration range where light-scattering, gel permeation chromatography, etc. is performed.

The model is derived as follows. At the melting temperature equilibrium between repetition units in crystallites and repetition units in solution exists; stated otherwise this means that $\mu_u{}^c = \mu_u$ where $\mu_u{}^c$ and μ_u are the chemical potential of a repetition unit in the last crystallite and a repetition unit in solution, respectively. $\mu_u{}^c$ and μ_u are expressed as functions of temperature, molecular weight, the melting temperature of crystallites in pure polymer, the interaction parameter, and volume fraction of polymer. From the condition $\mu_u{}^c = \mu_u$ one can then isolate the melting temperature as a function of other variables.

The derivation of an expression for μ_u is performed by

adopting the theory for (a) extremely dilute solutions and (b) the Flory–Huggins theory for solutions with uniform segment distribution to the intermediate polymer concentration.

The chemical potential of a repetition unit in the reference state for a and b are $\mu_u{}^*$ and $\mu_u{}^0$, respectively.

It should be emphasized that[13] $\mu_u{}^*$ is the standard state for a hypothetical form of polymer which obeys the expression for $\mu_u{}^F$ in extreme dilute solutions and continues to obey it at all values of polymer concentration. $\mu_u{}^0$ is the standard state for pure liquid polymer.

If the chemical potential per repetition unit at extreme dilution is called $\mu_u{}^F$ and the chemical potential corresponding to polymer volume fraction v_2 is μ_u the following identity can be written:

$$\mu_u{}^F - \mu_u{}^* + \mu_u{}^* - \mu_u{}^0 = \mu_u{}^F - \mu_u + \mu_u - \mu_u{}^0 \quad (1)$$

(going to extreme dilution in a solution at Θ conditions → interaction parameter $\chi = 0.5$ and degree of polymerization $X \to \infty$) we have

$$\mu_u{}^F - \mu_u{}^* = 0$$

and[17]

$$\mu_u{}^* - \mu_u{}^0 = (\mu_u{}^F - \mu_u{}^0)_\theta = -\frac{RTV_u}{V_1}(1 - \chi) \quad (2)$$

where V_u is the molar volume of a repeating unit, V_1 is the molar volume of a solvent molecule, T is absolute temperature, and R is the gas constant.

$\mu_u - \mu_u{}^0$ is found from

$$\mu_u - \mu_u{}^0 = \mu_u{}^F - \mu^* + \mu_u{}^* - \mu_u{}^0 - (\mu_u{}^F - \mu_u) \quad (3)$$

$\mu_u{}^F - \mu_u{}^*$ is found as follows.[18] As a consequence of the standard state definition at extreme dilution we have[18]

$$\Delta F_{mix} = -T \Delta S_{mix}$$

Under conditions so dilute that the solute molecules are far apart and essentially independent of one another ΔS_{mix} can be written[18]

$$\Delta S_{mix} = R \left(n_2 \ln \frac{n_1 V_1{}^0 + n_2 \bar{V}_2{}^0}{n_2 \bar{V}_2{}^0} - \frac{n_2{}^2 Nu}{2(n_1 V_1{}^0 + n_2 \bar{V}_2{}^0)} + \frac{n_2 Nu}{2 \bar{V}_2{}^0} \right) \quad (4)$$

where n_1 is the number of moles of solvent, n_2 the number of moles of solute, N is Avogadros number, $V_1{}^0$ is the molar volume of solvent, $\bar{V}_2{}^0$ is the partial molar volume of solute at infinite dilution, and u is the excluded volume at infinite dilution.

$$\mu_u{}^F - \mu_u{}^* = \frac{(\mu_2{}^F - \mu_2{}^*)V_u}{V_1 x} = \left(\frac{\delta \Delta F_{mix}}{\delta n_2} \right)_{T,P,n_1} \times$$

$$\frac{V_u}{V_1 x} = \frac{RTV_u}{V_1 x} \left\{ \frac{Nu}{2\bar{V}_2{}^0} - 1 \right\} \simeq \frac{RTV_u}{V_1 x} \frac{Nu}{2\bar{V}_2{}^0} \quad (5)$$

in good solvents.

A simple explicit expression for $\mu_u{}^F - \mu_u$ cannot be found. (A monstrous series solution is found.) However, a good working approximation is found as follows.

Flory[17] found the free energy change, ΔF_a, accompanying the process of bringing two molecules originally completely separated to a distance of separation between their centers of gravity equal to a, could be given by

$$\Delta F_a = kT2(\alpha^2 - 1) \exp\left[-\left(\frac{a\sqrt{3}}{2S} \right)^2 \right] \quad (6)$$

where S is the radius of gyration, the expansion factor $\alpha = S/S_0$ (S_θ the radius of gyration at Θ conditions), k is the Boltzmann constant, and T the absolute temperature.

To simplify the calculations two approximations are used. First when a situation with uniform segment distribution exists then the probability (p) of finding the center of gravity of a neighboring polymer molecule in a distance a from the center of gravity of a reference molecule is proportional to $4\pi a^2\,da\,(n_2'/V)$ where n_2' is the total number of polymer molecules and V is the total volume. As one goes from this situation to extremely dilute solutions, the above expression for p will become a poorer approximation. As a first approximation, however, p is given as $4\pi a^2\,da\,(n_2'/V)$.

Secondly when going from a situation with uniform segment distribution to more dilute solutions a situation arises where the center of gravity of the polymer molecules in the solution will be located more or less on a face-centered cubic lattice (NaCl lattice). This will be the stable state for a dilute solution at given conditions of temperature, pressure, and polymer concentration, i.e., the state where the function ΔF_a is at a minimum. The stable state corresponds to the equidistance pattern which is characteristic for the face-centered cubic lattice as a consequence of the exponential form of eq 6.

The characteristic situation for an arbitrary polymer molecule is thus that it is surrounded by six equivalent neighboring polymer molecules.

The change in free energy brought about by bringing segments belonging to two different polymer molecules i and j located in the volume element δV from an infinite distance to a distance a is given by[17]

$$\delta(\Delta F_a) = 2kT(1/2 - \chi)v_i'v_j' \frac{\delta V}{V_1} \quad (7)$$

where V_1 represents the volume of a solvent molecule and v_i' and v_j' are the volume fractions of polymer in the volume element. The change in energy brought about by bringing one polymer molecule from an infinite distance to a situation with mutual interaction with six neighboring polymer molecules a distance a away and located in a face-centered cubic lattice is

$$\delta(\Delta F_a) = 2kT(1/2 - \chi)v_i' \sum_1^6 v_j' \frac{\delta V}{V_1} =$$

$$6kT2(1/2 - \chi)v_i'v_j' \frac{\delta V}{V_1} \quad (8)$$

Only the nearest neighboring polymer molecules will contribute appreciably to the free energy change. The change in free energy by bringing seven interacting nearest neighbor polymer molecules from infinite distance to a distance a in a face-centered cubic lattice occupied by centers of gravity of polymer molecules will be

$$\delta(\Delta F_a) = 42kT2(1/2 - \chi)v_i'v_j' \frac{\delta V}{V_1} \quad (9)$$

giving

$$\Delta F_a = 42kT2(\alpha^2 - 1) \exp\left(-\left(\frac{a\sqrt{3}}{2S} \right)^2 \right) \quad (10)$$

A unit cell contains two centers of gravity and only nearest neighboring molecules contribute to the free energy change.

The total change in free energy by bringing n_2' molecules originally completely separated to an average distance

characterized by concentration of centers of gravity equal to n_2/V (V = total volume) can therefore be written

$$\Delta F \simeq 42 n_2' \int_0^\infty kT2(\alpha^2 - 1) \exp\left(-\left(\frac{a\sqrt{3}}{2S}\right)^2\right) \times$$

$$4\bar{\pi}a^2 \frac{n_2'}{V}\, da \quad (11)$$

since the concentration of centers of gravity in a volume element a distance a from each center of gravity is $4\pi a^2\, da$ (n_2'/V).

$$\Delta F = 42kT2(\alpha^2 - 1)\left(\frac{4\pi}{3}\right)^{3/2} S^3 \frac{n_2'^2}{V} \quad (12)$$

The chemical potential per mole of solute is obtained by differentiation with respect to n_2: $(n_2' = Nn_2)$

$$-(\mu_2{}^F - \mu_2) = \left(\frac{\delta \Delta F}{\delta n_2}\right)_{T,P,v_1} =$$

$$4(42RT)(\alpha^2 - 1)\left(\frac{4\pi}{3}\right)^{3/2} S^3 \frac{Nn_2}{V} \quad (13)$$

The chemical potential per repeating unit is

$$-(\mu_u{}^F - \mu_u) = \frac{V_u}{V_1 x} 4(42RT)(\alpha^2 - 1)\left(\frac{4\pi}{3}\right)^{3/2} S^3 N \frac{n_2}{V} \quad (14)$$

Insertion of (2), (5), and (12) into (3) gives

$$\mu_u - \mu_u{}^0 = \frac{RTV_u}{V_1 x} \frac{u}{2\bar{V}_2{}^0} - \frac{RTV_u}{V_1}(1 - \chi) +$$

$$\frac{RTV_u}{V_1 x} 4(42)(\alpha^2 - 1)\left(\frac{4\pi}{3}\right)^{3/2} S^3 N \frac{n_2}{V} \quad (15)$$

The excluded volume u may be written[18]

$$u = 2\left(\frac{4\pi}{3}\right)^{3/2}(\alpha^2 - 1)S^3 NJ(2(\alpha^2 - 1)) \quad (16)$$

where J is a function of $2(\alpha^2 - 1)$ stipulated by Flory.[17]

Equation 15 can be written

$$\mu_u - \mu_u{}^0 = \frac{RTV_u}{V_1 x} \frac{N\left(\frac{4\pi}{3}\right)^{3/2}(\alpha^2 - 1)S^3 J}{x V_u} - \frac{RTV_u}{V_1}(1 - \chi) +$$

$$\frac{RTV_u}{V_1 x} \frac{N\left(\frac{4\pi}{3}\right)^{3/2}(\alpha^2 - 1)S^3}{x V_u} 4(42)v_2 \quad (17)$$

where $\bar{V}_2{}^0 \simeq xV_u$ and $n_2 V_u x/V = v_2$.

The condition of equilibrium between crystalline polymer units and polymer units in solution is

$$\mu_u{}^c - \mu_u{}^0 = \mu_u - \mu_u{}^0 \quad (18)$$

where $\mu_u{}^c$ is the chemical potential of a crystalline repetition unit.

Following Flory[17] we have

$$\mu_u{}^c - \mu_u{}^0 \simeq -\Delta H_u\left(1 - \frac{T}{T_m{}^0}\right) \quad (19)$$

Substituting (17) and (19) into (18) gives

$$\frac{1}{T} - \frac{1}{T_m{}^0} = \frac{RV_u}{\Delta H_u V_1}\left[-\frac{N\left(\frac{4\pi}{3}\right)^{3/2}(\alpha^2 - 1)S^3 J}{x^2 V_u} + (1 - \chi)\right] -$$

$$4(42)\frac{RV_u}{\Delta H_u V_1}\frac{N\left(\frac{4\pi}{3}\right)^{3/2}(\alpha^2 - 1)S^3}{x^2 V_u} v_2$$
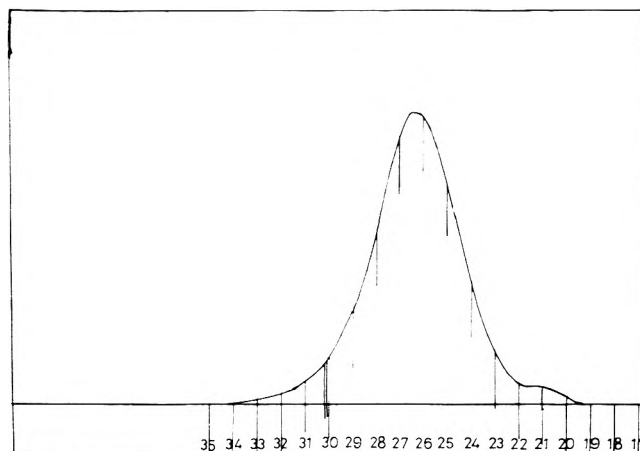
Figure 1. GPC curve for Corvic D 65/8. Elution volume is given in counts (1 count = 5 ml) as the abscissa and the ordinate is proportional to polymer concentration.

or since the first term in brackets is orders of magnitude less than the second term

$$\frac{1}{T} - \frac{1}{T_m{}^0} = \frac{RV_u}{\Delta H_u V_1}(1 - \chi) -$$

$$168\frac{RV_u}{\Delta H_u V_1}\frac{N\left(\frac{4\pi}{3}\right)^{3/2}(\alpha^2 - 1)S^3}{x^2 V_u} v_2 \quad (20)$$

or

$$\frac{1}{T} = A + \frac{1}{T_m{}^0} - Bv_2$$

or again

$$\frac{1}{T} = A^1 - Bv_2$$

where A and B are functions of the molecular weight and interaction parameter. If the interaction parameter (and therefore α) is independent of temperature and concentration we have that A and B are functions only of molecular weight.

Since all of the variables in eq 20 can be measured by independent methods and can be found in the literature the melting behavior of crystallites (at high dilution) can be predicted from eq 20.

Experimental Section

Gel permeation chromatography (GPC) was chosen as an appropriate method for testing the validity of eq 20.

The GPC curve gives corresponding values of concentration and dimensions in dilute solution. Since aggregates have larger dimensions than single molecules they normally gives rise to a separate distribution on the GPC curve. The fact that the high molecular weight peak is caused by crystallites has been inferred from the fact that heating a sample solution removes the crystallite peak.[12,19] Furthermore, a direct correlation between the degree of tacticity of a polymer sample and the area below the aggregate peak has been found.[8] The weight fraction of crystallite aggregates can therefore be estimated as the ratio of the area of the aggregate top on the GPC curve to the total area under the curve and the base line as shown in Figure 1.

The GPC apparatus was a Waters Associates Model 200: column combination 10^6, 2×10^4, 10^4, 10^3 Å polystyrene
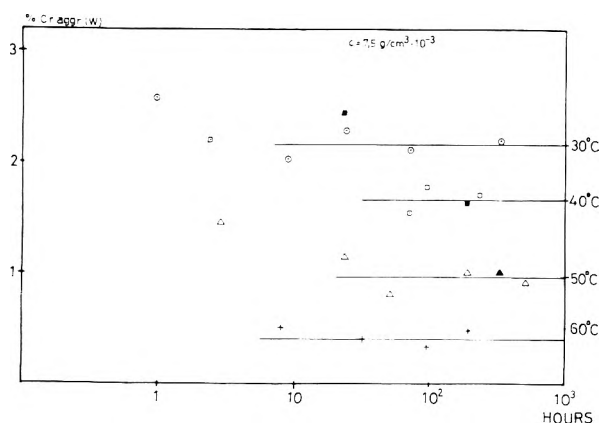
Figure 2. Data (unfilled symbols) measured on a solution prepared at room temperature and placed in a thermostat at subsequently higher temperatures in the time lapse given as abscissa; (filled symbols) solutions prepared at the given temperature: (⊙) 30 °C, (▣) 40 °C, (△) 50 °C, and (+) 60 °C.

Figure 4. A plot of w against temperature (T) with polymer volume fraction as discrete variable for Corvic D 65/8: (⊙) 5.36×10^{-3} g/cm^3; (□) 17.86×10^{-3} g/cm^3.

Figure 3. Delineation of percent crystallite aggregates (w) against the logarithm of the polymer volume fraction: (△) 20 °C; (●) 25 °C; (□) 30 °C; (⊙) 40 °C; (○) 50 °C; and (+) 60 °C.
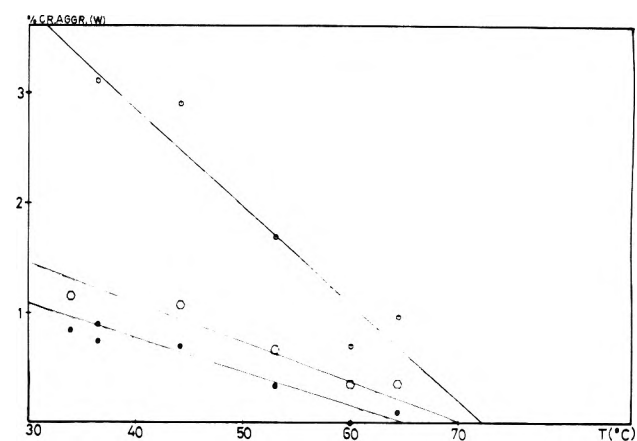
Figure 5. A plot of w against T for (●) Vinnol H60d, (○) Vinnol H70d, and (⊙) Vinnol H80f (10×10^{-3} g/cm^3).

gel; flow rate 1 ml/min, injection volume 2 ml; solvent tetrahydrofuran (THF). Details of calibration etc. are given in ref 16.

Sample Materials. Corvic D 65/8 from ICI was used. $\bar{M}_w$ = 110 000, $\bar{M}_n$ = 5000. Furthermore, Vinnol H 60d ($\bar{M}_w$ = 70 000, $\bar{M}_n$ = 32 000), Vinnol H 70d ($\bar{M}_w$ = 110 000, $\bar{M}_n$ = 52 000), and Vinnol H 80f ($\bar{M}_w$ = 166 000, $\bar{M}_n$ = 80 000) from Wacker have been investigated. Vinnol H 70d and Corvic D 65/8 are assumed to have the same melting point.

Results

The melting point is defined as the temperature where the last trace of crystallinity disappears. The melting point is found by extrapolation of corresponding values of temperature and/or of polymer concentration and content of crystallite aggregates to zero crystallite contents.[20]

The equilibrium crystallite content (w) was determined from a delineation of crystallite content vs. time (for example, see Figure 2). The time to reach equilibrium crystallite content depends on the method of preparation. It does take a longer time to reach an equilibrium if a concentrated solution is diluted than if pure polymer and solvent is mixed to the same final polymer concentration, but approximately the same equilibrium content is nevertheless found.

For sufficiently small concentrations a delineation of the

amount of crystallite aggregates (w) against log c gave a straight line at isothermal conditions.

The melting points for a given polymer concentration were found by extrapolation of the weight fraction of aggregates (w) against log c to w = 0, as seen in Figure 3.

The melting points can also be found by extrapolation in a plot of w against solution temperature as shown in Figures 4 and 5.

Discussion

Equation 20 does not contain any dependency on crystallite size. Equation 20 is a theoretical equation and from a theoretical point of view the melting point of a copolymer is sharply defined.[20] However, the experimentally observed, or apparent, melting point may be appreciably below T_m, because of insensity of the method employed for detecting traces of crystallinity. The GPC technique used in this work can detect fractions of weight percentages of crystalline material present in very dilute solutions. This extreme sensitivity is a consequence of the fact that the aggregates are built of several single molecules bound together by a crystalline nucleus.[16] Since the GPC method is very sensitive and since the melting temperature is found by extrapolation to zero crystallite content, the melting points referred to in this paper should correspond to the ideal melting temperature.
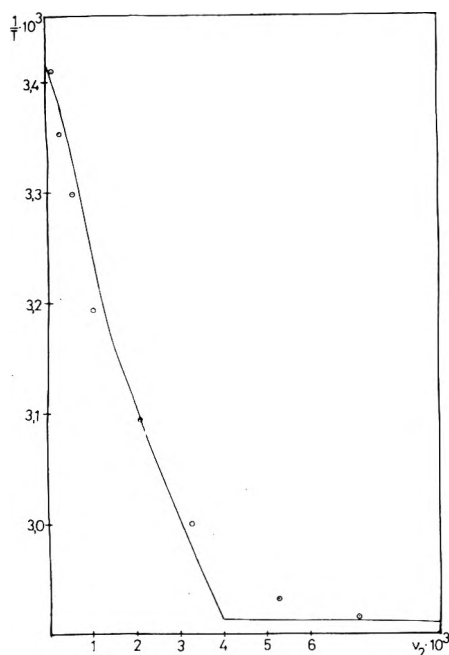
Figure 6. A delineation of reciprocal temperature (K^{-1}) against polymer volume fraction. The solid line is the theoretical curve.

To test the validity of eq 20 the following values measured by independent methods were used: ΔH_u = 785 cal/mol;[21] V_u = 44.65 cm^3; R = 1.9869 cal/(°C mol); V_1^{THF} = 81.2 cm^3; N = 6.0228 × 10^{23} mol^{-1}; S = 1.831 × 10$^{-9}M^{0.59}$ (ref 22); α = $S/S\theta$ = (1.831 × 10$^{-9}M^{0.59}$)/(2.885 × 10$^{-9}M^{0.5}$) = 0.6347$M^{0.09}$; {S_θ from Kurata and Stockmeyer[23]}; χ = −0.424 + 2.16 × 10^{-3}T;[24] M_0 = 62.5 g/mol; π = 3.14159; $\bar{M}_n$ = 54 000; T_m = 238 °C measured by the method given in ref 25.

According to Flory[17] the expansion factor α can approximately be expressed as a function of the interaction parameter by

$$\alpha_T = \left[\frac{\chi_T - 0.5}{\chi_{T_{ref}} - 0.5} \right]^{1/5} \alpha_{T_{ref}} \quad \text{(for } \alpha > 1\text{)} \quad (21)$$

were $\chi_{T_{ref}}$ and $\alpha_{T_{ref}}$ are the interaction parameter and the expansion factor at 20 °C, respectively.

This expression has been used to find α at temperatures other than 20 °C.

With these values corresponding values of $1/T$ and v_2 can be found from eq 20. A delineation of $1/T$ against v_2 is

shown in Figure 6 together with a delineation of the Flory expression[17]

$$\frac{1}{T} - \frac{1}{T_m} = \frac{RV_1}{\Delta H_u V_u} (v_1 - \chi v_1^2) \quad (22)$$

for uniform segment distribution.

As seen from Figure 6 eq 20 predicts the experimental results remarkable well.

Since the theoretical curve in Figure 6 is almost independent of the molecular weight used ($\bar{M}_w$ or $\bar{M}_n$) and is rather insensitive to the variation in the magnitude of the expansion factor it must be concluded that eq 20 is an applicable model and thus that the underlying simplifying assumptions are reasonable approximations.

References and Notes

(1) P. Doty, H. Wagner, and S. Singer, *J. Phys. Colloid Chem.*, **51**, 32 (1947).
(2) E. Schroder, *Plaste Kautsch.*, **15**, 2 (1968).
(3) P. Munk, *Collect. Czech. Chem. Commun.*, **32**, 787 (1967).
(4) J. Hengstenberg and E. Schuch, *Makromol. Chem.*, **74**, 55 (1964).
(5) G. Vidotto, R. Zannetti, and L. Cavalli, *Makromol. Chem.*, **146**, 159 (1971).
(6) M. Carenza, G. Palma, and M. Tavan, *J. Polym. Sci., Part C*, **42**, 1031 (1973).
(7) J. Franz, E. Schroder, and K. Thinius, *Plaste Kautsch.*, **18**, 180 (1971).
(8) A. H. Abdel-Alim and A. E. Hamielec, *J. Appl. Polym. Sci.*, **16**, 1093 (1972).
(9) P. Kratochvil, M. Bohdanecky, K. Solc, M. Kolinsky, M. Ryska, and D. Lim, *J. Polym. Sci., Part C*, **23**, 23 (1968).
(10) R. Gautron and C. Wippler, *J. Chem. Phys.*, **58**, 754 (1961).
(11) T. Kobayashi, *Bull. Chem. Soc. Jpn.*, **35**, 637 (1962).
(12) J. Lyngaae-Jørgensen, *J. Chromatogr. Sci.*, **9**, 331 (1971).
(13) M. Carenza, G. Palma, and M. Tavan, IUPAC Symposium, Helsinki, July 2–7 1972, Preprint, Vol. 3, pp 11–13.
(14) A. Grugnola and F. Danusso, *J. Polym. Sci., Part B*, **6**, 535 (1968).
(15) A. H. Abdel-Alim and A. E. Hamielec, *J. Appl. Polym. Sci.*, **17**, 3033 (1973).
(16) J. Lyngaae-Jørgensen, *Makromol. Chem.*, **167**, 311 (1973).
(17) P. J. Flory, "Principles of Polymer Chemistry", Cornell University Press, Ithaca, N.Y., 1953.
(18) C. Tanford, "Physical Chemistry of Macromolecules", Wiley, New York, N.Y., 1961.
(19) R. Salovey and R. C. Gebauer, *J. Appl. Polym. Sci.*, **17**, 2811 (1973).
(20) P. J. Flory, *J. Chem. Phys.*, **17**, 223 (1949).
(21) A. Nakajima, H. Hamada, and S. Hayashi, *Makromol. Chem.*, **95**, 40 (1966).
(22) J. Lyngaae-Jørgensen, Thesis, Technical University of Denmark, 1970.
(23) M. Kurata and W. H. Stockmeyer, *Fortschr. Hochpolym.-Forsch.*, **3**, 196 (1963).
(24) S. H. Maron and M. Shiu Lee, *J. Macromol. Sci. Phys.*, **B7** (1), 61 (1973).
(25) J. Lyngaae-Jørgensen, *Polym. Eng. Sci.*, **14**, 342 (1974).

Solubility of Nonelectrolytes in Polar Solvents. VI. Refinements in Molecular Surface Area Computations

S. C. Valvani,* S. H. Yalkowsky,

Pharmacy Research, The Upjohn Company, Kalamazoo, Michigan 49001

and G. L. Amidon

Center for Health Sciences, School of Pharmacy, University of Wisconsin, Madison, Wisconsin 53706 (Received June 3, 1975; Revised Manuscript Received January 22, 1976)

A simplified calculation method for computation of molecular and group surface area of organic molecules is proposed. For surface area calculations the molecule is treated as a collection of intersecting spheres comprised of individual atoms or molecular groups. The importance and use of a solvent radius for molecular surface area calculations is critically examined, and it is shown that the solvent radius is not an essential determinant in describing the aqueous solubility–surface area relationship. The application of the proposed method for correlating the surface areas with aqueous solubilities of several linear, branched, and cyclic aliphatic alcohols and hydrocarbons is presented. A quantitative comparison of the new calculation method with a previously published method is presented and several advantages of the proposed method are discussed.

Introduction

One of the main objectives in the field of solution thermodynamics is the prediction of the effects of structural modification on solution properties. The importance of aqueous solubility, activity coefficients, free energy, and partition coefficients in various physical and biological studies cannot be overemphasized. The application of these thermodynamic properties in understanding solution behavior, the degree of hydrophobic interaction, chromatography, azeotrope formation, structure–activity relationships, and other areas has been demonstrated. Considerable research has been directed to the correlation of these properties with a number of empirical and semiempirical parameters. Several of these reports have been concerned with the consideration of either molecular surface area or molecular volume as a predictor of solubility of nonpolar solutes in aqueous solvents.

Because of a lack of a suitable method for calculation of surface area of organic molecules and because of ample availability of molar volume data, most of the early attempts have been related to correlating the aqueous solubilities with molar volumes. For example, recently McAuliffe[1] has shown a linear relationship between the logarithm of the solubility of straight chain hydrocarbons and their molar volumes. Klevens[2] correlated the aqueous solubility of aromatic hydrocarbons with molar volumes and the size of the solute molecules along their long axis. These estimates of molecular size were based on the consideration of a molecule as a single sphere of known molecular volume and also from standard bond lengths and bond angles. Parachors have been used as a measure of molecular volume in describing the solubility relationship.[3-5]

Historically, Langmuir[6] first introduced the concept that the surface area of the solute is a determinant of its activity. This concept considers that the major factor in solubility relationships is the energy required to create a cavity in the solvent into which the solute is placed. The energy needed for the hole formation was considered to be proportional to the surface area of the solute and has been utilized by several workers. Harris and coworkers[7] determined the relative surface area mechanically by packing spherical balls representing water molecule protons around molecular models and counting the number of spheres in contact with the molecule. Realizing the difficulty, and importance, of surface area measurements, Hermann[8] has developed a computer program for estimation of surface area of nonspherical molecules with fixed conformation. The usefulness of this method has been demonstrated by correlating the solubilities of hydrocarbons in water with the calculated surface areas.[8] Recently, Amidon et al.[9] have successfully applied the method to the effective surface areas and aqueous solubility of several aliphatic alcohols and hydrocarbons.

There are certain difficulties associated with the use of Hermann's computer program for surface area calculations. Preparation of input required for calculations is rather time consuming for relatively large molecules especially when the conformation is not readily visualized. Furthermore, the cost of computer run for each molecule represents a significant portion of total expenses involved in complete analysis of the surface area–solubility relationship. The computer cost is an approximate function of the square of the total number of atoms in the molecule. Lastly, the addition of a solvent radius to each atom in the molecule is another complication whose importance is not completely clear.

The main objective of this report was to explore means of overcoming the above difficulties. This has led us to propose a simplified version of the calculation method. A critical evaluation of the assumptions involved in the proposed method, including the use of a solvent radius in effective surface area calculations, will be discussed. A quantitative comparison of the original and proposed methods, along with their advantages and limitations, will be presented.

TABLE I. SURFACE AREA VALUES OF ALIPHATIC ALCOHOLS AND HYDROCARBONS*

NO.	COMPOUND	STRUCTURE	METHOD A	METHOD B	METHOD C
1	N-BUTANOL		272.1	264.5	115.8
2	2-METHYL,1-PROPANOL		263.8	257.7	113.8
3	2-BUTANOL		264.1	259.6	114.6
4	N-PENTANOL		303.9	294.4	134.9
5	3-METHYL,1-BUTANOL		291.4	285.8	131.0
6	2-METHYL,1-BUTANOL		289.4	283.0	131.2
7	2-PENTANOL		295.9	289.5	132.8
8	3-PENTANOL		293.5	286.7	132.0
9	3-METHYL,2-BUTANOL		284.3	280.9	129.8
10	2-METHYL-2-BUTANOL		282.5	279.4	129.4
11	2,2-DIMETHYL,1-PROPANOL		283.5	277.8	128.7

NO.	COMPOUND	STRUCTURE	METHOD A	METHOD B	METHOD C
12	N-HEXANOL		335.7	324.3	152.1
13	2-HEXANOL		327.7	319.5	150.9
14	3-HEXANOL		325.3	316.6	150.1
15	3-METHYL,3-PENTANOL		315.8	312.3	145.1
16	2-METHYL,3-PENTANOL		314.3	309.3	147.6
17	2-METHYL,2-PENTANOL		314.3	308.0	147.2
18	3-METHYL,2-PENTANOL		311.3	305.9	146.7
19	2,3-DIMETHYL,2-BUTANOL		301.2	299.0	143.9
20	3,3-DIMETHYL,1-BUTANOL		307.5	304.3	145.0
21	3,3-DIMETHYL,2-BUTANOL		296.7	297.7	143.1
22	4-METHYL,1-PENTANOL		323.0	315.7	149.2
23	4-METHYL,2-PENTANOL		314.9	310.4	148.0
24	2-ETHYL,1-BUTANOL		318.6	295.7	142.1
25	CYCLO HEXANOL		290.5	281.4	130.3

NO.	COMPOUND	STRUCTURE	METHOD A	METHOD B	METHOD C
26	N-HEPTANOL		367.5	354.2	170.3
27	2-METHYL,2-HEXANOL		346.1	339.2	165.7
28	3-METHYL,3-HEXANOL		337.1	332.1	163.2
29	3-ETHYL,3-PENTANOL		324.4	321.6	159.6
30	2,3-DIMETHYL,2-PENTANOL		323.8	323.0	159.4
31	2,3-DIMETHYL,3-PENTANOL		321.8	320.6	158.7
32	2,4-DIMETHYL,2-PENTANOL		328.6	323.8	159.1
33	2,4-DIMETHYL,3-PENTANOL		331.7	326.5	161.4
34	2,2-DIMETHYL,3-PENTANOL		326.1	324.6	160.3
35	3-HEPTANOL		357.1	346.5	168.3
36	4-HEPTANOL		357.1	346.5	168.3
37	1-OCTANOL		399.4	384.1	188.4
38	2,2,3-TRIMETHYL,3-PENTANOL		355.2	357.4	171.9
39	2-OCTANOL		391.0	379.3	187.2

NO.	COMPOUND	STRUCTURE	METHOD A	METHOD B	METHOD C
40	2-ETHYL,1-HEXANOL		371.3	355.5	178.3
41	1-NONANOL		431.2	414.0	206.5
42	2-NONANOL		423.2	409.2	205.3
43	3-NONANOL		420.8	406.3	204.5
44	4-NONANOL		420.8	406.3	204.5
45	5-NONANOL		420.8	406.3	204.5
46	2,6-DIMETHYL,4-HEPTANOL		394.0	386.7	198.7
47	3,5-DIMETHYL,4-HEPTANOL		379.3	370.5	190.0
48	2,2-DIETHYL,1-PENTANOL		372.5	368.4	191.0
49	7-METHYL,1-OCTANOL		418.7	405.5	203.6
50	3,5,5-TRIMETHYL,1-HEXANOL		376.6	371.3	189.5
51	1-DECANOL		463	443.9	224.6
52	1-DODECANOL		527	503.7	260.8
53	1-TETRADECANOL		591	563.5	297.1

NO.	COMPOUND	STRUCTURE	METHOD A**	METHOD B	METHOD C
54	1-PENTADECANOL		623	593.4	315.2
55	1-HEXADECANOL		655	623.4	333.2
56	N-BUTANE		255.0 (255.2)	247.6	105.9
57	ISOBUTANE		251.7 (249.1)	247.2	105.9
58	N-PENTANE		286.9 (287.0)	277.6	124.0
59	2-METHYLBUTANE		274.4 (274.6)	269.0	121.1
60	3-METHYLPENTANE		300.8 (300.1)	294.1	137.5
61	NEOPENTANE		265.1 (270.1)	266.0	120.3
62	2,2-DIMETHYLBUTANE		289.2 (290.8)	287.4	135.1
63	2,4-DIMETHYLPENTANE		323.4 (324.7)	319.0	154.2
64	2,2,4-TRIMETHYLPENTANE		352.4 (358.9)	329.2	163.1
65	2,2,5-TRIMETHYLHEXANE		370.2 (373.0)	367.9	186.6
66	CYCLOHEXANE		279.5 (279.1)	266.6	120.8
67	(E)-METHYLCYCLOHEXANE		305.2 (304.9)	292.7	137.7

NO.	COMPOUND	STRUCTURE	METHOD A**	METHOD B	METHOD C
68	1-CIS-2-DIMETHYLCYCLO-HEXANE		319.1 (315.5)	309.2	150.2
69	CYCLOHEPTANE		295.8 (301.9)	284.4	133.2
70	CYCLO OCTANE		315.8 (322.58)	305.7	148.8
71	N-HEXANE		318.7 (319)	307.5	142.1
71	N-HEPTANE		350.5 (351)	337.4	160.3
72	N-OCTANE		382.3 (383)	367.3	178.4

* FOR SOLUBILITY VALUES USED IN REGRESSION ANALYSIS SEE G.L. AMIDON, S.H. YALKOWSKY AND S. LEUNG, J. PHARM. SCI., 63, 1858 (1974).

** TSA VALUES IN PARENTHESES FOR COMPOUNDS 56-73 ARE FROM R.B. HERMANN, J. PHYS. CHEM., 76, 2754 (1972).

Experimental Section

Computer Program. The surface area calculations were carried out by a modified version of a computer program, MOLAREA, developed by Hermann.[8] The original program (QCPE 225) was obtained through the Quantum Chemistry Program Exchange, Chemistry Dept., Indiana University, Bloomington, Ind. For the program, the molecule is considered as a collection of intersecting spheres with each radius located at the nuclear center. Standard interatomic bond lengths, bond angles, van der Waals radii, and torsional angles between various atoms in a molecule are the required input for the program. A radius for the solvent (water) may be added to each radius on the solute

molecule. Planes of intersection between spheres are used to estimate the contribution to surface area from individual atoms or groups. The program computes the surface area of individual atoms or groups by numerical integration, and the overlap due to intersecting spheres is excluded from the calculation. Total surface area is calculated by the summation of individual group contributions.

The surface area values for all the aliphatic alcohols and hydrocarbons in Table I were calculated by the following three methods.

Method A. This method is essentially that of Hermann.[8] The molecule is composed of intersecting spheres of carbon, hydrogen, and oxygen with their radii being equiva-

lent to van der Waals radii. To each radius in the molecule a radius for solvent (1.5 Å) was added. Standard geometry, standard interatomic bond lengths,[10] and bond angles were used in constructing the molecules. The following values for interatomic bond lengths were used: aliphatic C–C, 1.54 Å; C–H, 1.09 Å; C–O (in alcohols), 1.43 Å; and O–H (in alcohols) 0.97 Å.[10] The van der Waals radii used were: aliphatic carbon, 1.6 Å; hydrogen, 1.2 Å; and oxygen, 1.4 Å.[11]

Method B. In this method the molecule is considered as a collection of spherical groups rather than individual atoms. The methyl and methylene groups are approximated as a single sphere of radius 2.0 Å, instead of being composed of a carbon and two or three hydrogen atoms with their individual van der Waals radii and bond lengths as in method A. The hydroxyl group in alcohols was also treated as being a single sphere with a radius of 1.7 Å. To each of these spherical groups a radius for solvent (1.5 Å) was added as in method A. The same standard geometry was used for locating the groups in a molecule, e.g., the CH_3–CH_2 groups were located at C–C bond distance of 1.54 Å, and the OH group in the alcohols was located at C–O bond length at 1.43 Å.

Method C. For this method, the molecule was treated as a collection of spherical groups as described in method B, the only difference being the omission of a solvent radius.

Solubility Data. Aqueous solubilities for all these compounds have been reported in a previous publication,[9] and the reader is referred to the original references cited therein. All the multiple aqueous solubility values were utilized for statistical analysis. The logarithms of molal solubilities were correlated with the total surface area, number of functional groups term, and functional group surface area according to the models described previously.[9]

Results

The total surface area (TSA) values for all the alcohols and hydrocarbons as calculated by all three methods are presented in Table I (see paragraph at end of text regarding miniprint material). For the sake of brevity, the aqueous solubility values are not presented in the table.

Statistical results for a number of models using surface area values calculated by all three methods are included in Tables III–VI.

Discussion

The results of correlation of the logarithm of aqueous solubility and total surface area values, calculated by method A, are essentially those that have appeared in a previous report.[9] They have been discussed in great detail and the physical interpretation of most of the parameters considered has also been dealt with in the original paper.[9] In this report, we will restrict ourselves to a discussion of the results based on surface areas calculated by methods B and C and their comparison with those by method A.

Table I shows that the total surface area values calculated by method B for all the molecules are, in general, very comparable to those by method A. For larger molecules the difference in TSA values by both the methods appears to increase slightly. This is largely due to a smaller contribution to total surface area for each normal methylene group by method B (29.9 Å²) as compared with that by method A (31.8 Å²). Both methods seem to weigh the contribution for branched methyl groups and hydroxyl groups slightly differently, but the difference is rather insignificant. A comparison of the contribution to surface area of methyl groups

TABLE II: Group Surface Areas from Noncyclic Aliphatic Alcohols and Hydrocarbons (Compounds 1–73) by Various Methods

	Surface area[b] ($Å^2$) as computed by		
Group	Method A	Method B	Method C
Primary OH	44.6–59.2	44.0–58.5	19.4–21.0
Secondary OH	29.8–42.8	35.3–46.1	17.9–19.6
Tertiary OH	26.7–38.6	29.7–41.2	15.6–18.9
Primary CH_3	56.0–84.9	55.8–84.4	29.4–33.2
Secondary CH_3	45.6–75.3	43.7–75.3	27.6–31.0
Tertiary CH_3	44.6–66.2	45.9–66.6	26.1–29.3
CH_2	14.9–45.4	14.6–48.2	13.4–22.8
CH	5.0–17.4	4.8–17.6	6.2–10.6
C	0	0	0–0.7
Incremental CH_2[a]	31.8	29.9	18.1
Terminal CH_3[a]	84.9	84.4	33.2

[a] In straight chain extended conformation. [b] Group surface area will depend on the degree of substitution surrounding the molecular group. In general, the greater the substitution, the smaller the group surface area and vice versa.

TABLE III: Solubility (sol) of Aliphatic Alcohols (Compounds 1–55) as a Function of Total Surface Area (TSA)

$$\text{Log (sol)} = \beta \cdot \text{TSA} + \alpha \quad n = 75$$

Eq	TSA Computation method	β	α	Correlation coef r	Std Dev s
1	A	−0.0176	4.74	0.989	0.208
2	B	−0.0189	5.04	0.989	0.212
3	C	−0.0317	3.80	0.986	0.233

and hydroxyl groups in various positions on the molecule is shown in Table II. The agreement between these terms by methods A and B is obvious. The data from Table II may be used to estimate with reasonable accuracy the total surface area values for the hydrocarbons and alcohols not included in this report. It should be borne in mind that the group surface area values are highly dependent on the degree of substitution surrounding the molecular group. A group with greater substitution has a smaller surface area contribution and an isolated group has the largest surface area.

The important criterion for comparison purposes is the overall statistics of activity coefficients and surface area data based on all the methods. The solubility of a slightly soluble liquid solute in mole fraction concentration units is equivalent to the reciprocal of the activity coefficient. We have used the molal solubility in water for all the liquid alcohols and hydrocarbons. For the solid alcohols (compounds 11, 53–55) solubility of the pure supercooled liquid at 25 °C has been used.[9] When the data for all the alcohols (compounds 1–55) are used for correlation of TSA with logarithm of aqueous solubility, the results of analysis by both methods are represented by eq 1 and 2 in Table III. The slope and the intercept values of these equations are not significantly different from each other; the correlation coefficients and the standard deviation values are comparable for both methods.

One of the physical models considers the solute molecule as being composed of a nonpolar hydrocarbon portion and a polar hydroxyl group. When the contributions from these

TABLE IV: Solubility (sol) of Aliphatic Alcohols (Compounds 1–55) as a Function of Hydrocarbon Surface Area (HYSA) and Hydroxyl Group Surface Area (OHSA)

$$\text{Log (sol)} = \beta \cdot \text{HYSA} + \gamma \cdot \text{OHSA} + \alpha \quad n = 75$$

Eq	TSA Computation method	β	γ	α	Multiple correlation coef r	Std dev s
4	A	−0.0174	−0.0224	4.90	0.989	0.202
5	B	−0.0186	−0.0300	5.47	0.991	0.187
6	C	−0.0309	−0.172	6.49	0.994	0.158

TABLE V: Solubility (sol) of Hydrocarbons (Compounds 56–73) as a Function of Total Surface Area (TSA)

$$\text{Log (sol)} = \beta \cdot \text{TSA} + \alpha \quad n = 18$$

Eq	TSA Computation method	β	α	Correlation coef r	Std Dev s
7	A	−0.0199	2.29	0.980	0.154
8	B	−0.0205	2.32	0.980	0.154
9	C	−0.0323	0.73	0.980	0.157

Figure 1. A planar view of a terminal methyl group. The solid curves show a carbon atom in the center with van der Waals radius of 1.6 Å and, three hydrogen atoms with van der Waals radius 1.2 Å. The broken curve shows the whole methyl group treated as a single sphere with radius of 2.0 Å.

groups, the hydroxyl group surface area, OHSA, and hydrocarbon group surface area, HYSA = TSA − OHSA, are included in the regression analysis, the results of data from three methods are shown as eq 4–6 in Table IV. Again, the multiple correlation coefficients by both methods are essentially unchanged, and the standard deviation term for eq 5 (method B) is slightly smaller than that by eq 4 (method A). This suggests that the contribution of hydroxyl group surface area to the total surface area calculated by method B is able to account for the change in solubility marginally better than the treatment by method A.

An analysis of hydrocarbon solubility data by both methods (Table V, eq 7 and 8) shows that the respective slope, intercept, correlation coefficient, and standard deviation values are not significantly different from each other, lending support for the less complex calculations by method B.

The justification for the selection of a 2.0-Å radius sphere for the methyl or methylene group is derived from Pauling's[11] account of experimental measurements on several molecules. A schematic diagram (Figure 1) shows a planar view of a terminal methyl group as treated by both methods (without the solvent radius). Solid curves show a carbon atom in the center (van der Waals radius 1.6 Å) and three tetrahedral hydrogens (van der Waals radius 1.2 Å) located at 1.09 Å from the center of the carbon atom. The dotted curve shows the methyl group as a single sphere with a radius of 2.0 Å. As can be seen, the parts of hydrogen atoms are compensated for by filling the void spaces around the carbon atom. The agreement between the methylene group and methyl group surface areas calculated by both methods (see Table II) is evidence of good approximation. The selection of a single sphere of radius 1.7 Å for the hydroxyl group is rather arbitrary, and was chosen since it gives a close agreement between hydroxyl group surface area in normal alcohols by both methods. This choice for the single sphere radius of 1.7 Å for the hydroxyl group in a molecule is also consistent with the value obtained from the closest packed spherical molecules of water with a density of 1.
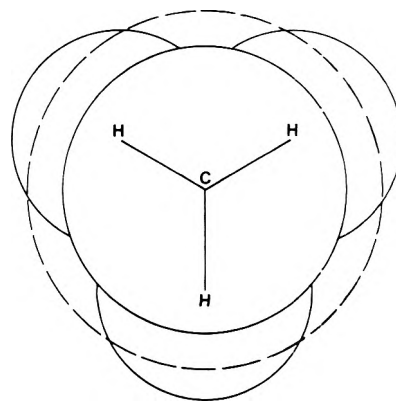
One of the limitations of surface area calculation by all the above methods is that the results are largely dependent on the conformation of a molecule. In order that the calculation method be attractive, simple, and have practical utility as a tool for predicting the effects of molecular modification, it should not be restricted only to molecules whose conformations are known. Often, several conformations for atoms or groups in a molecule are possible, and the selection of a specific conformation for an atom or group in a molecule is somewhat arbitrarily based on intuition to minimize the overall interactions between atoms and groups.

Calculations by method B afford several advantages over method A. In calculating surface area by method B, choosing a single sphere for a methyl, methylene, or hydroxyl group allows one to eliminate the arbitrary selection of a specific arrangement of hydrogen atoms in these groups in a molecule. This is particularly helpful in calculations involving rather large molecules whose preferred conformation is not known. The surface area calculations are still dependent on the overall conformation of a molecule. The spherical approximation utilized for method B only eliminates the conformational effects due to hydrogen atoms in a molecule.

We have chosen the simplest standard geometry to represent the group or atoms in a molecule. Hermann[8] has used exact conformation or weighted average when several conformations were possible for his hydrocarbon surface area calculations. His data for hydrocarbons (compounds 56–73) are included in parentheses (in Table I) for comparison purposes. An examination of the data reveals that the maximum difference between the surface area values calculated by using standard geometry is less than 2%, a small difference when considering the uncertainty and the extent of experimental error involved in the solubility values reported.

In addition, method B offers considerable economic advantages in terms of time and the computer cost. For example, the surface area calculations of 1-octanol by method A involve preparing an input for a total of 26 atoms, while an input of eight methyl–methylene groups and one hydroxyl group suffices for calculations by method B. This is extremely helpful and time saving, especially when the standard geometry of hydrogen atoms in a molecule cannot be visualized and one has to resort to the use of atomic models. The computer cost for the same molecule translates to
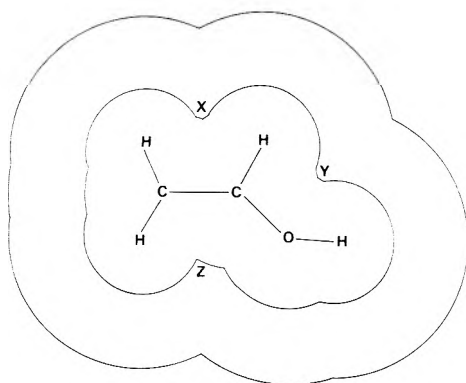
Figure 2. A schematic diagram of a planar section of an ethanol molecule. The outer curve represents the molecular surface as treated for calculations by method A (including the solvent layer). The molecular surface of the solute (ethanol) is shown as the inner surface.

Figure 3. A schematic diagram of a planar view of an ethanol molecule. The outer curve represents the molecular surface as treated for calculations by method B (including the solvent layer). The molecular surface of the solute (ethanol) is shown as the inner surface.

Figure 4. A planar view of ethanol molecular surface as treated for calculations by method C.

a savings of about ten-fold for method B as compared to method A. This is a very important savings, since the computations involve rather large iterative loops and the computer cost represents the most significant portion of the total cost involved in solubility–surface area relationships.

The preceding analysis has shown that method B can give at least as good a correlation, or slightly better a correlation, as method A. It lends support to the argument that basic features of method B (the approximation of the methyl–methylene group as a single sphere with a radius of 2.0 Å and other groups as a single sphere) can be consistently utilized to explain the solubility–surface area relationship.

Both methods A and B have utilized a solvent radius of 1.5 Å for total effective surface area calculations. The inclusion of a solvent radius for total surface area calculations was based on the assumption that the water layer around the solute or the number of water molecules that can be packed around the solute molecule is an important and necessary parameter in describing the solubility–surface area relationship. Another argument for using the solvent radius is that it eliminates from the total surface area of a solute molecule those areas not exposed or accessible to the solvent. The following discussion is devoted to a critical examination of the above arguments and determining whether the inclusion of a solvent radius is an essential determinant for adequately describing the solubility–surface area relationship.

The surface area calculations by method C are essentially similar to method B with the exception of a solvent radius term used for the individual atoms or groups in the molecule. As expected, the total surface area and hydroxyl group surface area values for all the molecules calculated by this method are smallest of the three methods.

A schematic representation of a planar view of an ethanol molecule as treated by all three methods is shown in Figures 2–4. The outer curves in Figures 2 and 3 depict the centers of solvent molecules surrounding the solute molecule. As evident from the total surface area values in Table I, the overall exposed surface of the molecule (including the solvent) by both methods A and B is essentially the same.

It is instructive to note that the solute molecule as treated by method A has several portions of intersecting atoms (small crevices labeled X, Y, and Z in Figure 2) which are inaccessible to solvent. Inclusion of a solvent radius for each atom in the molecule eliminates these inaccessible
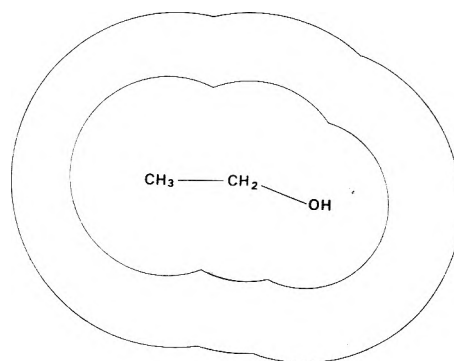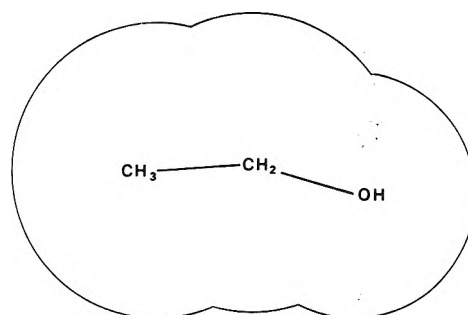
portions (see molecule enclosed by outer surface in Figure 2). However, the treatment of the solute molecule as a collection of spherical groups (without the use of a solvent radius) instead of individual atoms accomplishes the same desirable feature of eliminating from the surface the inaccessible portions of the molecule (Figure 4). In other words, the use of 2-Å radius has a similar smoothing effect on the molecular surface as does the use of a solvent radius. Furthermore, the treatment of cyclic molecules, e.g., cyclohexane as a collection of individual carbon and hydrogen atoms leaves a hole in the center, and the molecular surface has several small crevices. However, method C treats the cyclohexane molecule as a collection of six methylene groups, leaving no hole in the center, and the resulting molecular surface is fairly smooth.

A comparison of all the alcohol data, when total surface area computed by method C and log aqueous solubility are considered, reveals that the slope and intercept values for the regression equation, as expected, are different from those by other methods. However, what is more important is that the correlation coefficient and overall standard deviation values of eq 3 (method C) are not significantly different from those of eq 1 and 2. This is quite significant in view of the fact that the computations by method C do not include the added complexity of a solvent radius term.

Superiority of the correlation with the calculations by method C over that of methods A and B can be seen from the results in Table IV. Here the regression is performed between the logarithm of the solubility of all the alcohols (compounds 1–55) and their hydrocarbon portion and hydroxyl group contributions to the surface area. A significant reduction in the overall standard deviation and a slight improvement in the multiple correlation coefficient

TABLE VI: Solubility (sol) of Aliphatic Alcohols and Hydrocarbons (Compounds 1–73) as a Function of Hydrocarbon Surface Area (HYSA), Hydroxyl Group Surface Area (OHSA), and Number of Functional Groups (NFG)

$$\text{Log (sol)} = \beta \cdot \text{HYSA} + \gamma \cdot \text{OHSA} + \delta \cdot \text{NFG} + \alpha \quad n = 93$$

Eq	TSA compu- tation method	β	γ	δ	α	Multiple correlation coef r	Std dev s
10	A	−0.0175	−0.0222	3.37	1.57	0.992	0.197
11	B	−0.0187	−0.0299	3.72	1.78	0.994	0.183
12	C	−0.0310	−0.172	5.95	0.55	0.995	0.158
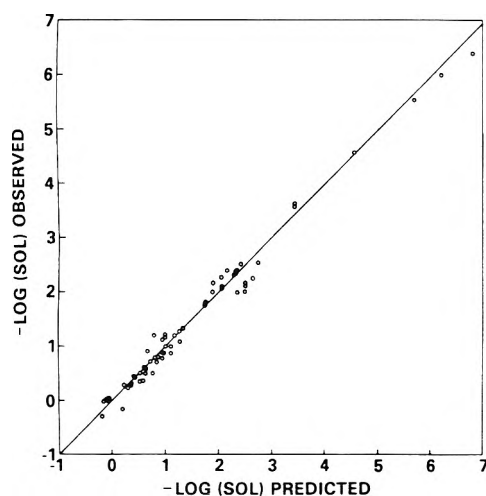
Figure 5. Observed solubility of alcohols (compounds 1–55) vs. predicted solubility from eq 6 (Table IV): slope = 0.999, r = 0.995, s = 0.158.

of eq 6 vs. those values of eq 4 is observed. This suggests that calculations by method C for both the hydrocarbon group and hydroxyl group are making a constant contribution (per unit area) to the solubility of alcohols. A logarithmic plot of the observed solubility vs. predicted solubility based on eq 6 for all the alcohols appears as Figure 5. As expected, the slope of such a plot is very close to unity (0.999) and the correlation coefficient is 0.995.

For hydrocarbon data also it can be seen that the agreement between overall statistics on surface areas computed by method C and method A is rather good (eq 9 and eq 7).

Combination of alcohol and hydrocarbon data and analysis according to the model which relates the log solubility with hydrocarbon group surface area, hydroxyl group surface area, and number of hydroxyl groups (NFG) term yields a multiple correlation coefficient and standard deviation (eq 12) which show a slight improvement over those obtained with method A (eq 10) or method B (eq 11).

Method C has all the advantages as outlined for method B and in addition the following important arguments can be made in favor of using method C for surface area calculations.

The molecular surface area calculated by method C is independent of the nature of the solvent and thus eliminates the need to arbitrarily select an appropriate solvent radius (which may vary from solvent to solvent). The results calculated by this method represent an estimate of true surface area of the molecule in the gas phase or any solvent. This is particularly useful in studying the partitioning behavior of nonpolar solutes and the effect of molecular modification.

Since no packing of the solvent molecules around the so-

lute molecule is involved, the usual difficulties that may arise in calculating the surface area of the molecule in a folded conformation are quite readily overcome. Furthermore, the types of cavity shapes presenting special problems as described by Hermann[8] would not be encountered in the proposed method. Whether there are any real physical effects due to omission of solvent packing remains to be seen.

The dimensions used in this calculation method would be expected to be most consistent with molecular volume. The relative surface area results by method C seem to be more in agreement with the relative size of the molecule, a result not seen in calculations by methods A and B. Work related to a computer program for calculation of molecular volume of organic molecules is in progress.

Extrapolation of the log solubility and total surface area values by methods A and B to zero surface area (the intercept value) poses problem, such that, even for an infinitesimally small atom or molecule approaching zero van der Waals radius, a finite total surface area value would be estimated because of inclusion of a solvent radius around the molecule. The zero total surface area value would actually correspond to a hypothetical atom with a negative van der Waals radius equal to the solvent radius, a physical unreality. However, the extrapolation to zero surface area value by method C gives a very meaningful estimate of total area of an infinitesimally small molecule or group. Thermodynamically, the intercept of log molal solubility and total surface area corresponding to zero surface area would be expected to have a theoretical value of approximately 1.74 (on log scale). There appears to be some deviation in this value from the analysis of alcohols and hydrocarbons solubility data. The reasons for this inconsistency and possible explanations have already been dealt with in a separate publication.[12]

The coefficients of the surface area terms represent the interfacial free energy per unit solute surface area. In the case of the hydrocarbon surface area, the coefficient is analogous to the bulk hydrocarbon–water interfacial tension as described previously in greater detail.[9,12] This analogy has been successfully extended to several nonaqueous polar solvents and to mixed aqueous solvent systems with excellent results.[13]

This approach has recently been used to show that octanol–water partition coefficients of several alkyl benzenes can be successfully explained on the basis of molecular surface area.[14]

While the data in support of the proposed method of surface area calculation have been presented only for aliphatic alcohols and hydrocarbons, the analysis is being carried out with a series of other solutes with various functional groups, viz., esters, aldehydes, ketones, ethers, and acids. Preliminary findings indicate that calculations by method

C describe the aqueous solubility–surface area relationship extremely well and that the correlation of these relationships is at least as good as has been reported previously.[12] A forthcoming report will include a complete analysis and interpretation of all the data contained therein.

Miniprint Material Available: full-size photocopies of Table I (6 pages). Ordering information is available on any current masthead page.

References and Notes

(1) C. McAuliffe, *J. Phys. Chem.*, **70**, 1267 (1966).
(2) H. B. Klevens, *J. Phys. Colloid. Chem.*, **54**, 283 (1950).
(3) N. C. Deno and H. E. Berkheimer, *J. Chem. Eng. Data*, **4**, 1 (1960).
(4) J. C. McGowan, *J. Appl. Chem.*, **2**, 323 (1952).
(5) J. C. McGowan, *J. Appl. Chem.*, **4**, 41 (1954).
(6) I. Langmuir, *Colloid Symp. Monogr.*, **3**, 3 (1925).
(7) M. J. Harris, T. Higuchi, and J. H. Rytting, *J. Phys. Chem.*, **77**, 2694 (1973).
(8) R. B. Hermann, *J. Phys. Chem.*, **76**, 2754 (1972).
(9) G. L. Amidon, S. H. Yalkowsky, and S. Leung, *J. Pharm. Sci.*, **63**, 1858 (1974).
(10) "Table of Interatomic Distances", Supplement, L. E. Sutton, Ed., Chemical Society, London, 1965.
(11) L. Pauling, "The Nature of the Chemical Bond", Cornell University Press, Ithaca, N.Y., 1960, pp 260–262.
(12) G. L. Amidon, S. H. Yalkowsky, S. Anik, and S. C. Valvani, *J. Phys. Chem.*, **79**, 2239 (1975).
(13) S. H. Yalkowsky, G. L. Amidon, G. Zografi, and G. L. Flynn, *J. Pharm. Sci.*, **64**, 48 (1975).
(14) S. H. Yalkowsky and S. C. Valvani, *J. Med. Chem.*, in press.

A Kinetic Study of the Interaction between Atomic Oxygen and Aerosols[1]

F. I. Akers and J. P. Wightman*

Chemistry Department, Virginia Polytechnic Institute and State University, Blacksburg, Virginia 24061 (Received June 13, 1975; Revised Manuscript Received November 24, 1975)

This study was concerned with the effects of NH_4Cl and $(NH_4)_2SO_4$ aerosols on the kinetics of disappearance of atomic oxygen. Atomic oxygen was generated by a 2.45-GHz microwave discharge and the kinetics of disappearance measured in a fast flow system using NO_2 titration. Values of the recombination coefficient, γ, for heterogenous wall recombination were determined for clean, H_2SO_4-coated, and $(NH_4)_2SO_4$-coated Pyrex to be 5.0×10^{-5}, 2.0×10^{-5}, and 1.9×10^{-5}, respectively. A rapid exothermic chemical reaction was found to occur between atomic oxygen and an NH_4Cl wall coating; the products were NH_3, NO, H_2O, and HCl. The NH_4Cl aerosol was generated by gas phase reaction of NH_3 with HCl. The aerosol particles were approximately spherical and nearly monodisperse with a mean diameter of 1.6 ± 0.2 μm. The rate constant (k_{aero}) for the disappearance of atomic oxygen in the presence of the NH_4Cl aerosol was measured. For an aerosol concentration of 4.75×10^3 μg/m^3, a value of $k_{aero} = 2.8 \pm 0.5$ s^{-1} was found. An $(NH_4)SO_4$ aerosol was generated by the gas phase reaction of NH_3 with H_2SO_4. The aerosol particles were irregularly shaped with a mean diameter of 2 μm. No significant decrease was observed in the rate of disappearance of atomic oxygen in the presence of an $(NH_4)_2SO_4$ aerosol at a concentration of 285×10^3 μg/m^3.

Introduction

The stratosphere is quite important to life because of its ability to shield the earth's surface from biologically damaging radiation. This is due in large part to the absorption of ultraviolet radiation by ozone.[2] It is of interest therefore to study chemical reactions which may occur in the stratosphere and possibly lead to significant reductions of ozone. Increasing amounts of aerosols such as H_2SO_4 and $(NH_4)_2SO_4$ have been detected in the stratosphere.[3-5] The present work is concerned with the effects of some aerosols on the recombination kinetics of atomic oxygen, a reactant necessary for the formation of ozone.[6,7]

In the experiments reported here, atomic oxygen disappearance was measured in a flow system having clean and coated walls, and in the presence of NH_4Cl and $(NH_4)_2SO_4$ aerosols. In conjunction with these studies, coated reactor wall samples were characterized by ESCA (electron spectroscopy for chemical analysis), products of the reaction between NH_4Cl(s) and atomic oxygen were analyzed by

mass spectroscopy, and the aerosols produced were characterized using scanning electron microscopy.

Experimental Section

Atom Recombination Rate Experiments. Wall Recombination. Description of Apparatus. Kinetic measurements for wall recombination were made using the fast-flow system shown schematically in Figure 1. Airco USP oxygen was admitted to the flow tube through a stainless steel needle valve (NV1). The flow tube was pumped directly by a 500 l./min mechanical pump. Pressures were measured with an MKS Baratron pressure meter Type 144 (MKS). The entire "reactor" portion of the flow tube was removable for cleaning or coating. The upper portion of the reactor was the discharge region made of 13-mm o.d. Pyrex glass.

Microwave power was generated with a Raytheon Microtherm unit, KV104 A, capable of 125 W output. The generator was coupled to a Raytheon Model FC-7097 NBS waveguide cavity. The percent dissociation of the oxygen stream varied between 2 and 7%.

The titration region had four gas inlet jets, J1–J4, each

* Address correspondence to this author at the School of Chemistry, University of Bristol, Cantock's Close, Bristol BS8 1TS, England.
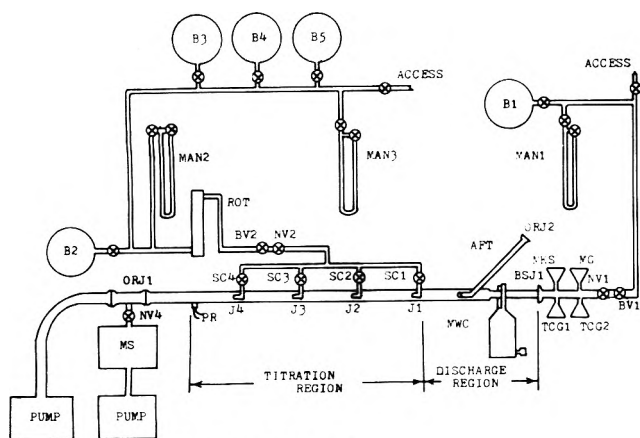
Figure 1. Fast flow system schematic.

centered in the flow tube. Each Pyrex jet could be opened or closed with a Teflon stopcock (SC1–SC4). A photoresistor (PR) with a peak response at 5150 Å was located about 20 cm downstream from J4. This wavelength was suitable since the chemiluminescence from the oxygen atom–nitrogen dioxide titration reaction was a continuum from 3700 to 9000 Å, with a maximum near 6500 Å.[8] Oxygen atom concentrations were measured by the NO_2 chemiluminescent titration method of Kaufman.[9] A capillary rotameter was used to monitor NO_2 flow. The NO_2 pressure was maintained at 50 ± 1 Torr to keep the N_2O_4 concentration low.[10]

Flow Rate Determination. Operating pressures were 0.50, 0.80, 1.0, 1.3, and 1.5 Torr. Linear flow velocity at each operating pressure was calculated from the measured volume flow rate. The linear flow velocities gave elapsed time values which were used in the kinetic calculations. O_2 linear flow velocities and elapsed times ranged from 303 to 769 cm/s and from 1.32 to 10.04 × 10^{-2} s, respectively.

The determination of NO_2 flow rates and calibration of the NO_2 flowmeters were carried out in a manner similar to the O_2 flow rates.

Kinetics of Wall Recombination. Kinetic determinations were carried out by adjusting the oxygen flow by NV1 so that a constant pressure corresponding to one of those selected and characterized earlier was maintained. The microwave discharge was initiated. Stopcock SC1 was opened and NV2 was adjusted so that a maximum was noted on the photodetector meter. The NO_2 rotameter reading was then recorded. The NO_2 flow at maximum intensity was recorded for each of the other jets in turn.

Wall Treatments. The term "clean wall treatment" means that the reactor tube had a nitric acid wash and a distilled water rinse. Concentrated H_2SO_4 was applied to all the area inside the reactor except the discharge region. A saturated aqueous solution of $(NH_4)_2SO_4$ was applied to the inside of the reactor. The discharge was operated for 10 min to condition the reactor before the kinetic determinations were begun. A dilute aqueous solution of NH_4Cl was applied to the reactor in the same fashion as the $(NH_4)_2SO_4$.

A reaction was observed between NH_4Cl and atomic oxygen. An AEI MS-10 mass spectrometer (MS) was positioned as shown in Figure 1 and used for product analysis.

Atom Recombination Rate Experiments. Aerosol Interaction. Description of Apparatus. The system used for aerosol studies was basically the same as that used for wall recombination measurements. A removable particle sam-

pler was installed at ORJ1 (see Figure 1). The sampler had four indentations which supported a plastic collector. The collector had 15 holes of 2 mm diameter bored through it. The collector fit snugly into the sampler and could be removed for weighing. Aerosols were collected by impaction on the collector for size, shape, and particle concentration determinations.

An NH_4Cl aerosol generator was constructed, using the gas phase reaction of NH_3 and HCl as the formation technique. The apparatus consisted of a 5-l. Pyrex bulb with an oxygen carrier gas inlet, an aerosol stream outlet, and two removable Pyrex jets which reached to the center of the bulb. Matheson Anhydrous NH_3 and Matheson Technical, 99.0% purity, HCl were used without further purification.

For $(NH_4)_2SO_4$ aerosol generation, a custom-built H_2SO_4 boiler replaced the HCl jet. A standard taper joint and jet were made to fit the aerosol bulb, and H_2SO_4 vapor was produced by heating the concentrated acid with a 900-W heater controlled by a Variac. Acid flow was controlled by a teflon stopcock.

The discharge region of the flow tube was altered to accommodate the aerosol generator. The aerosol flow tube (AFT) was centered through the side of the reactor (Figure 1). The generator exit was 10 cm above J1 to allow mixing before reaching the titration region. An O-ring joint, ORJ2, facilitated removal of the reactor.

Aerosol Characterization. The particle concentration in the aerosols was estimated by measuring the mass of the aerosol collected after varying collection times. For NH_4Cl, a particle concentration of 4.75 × 10^3 $\mu g/m^3$ was calculated from the ratio of mass collected per unit time to volume flow rate. The collected particles were examined using an Advanced Metals Research Model 900 scanning electron microscope. The NH_4Cl particles were approximately spherical and were all about the same size. The mean particle diameter was estimated to be 1.6 ± 0.2 μm on a 4800 X photomicrograph.

The $(NH_4)_2SO_4$ aerosol was generated and characterized in a like manner. The H_2SO_4 boiler was operated between 200 and 205 °C. Mass vs. collection time data indicated a particle concentration of 285 × 10^3 $\mu g/m^3$. A 4800 X photomicrograph showed irregularly shaped particles with a mean diameter of 2 μm. The irregular shape of the $(NH_4)_2SO_4$ particles contrasted with the nearly spherical NH_4Cl particles.

Kinetic Determinations with Aerosol Present. All aerosol runs were performed at a system pressure of 1.5 Torr. The constant pressure was attained by first adjusting NV1 (Figure 1) so that the oxygen flowing through the discharge portion gave a system pressure of 1.0 Torr; then oxygen carrier flow through the aerosol generator was adjusted to give a total system pressure of 1.5 Torr. Atom concentrations were measured in the same way as described above.

Aerosol runs were preceded by "presol" runs and followed by "postsol" runs to monitor changes in wall recombination. The effect of possible excess NH_3, HCl, or H_2SO_4 on the oxygen disappearance kinetics was ascertained by allowing these substances to flow individually in the system.

Results and Discussion

Determination of k_{APP}. Any kinetic run yielded four data points. Each point consisted of the flow rate of NO_2 at maximum emission intensity measured as a function of distance in the flow tube. The flow tube distance was related to elapsed time of reaction through known flow rates.

Since, under the experimental conditions selected, the disappearance of oxygen atoms has been shown to follow first-order kinetics,[8] the data were treated as follows.

The NO_2 titrant flow at J1, measured in moles per second, was taken as equal to one-half the molar flow rate of atomic oxygen at $t = 0$, $[O]_0$. The flows at jets two through four, $[O]_t$, were then compared to $[O]_0$ in a ratio $[O]_t/[O]_0$, hereafter referred to as R. Slopes of plots of the natural logarithm of R (ln R) vs. elapsed time (t) were found by least-squares analysis. The negative of the slope of the straight line obtained was taken to be the rate constant for the first-order disappearance of atomic oxygen, and will be referred to as the apparent rate constant, k_{app}.

Heterogeneous Wall Recombination. Values of k_{app} (s^{-1}) were determined at several pressures for clean Pyrex walls and walls coated with either H_2SO_4, $(NH_4)_2SO_4$, or NH_4Cl. An average value of k_{app} at a given pressure was calculated using least-squares analysis, by including all the data taken at the pressure. The results for each system are shown in Table I. For a given pressure and wall treatment, the calculated value of k_{app} is listed with an error band of one standard deviation. The numbers in parentheses indicate the number of separate determinations which were made to obtain the tabulated value of k_{app}. Kaufman[8] has stated that values of k_{app} range between 1 and 5 s^{-1} for a clean Pyrex wall system. Present data are seen to fall in this range. The value of k_{app} could not be measured with an NH_4Cl wall coating. When measurements were attempted in the usual way, no glow whatsoever could be detected at J1. As atomic oxygen was generated, the NH_4Cl coating was progressively removed from the tube, beginning at the end nearest the discharge. The flow tube felt hotter in the area where NH_4Cl was disappearing. The coating did not disappear when O_2 was flowing with the discharge turned off. This indicated negligible reaction of NH_4Cl_s with O_2 and negligible sublimation of NH_4Cl_s. It was assumed that a very fast exothermic reaction was taking place between NH_4Cl and atomic oxygen. This is entirely different from wall-catalyzed recombination. No report of this reaction was found in the literature. The reaction products between atomic oxygen and NH_4Cl_s were identified from mass spectrometric analysis as NH_3, H_2O, NO, and HCl.

Values of k_{app} were resolved into component rate constants by assuming that wall recombination was the only unimolecular mode of atom recombination, and that any competing gas phase reactions were termolecular and dependent on the square of the oxygen molecule concentration. Thus, a plot of k_{app} vs. oxygen pressure squared was assumed[8,11] to yield a y intercept equal to the wall recombination rate constant, k_{wall}, as derived from

$$k_{app} = k_{wall} + 2k_{gas}[O_2]^2 \qquad (1)$$

The linearity of this plot should give an indication of whether the assumption was valid. The data from Table I were plotted with error bars of one standard deviation as shown in Figure 2. The resulting plots showed linear relationships over the pressure ranges used. Least-squares analysis provided the value of k_{wall} (y intercept) and its error indicated to one standard deviation as listed in Table II.

Variations in k_{wall} for a clean reactor, as reflected in the k_{wall} error band, can be seen in Table II. An extensive series of ESCA studies was made to account for such variation. There was no significant systematic change in surface composition of the Pyrex surface from ESCA spectra to account for these variations in k_{wall}.

TABLE I: Calculated Values of k_{app}

Pressure, Torr	k_{app}, s^{-1} clean	For wall treatment	
		H_2SO_4-coated	$(NH_4)_2SO_4$-coated
0.5		0.96 ± 0.16(5)	1.15 ± 0.14(6)
0.8	2.87 ± 0.23(3)	1.08 ± 0.17(4)	1.18 ± 0.15(6)
1.0	2.93 ± 0.11(3)	1.09 ± 0.31(6)	1.24 ± 0.18(4)
1.3	3.72 ± 0.40(3)	1.18 ± 0.22(3)	1.93 ± 0.56(3)
1.5	4.14 ± 0.53(3)		

TABLE II: Calculated Values of k_{wall} and γ for Each Wall Treatment

Wall treatment	k_{wall}, s^{-1}	$10^5\gamma$	$10^5\gamma$
Clean Pyrex	2.3 ± 0.7	5.0 ± 1.5	2[a] 3.1–4.5[b] 5.4–6.8[c]
H_2SO_4-coated	0.95 ± 0.03	2.0 ± 0.1	2.3[c]
$(NH_4)_2SO_4$-coated	0.88 ± 0.18	1.9 ± 0.4	

[a] Reference 12. [b] Reference 13. [c] Reference 14.

TABLE III: Summary of Aerosol and Postsol k_{app} Values with Calculated Values of k_{aero}

Run no.	k_{app}(aerosol), s^{-1}	k_{app}(postsol), s^{-1}	k_{aero}, s^{-1}
7-2-11A, 12	2.42	0.56	1.86
7-3-10A, 11	4.18	0.15	3.61
7-6-7A, 8	1.43	0	1.43
7-6-9A, 10	3.21	0	3.21
7-6-11A, 12	1.43	0	1.43
7-6-17A, 18	4.77	0	4.77
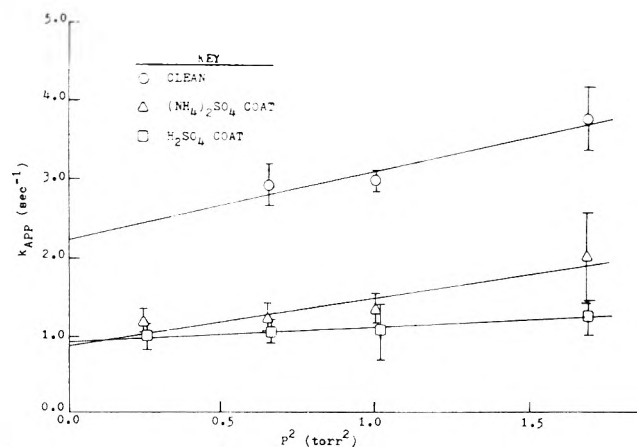
Figure 2. Plot for resolution of k_{app}.

Values of k_{wall} were then converted to recombination efficiency, γ, by

$$\gamma = k_{wall}d/\bar{v} \qquad (2)$$

where $d = 1.36$ cm, and $\bar{v} = 6.3 \times 10^4$ cm/s for atomic oxygen at 300 K. Calculated values for γ are listed in Table II for each wall treatment shown in column 1. The clean wall value represents an average of the results of five separate sets of runs. Values calculated for γ are compared to some literature values in column 4 of Table II. The value of γ on clean Pyrex and for the H_2SO_4-coated wall is seen to be in good agreement with reported values. The value of γ on the $(NH_4)_2SO_4$-coated wall is the first reported value for this

coating. This is surprising since $(NH_4)_2SO_4$ aerosol is prevalent in the stratosphere. It can be seen that H_2SO_4 significantly lowers γ and has been used as a wall coating to prolong atomic oxygen and ozone lifetimes.[14] The present work indicates that $(NH_4)_2SO_4$ may lower γ as much as H_2SO_4, and thus suggests the use of $(NH_4)_2SO_4$ as an effective and easily handled wall treatment.

Kinetic Determinations with NH$_4$Cl Aerosol Present. When initiating the plasma first, and then beginning the aerosol flow, no buildup of particles was observed. Values of k_{app} were measurable in this case and on the same order of magnitude as those measured earlier for clean wall recombination. It was therefore assumed that k_{app} values calculated on the basis of this method gave the most accurate results for estimation of the effect of the aerosol on disappearance. This method was assumed to minimize the effect of loss of oxygen atoms to reaction with excess NH_4Cl on the walls.

Values of k_{app} for no aerosol present were determined before and after aerosol runs. It was found that k_{app} for postsol runs was usually significantly lower than k_{app} for presol runs. It was assumed that some species generated during the atom–aerosol run was poisoning (deactivating) the wall toward atom recombination. It was also assumed that this poisoned wall condition was effective during the aerosol run. The rate constant for the disappearance of oxygen as influenced by the aerosol, k_{aero}, was thus assumed to be equal to the difference in k_{app} values for two consecutive runs, one run with aerosol flowing ($k_{app}^{aerosol}$) and the other run with no aerosol ($k_{app}^{postsol}$) as given by

$$k_{aero} = k_{app}^{aerosol} - k_{app}^{postsol} \tag{3}$$

Values of k_{app} are summarized in Table III. Column 1 gives the numbers of the aerosol and postsol run. The values of k_{app} for the aerosol and postsol runs are given in columns 2 and 3, and the difference, k_{aero}, is listed in column 4. The mean value calculated for k_{aero} is 2.7 ± 0.5 s^{-1} to one standard deviation. This value could not be compared as it was the first such reported value. The value of k_{aero} reflects primarily the rate of reaction between atomic oxygen and NH_4Cl. Although catalytic oxygen recombination may be taking place on the surface of the particles, it would seem to contribute only slightly to atom disappearance because of the rapid exothermic reaction shown above to occur between these species.

It was of interest to compare the value of k_{aero} to a calculated value of the rate constant upper limit for an aerosol–gas reaction. The model of Judeikis and Siegel[15] estimates the reaction rate based on the number of collisions with the surface of an aerosol particle. Equation 4 was used to calculate the value of k_{calcd}, the upper limit ($\Phi = 1$) to the rate of reaction

$$k_{calcd} = (RT/2\pi M)^{1/2}(3\Gamma W/\rho r)\Phi \tag{4}$$

where W is the mass of particles per unit volume (4.75×10^{-6} kg/m^3), ρ is the particle density (1500 kg/m^3), r is the mean particle radius (8×10^{-5} cm), M is the atomic weight of oxygen (16 g/mol), Γ is a dimensionless factor related to the particle size distribution (2), and Φ is the fraction of collisions leading to reaction. For $T = 300$ °C, the average value of k_{calcd} is 3.7 s^{-1}. This value is close to the value of

2.7 ± 0.5 s^{-1} obtained for k_{aero} (Table III). Although this agreement may be fortuitous, it indicates that this model may have merit and should be studied further. If indeed the model were adequate for describing the NH_4Cl–O system, the close agreement between the measured and the calculated rates would indicate a very high probability of reaction upon collision of an oxygen atom with an NH_4Cl particle.

Kinetic Determinations with $(NH_4)_2SO_4$ Aerosol Present. The very significant result was that there was no detectable decrease in the concentration of atomic oxygen in the presence of the $(NH_4)_2SO_4$ aerosol. Thus, k_{aero} corresponds to a just measurable decrease in atomic oxygen with the present apparatus using NO_2 titration. This result is in marked contrast to the results for the NH_4Cl aerosol where a pronounced effect of the aerosol on the rate constant was observed. The model of Judeikis and Siegel[15] was used to check again agreement with the experimental observation of a negligible value of k_{aero}. A value of k_{calcd} was calculated using eq 4, setting $W = 285 \times 10^{-6}$ kg/m^3, $\rho = 1769$ kg/m^3, $r = 1 \times 10^{-4}$ cm, $M = 16$ g/mol, $\Gamma = 2$, $\Phi = 1.9 \times 10^{-5}$, and $T = 300$ K. The value of Φ was taken as the measured wall recombination rate on a $(NH_4)_2SO_4$ coating (see Table II). The calculated value of k_{calcd} was 3×10^{-3} s^{-1} which represents a rate constant too small to produce a detectable decrease in the atomic oxygen concentration as determined by the NO_2 titration technique. Again, as was true in the case of NH_4Cl aerosol, the model of Judeikis and Siegel is in qualitative agreement with the experimental results and the model certainly merits further experimental verification. If values of γ from flow tube studies (Table II) can be substituted for Φ in eq 4, a useful technique for modeling atmospheric aerosol–gas reactions would be available.

References and Notes

(1) Supported by National Aeronautics and Space Administration Contract No. NAS1-10646-20.
(2) M. I. Ratner and J. C. G. Walker, *J. Atmos. Sci.*, **29**, 803 (1972).
(3) C. E. Junge, C. W. Chagnon, and J. E. Manson, *J. Meteorol.*, **18**, 81 (1961).
(4) S. C. Mossop, *Nature (London)*, **199**, 325 (1963).
(5) S. I. Rasool and S. H. Schneider, *Science*, **173**, 138 (1971).
(6) S. Chapman, *Q. J. R. Meteorol. Soc.*, **3**, 103 (1930).
(7) M. Nicolet, *Can. J. Chem.*, **52**, 1381 (1974).
(8) F. Kaufman, *Prog. React. Kinet.*, **1**, 1 (1961).
(9) F. Kaufman, *J. Chem. Phys.*, **28**, 352 (1958).
(10) F. Kaufman, *Proc. R. Soc. London, Ser. A*, **247**, 123 (1958).
(11) P. D. Francis, *Brit. J. Appl. Phys.*, **2**, 1717 (1969).
(12) I. R. Slagle, J. A. Samlaska, F. J. Pruss, Jr., and D. Gutman, *J. Phys. Chem.*, **78**, 208 (1974).
(13) D. Garvin, Ed., "Chemical Kinetics Data Survey IV. Preliminary Tables of Chemical Data for Modelling of the Stratosphere," National Bureau of Standards IR-203, U.S. Government Printing Office, Washington, D.C., 1973.
(14) D. J. Williams and M. F. R. Mulcahy, *Aust. J. Chem.*, **19**, 2163 (1966).
(15) H. S. Judeikis and S. Siegel, *Atmos. Environ.*, **7**, 619 (1972).

Determination of the Orientation of a Cyanine Dye on Silver Chloride and Glass Surfaces by Internal Reflection Spectroscopy

Alexander M. Yacynych,* Harry B. Mark, Jr.,

Department of Chemistry, University of Cincinnati, Cincinnati, Ohio 45221

and Charles H. Giles

Department of Pure and Applied Chemistry, University of Strathclyde, Glasgow, Scotland (Received March 27, 1975; Revised Manuscript Received January 14, 1976)

The orientation of a cyanine dye, 1,1'-diethyl-2,2'-carbocyanine bromide, on silver chloride and glass substrates was determined by internal reflection spectroscopy using parallel and perpendicularly polarized incident light. On a silver chloride substrate the cyanine dye was found to be adsorbed as a multimolecular aggregate or micelle, with the plane of the molecule perpendicular to the surface. With the glass substrate, the cyanine dye was adsorbed predominently in molecular form or small sandwich aggregates, although some also was adsorbed as large multimolecular aggregates. The adsorbed dye seemed to have no preferred orientation on glass, although the possibility of parallel orientation of the planes of the dye molecules to the surface cannot be conclusively ruled out.

Introduction

A necessary condition for optical sensitization in photography is the presence of the sensitizing dye in the adsorbed state at the surface of the silver halide grains in the photographic emulsion. Knowledge of the orientation of these adsorbed dyes could help in interpreting the mechanism of optical sensitization, which, in turn, could lead to a better understanding of the photographic process in general. We have applied an internal reflection spectroscopic technique to the direct determination of the orientation of a cyanine dye.[1,2]

Previous studies of cyanine dye adsorption on silver halides by adsorption isotherms indicated that the dye molecules form micelles or multimolecular aggregates which then adsorb with the plane of the molecule perpendicular to the silver halide surface.[3,4] This edge on adsorption was observed to occur irreversibly from aqueous solutions, and to account for this it was postulated that the polar edge of the cyanine dye molecule was adsorbed onto the silver halide surface and the nonpolar edge faced out into the aqueous solution.[3] However, similar studies on other such dyes implied that adsorption on nonionic surfaces, such as graphite, occurred with the micelles being adsorbed with the plane of the molecule parallel to the surface.[5]

The use of an adsorption isotherm is an indirect method of determining molecular orientation, in the sense that a macroscopic property of a large number of molecules is being measured. Thus, orientation cannot be unambiguously determined. Spectroscopy, on the other hand, is a direct method, as it measures a microscopic molecular property, the absorption of light, and this property can be used directly to determine molecular orientation.

Internal reflection spectroscopy is ideally suited for the study of such adsorbed layers provided the substrate of interest is optically transparent.[1,2] Sampling occurs only a couple hundred angstroms past the substrate surface, therefore, essentially only the spectrum of the first few molecular layers in contact with the substrate is obtained. In this manner, adsorbed film spectra can even be obtained in contact with the bulk solution if desired. The relative dif-

ference between the optical absorption of perpendicular and parallel polarized light by the adsorbed molecular layer is used to determine the orientation of that layer.[6] The orientation of the adsorbed cyanine dye was determined on both silver chloride and glass for comparison.

Experimental Section

A Cary Model 14 recording spectrophotometer was used to make all the measurements. An expanded scale (0–0.1, 0.1–0.2 absorbance unit) slidewire was used when determining the internal reflection spectra (IRS), and a normal scale (0–1.0, 1.0–2.0 absorbance units) slidewire was used to determine the absorption spectra. Both perpendicular and parallel polarized light were used in the IRS studies, while unpolarized light was used to obtain the absorption spectra.

A cyanine dye, 1,1'-diethyl-2,2'-carbocyanine bromide (I), film was prepared by placing one face of an optically

I
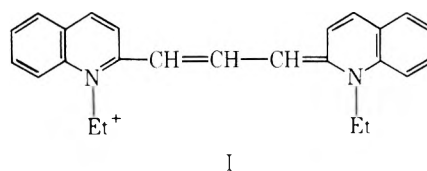
polished silver chloride plate (25 × 25 × 1 mm) in contact with an unstirred 10 mM aqueous solution of the dye for 24 h at ambient temperature. The cyanine dye was a pure sample obtained from the research laboratory of Kodak Ltd., Harrow, London, England. The silver chloride plate was then removed from the solution, dried in air, and placed in a variable angle single reflection IRS unit, and the spectra were taken employing an apparent incident angle of 45° using both perpendicular and parallel polarized light.[6] The variable angle single reflection IRS unit, shown in Figure 1, and the silver chloride plates were manufactured by Harrick Scientific Corp.[7] The silver chloride plates were used in conjunction with a truncated fused silica hemicylinder which was used as the internal reflection element in the unit.
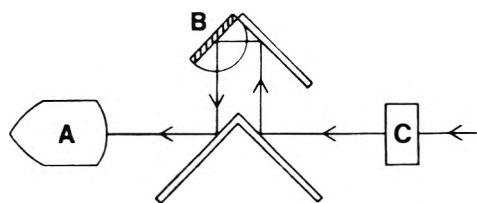
Figure 1. A variable angle single reflection IRS unit: (A) detector, (B) adsorbed dye and IRS element, (C) polarizer.

Using Snell's law.[1] the true incident angle at the AgCl–air interface is calculated to be 30.1°. This is caused by the refractive index difference between the fused silica IRS element and the silver chloride substrate. This incident angle is near the critical angle, 28.9°, of the AgCl–air interface. A cyanine dye film was also prepared on an optically polished glass plate in a similar manner. When a glass plate is used with a truncated fused silica hemicylinder internal reflection element instead of a silver chloride plate, no correction of the incident angle due to refraction is required, as the refractive indices of glass and fused silica are virtually the same. Therefore, the incident angle was 45°, which is near the critical angle, 42.9°, of the glass–air interface.

The final spectra were obtained by manually subtracting a reference or baseline spectrum from a sample spectrum. The reference spectrum was an IRS spectrum of the silver chloride or glass plate without any cyanine dye adsorbed and the sample spectrum was taken with the dye adsorbed on the substrate plate. The spectra were then subtracted to obtain only the spectrum of the adsorbed dye.

Results

All spectra were taken in the visible region of the spectrum, from 430 to 700 nm. The silver chloride plate is transparent in the visible region, but the absorbance increases sharply below 430 nm. This, of course, is expected, as uv absorption causes the photodecomposition of silver chloride.

In Figure 2, the dashed line shows the absorption spectrum of a dilute aqueous solution of the cyanine dye for reference, with its absorption maxima at 550 and 600 nm. At higher solution concentrations and from specular reflectance spectra of solids it has been reported that cyanine dyes exhibit new peaks which are probably due to the formation of multimolecular aggregates or micelles.[3,4,8]

The internal reflection spectra of the cyanine dye adsorbed on the silver chloride plate are the solid lines shown in Figure 2. The internal reflection spectrum of the adsorbed dye is quite different from the absorption spectrum, with an absorption maximum for both the perpendicular and parallel polarized spectra at 650 nm. This peak is thought to be characteristic of a multimolecular aggregate of the dye.[3,4,8] The reflection absorbance ($\Delta A_{\parallel}$ or $\Delta A_{\perp}$) differs greatly at the absorption maximum for the two modes of polarization: $\Delta A_{\parallel}$ = 0.194 and $\Delta A_{\perp}$ = 0.029 absorbance units.

The experiment was repeated using a glass plate as the substrate. As shown in Figure 3, the spectra have a broad peak at 520 nm in both modes of polarization which is similar to the solution phase spectra. There is also a small peak in each IRS spectrum at 650 nm, which is at the same wavelength as the absorption maximum for the dye adsorbed on the silver chloride. This appears to indicate that a majority of the dye is adsorbed on the glass in molecular form or small molecular aggregates and only a small
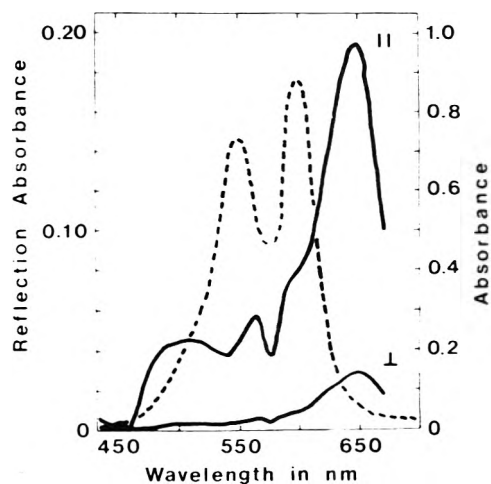
Figure 2. Absorption spectrum and internal reflection spectra of the cyanine dye adsorbed on silver chloride. The dash line shows the absorption spectrum of a 1,1'-diethyl-2,2'-carbocyanine bromide solution. A 1-cm cell was used with approximately a 1 mM aqueous solution of the dye. The solid lines are the internal reflection spectra of the same cyanine dye adsorbed on silver chloride, using parallel, $\parallel$, and perpendicularly, $\perp$, polarized light.
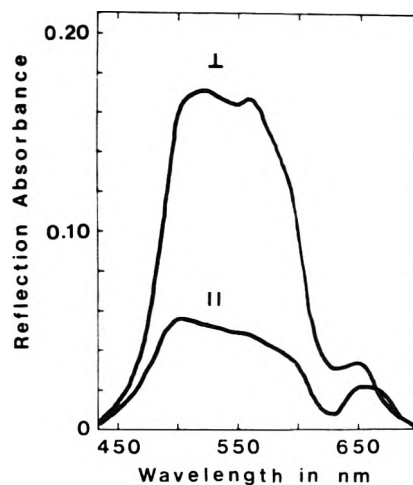
Figure 3. Internal reflection spectra of 1,1'-diethyl-2,2'-carbocyanine bromide adsorbed on glass, using parallel, $\parallel$, and perpendicularly, $\perp$, polarized light.

amount of the dye appears to be adsorbed as large multimolecular aggregates. The peak at 650 nm is not present in the absorption spectrum. The reflection absorbance at 520 nm is $\Delta A_{\parallel}$ = 0.054 and $\Delta A_{\perp}$ = 0.171 absorbance units.

Discussion

It is known that the direction of the electronic transition moment vector for a molecule dictates the plane of polarization of the absorbed radiation and, that for transitions involving the π orbitals of planar molecules, this vector is always in the plane of the molecule.[9] There are two possible orientations for the transition moment in the cyanine dye: along either the short or long in-plane axis of the molecule. The transition moment vector is difficult to determine experimentally, but in planar molecules such as naphthalene and anthracene it is calculated to be along the short in-plane axis of the molecule.[9]

Figure 4 illustrates schematically the interface in an internal reflection experiment. The mode of polarization re-
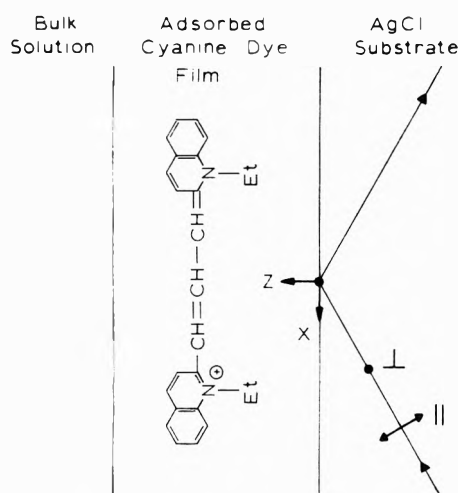
Figure 4. Schematic of the dye–AgCl interface on internal reflectance, illustrating the direction of polarization and the coordinate system used to describe the electric field vector components.

TABLE I: Optical Constants of Various Phases[a]

AgCl	Glass	Cyanine dye	Air
$n_1 = 2.07$	$n_1 = 1.46$	$n_2 = 1.60$	$n_3 = 1.00$
		$k_2 = 0.60$	

[a] "Handbook of Chemistry and Physics", 54th ed, Chemical Rubber Company, Cleveland, Ohio.

TABLE II: Values for the Ratio ($\Delta A_\parallel / \Delta A_\perp$)

Substrate	$(\Delta A_\parallel / \Delta A_\perp)_{calcd}$	$(\Delta A_\parallel / \Delta A_\perp)_{expt}$	% change from $(\Delta A_\parallel / \Delta A_\perp)_{calcd}$
Silver chloride (at 650 nm)	0.51	6.7	+1214
Glass (at 520 nm)	0.25	0.32	+28

fers to the plane formed by the incident and reflected light. Parallel polarization is in the plane of the incident and reflected light beam (the plane of the page referring to Figure 4), while perpendicular polarization is, thus, perpendicular to the plane of the page. Perpendicularly polarized light has only one electric field vector component, $\bar{E}_y$, along the y axis (following the coordinate system shown in Figure 4 where the y axis points outward), while parallel polarization has two electric field vector components, $\bar{E}_x$ and $\bar{E}_z$, oriented along the x axis and z axis, respectively.[1,2] The relative magnitudes of these electric field vector components at the interface and adsorbed layer are in the order $\bar{E}_z > \bar{E}_y > \bar{E}_x$.[1,2]

By determining the absorbance of parallel and perpendicularly polarized light by the adsorbed cyanine dye layer its orientation can be directly determined. Hansen has derived equations which are applicable to the determination of orientation of adsorbed thin films by IRS.[10] At the critical angle:

$$\Delta A_\parallel = \frac{4}{\ln 10}\left(\frac{n_1^2 n_3^2}{n_1 \cos \theta_1}\right)\frac{n_2 \alpha_2 h_2}{(n_2^2 + k_2^2)^2} \qquad (\theta_1 = \theta_c) \quad (1)$$

$$\Delta A_\perp = \frac{4}{\ln 10}\left(\frac{1}{n_1 \cos \theta_1}\right) n_2 \alpha_2 h_2 \qquad (\theta_1 = \theta_c) \quad (2)$$

where $\Delta A_\parallel$ and $\Delta A_\perp$ are the reflectance absorbance for parallel and perpendicular polarized incident light, respectively. The subscripts in each case refer to the phase or medium; phase 1, the incident phase, silver chloride or glass in this work, phase 2 being the absorbing cyanine dye film, and phase 3 being air. The refractive index is n, θ is the refractive angle in a particular phase (in the case of the incident phase, it is the incident angle), α is the absorption coefficient, k is the extinction coefficient, and h_2 is the film thickness.[6,10] The assumptions made in the derivation were: (i) that the adsorbing film is thin, less than a quarter wavelength, (ii) that the system consisted of an ideal stratified medium, i.e., parallel plane-bounded phases, and (iii) that the film is isotropic and homogeneous, i.e., a nonoriented adsorbed film. The ratio of $\Delta A_\parallel$ to $\Delta A_\perp$ is given by

$$\Delta A_\parallel / \Delta A_\perp = n_1^2 n_3^2 / (n_2^2 + k_2^2)^2 \quad (3)$$

Table I shows the values of the optical constants of various phases of the system. The optical constants for the ad-

sorbed film phase (n_2, k_2) were assumed to be approximately the same as the optical constants of dyes with structures similar to the cyanine dye. These values were estimated to be $n_2 = 1.60$ and $k_2 = 0.60$.[6]

A calculated reflectance absorbance ratio, $(\Delta A_\parallel / \Delta A_\perp)_{calcd}$, for a nonoriented thin film can be obtained by using the optical constants in Table I and eq 3, and for comparison, an experimental ratio, $(\Delta A_\parallel / \Delta A_\perp)_{expt}$, is obtained from the internal reflection spectra. Table II shows the values of both $(\Delta A_\parallel / \Delta A_\perp)_{calcd}$ and $(\Delta A_\parallel / \Delta A_\perp)_{expt}$ for the silver chloride and glass substrates.

According to Hansen, the best agreement of eq 1 and 2 with experimental data occurs in the central region of the absorption band.[10] Thus, the values for the reflection absorbance, which were used to determine $(\Delta A_\parallel / \Delta A_\perp)_{expt}$, were taken at an absorption maximum; in the case of silver chloride as the substrate, at 650 nm, and with glass as the substrate, at 520 nm. If the angle of incidence at which the experiment is performed differs greatly from the critical angle, then the more complex forms of eq 1 and 2, given in ref 10, must be used for the calculations. However, Hansen[10] has shown that for a 1 to 2° difference from the critical angle, eq 1 and 2 are applicable.

If a system obeys all assumptions, then $(\Delta A_\parallel / \Delta A_\perp)_{calcd}$ should correspond to $(\Delta A_\parallel / \Delta A_\perp)_{expt}$. If the two values differ, however, this difference can only be due to a variation in the assumption of the film being isotropic and homogeneous. If the adsorbed film is not isotropic or homogeneous, then the possibilities are that the film is preferentially adsorbed with the planes of the molecules either perpendicular or parallel to the substrate surface. The transition moment vector can be along either the short or long axis for each orientation. Of these four possibilities, only a perpendicular orientation with the transition moment along the short in-plane axis of the molecule would yield $(\Delta A_\parallel / \Delta A_\perp)_{expt}$ significantly greater than $(\Delta A_\parallel / \Delta A_\perp)_{calcd}$, as any absorption of energy would be primarily from the $\bar{E}_z$ electric field vector component which is the major component of parallel polarization. In this case, the energy of the electric field vector components $\bar{E}_x$ and $\bar{E}_y$ would not be significantly absorbed. Perpendicularly polarized light was found to be absorbed to a small extent, as all of the adsorbed molecules may not be perpendicularly oriented and/or forbidden transitions have small but finite absorbances. Of the three other adsorption orientation possibilities, none would absorb any significant amount of energy from the $\bar{E}_z$ electric field vector component and, thus, the energy

absorption would be primarily from the $\bar{E}_x$ and $\bar{E}_y$ electric field vector components. The long axis of the adsorbed molecule would not be expected to be preferentially oriented along either the x or y direction on the substrate surface, only the plane of the molecule would have a preferred orientation with respect to the substrate surface. Therefore, with the random orientation of the long axis of the molecule in the xy plane (substrate surface), the absorption of the $\bar{E}_x$ and $\bar{E}_y$ electric field vector components would be expected to be qualitatively proportional to their relative magnitudes at the interface. As $\bar{E}_y > \bar{E}_x$, then $\Delta A_\perp$ would be greater than $\Delta A_\parallel$, which could not account for $(\Delta A_\parallel / \Delta A_\perp)_{\text{expt}}$ being significantly greater than $(\Delta A_\parallel / \Delta A_\perp)_{\text{calcd}}$ (the case of the cyanine dye adsorbed on the silver chloride substrate). Therefore, it can be concluded that on the silver chloride substrate the cyanine dye is adsorbed with the plane of the molecule perpendicular to the substrate surface and with the electronic transition moment vector being along the short in-plane molecular axis. The large 650-nm peak indicates that the dye is also adsorbed as multimolecular aggregates. These aggregates are probably formed by stacking the dye molecules face-to-face with each other, with the longest axis of the whole aggregate lying lengthwise on the surface, held down by electrostatic forces from the dye cationic groups.

However, with glass as the substrate, $(\Delta A_\parallel / \Delta A_\perp)_{\text{expt}}$ is slightly but not significantly larger than the calculated value. Therefore, on glass, it seems that most aggregates are small (dimers, trimers, or tetramers of the sandwich type) and are probably randomly oriented. However, parallel orientation on the glass cannot be completely ruled out without quantitatively knowing the value of $\Delta A_\parallel / \Delta A_\perp$ for an adsorbed layer with parallel orientation. This can only be done by deriving equations for oriented adsorbed layers which are analogous to Hansen's equations for isotropic adsorbed layers. Although this IRS procedure cannot be considered to be strictly quantitative, the direct microscopic information does give an answer as to the preferred orientation and chemical nature of adsorbed films in such cases.

References and Notes

(1) N. J. Harrick, "Internal Reflection Spectroscopy", Interscience, New York, N.Y., 1967.
(2) H. B. Mark, Jr., and E. N. Randall, *Symp. Faraday Soc.*, **4**, 157 (1970).
(3) S. E. Sheppard, R. H. Lambert, and R. D. Walker, *J. Chem. Phys.*, **7**, 265 (1939).
(4) W. West, B. H. Carroll, and D. M. Whitcomb, *J. Phys. Chem.*, **56**, 1054 (1952).
(5) C. H. Giles, I. A. Easton, R. B. McKay, C. C. Patel, N. B. Shah, and D. Smith, *Trans. Faraday Soc.*, **62**, 1963 (1966).
(6) E. N. Randall, Ph.D. Thesis, University of Michigan, 1971, pp 94–97.
(7) Harrick Scientific Corp., Croton Dam Road, Box 867, Ossining, N.Y. 10562.
(8) J. A. Leermakers, B. H. Carroll, and C. J. Staud, *J. Chem. Phys.*, **5**, 878 (1937).
(9) R. Daudel, R. Lefebure, and C. Moser, "Quantum Chemistry", Interscience, New York, N.Y., 1959.
(10) W. N. Hansen, *Symp. Faraday Soc.*, **4**, 27 (1970).

Tumbling of an Adsorbed Nitroxide Using Rapid Adiabatic Passage

Colin Mailer and Brian M. Hoffman*

Department of Chemistry and Materials Research Center, Northwestern University, Evanston, Illinois 60201 (Received October 15, 1975)

In order to extend electron spin resonance (ESR) studies of the tumbling of adsorbed nitroxide free radicals into the regime of slower motions we have employed rapid adiabatic passage (RAP) dispersion methods. We report combined observations of the temperature variations of ESR absorption and RAP dispersion signals for di-*tert*-butyl nitroxide (DTBN) dissolved in *sec*-butylbenzene and for DTBN adsorbed on silica. Motion of the adsorbate is observed over a large temperature range, and the combination of ESR techniques shows that surface nitroxides exhibit a broad distribution correlation times and a range of activation energies for motion.

Introduction

An adsorbed aliphatic nitroxide provides a useful probe of the nature and strength of interactions between a catalyst surface and an adsorbate. Low-temperature electron spin resonance (ESR) spectra give information about the surface interactions of the free radical in a fixed orientation or ensemble of orientations with respect to the surface binding sites(s). Hydrogen bonding to surface hydroxyl groups has been studied, and on catalyst surfaces containing surface Al^{3+} sites, these sites were observed to complex with the nitroxide acting as a Lewis base.[1,2] At higher temperatures, further information about surface interactions was obtained by examining the motion of di-*tert*-butyl nitroxide (DTBN) adsorbed on silica and silica–alumina and interpreting the results in terms of a single correlation time for surface rotation (τ_c).

The technique employed, measurement of the separation between extremal features in the absorption-derivative ESR spectrum, is limited to correlation times $\tau_c \lesssim 10^{-7}$ s, as for longer times (slower rotation) the rigid lattice limit of the spectrum is reached. In an attempt to extend the study

of adsorbate–surface interactions into the regime of slower motions we have now employed rapid adiabatic passage (RAP) methods.[3-5] In this technique the dispersion (χ') component of the ESR signal is detected under moderate microwave saturation and with rapid magnetic field modulation at frequency ω_m. The dispersion signal is phase detected at the modulation frequency but with the reference phase adjusted 90° out-of-phase with the modulating magnetic field.

The RAP spectrum of immobilized radicals typically resembles the undifferentiated absorption envelope. Hyde and Dalton[4,5] have shown that if the nitroxides rotate fast enough to significantly change orientation during the period of one field-modulation cycle then the RAP spectrum is altered. As τ_c shortens ($0.001 < \omega_m \tau_c < 1$) the passage spectrum loses intensity between the turning points and is thus sensitive to motion. For the 100-kHz field modulation typically employed this means that RAP is useful for systems with $10^{-5} \gtrsim \tau_c \gtrsim 10^{-7}$ s, a region throughout which the ESR absorption signal remains "frozen" and thus insensitive to motion. For $\tau_c < 10^{-7}$ s, the effects of motion also become visible in the normal ESR absorption spectra.

We here report parallel observations of the temperature variations of absorption and RAP dispersion signals for the model system DTBN dissolved in sec-butylbenzene (SBB) and for DTBN adsorbed on silica. Over the large temperature range where motion is observed, the surface nitroxides do not form a homogeneous population. Contrary to our original interpretation,[2] DTBN tumbling on a silica surface appears to exhibit a broad range of correlation times and a range of activation energies for motion. However, the absorption spectra indicate a range in τ_c of only ca. tenfold over a broad temperature interval whereas RAP signals show that the range can be as much as 10^4 or more.

Experimental Section

Spectrometer. The ESR spectrometer was a Varian E-4, modified as follows. (i) A microwave bias arm[6] was added, allowing both dispersion and absorption mode measurements; (ii) the 100-kHz ESR signal was detected with a two-channel Princeton Applied Research (PAR) phase detector, allowing observation of signals either in-phase with the 100-kHz magnetic field modulation, or in quadrature; (iii) the automatic frequency control (AFC) signal was obtained from a 10-dB coupler in the cavity arm.

Samples. DTBN (Eastman) was dissolved in SBB (Aldrich Chem. Co. Milwaukee, 99+%) to 3 × 10^{-3} M and degassed by the freeze–thaw technique. DTBN vapor was adsorbed onto previously degassed (125 °C) silica gel (grades 950 and 59, Davison Grace Chem. Co.) as described.[2]

Procedure. With the bridge set to observe absorption a microwave power study was first performed. Dispersion was then observed by changing the bias arm phase by 90°,[6] and the RAP spectrum 90° out-of-phase with the 100-kHz modulation was detected in the quadrature channel of the PAR detector using the microwave power which gave maximum absorption-derivative signal height.

Results

DTBN–SBB. As the temperature was lowered the spectrum of DTBN in SBB changed smoothly from the three sharp lines of a rapidly tumbling nitroxide to the "frozen" or powder spectrum whose overall breadth is equal to twice the parallel component of the ^{14}N hyperfine splitting ($2A_N$), Figure 1A. The corresponding RAP spectrum (Fig-

DTBN/SBB
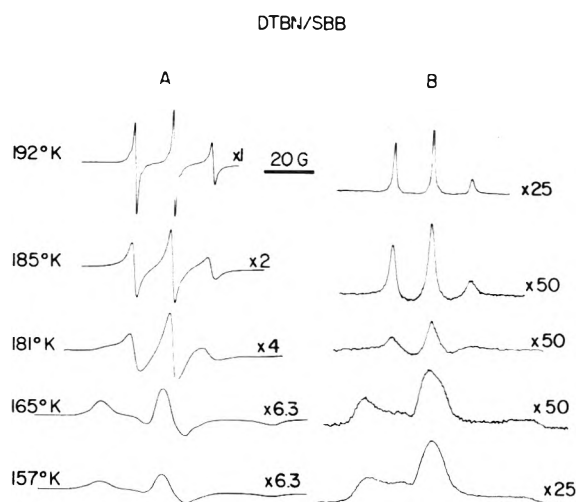
Figure 1. First derivative ESR spectra of 3 × 10^{-3} M DTBN in SBB, taken by *cooling* to the indicated temperature: microwave power ≈ 10 MW; modulation amplitude, 0.5 G at 100 kHz; relative gains as indicated: (a) absorption, (b) RAP dispersion, detected 90° out-of-phase with 100-kHz modulation (see Experimental Section).

ure 1B) also changes with decreasing temperature. The three absorption-shaped lines of differing width (room temperature) broaden and decrease in height upon cooling. By ~165 K, absorptive features, split by $2A_N$, have appeared at the turning points of the powder spectrum, with motion destroying the passage signal between turning points. As the temperature is further lowered the RAP spectrum shape attains the frozen, slow motion shape. These results are completely analogous to those of Hyde for a related nitroxide in supercooled SBB glass.[4,5]

Upon gradually rewarming a cooled sample at a temperature still below the melting point of SBB (197.8 K) the shape of the RAP spectrum underwent a sudden change and the amplitudes increased (Figures 2 and 3) in contrast to the gradual changes on cooling. We assign this abrupt transition (at 165 K in Figures 2 and 3) to a phase change from supercooled SBB glass to a polycrystalline state. The exact temperatures at which the phase change occurs is a function of the temperature history of the sample, and could easily vary by 10°.

Concomitant with this transition, all motional effects disappeared. The RAP spectrum remained strong and "frozen" up to the SBB melting point (Figure 2B). The absorption spectrum also remained frozen in shape, except near the SBB melting point, where a three-line component appears, indicating that some radicals are undergoing rapid motion.

The microwave power saturation behavior of DTBN–SBB is also of interest (Figure 4). At room temperature (295 K) the three sharp lines of the isotropic spectrum saturate identically. At 183 K, the three lines no longer saturate equally, the ease of saturation being center > low > high field. The value of T_{1e} is thus m_1 and therefore field dependent (see discussion and ref 7). At 141 K all lines again saturate similarly, but at a lower power, indicating that T_{1e} further increases with decreasing temperature. At temperatures where the field-dependent saturation is observed, the effect causes the absorption ESR spectrum to change shape as a function of microwave power (Figure 6A). In particular, the apparent splitting $2A_N'$ decreases with increasing microwave power because the wings of the
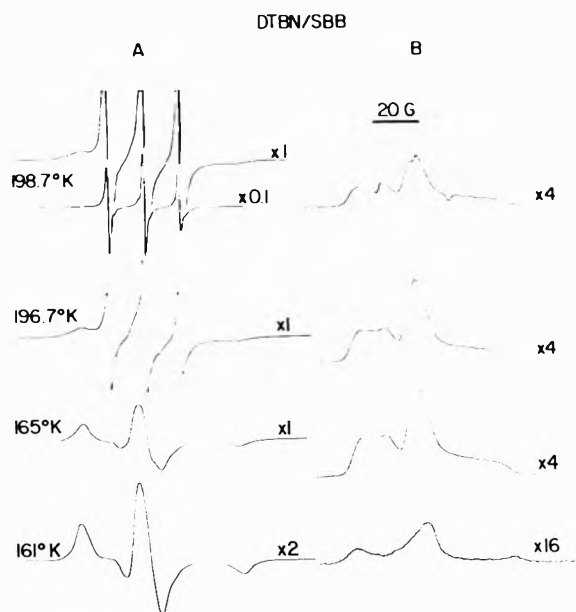
Figure 2. First derivative ESR spectra of 3 × 10⁻³ M DTBN in SBB, taken by *warming* from 161 K to indicated temperature; conditions as Figure 1: (a) absorption, (b) RAP dispersion.
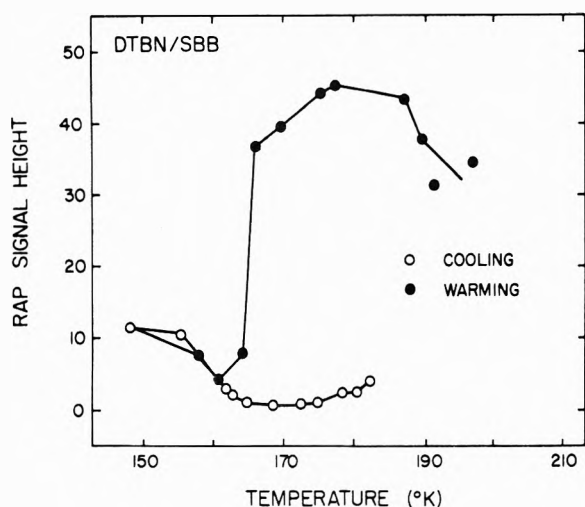
Figure 3. Maximum RAP signal height for 3 × 10⁻³ M DTBN in SBB vs. *T*, as sample was cooled (O), then rewarmed (●).

Figure 4. Microwave power study of absorption spectra 3 × 10⁻³ M DTBN in SBB at (a) 295 K, (b) 183 K, and (c) 141 K. L, M, and H are the heights of the low-field maximum center peak and high-field minimum, respectively: 0 db = 200 mW incident power.
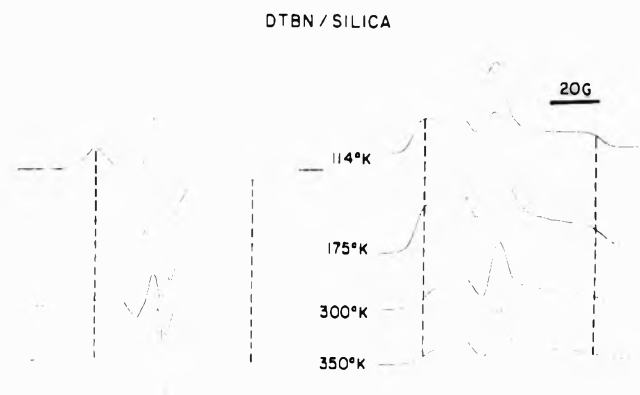
DTBN / SILICA

Figure 5. First derivative ESR spectra of DTBN–silica; conditions as in Figure 1. Dotted lines indicate outer turning points split by 2A_N: (a) absorption, (b) RAP dispersion.

spectrum saturate more readily than the center. However, note that the wings retain well-defined local maxima.

DTBN–Silica. ESR absorption spectra of DTBN adsorbed on silica are shown in Figure 5A. The increasing spread of the spectrum from 350 to 114 K is qualitatively similar to that observed upon cooling DTBN–SBB from 180 to 150 K. However, spectra of comparable width differ in details of shape. For example, the spectrum of DTBN–SBB at 181 K (Figure 1A) is significantly affected by motion, yet shows well-defined outer peaks. In contrast, DTBN–silica at 300 K (Figure 5A) shows a comparable total breadth, but outer "peaks" are broad and flat-topped, plateaus rather than sharp maxima.

The breadth of the DTBN–silica absorption signal also decreases with increasing power, but in contrast to DTBN–SBB, the inner edges of the low-power "plateau" remain, with the outer edges eroding as the power is raised (Figure 6B). Table I gives the apparent values of the extre-

mal splitting, $2A_N'$, for low (40 dB; 0.2 mW) and high (0 dB; 200 mW) incident power for the range of temperatures studied. At 114 K a powder spectrum is observed and measured $2A_N'$ is independent of power. By ~400 K the limit of isotropic motion is being approached and the effect of power is also minimal. In the broad intermediate temperature range, 150 K < T < 400 K, the apparent $2A_N'$ decreases at high incident power, the effect being quite marked between ~200 and 300 K.
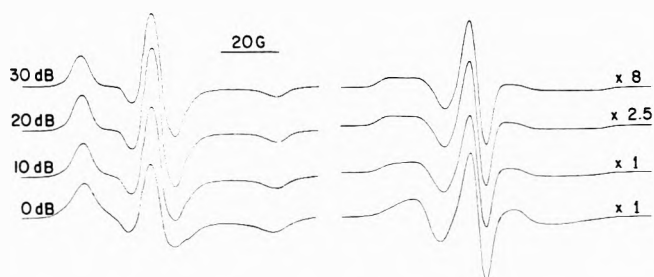
Figure 6. Power dependence of first derivative ESR absorption spectra of (A) DTBN–SBB, T = 165 K, and (B) DTBN–silica, T = 300 K. Dotted lines as in Figure 5.

TABLE I: Apparent ^{14}N Hyperfine Splitting $(2A_N')$ of DTBN–Silica at High and Low Microwave Powers

T, K	$2A_N'$, G	
	200 mW[a]	0.2 mW[a]
400	39.8	39 (39)[b]
350	44	42.3 (50)
300	45	70.8 (51.5)
260	57.5	73.5
225	66.4	75.5
200	69.5	76.5
175	72.4	77.0
145	74.5	78.0
114	76.0	77.5
77	77.0	78.8

[a] Incident microwave power. [b] Splitting in parentheses is minimum $2A_N'$ from plateau in spectra; see text.

Thus, a correlation time for DTBN–silica calculated from a measured splitting will be valid only for sufficiently low powers. Furthermore, a study carried out at fixed power may give correct values of τ_c at both low and high temperatures, yet err between. Since our previous determination[2b] of τ_c for DTBN–silica employed a fixed, relatively high power (10 dB) the results are thus quantitatively incorrect.

The RAP spectra of DTBN–silica (Figure 5B) resemble those obtained from rewarmed DTBN–SBB between the glass–crystalline transition and the SBB melting point (Figure 2B); they (i) show small intensity change with temperature, and (ii) do not show typical effects of motion. At no temperature is there a loss of signal *between* turning points (Figure 5B), in contrast with such an effect observed, for example, in DTBN–SBB cooled to 165 K (Figure 1B). This difference occurs despite the fact that the absorption signal of the surface radical is strongly indicative of motion (Figure 5A). Instead, the DTBN–silica RAP spectra at elevated temperature show a noticeable relative decrease in intensity *at* the outer turning points.

Discussion

The motional properties of a solution free radical can typically be discussed in terms of a single rotational correlation time, τ_c. The effective relaxation rate is dependent on the relative values of τ_c and the electron spin–lattice relaxation time (T_{1e}). When $\tau_c < T_{1e}$, the outer limits of the spectrum saturate less readily than the center, while when $\tau_c > T_{1e}$ the reverse occurs and the wings saturate more readily.[10] When $\tau_c < T_{1e}$ the RAP spectrum is affected by
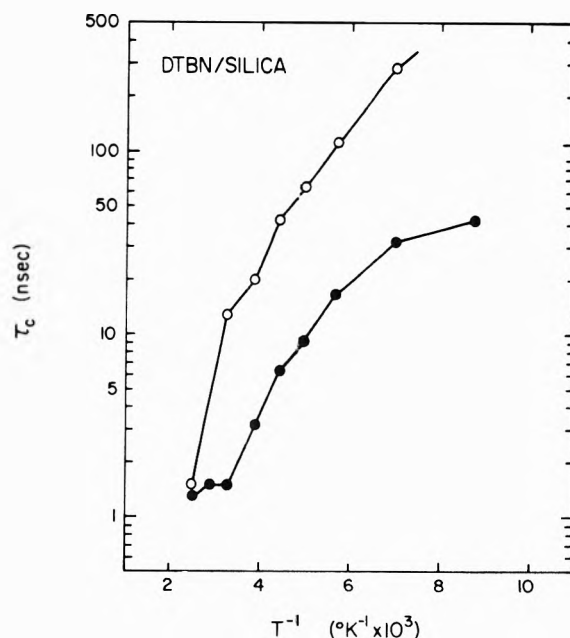
Figure 7. Longest (O) and shortest (●) correlation times (τ_c) for DTBN–silica vs. temperature, as obtained from first derivative ESR absorption spectra by method described in text.

the motion (if $\omega_m\tau_c$ is less than unity) with loss of signal intensity between turning points; when $\tau_c > T_{1e}$ the system maintains a broad "frozen" absorption envelope.[4,5] The results obtained here for DTBN–SBB confirm those of Hyde and Dalton,[4] and in so doing show that DTBN does not exhibit any special or unusual motional properties.

The results for DTBN–silica are quite different from those for a nitroxide in SBB. The saturation behavior and shape changes with microwave power and temperature all suggest that $\tau_c < T_{1e}$ while the frozen RAP dispersion spectra suggest $\tau_c > T_{1e}$. This apparent paradox can be resolved by assuming that nitroxides on a silica surface can exhibit a range of values for τ_c. At low temperature (e.g., 77 K), $\tau_c \rightarrow \infty$ and all surface nitroxides are immobile. DTBN hydrogen bonds to the silanol groups of a silica surface, as is evidenced by an increased value of $2A_N$ for DTBN–silica over that for DTBN in an inert solvent.[2]

As the temperature is raised, if nitroxides at different surface sites exhibit different activation energies for rotational motion, a distribution of τ_c will develop. Nitroxides with relatively short values of τ_c will exhibit a motionally decreased value of $2A_N'$ and will tend to dominate the ESR absorption spectra. On the other hand, as seen in the crystalline phase of DTBN–SBB, the slowly moving, long τ_c sites will dominate the RAP spectrum, causing the general features of the "frozen" spectrum to persist. Further, the relatively rapidly moving spins will contribute to the RAP spectrum in the regions of magnetic field between the turning points of the frozen spectrum. Thus, the observed decrease in relative intensity of the outer turning points as T increases is interpretable as the result of a shift in the distribution of τ_c values, a decrease in the number of spins with long τ_c (frozen spectrum), and concomitant increase in more rapidly tumbling radicals with shorter τ_c. Finally, a further, real decrease in $2A_N$ may contribute to the decrease of extremal features of the spectrum. As motional effects become pronounced, H bonding to the surface may be less able to perturb the radical and so increase A_N.

What is the nature of the distribution of τ_c? First, the

presence of a frozen RAP shape at all temperatures shows that at least some of the nitroxides are essentially immobile, having $\tau_c > \omega_m^{-1} \sim 10^{-5}$ s. Second, the outer features of the DTBN–silica ESR absorption spectra are plateaus, not the well-defined maxima of the solution system characterized by a single value of $2A_N'$ and thus a single τ_c, and probably represent the summation of spectra from radicals with a range of $2A_N'$ and thus of τ_c. The longest τ_c which significantly contributes to the ESR absorption (not the longest which occurs, for that is shown by the RAP signal to be $\tau_c > 10^{-5}$ s) is obtained from the separation between the outer edges of the plateau; the shortest τ_c of a surface nitroxide as seen in absorption can be estimated from the separation of the inner plateau edges. However, in the ordinary low power spectra, it is difficult to accurately obtain the inner separation over the whole range of temperatures, and it is easier to estimate the minimum τ_c from the splitting measured at high microwave power: the radicals with the shortest τ_c have the shortest spin–lattice relaxation time,[9] saturate least readily, and will thus tend to dominate the high-power spectra. Anomalous saturation further suppresses the wings of the spectra of radicals with longer τ_c[7] again tending to enhance the relative intensity from the radicals with the shortest τ_c. Results from the low- and high-power spectra are nevertheless in satisfactory agreement.

Table I presents the largest and smallest values of $2A_N'$ observed in the ESR absorption of DTBN–silica at various temperatures. Figure 7 shows the corresponding correlation times calculated by the method of Freed and co-workers[8] as described previously.[2] Between ~140 and ~280 K the spread in τ_c as seen in ordinary ESR can be estimated and remains roughly a factor of 10. The shortest τ_c decreases with temperature in an approximately exponential fashion, with an activation energy of $\Delta \sim 1.5$ kcal/mol. Interestingly, this value is not significantly different from that previously obtained from relatively high power spectra.[2] However, at a given temperature, the *combination* of RAP and ordinary ESR shows that the distribution of surface nitroxide correlation times extend from $\tau_c > 10^{-5}$ s to the shortest time as presented in Figure 7, a spread of almost four orders of magnitude at the higher temperatures.

Conclusion

ESR spectra of DTBN–silica at low temperature show

that the nitroxide is perturbed by hydrogen bonding to surface hydroxyls.[1,2] Although the surface silanols fall into two main classes,[10] neither the ir of a typical adsorbate (e.g., NH_3 or pyridine),[10] nor the ESR of DTBN on silica[1,2] give resolved structure indicative of surface heterogeneity. However, by combining absorption and RAP dispersion observations, the present study does show that adsorbed nitroxides can exhibit a broad distribution of rotational mobility. For example, near room temperature, RAP shows that there is a population of nitroxides which are virtually immobilized on the surface with $\tau_c > 10^{-5}$ s, while in absorption, the fastest tumbling radicals are seen to exhibit $\tau_c \sim 3 \times 10^{-9}$ s. Although the nature of the distribution function within these extremes of τ_c cannot yet be described, the relative number of radicals with long τ_c (slowly rotating) clearly grows relative to the rapidly moving, short τ_c population as the temperature decreases.

This work represents an initial attempt to extend the study of surface interactions into hitherto inaccessible regimes of molecular motion, and demonstrates that a study which combines observation of ESR absorption and RAP dispersion spectra offers significant advantages for probing the properties of adsorbed molecules. Further experiments on catalytic surfaces, such as silica/alumina, and the utilization of newly developed computer simulation techniques applicable to the slow-motion regime[11] are now in prospect.

References and Notes

(1) (a) V. I. Evreinov, V. B. Golubev, and E. V. Lunina, *Russ. J. Phys. Chem.*, **47**, 118 (1973); (b) V. I. Evreinov, E. V. Lunina, and V. B. Golubev, *ibid.*, **47**, 578 (1973).

(2) (a) G. P. Lozos and B. M. Hoffman, *J. Phys. Chem.*, **78**, 200 (1974); (b) *ibid.*, **78**, 2110 (1974).

(3) J. S. Hyde, *Phys. Rev.*, **110**, 1483 (1960).

(4) J. S. Hyde and L. Dalton, *Chem. Phys. Lett.*, **16**, 568 (1972).

(5) J. S. Hyde and D. D. Thomas, *Ann. N.Y. Acad. Sci.*, **222**, 680 (1972).

(6) J. C. M. Henning, *Rev. Sci. Instrum.*, **32**, 35 (1961).

(7) J. S. Hyde, L. E. Goran Eriksson, and A. Ehrenberg, *Biochim. Biophys. Acta*, **222**, 688 (1970).

(8) S. Goldman, G. V. Bruno, and J. H. Freed, *J. Phys. Chem.*, **76**, 1858 (1972).

(9) M. Huisjen and J. S. Hyde, *J. Chem. Phys.*, **60**, 1682 (1974).

(10) See M. L. Hair, "Infrared Spectroscopy in Surface Chemistry", Marcel Dekker, New York, N.Y., 1967.

(11) P. Coffey, B. H. Robinson, and L. R. Dalton, unpublished manuscript.

A Spectroscopic Study of the NO$_2$–N$_2$O$_4$ System by the Infrared Absorption Technique

Robert J. Nordstrom* and Walter H. Chan

Department of Physics, and the Department of Chemistry, The Ohio State University, Columbus, Ohio 43210
(Received October 24, 1975)

We report the results of a new technique for the determination of the equilibrium constant for the reactions N$_2$O$_4$ ⇌ 2NO$_2$. Fourier transform spectroscopy was used to record infrared spectra of the ν_2 band of NO$_2$ near 13.3 μ. Spectra were recorded alternately through two absorption cells of different lengths. Working within the validity of the Beer–Lambert law of absorption of radiation, an equation is derived which relates the equilibrium constant to pairs of gas pressures which give the same spectral absorbance of NO$_2$ in the two unequal cells. No knowledge of the absorption coefficient is needed using this technique. All samples were pressurized to 740 Torr with high-purity nitrogen and measurements were taken at room temperature (296 ± 1 K). Using this two cell technique, we have found K_{eq} = 0.14 ± 0.02 atm at room temperature.

I. Introduction

During the past few years, nitrogen dioxide has become the subject of an increasing number of research studies. This interest stems largely from attempts to monitor NO$_2$ effluents in the troposphere and from attempts to follow photochemical processes involving NO$_2$ both in the troposphere and in the stratosphere.[1]

Laboratory studies involving NO$_2$, however, are often compromised by the presence of dinitrogen tetroxide in the sample. This N$_2$O$_4$ interference can be eliminated either by heating the sample chamber[2,3] to dissociate the N$_2$O$_4$, or by using extremely low partial pressures of NO$_2$ to reduce the quantity of N$_2$O$_4$ to a negligible amount. Both of these techniques suffer from possible shortcomings. They force the experimenter to investigate properties of NO$_2$ in a temperature or pressure region which might not be feasible or relevant. For studies of NO$_2$ at temperatures and pressures at which N$_2$O$_4$ is present, then, it is necessary to know the equilibrium constant for the dissociation–association reactions N$_2$O$_4$ ⇌ 2NO$_2$.

This paper reports our results on the determination of this equilibrium constant. This work constitutes the preliminary steps of an investigation of gas kinetics involving NO$_2$ and other gases at room temperature, using Fourier transform spectroscopy. Our value for the equilibrium constant K is in good agreement with values previously reported. The emphasis of this paper is on the technique used to investigate the equilibrium of the system. We have developed a method using infrared spectroscopy and two absorption cells of different lengths to study the equilibrium. This method is significantly different from the method of Vosper[4] who reported the use of two absorption cells to study the equilibrium constant. Furthermore, our method differs from the infrared study of Dunn, Wark, and Agnew[3] which relied on data taken at higher temperatures for the evaluation of the equilibrium constant at room temperature. Harris and Churney[5] evaluated the equilibrium constant by observing the transmittances of the 5461-Å mercury line through a cell containing NO$_2$ + N$_2$O$_4$ at several

pressures. The equations which they developed are similar to those developed in this paper.

II. Experimental Section

The apparatus used to measure the equilibrium constant of the NO$_2$–N$_2$O$_4$ system is shown in Figure 1. Radiation from the Nernst glower is collimated and passes through the interferometer. The beam exists the interferometer and passes through one of the two absorption cells. The radiation is then focused on the Cu–Ge detector.

The output from the detector is called the interferogram and is the autocorrelation function of the electric field. This interferogram signal is digitized by the analog-to-digital converter and is stored by the computer. Our computer is a Nova 1200 minicomputer with 4K (4096) of core and 128K additional data storage on a fixed head disk. The entire apparatus including the interferometer was purchased from Digilab Inc.

Once the interferogram has been stored in the computer, it is transformed to produce the spectrum. The usable spectral region is defined by the response of the Cu–Ge detector which is from about 500 to 3500 cm^{-1}.

Both absorption cells which were used were constructed of stainless steel and were fitted with sodium chloride windows. The lengths of the cells were L_1 = 39.5 cm and L_2 = 7.5 cm, which gives a ratio L_1/L_2 = 5.27.

The NO$_2$ (+ N$_2$O$_4$) was obtained from Matheson Gas Co. Nominal purity was 99.5%. The gas was expanded into a gas handling system which was connected to the absorption cells and pressure gauges. The gas handling system was built entirely of glass and stainless steel and is fitted with Teflon stopcocks. A line sketch of this apparatus is shown in Figure 2. The gas was first collected in a liquid nitrogen cooled trap and degassed to remove any volatile impurities (NO, N$_2$O, etc.). When the cold trap was warmed to room temperature, the sample gas was expanded into an evacuated storage bulb. From this storage bulb, the gas was injected into the two sample cells simultaneously. The pressure of NO$_2$ + N$_2$O$_4$ was measured on a calibrated Wallace-Tiernan gauge and a mercury manometer both of which were isolated from the reactive gas by a glass spiral gauge, which was used as a null instrument. Pressures could be

* Address correspondence to this author at the Department of Physics, Ohio State University.
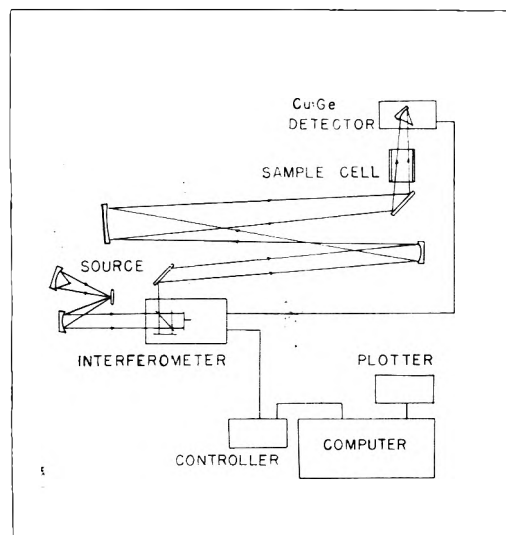
Figure 1. The experimental apparatus. Either the 7.5-cm sample cell or the 39.5-cm sample cell can be positioned in the infrared beam.
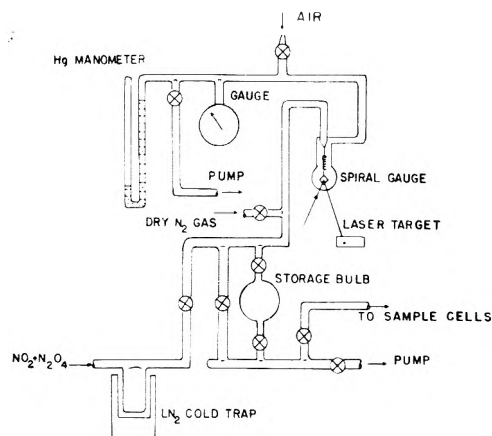
Figure 2. The gas handling system. The sample gas is injected into the storage bulb and the pressure is read on the Wallace-Tiernan gauge and mercury manometer which are isolated from the $NO_2 + N_2O_4$ by a glass spiral gauge.

measured with reasonable accuracy in a range from a few Torr to 760 Torr.

After the absorption cells were filled to the desired pressure of sample gas, the valves on the cells were closed. The $NO_2 + N_2O_4$ in the glass tubing of the gas handling system was pumped out, and the system was flushed with high-purity nitrogen gas. The valves on the absorption cells were again opened and nitrogen was injected into the cells until the total pressure in both cells was 740 Torr. The valves on the cells were finally closed and the two absorption cells were removed from the gas handling system, and each cell in turn was positioned in the optical path.

Single beam spectra were recorded through each cell. All spectra taken through the 39.5-cm cell were ratioed against a background spectrum through the same cell. Similarly, all spectra taken through the 7.5-cm cell were ratioed against a background spectrum recorded through that cell. These two background spectra were prepared by filling each absorption cell to 740 Torr with high-purity nitrogen and recording a spectrum through each cell. These background spectra were stored in the computer and could be recalled
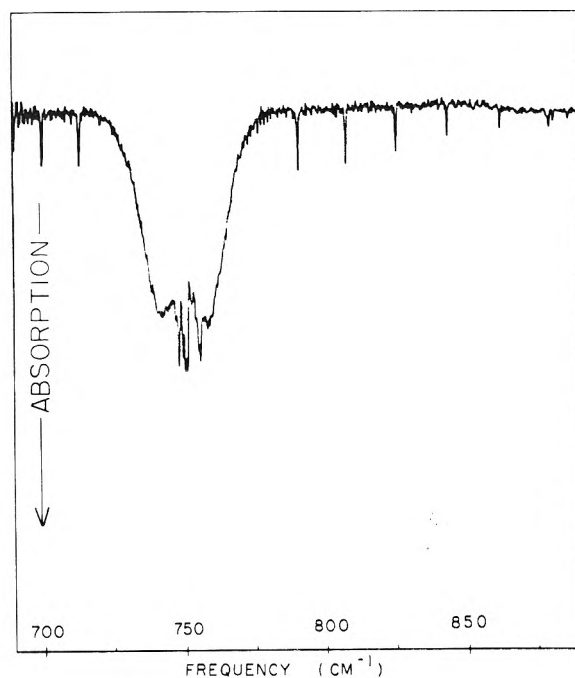
Figure 3. Transmission spectrum of $NO_2 + N_2O_4$ in the region from 700 to 900 cm^{-1}.

when needed. This ratioing procedure gave transmission spectra of $NO_2 + N_2O_4$ from which absorbance data could be obtained.

III. Theory

When radiation passes through a cell of length L which contains an absorbing gas at partial pressure p, the spectral absorbance can be written

$$A(\nu) = -\ln \{T(\nu)\} = \alpha(\nu)pL \tag{1}$$

This equation is a form of the Beer–Lambert law of absorption of radiation which includes the added assumption of the validity of the ideal gas law. Here $T(\nu)$ is the spectral transmittance at frequency ν and $\alpha(\nu)$ is the absorption coefficient. When the product of pressure times length becomes too large the approximations of the Beer–Lambert law no longer apply and the absorbance deviates from this simple linear behavior. For cells of fixed length, then, there is an upper limit to the pressure which can be used with eq 1.

The equilibrium constant for the reactions $N_2O_4 \rightleftarrows 2NO_2$ can be calculated from

$$K_{eq} = p_{NO_2}^2/p_{N_2O_4} \tag{2}$$

where p_{NO_2} and $p_{N_2O_4}$ are the partial pressures of the two gasses. Expressing the equilibrium constant in terms of the total sample gas pressure

$$p = p_{NO_2} + p_{N_2O_4} \tag{3}$$

the equilibrium constant can be written

$$K_{eq} = p_{NO_2}^2/(p - p_{NO_2}) \tag{4}$$

The only directly measurable quantity in this expression is the total gas pressure p. The partial pressure of NO_2 can be monitored indirectly by infrared absorption measurements if the absorption coefficient for NO_2 is known. If the ab-
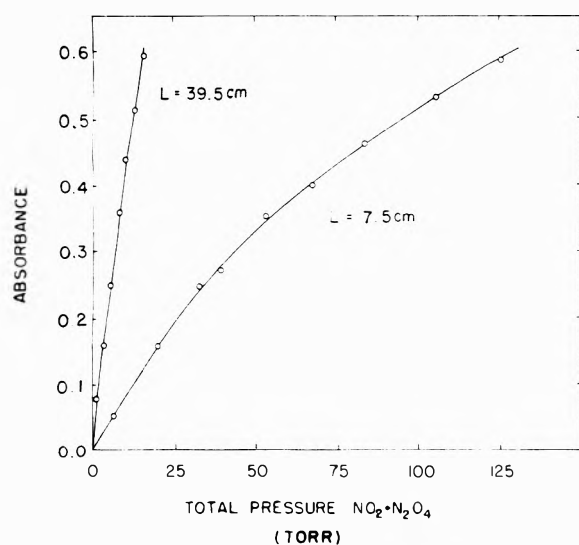
Figure 4. Plots of absorbance of the 791-cm⁻¹ NO₂ Q branch as a function of total sample gas pressure.

TABLE I: Data for the Determination of the Equilibrium Constant of the NO₂–N₂O₄ System

Approximate Q branch location (in cm⁻¹)	Spectral absorbance	P_1, Torr	P_2, Torr	K_{eq}, Torr
791	0.05	1.00	5.47	112
791	0.10	2.10	12.00	102
791	0.15	3.15	18.65	103
807	0.05	1.22	6.75	102
807	0.10	2.50	14.40	110
807	0.15	3.72	22.40	105
823	0.05	1.44	8.00	111
823	0.10	2.70	15.70	106
823	0.15	3.94	23.90	104

Av 105.7

(0.140 ± 0.020 atm)

TABLE II: Comparison of Results with Previously Reported Data

Ref	Temp, K	Equilibrium constant, atm
3	296	0.13[a]
4	273.2	0.016
5	299.7	0.1624
6	298	0.1426[b]
This work	296	0.14

[a] This number was read from graph. [b] Ignoring their correction factor for pressure variation.
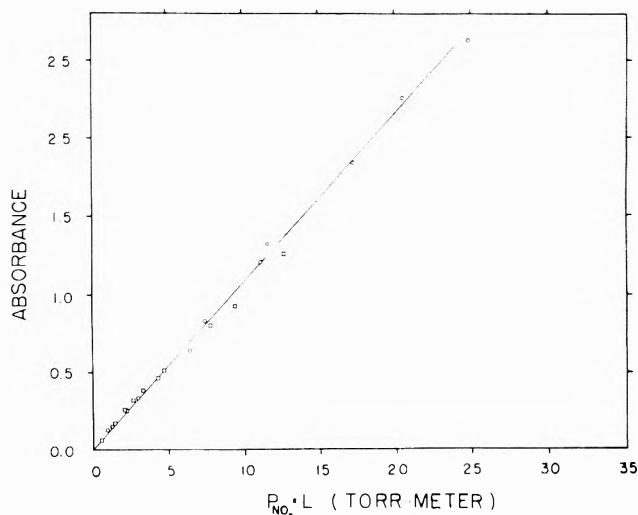
Figure 5. Plot of absorbance of the 791-cm⁻¹ NO₂ Q branch as a function of partial pressure of NO₂ times the path length. Data from the 39.5-cm cell (circles) and the 7.5-cm cell (squares) are plotted.

sorption coefficient is not known, the following method can be used.

Using two cells of different lengths, the NO₂ absorbances at a given frequency ν_0 are equal through the two cells when

$$(A_{NO_2}(\nu_0))_1 = \alpha_{NO_2}(\nu_0)(p_{NO_2})_1 L_1 =$$
$$\alpha_{NO_2}(\nu_0)(p_{NO_2})_2 L_2 = (A_{NO_2}(\nu_0))_2 \quad (5)$$

where the subscript 1 refers to the first cell and subscript 2 refers to the second cell. From eq 5

$$(p_{NO_2})_1 L_1 = (p_{NO_2})_2 L_2 \quad (6)$$

When this condition applies, the absorbances in the two cells are equal. If the slight correction due to pressure is ignored,[6] the equilibrium constant for the two cells can be written

$$K_{eq} = \frac{(p_{NO_2})_1{}^2}{p_1 - (p_{NO_2})_1} = \frac{(p_{NO_2})_2{}^2}{p_2 - (p_{NO_2})_2} \quad (7)$$

where p_1 and p_2 are the total pressures of sample gas in cell 1 and cell 2, respectively. Now, combining eq 6 and 7

$$(p_{NO_2})_1 = \frac{p_1\sigma^2 - p_2}{\sigma(\sigma - 1)} \quad (8)$$

where $\sigma = L_1/L_2$. By substituting this equation into the expression for K_{eq} in eq 7

$$K_{eq} = \frac{(p_1(\sigma)^2 - p_2)^2}{\sigma(\sigma - 1)(p_2 - \sigma p_1)} \quad (9)$$

Thus, the value of the equilibrium constant K_{eq} for the NO₂–N₂O₄ system can be determined at a single temperature by measuring the total sample gas pressures p_1 and p_2 in cells of length L_1 and L_2 which give equal absorbances.

IV. Results

The infrared absorption band of NO₂ which was chosen to study the equilibrium constant expressed in eq 9 was the ν_2 band near 13.3 μ. Only the abundant isotope ¹⁴N¹⁶O₂ was investigated.[2] This band is partially overlapped by the ν_{12} band of N₂O₄. Figure 3 shows a spectrum of this region recorded through the 7.5-cm cell at a nominal resolution of 0.5 cm⁻¹. The pressure of NO₂ + N₂O₄ was 12 Torr and the

cell was filled with nitrogen to 740 Torr. The regularly spaced absorption spikes are due to NO₂ Q-branch transitions, while the broad central feature is mostly due to N₂O₄ and partially due to NO₂.

All spectra were recorded at 0.5-cm⁻¹ resolution. The absorbance at several NO₂ Q-branch center frequencies were chosen as monitors of the NO₂ concentration. Although peak absorbance in a spectrum is dependent on the resolution used to record the spectrum, nevertheless the peak absorbance provides an unambiguous measure of concentration of all spectra which are recorded at the same resolution.

From the recorded spectra, the absorbances of the NO_2 Q-branches near 791, 807, and 823 cm^{-1} were measured. Plots of the absorbances as a function of sample gas pressure in both cells were made. Figure 4 shows absorbance plots for the 791-cm^{-1} Q-branch through the 7.5-cm cell and the 39.5-cm cell. Using these plots and similar plots for the other Q-branch absorbances, a pair of pressures p_1 and p_2 can be determined for any chosen absorbance of a particular Q branch. From these pressures, values of the equilibrium constant were calculated using eq 9. A region of linear dependence of absorbance on pressure is not apparent in these plots because the independent variable is the total sample gas pressure, not the NO_2 partial pressure. The absorbance values used to calculate the equilibrium constant were chosen to be sufficiently small to assure that we were well within the pressure limits defined by the validity of the Beer–Lambert law of both cells.

Table I shows the results of these calculations for the three NO_2 Q branches which were studied. The average of the calculated equilibrium constants is 0.140 atm at 296 $\pm$ 1 K and is in good agreement with values reported previously.

V. Conclusions

The results in Table I show that the two cell technique provides a reasonable method for the determination of the equilibrium constant for the NO_2–N_2O_4 system. Using the average value of the equilibrium constant determined by this technique, the partial pressure of NO_2 can be evaluated. Plotting the absorbance of each Q branch vs. the product $p_{NO_2}L$ for both cells shows a linear dependence. The linear region extends well beyond the largest values of

absorbance used in Table II to evaluate K_{eq}. This indicates that the data were recorded within the limits of the validity of the Beer–Lambert law. Figure 5 shows the dependence of the 791 Q-branch absorbance on the product $p_{NO_2}L$.

Error treatment suggests that a theoretical error of about 15% is expected with this technique. This error is based on an estimate of a 1% error in measuring the pressure. Thus, by this technique, we estimate the value of the equilibrium constant for the reactions $N_2O_4 \rightleftharpoons 2NO_2$ at room temperature to be 0.14 $\pm$ 0.02 atm. Table II shows a comparison of this result with previously reported values. The value of Harris and Churney[5] is their data taken closest to 296 K.

This two cell technique provides a reasonably accurate method for determining the equilibrium constant of a two component system. A variation of this method would be to use a single multiple-traversal cell and record spectra of various concentrations of sample at several different path lengths. These data could be used with eq 9 to make the equilibrium determination.

References and Notes

(1) J-C. Fontanella, A. Girard, L. Gramont, and N. Louisnard, *Appl. Opt.*, **14**, 825 (1975).
(2) S. Hurlock, K. Narahari Rao, L. A. Weller, and P. K. L. Yin, *J. Mol. Spectrosc.*, **48**, 372 (1973).
(3) M. G. Dunn, K. Wark, Jr., and J. T. Agnew, *J. Chem. Phys.*, **3**, 2445 (1962).
(4) A. J. Vosper, *J. Chem. Soc. A*, 625 (1970).
(5) L. Harris and K. L. Churney, *J. Chem. Phys.*, **47**, 1703 (1967).
(6) F. H. Verhoek and F. Daniels, *J. Am. Chem. Soc.*, **53**, 1250 (1931).

Spectroscopic Studies of Ionic Association in Propylene Carbonate

Howard L. Yeager* and Henry Reid

Department of Chemistry, The University of Calgary, Calgary, Alberta, Canada T2N 1N4 (Received July 13, 1975; Revised Manuscript Received January 13, 1976)

Far-infrared and ^{19}F NMR spectroscopic techniques have been used to study lithium, sodium, potassium, and rubidium trifluoroacetates in propylene carbonate solutions. NMR results indicate that simple ion pairing predominates for the potassium and rubidium salts but that ion aggregation occurs for the lithium and sodium salts. The far-infrared cation solvation bands for the alkali metal trifluoroacetates are shifted from the corresponding nitrate and perchlorate salt band positions, the lithium ion band to lower frequency, and the other bands to higher frequencies. Plots of integrated absorbance vs. concentration for the lithium and sodium salts are linear. Results of the two techniques are compared, and the utility of the far-infrared method as a tool for studying ion association is discussed.

Introduction

A number of investigators have used far-infrared spectroscopy to study alkali metal ion solvation in a variety of solvents.[1-5] The main features of this approach have been discussed by Edgell.[6] Alkali metal ions in solution exhibit

broad absorption bands in the far-infrared region corresponding to their vibration with adjacent solution species. Band positions depend upon the alkali metal ion and solvent used, but generally do not depend on the anion of the salt. However, for solvents which have poor donor properties or low dielectric constants, the band positions may also

show anion dependence. This behavior is explained by assuming that the anion penetrates into the inner solvation shell of the cation. In these cases, a general trend of decreasing band frequency with decreasing anion size (and presumably increasing association) for a given alkali metal ion is found. The variation of absorbance with concentration of these bands has also been measured in several solvents. Linear dependence is found in all cases, even those in which ion pairing is suggested, as for NaCo(CO)$_4$ in tetrahydrofuran.[1b] Edgell concludes from the results of infrared and Raman studies[6,7] of this system that the salt exists as both contact and solvent-separated ion pairs in THF. Both of these species would exhibit far-infrared cation vibration bands, presumably of similar frequency. Since the relative amounts of the two types of ion pairs do not vary with concentration, the linear absorbance–concentration dependence is expected.

The reason for band shifts to lower frequencies with increasing ion association is not well understood, however. Also, relative band positions for the same salts in different solvents are not always identical. For example, absorption frequencies for lithium salts in THF[1b] decrease in the order $BPh_4^- > NO_3^- > Cl^- > Br^- > I^-$ while in acetone[2c] the order is $BPh_4^- > NO_3^- > I^- > Br^- > Cl^-$. We sought to explore these problems by studying a series of salts with widely differing extents of ion association, the alkali metal trifluoroacetates in the solvent propylene carbonate.

Propylene carbonate (PC) has a high dielectric constant (64.92 at 25 °C)[8] but only moderate donor ability. Electrolytic conductance studies have shown that alkali metal perchlorates in dilute solution are unassociated while the corresponding trifluoroacetates all show ion pairing.[9,10] Association constants for the trifluoroacetate salts in PC are: Li$^+$, 1900; Na$^+$, 190; K$^+$, 42; Rb$^+$, 26; and Cs$^+$, 18 M^{-1}.[10] Evidence of extensive ion aggregation for the lithium salt, even in dilute solution, was found. The possibility of slight ion aggregation for the sodium salt was also suspected. Thus, association constants vary by two orders of magnitude for this series of salts, providing a good opportunity for studying the influence of ion pairing and ion aggregation on the far-infrared cation solvation bands. Therefore the spectra of these salts in PC were measured and are compared to the results of similar measurements by Popov and coworkers on the alkali metal perchlorates and nitrates in PC.[2g] In addition, the ^{19}F NMR spectra of PC solutions of the trifluoroacetates were measured as a function of concentration in order to provide a complimentary spectroscopic probe of these solutions.

Experimental Section

The preparation, purification, and analysis of the alkali metal trifluoroacetates have been described previously.[10] The purification and analysis of propylene carbonate have also been described.[9] All solution preparation and transfer operations were performed in a glovebox under N$_2$ atmosphere.

Far-infrared spectra were recorded using a Digilab FTS-16 Fourier transform spectrometer. Spectral measurements in the 600–200 and 450–80-cm^{-1} ranges were made with 3 and 6-μ mylar beam splitters, respectively. Standard demountable cells (Barnes Engineering) of 0.1-mm pathlength and polyethylene windows were used. With the instrument being operated in the single beam mode, a spectrum of the pure solvent was first recorded and stored in the computer and then subtracted from the spectrum of

TABLE I: Frequencies of Cation Solvation Bands in Propylene Carbonate (cm^{-1})^a

Anions	Cations				
	Li$^+$	Na$^+$	K$^+$	Rb$^+$	Cs$^+$
ClO$_4^-$	398 ± 4 (397 ± 4)	183 ± 4 (186 ± 4)	b	b	b
NO$_3^-$	(401 ± 6)	(188 ± 4)	(144 ± 6)	(115 ± 6)	(112 ± 6)
CF$_3$CO$_2^-$	367 ± 3	196 ± 4	159 ± 6	118 ± 8	b

^{a} The numbers in parentheses are those of ref 2g. ^{b} Insufficient solubility.
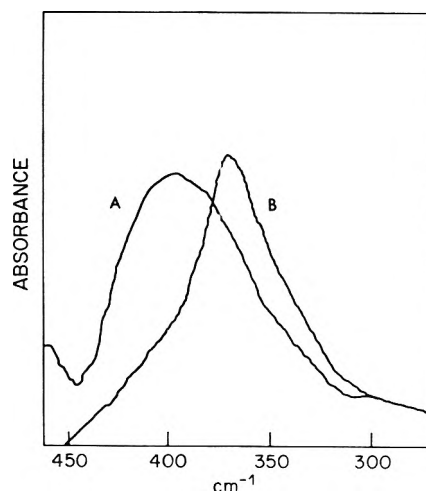
Figure 1. Cation solvation bands in propylene carbonate: (A) LiClO$_4$; (B) LiCF$_3$CO$_2$.
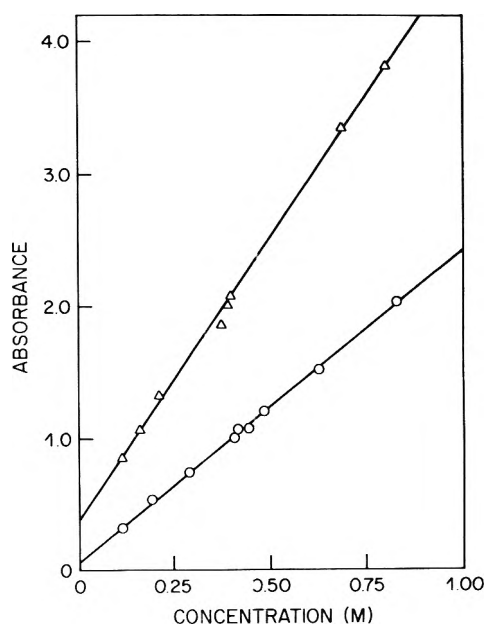
Figure 2. Integrated absorbance vs. concentration of cation solvation bonds in propylene carbonate: (O) LiCF$_3$CO$_2$; (Δ) NaCF$_3$CO$_2$.

the solution. ^{19}F NMR spectra were recorded using a modified Varian HA-100 spectrometer, with trifluoroacetic acid (Eastman Kodak) as external reference.
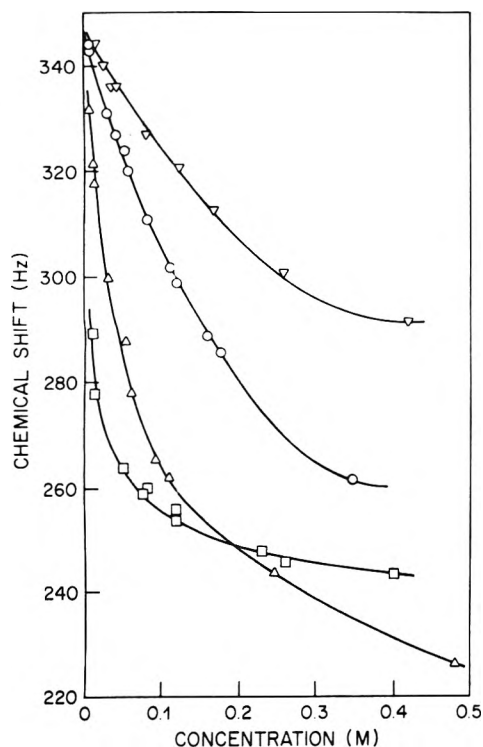
Figure 3. [19]F chemical shift vs. concentration for alkali metal trifluoroacetates in propylene carbonate: (□) $LiCF_3CO_2$; (△) $NaCF_3CO_2$; (○) KCF_3CO_2; (▽) $RbCF_3CO_2$.

Figure 4. ^{19}F NMR plots of eq 2 for lithium and rubidium trifluoroacetate in propylene carbonate.

Results

The frequencies of solvation bands in PC for the alkali metal trifluoroacetates and lithium and sodium perchlorate are shown in Table I. Cesium trifluoroacetate had insufficient solubility for an accurate determination of its band position. Values in parentheses are those of Popov and coworkers.[2g] The nitrate and perchlorate salts are listed to show the alkali metal ion band positions for salts where contact ion pairing is expected to be minimal. The lithium trifluoroacetate peak shifts to lower frequency, the sodium and potassium bands shift to higher frequencies, and the rubidium band remains essentially unchanged in position from the corresponding nitrate and perchlorate bands. The trifluoroacetate band contours are broad and similar to those observed in other solvents, with the exception of the lithium salt. This band is noticeably narrower, as shown in Figure 1, in comparison to the lithium perchlorate band. Plots of integrated absorbance vs. concentration for lithium and sodium trifluoroacetate in PC are shown in Figure 2. The dependence is linear within experimental error in each case.

A sharp band which can be assigned to a $-CCF_3$ out-of-plane rock[11] was observed in all spectra. The band position for lithium, sodium, potassium, and rubidium trifluoroacetate solutions was 279 ± 2, 272 ± 2, 267 ± 2, and 266 ± 2 cm^{-1}, respectively.

The results of ^{19}F NMR concentration studies for these salts in PC are shown in Figure 3. Pronounced deshielding of fluorine in the trifluoroacetate ion with increasing concentration is observed for all salts. The relative magnitudes of shift are in the same order as the respective ion association constants, with the exception of lithium trifluoroacetate at high concentrations. In order to test the ability of the ion association constants to quantitatively describe the

concentration dependences of the shifts, the data were analyzed using the equation

$$\delta_{obsd} = \chi_f \delta_f + \chi_p \delta_p \qquad (1)$$

where the observed chemical shift, δ_{obsd}, is related to the chemical shifts of free and ion-paired trifluoroacetate ions, δ_f and δ_p, and the respective fractions of total trifluoroacetate present as each species, χ_f and χ_p. This equation assumes rapid exchange between the two ion environments compared to the NMR time scale and neglects the presence of ionic aggregates. Eq 1 may be rearranged to

$$\frac{\delta_{obsd}}{\chi_p} = \frac{\chi_f}{\chi_p}\delta_f + \delta_p \qquad (2)$$

so that a plot of δ_{obsd}/χ_p vs. χ_f/χ_p yields δ_f and δ_p as the slope and intercept, respectively. The fractions were calculated using the ion association constants determined in ref 10; activity corrections were applied. The resulting plots for the lithium and rubidium salts are shown in Figure 4.

Both the potassium and rubidium plots were linear throughout the concentration range studied, but the lithium and to a lesser extent the sodium plots showed curvature at higher concentrations. These deviations are probably due to ion aggregation and cast doubt on using eq 2 for the lithium and sodium salt data. Least-squares results for potassium and rubidium trifluoroacetate along with standard deviations for each parameter are listed in Table II. The straight line portions of the lithium and sodium trifluoroacetate plots were used to graphically obtain values of δ_f and δ_p. These values are also listed in Table II for comparison.

TABLE II: Limiting ^{19}F NMR Chemical Shifts of Trifluoroacetate Ion in Propylene Carbonate (Hz)[a]

Salt	δ_f	δ_p
$LiCF_3CO_2$	397	246
$NaCF_3CO_2$	388	242
KCF_3CO_2	368 ± 3	242 ± 10
$RbCF_3CO_2$	367 ± 3	253 ± 8

[a] Values are referenced to external trifluoroacetic acid.

Discussion

In order to interpret the results of the far-infrared study, the prominent solution species for each salt must be identified. Dilute solution conductance measurements[10] support

the ^{19}F NMR results for potassium and rubidium trifluoroacetates, indicating that free ions and ion pairs are the only species present at concentrations up to 0.5 M. Extensive ion aggregation is indicated by both techniques for lithium trifluoroacetate. The sodium trifluoroacetate results suggest that although ion pairs predominate at low concentration, ion aggregation becomes important in the concentration region in which far-infrared measurements have been made. The deshielding of fluorine in trifluoroacetate at high concentration is greater for sodium than for the lithium salt, perhaps indicating the relative extents of ion aggregation. The trifluoroacetate ion probably exists in large ion clusters with lithium ion but only in smaller clusters with sodium ion. The net deshielding of fluorine may be less pronounced in larger ionic aggregates, yielding the observed concentration dependence shown in Figure 3. Nevertheless, both lithium and sodium trifluoroacetate show evidence of ion aggregation at concentrations above 0.1 M.

The δ_f values obtained for each salt would be expected to be equal if eq 1 properly described each system. Also, δ_p values should shift to lower field with increasing charge density of alkali metal ion. Although these expectations are consistent with the potassium and rubidium results, there is no such consistency with the lithium and sodium values, again suggesting additional solution species for these systems.

The far-infrared results also indicate association for each of the salts in PC. Edgell has concluded that when alkali metal ion solvation bands shift with the anion used, contact ion pairs are present in solution. (Solvent-separated ion pairs are expected to show the same absorption band as a free solvated cation.)[6] Lithium, sodium, and potassium trifluoroacetate all show such shifts, reflecting anion–cation contact. However, neither the magnitudes nor the directions of the shifts can be simply related to the extent of association. The highly aggregated lithium trifluoroacetate shifts to lower frequency while the aggregated sodium salt, along with potassium trifluoroacetate, shift to higher frequency. The uncertainties in these band positions are due to their broadness, but we believe the shifts are real and reflect the cation environment in the associated species.

When anion-induced shifts have been found for these alkali metal solvation bands in other solvents, they are to lower frequency and become larger with increasing anion charge density. Therefore the contact ion pair species is identified with a low-frequency component of the band. This may be due to an effective increase in the mass of the vibrating species, as would occur if the anion partially vibrates (or oscillates)[12] in phase with the cation. Since a contact pair has no net charge, the force constant in this interaction would be predominately due to dipole–dipole rather than ion–dipole forces. Both of these factors would generate a low-frequency component to the cation solvation band. The shift to higher frequency for sodium and potassium trifluoroacetate in PC may be due to a different behavior of the anion in the associated species. The metal

ion would be expected to be in close contact with the carboxylate function of the trifluoroacetate ion. This carboxylate grouping may be able to induce a localized ion–ion vibration component to the band which is not present with anions of more spherically symmetrical charge density. This would give rise to an overall band shift to higher frequency. Lithium trifluoroacetate's shift to lower frequency contradicts this interpretation. However, lithium ion exists in large ion aggregates which may be quite different in their influence on the cation vibration than are ion pairs or even small aggregates. The narrower band contour of the lithium trifluoroacetate absorbance suggests that there is not as wide a range of cation environments in these ion aggregates as with the other salts studied.

The absorbance–concentration plots of Figure 2 were performed in order to test the ability of this approach to reveal different solution species, using the most associated salts. The linearity suggests that all cation environments have about the same molar absorptivity, and that such plots are not an effective method for determining the number or character of cation environments in solution.

It appears that shifts in far-infrared cation solvation bands are a function not only of anion penetration into the cation solvation shell but also of the structure and charge distribution in the ion pair or ion aggregate. Studies with additional anions should help to identify the specific factors which determine these shifts.

References and Notes

(1) (a) W. F. Edgell, A. T. Watts, J. Lyford, IV, and W. Risen, Jr., *J. Am. Chem. Soc.*, **88**, 1815 (1966); (b) W. F. Edgell, J Lyford, IV, R. Wright, W Risen, Jr., and A. Watts, *ibid.*, **92**, 2240 (1970).

(2) (a) B. W Maxey and A I. Popov, *J. Am. Chem. Soc.*, **89**, 2230 (1967); **91**, 20 (1969); (b) J. L. Wuepper and A. I. Popov, *ibid.*, **91**, 4352 (1969); **92**, 1493 (1970); (c) M. K. Wong, W. J. McKinney, and A. I. Popov, *J. Phys. Chem.*, **75**, 56 (1971); (d) W. J. McKinney and A. I. Popov, *ibid.*, **74**, 535 (1970); (e) M. K. Wong and A. I. Popov, *J. Inorg. Nucl. Chem.*, **33**, 1203 (1971); (f) P. R. Handy and A. I. Popov, *Spectrochim. Acta, Sect. A*, **28**, 1545 (1972); (g) M. S. Greenberg, D. M. Weid, and A. I. Popov, *ibid.*, **29**, 1927 (1973).

(3) (a) A. T. Tsatsas and W. M. Risen, Jr., *J. Am. Chem. Soc.*, **92**, 1789 (1970); (b) A. T. Tsatsas, R. W. Stearns, and W. M. Risen, Jr., *ibid.*, **94**, 5247 (1972).

(4) T. L. Buxton and J. A. Caruso, *J. Phys. Chem.*, **77**, 1882 (1973).

(5) (a) A. Regis and J. Corset, *J. Chim. Phys. Physiochem. Biol.*, **69**, 1508 (1972); (b) *Can. J. Chem.*, **51**, 3577 (1973).

(6) W. F. Edgell in "Ions and Ion Pairs in Organic Reactions", Vol. 1, M. Szwarc, Ed., Wiley, New York, N Y., 1972, Chapter 4.

(7) (a) W. F. Edgell, M. T. Yang, and N. Koizumi, *J. Am. Chem. Soc.*, **87**, 2563 (1965); (b) W. F. Edgell, J. Lyford, IV, A. Barbetta, and C. I. Jose, *ibid.*, **93**, 6403 (1971); (c) W. F. Edgell and J. Lyford, IV, *ibid.*, **93**, 6407 (1971).

(8) R. Payne and I. E Theodorou, *J. Phys. Chem.*, **76**, 2892 (1972).

(9) M. L. Jansen and H. L. Yeager, *J. Phys. Chem.*, **77**, 3089 (1973).

(10) M. L. Jansen and H. L. Yeager, *J. Phys. Chem.*, **78**, 1380 (1974).

(11) M. J. Baillie, D. H. Brown, K. C. Moss, and D. W. A. Sharp, *J. Chem. Soc. A*, 3110 (1968).

(12) W. F. Edgell and A. Barbetta, *J. Am. Chem. Soc.*, **96**, 415 (1974).

Radical Yields in Irradiated Methanol and Ethanol.
An Electron Spin Resonance and Spin Trapping Method[1]

Frederick Peter Sargent* and Edward Michael Gardy

Research Chemistry Branch, Atomic Energy of Canada Limited, Whiteshell Nuclear Research Establishment, Pinawa, Manitoba, R0E 1L0, Canada   (Received January 7, 1976)

The use of spin trapping to measure the yields of radicals in radiation chemistry is reviewed and its application to electron irradiated methanol and ethanol described. Solutions of nitroso-*tert*-butane in alcohols were cooled and passed continuously through the ESR spectrometer where they were irradiated with 3-MeV electrons. The relative yields of the alkoxy and hydroxyalkyl radicals were determined by double integration of the ESR spectra of the nitroxides resulting from spin trapping R· + t-BuNO → t-Bu-N(O·)-R. The ratio of hydroxyalkyl to alkoxy radicals was found to be 0.4 for both liquid methanol and ethanol.

Introduction

The yields of radicals formed in the radiolysis of alcohols have been studied extensively.[1] However, these have been based on final product yields and the effects of various additives. The measurement of yields of primary radicals has not been possible due to complicating secondary reactions. For example, in γ-irradiated methanol, the G value for $\dot{C}H_2OH$ is 2.7 as derived from scavenger experiments.[2] However, as pointed out by Baxendale and Wardman,[1c] this yield may be almost completely formed from reactions of the methoxy radical, $CH_3O\cdot$, with methanol. The yield of this radical has been determined as 2.5, 2.0 of which escape from the spur.[3]

In principle, electron spin resonance (ESR) could be used to measure the relative yields of $CH_3O\cdot$ and $\dot{C}H_2OH$ in irradiated methanol. However, in a recent study of the ESR spectra directly observed during radiolysis of liquid alcohols, we were able to detect only the hydroxyalkyl radicals.[4] The failure to detect alkoxy radicals is not too surprising since their lifetime is short[3] and it is probable that their ESR spectra are very broad and consequently very weak. The latter is because, like OH, these radicals will have an orbitally degenerate ground state which leads, by spin–orbit coupling, to very short relaxation times and therefore broad ESR lines. This makes their detection by ESR very difficult and probably impossible. However, alkoxy radicals can be made visible to ESR by means of the spin trapping technique.[5,6] This involves the addition of a radical R· to a nitroso or nitrone compound to produce a stable nitroxide with an ESR spectrum characteristic of R·. Wargon and Williams[7] used this technique to detect the radicals formed in γ-irradiated liquid methanol with nitroso-*tert*-butane as the trapping agent.

$$t\text{-BuNO} + R\cdot \longrightarrow t\text{-Bu}-\underset{\underset{O\cdot}{|}}{N}-R \qquad (1)$$
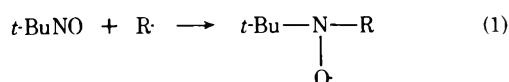
They found, at low concentrations of t-BuNO, nitroxides resulting from trapping of both CH_3O and $\cdot CH_2OH$ but at higher concentrations only $CH_3O\cdot$ was trapped.

$$CH_3O\cdot + CH_3OH \longrightarrow \dot{C}H_2OH + CH_3OH \qquad (2)$$

$$\dot{C}H_2OH + t\text{-BuNO} \longrightarrow t\text{-Bu}-\underset{\underset{O\cdot}{|}}{N}-CH_2OH \qquad (3)$$

$$1$$

$$CH_3O\cdot + t\text{-BuNO} \longrightarrow t\text{-Bu}-\underset{\underset{O\cdot}{|}}{N}-O-CH_3 \qquad (4)$$

$$2$$
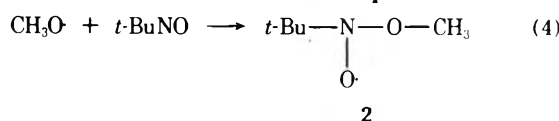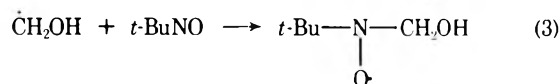
This suggested that $\dot{C}H_2OH$ arises solely from secondary reactions of $CH_3O\cdot$ and that the primary cation CH_3OH^+ formed in the radiolysis fragments to give only $CH_3O\cdot$. This is quite different from the methanol vapor radiolysis in the mass spectrometer where it has been shown that both $CH_3O\cdot$ and $\dot{C}H_2OH$ are formed.[8] However, Sargent et al.[9] showed that when methanolic solutions of t-BuNO were irradiated in the ESR spectrometer and the spectra recorded during radiolysis, both $\dot{C}H_2OH$ and CH_3O were trapped. The discrepancy between the direct and indirect observations was shown to be due to the relative stabilities of the nitroxides formed. It was shown that nitroxide 1, which results from trapping of $\dot{C}H_2OH$, decays to a low level in about 20 s at −80 °C. The direct observations showed that the yields of $CH_3O\cdot$ and $\dot{C}H_2OH$ were approximately of the same order of magnitude and Mao and Kevan came to a similar conclusion using a different trapping agent.[10] However, the conclusions of Sargent et al. were based on peak heights at one concentration rather than the total areas of the ESR spectra. We have repeated these experiments using a wide range of concentrations of t-BuNO and have monitored the relative yields of trapped $CH_3O\cdot$ and $\dot{C}H_2OH$ by performing double integration of the ESR spectra. It will be shown that the relative yield of $\dot{C}H_2OH$ is lower than previously reported and the ratio of hydroxyalkyl to alkoxy is lower than in the gas phase. Results for ethanol are also presented.

Experimental Section

The ESR spectrometer was coupled to a nominally 4-MeV electron accelerator by extending the flight tube axially into the magnet. The pole caps were fitted with a field
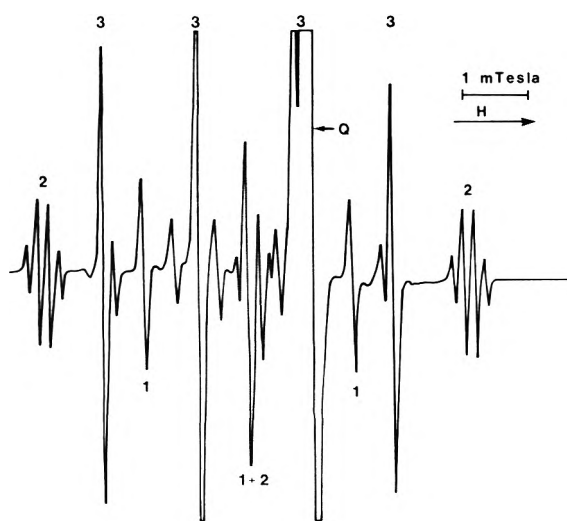
Figure 1. The ESR spectrum directly observed in 0.01 M *t*-BuNO methanol solution *during* radiolysis with 3-MeV electrons at 228 K. The ESR coupling constants in milliTesla for the nitroxides are **1**, a_N = 1.45, a_{CH_2} = 0.40; **2**, a_N = 2.96, a_{OCH_3} = 0.14; **3**, a_N = 1.35 a_H = 1.35 mT.
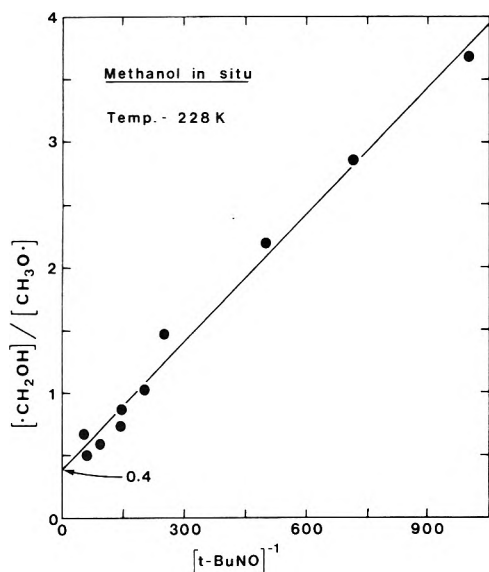
Figure 2. The ratio of yields of $\dot{C}H_2OH$ and $CH_3\dot{O}$ trapped by *t*-BuNO for in situ irradiated methanol solutions at 227 K.

compensating device to give a field homogeneity of 5 μT (50 mG) over the sample volume. The conventional T102 rectangular microwave cavity was modified to permit irradiation of the samples in situ.

Solutions of *t*-BuNO were deaerated at room temperature by bubbling with 99.999% argon. They were passed through a cooling coil and the ESR cavity where they were irradiated with a 3-MeV electrons at incident beam currents of 0.5–7 μA. Solutions were stored in the dark at room temperature for at least 30 min prior to use to allow the complete dissociation of the *t*-BuNO dimer.[11] NMR studies showed that rapid cooling of these solutions does not change the extent of *t*-BuNO dissociation in the time required for the solution to travel through the cooling coil and into the ESR cavity.

The ESR sample tubes were either high-purity synthetic quartz "flat cells" or special cells made of cerium-doped
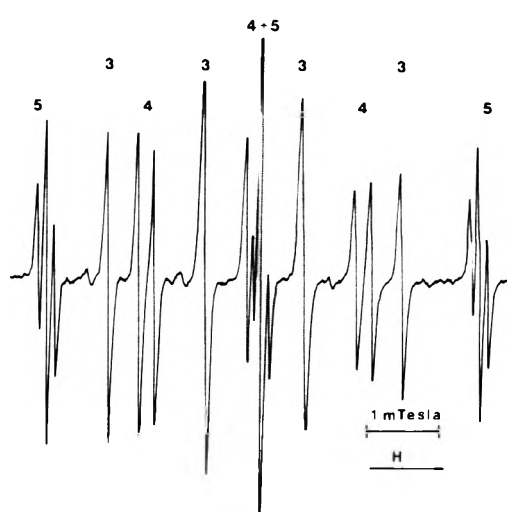
Figure 3. The ESR spectrum directly observed in 0.1 M *t*-BuNO ethanol solutions *during* radiolysis with 3-MeV electrons. The ESR coupling constants for the nitroxides are **4**, a_N = 1.45, a_H = 0.21; **5**, a_N = 2.91, a_{OCH_2} = 0.11; and *t*-BuNHO, a_N = A_H = 1.32 mT.

glass. The latter have the advantage of not giving a radiation induced glass signal. Nitroso-*tert*-butane was prepared by oxidation of *tert*-butylamine using the method of Stowell[11] and then recrystallized from *n*-pentane and stored in a refrigerator. Solutions of *t*-BuNO were always prepared in the dark to prevent the formation of di-*tert*-butyl nitroxide.[12,13] Fisher certified grade methanol and anhydrous ethanol from Commercial Alcohols Ltd., Quebec, were used as received.

The ESR spectrometer was a modified Varian V-4500 using 100-kHz modulation. The magnetic field was swept electronically using a modification to the Fieldial unit similar to that described by Glarum.[14] The spectra were stored in a Nicolet 1070 signal averaging system. Double integrations were usually performed by using the Nicolet to perform the first integration followed by readout onto chart paper and final integration with a planimeter.

Results and Discussion

The ESR spectrum observed while irradiating a solution of *t*-BuNO in methanol at −50 °C is shown in Figure 1. This is a composite of spectra from three nitroxides **1**, **2**, and **3** which are derived from the trapping of $\dot{C}H_2OH$, $CH_3\dot{O}$, and electrons and/or hydrogen atoms. The latter are not distinguishable because they ultimately lead to the same nitroxide

$$e^- + t\text{-BuNO} \longrightarrow [t\text{-BuNO}]^- \qquad (5)$$

$$[t\text{-BuNO}]^- + CH_3OH \longrightarrow t\text{-BuN-H} \qquad (6)$$
$$\underset{\overset{|}{O^-}}{}$$

$$H\cdot + t\text{-BuNO} \longrightarrow t\text{-BuN-H} \qquad (7)$$
$$\underset{\overset{|}{O\cdot}}{}$$
$$\mathbf{3}$$
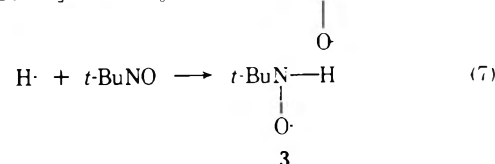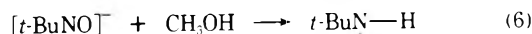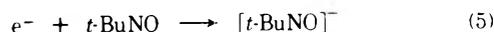
The ratio of the areas of nitroxide **1** to nitroxide **2** are plotted as a function of $[t\text{-BuNO}]^{-1}$ in Figure 2 together with the "least-squares" line. This linear behavior indicates a straightforward competition between reactions 2 and 4 for $CH_3\dot{O}$. It also demonstrates that the only fate for $\dot{C}H_2OH$ is reaction with *t*-BuNO. This simple reaction scheme, i.e., reactions 2–4, leads to eq 8–10 where $G(I)$ and

$$G(I) = G_0(\dot{C}H_2OH) + \frac{G_0(CH_3O\cdot)k_2[CH_3OH]}{k_2[CH_3OH] + k_4[t\text{-BuNO}]} \quad (8)$$

$$G(II) = \frac{G_0(CH_3O\cdot)k_4[t\text{-BuNO}]}{k_2[CH_3OH] + k_4[t\text{-BuNO}]} \quad (9)$$

$$\frac{G(I)}{G(II)} = \frac{k_2[CH_3OH]}{k_4[t\text{-BuNO}]} + \frac{G_0[CH_2OH]}{G_0(CH_3O\cdot)} + \frac{G_0[\dot{C}H_2OH]}{G_0(CH_3O\cdot)} \quad (10)$$

$G(II)$ are the radiation chemical yields of nitroxides 1 and 2 which are directly proportional to the area under the integrated ESR absorption curves. $G_0(CH_3O\cdot)$ and $G_0(\dot{C}H_2OH)$ are the yields of $CH_3O\cdot$ and $\dot{C}H_2OH$ before reactions 2 and 3 occur. The intercept of the line in Figure 2 is 0.4 and therefore $G_0(\dot{C}H_2OH) = 0.4G_0(CH_3O\cdot)$. The yield of methoxy radicals in irradiated methanol at room temperature has been determined to be 2.5 where 2.0 escape from the spur.[3] If these values also apply at 228 K, then the yield of $\dot{C}H_2OH$ radicals is 1.0. This result was shown to be independent of dose rate by varying the electron beam intensity from 1 to 7 μA. Increasing the temperature and the dose by changing the flow rate of the solutions through the irradiation zone also produced no effect.

Similar results were obtained for ethanol solutions of t-BuNO. The ESR spectrum of Figure 3 is a composite of nitroxides resulting from trapping of $CH_3\dot{C}HOH$, $CH_3CH_2O\cdot$, and electrons and/or hydrogen atoms. The plot of the ratio of $CH_3\dot{C}HOH$ trapped to $CH_3CH_2O\cdot$ vs. $[t\text{-BuNO}]^{-1}$ gave a good straight line with intercept of 0.4 as shown in Figure 4. This shows that a simple competition for the ethoxy radical is occurring and that all $CH_3\dot{C}HOH$ radicals with t-BuNO

$$CH_3CH_2O\cdot + CH_3CH_2OH \rightarrow CH_3\dot{C}HOH + CH_3CH_2OH \quad (11)$$

$$CH_3\dot{C}HOH + t\text{-BuNO} \longrightarrow t\text{-Bu}-\underset{\underset{O\cdot}{|}}{N}-\underset{\underset{OH}{|}}{\overset{\overset{CH_3}{|}}{C}}-H \quad (12)$$

$$CH_3CH_2O\cdot + t\text{-BuNO} \longrightarrow t\text{-Bu}-\underset{\underset{O\cdot}{|}}{N}-OCH_2CH_3 \quad (13)$$
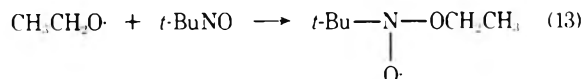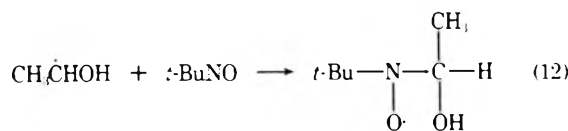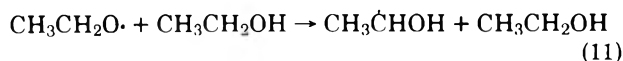
This can be analyzed in the same way as for methanol and the intercept of Figure 4 shows that $G(CH_3\dot{C}HOH) = 0.4G(CH_3CH_2O\cdot)$. The yield of ethoxy radicals in ethanol has been estimated to be 1.5 by pulse radiolysis.[3] Therefore the yield of $CH_3\dot{C}HOH$ radicals is 0.6. This result was shown to be independent of dose and dose rate.

The ratio of hydroxyalkyl to alkoxy measured here for the liquid (0.4) is smaller than in the gas phase (1.2). The latter is based on the mass-spectrometric determination of the cross sections for reactions

$$CH_3OH^+ + CH_3OH \rightarrow CH_3OH_2^+ + \dot{C}H_2OH \quad (14)$$

and

$$CH_3OH^+ + CH_3OH \rightarrow CH_3OH_2^+ + CH_3O\cdot \quad (15)$$

Several explanations are possible for this difference. For example, (14) and (15) might be phase dependent, (15) being more favored in the liquid. Alternatively, radicals are almost certainly produced in radiolysis by other reactions, from excited states for example, which are not included in the mass-spectrometric gas-phase yields because no ions
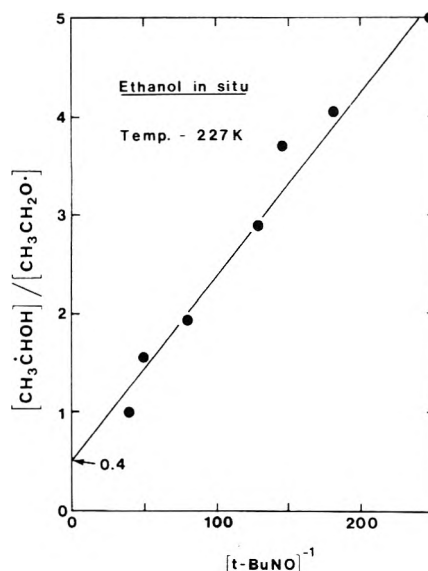
Figure 4. The ratio of yields of $CH_3\dot{C}HOH$ and $CH_3CH_2O\cdot$ trapped by t-BuNO for in situ irradiated ethanol solutions at 227 K.

are formed. Another possibility is the occurrence of reactions of radicals with t-BuNO other than spin trapping, for example

$$\dot{C}H_2OH + t\text{-BuNO} \rightarrow t\text{-BuNHO}\cdot + CH_2O \quad (16)$$

Reactions analogous to (16) are known for other electron acceptors.[15] If this reaction occurs to an appreciable extent, the yields of hydroxyalkyl radicals measured by spin trapping represent a lower limit.

The spin trapping experiments described here have shown that both hydroxyalkyls and alkoxy radicals are important intermediates in the radiolysis of liquid alcohols. The yield of $\dot{C}H_2OH$ in liquid methanol was determined to be at least 1.0 and that for $CH_3\dot{C}HOH$ in liquid ethanol at least 0.6.

References and Notes

(1) AECL No. 5362.
(2) (a) G. R. Freeman, *Actions Chim. Biol. Radiat.*, **14**, 73 (1970); (b) *Natl. Stand. Ref. Data Ser., Natl. Bur. Stand.*, **No. 48** (1974); (c) J. H. Baxendale and P. Wardman, *ibid.*, **No. 54** (1975).
(3) (a) G. E. Adams and J. H. Baxendale. *J. Am. Chem. Soc.*, **80**, 4215 (1958); (b) F. S. Dainton, I. Janovsky, and G. A. Salmon, *Proc. R. Soc. London, Ser. A*, **327**, 305 (1972).
(4) F. P. Sargent and E. M. Gardy, *J. Phys. Chem.*, **78**, 1977 (1974).
(5) E. G. Janzen, *Acc. Chem. Res.*, **4**, 31 (1971).
(6) C. Lagercrantz, *J. Phys. Chem.*, **75**, 3466 (1971).
(7) J. A. Wargon and F. Williams, *J. Am. Chem. Soc.* **94**, 7917 (1972).
(8) (a) L. P. Theard and W. H. Hamill, *J. Am. Chem. Soc.*, **84**, 1134 (1962); (b) J. C. J. Thynne, J. K. Amenu-kpodo, and A. G. Harrison, *Can. J. Chem.*, **44**, 1655 (1966).
(9) F. P. Sargent, E. M. Gardy, and H. R. Falle, *Chem. Phys. Lett.*, **24**, 120 (1974).
(10) S. W. Mao and L. Kevan, *Chem. Phys. Lett.*, **24**, 505 (1974).
(11) J. C. Stowell, *J. Org. Chem.*, **36**, 3055 (1971).
(12) A. Mackor, Th. A. J. W. Wajer, and Th. J. de Boer, *Tetrahedron Lett.*, 2115 (1966).
(13) M. J. Perkins, P. Ward, and A. Horsfield, *J. Chem. Soc. B*, 395 (1970).
(14) S. H. Glarum, *Rev. Sci. Instrum.*, **44**, 752 (1973).
(15) G. E. Adams and R. L. Willson, *J. Chem. Soc., Faraday Trans. 1*, **69**, 719 (1973).

The Anion Radical of Phenylcyclobutadienequinone. An Electron Spin Resonance Study

J. G. Concepcion and G. Vincow*

Department of Chemistry, Syracuse University, Syracuse, New York 13210 (Received October 16, 1975)

Publication costs assisted by Syracuse University

In search of a free radical possessing a cyclobutadiene-like framework, the anion radical of phenylcyclobutadienequinone (PCQ) has been generated in dimethyl sulfoxide, hexamethylphosphoramide, and ethereal solvents. The ESR proton and ^{13}C hyperfine splittings, line width, and lack of resolved phenyl proton splittings are analyzed with the aid of Hückel MO and some INDO calculations. In contrast with the parent compound PCQ, which is completely planar in the solid state, the phenyl group in the anion radical is twisted more than 70° out of plane and conjugation effects are essentially absent from the ESR spectrum. The PCQ anion is more closely related structurally to the cyclobutadiene moiety than is the parent compound PCQ or the previously investigated benzocyclobutadienequinone anion radical. Computer experiments indicate that the ESR parameters may have potential as a useful probe of the geometry of the four-membered ring. Two additional ESR signals are detected, a doublet of doublets (a^H = 2.00, 0.88 G) and a structureless line of width 5 G. Both have g values very similar to that of the PCQ anion and both grow in intensity at the expense of the PCQ anion signal. These results are interpreted in terms of an anionic polymerization of PCQ, with the doublet of doublets ascribed to a dimer radical and the broad line to a polymer radical.

Introduction

The characterization and study of cyclobutadiene and its derivatives has been of considerable interest to chemists.[1] The synthesis of analog compounds has been the object of many efforts in order to approach the parent species.[1a] Cyclobutadiene has been recently generated at very low temperatures in a rigid matrix,[1b-d] but many important questions concerning its geometry and electronic structure have not yet been resolved.[1e,f]

Among the analogs are the cyclobutadienequinones.[2] Of these, the only paramagnetic compound which has been studied is the anion radical of benzocyclobutadienequinone (I).[3] The analysis of the ESR spectrum of I reveals, how-

I   II
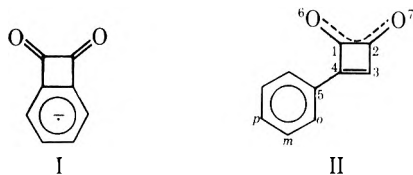
ever, that this compound is best characterized as an ortho-disubstituted benzene anion, with about 70% of the π-electron spin density located in the benzene ring. This compound is thus not a good example of an anion radical of a substituted cyclobutadiene.

In this work we have sought such a molecule. We have prepared the anion radical of phenylcyclobutadienequinone (PCQ), II, and have studied its ESR proton and ^{13}C hyperfine spectra. In addition, we have made some observations concerning the reactivity of this radical in the presence of excess PCQ.

Experimental Section

PCQ was kindly supplied by Dr. M. C. Caserio, The NMR singlet at 9.6 δ, multiplets at 8.6 and 7.6 δ from TMS, and mp 151.5–152.5 °C (lit. 152–153 °C) are consistent with those of the pure compound.[2a] The anion radical of PCQ was generated by various techniques: (1) with 0.04 M

potassium *tert*-butoxide (KTBO) in dimethyl sulfoxide (DMSO);[4] (2) by alkali metal reduction in ethereal solvents,[5] in hexamethylphosphoramide (HMPA),[6] or in a mixture of HMPA–ethereal solvent; and (3) electrolytically in acetonitrile (ACN) with tetra-n-butylammonium perchlorate as supporting electrolyte.[7] All solvents and reagents were purified prior to use. Whenever vacuum techniques were required, a 10^{-6} Torr vacuum was obtained by the use of a mercury diffusion pump. Solutions of KTBO–DMSO were prepared in a drybox, using an argon atmosphere.

X-Band ESR spectra were recorded with a Varian Associates E-9 spectrometer. The temperature in the cavity was measured by means of a copper–constantan thermocouple. Relative errors in the temperature were ±0.5 °C, and the absolute errors were ±2 °C. The dual-cavity method used for the determination of the g values and the measurement of the hyperfine splittings has been previously described.[8]

Results and Discussion

The reaction of a yellowish 0.02 M solution of PCQ in DMSO with a 0.04 M solution of KTBO in DMSO at 20 °C yielded an amber solution. Upon analysis of this amber solution by ESR at room temperature (20 °C), a spectrum of two lines of equal intensity was observed. The two components were separated by 11.35 G and had a line width of 0.35 G and a g value of 2.00510. No further resolution of this doublet could be observed by optimizing spectrometer conditions. This ESR spectrum is shown in Figure 1. The end portion of the figure depicts lines arising from radicals possessing ^{13}C nuclei, which are present in natural abundance. The relative intensity of each such line when compared with that of a doublet proton line is 0.012 to ±0.001, and the two coupling constants are of magnitude 4.63 and 8.26 G.

The reduction of PCQ in HMPA with potassium at 20 °C gave a similar amber solution. The measured coupling constant of the doublet spectrum was 12.2 G with a line width
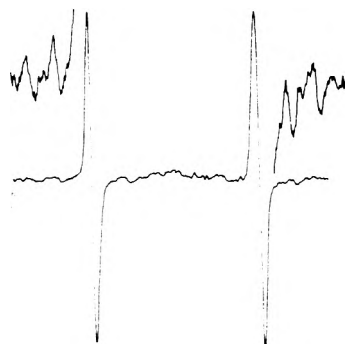
Figure 1. Experimental ESR spectrum of the phenylcyclobutadiene-quinone (PCQ) anion radical in DMSO-KTBO at 20 °C. The end portions depict part of the ^{13}C spectrum recorded with the gain increased by a factor of 10.

TABLE I: Values of the Proton Coupling Constant ($a_3{}^H$) for the Phenylcyclobutadienequinone Anion Radical

System[a]	$a_3{}^H$, G	ΔW,[b] G	g value[c]	Temp, °C
HMPA–K	12.30 ± 0.2	1.0	2.00500	20
(1 HMPA:6 DME)–K	10.75 ± 0.5	1.8		−57
(1 HMPA:5 DME)–Na	11.30 ± 0.5	2.0		−40
(3 HMPA:1 THF)–K	11.80 ± 0.3	2.0		−100
DME–K	10.70 ± 0.5	2.5		−69
ACN–electrolyte	11.00 ± 0.2	0.7		−40
DMSO–KTBO	11.25 ± 0.2	0.35	2.00510	20

[a] HMPA = hexamethylphosphoramide, DME = dimethoxyethane, THF = tetrahydrofuran, ACN = acetonitrile, DMSO = dimethyl sulfoxide. [b] ΔW denotes the peak-to-peak line width in the first derivative spectra. [c] The errors in the g value are ±0.00005.

of 1.0 G and a g value of 2.00500. In mixtures of HMPA and ethereal solvents at low temperatures (−100 to −40 °C), the value of the hyperfine splitting ranged between 10.7 and 11.8 G and the line width varied from 1.8 to 2.5 G (see Table I).[9]

We ascribe this spectrum to the PCQ anion radical (II) with the 11–12-G splitting due to the proton at the 3 position. Evidence for this assignment is: (1) the KTBO-DMSO method of reduction has been widely used to generate semidione radicals;[4] (2) alkali-metal reduction is the classical technique for producing anion radicals; (3) the g value of the doublet component is in the range expected for semidiones;[9] (4) the experimental coupling constants are in fairly good agreement with those obtained by Hückel MO and INDO calculations (see below).[10]

Between the lines of the doublet spectrum, another line appears in the mixtures of HMPA and ethereal solvents as the temperature is increased. The intensity of this center line increases irreversibly while that of the doublet decreases. At −20 °C only one broad line of approximately 5-G line width could be observed. In most of the spectra recorded, a small shoulder was detected on each of the wings of this 5-G line.

In KTBO–DMSO at 20 °C a similar phenomenon was observed as a function of time, i.e., another line (g = 2.0050) developed within a few minutes in the center of the doublet spectrum. After approximately 45 min only this center line of width approximately 5 G was detected.

Shortly after mixing solutions of PCQ–DMSO and KTBO–DMSO not only was the development of the center line observed, but also on the wings of this line a partially resolved doublet of doublets (g = 2.0051) was detected. Proton coupling constants of 2.00 and 0.88 G were obtained through comparison with computer simulations (see Figure 2). This spectrum was resolved in DMSO but appeared only as shoulders in the case of HMPA–ethereal solvents because of the smaller line width in the former solvent. As will be discussed in detail below, we have tentatively assigned this doublet of doublets to a paramagnetic dimer of PCQ. Subsequent reaction of this dimer radical with more neutral PCQ could account for the broad line, due to the formation of a polymer radical.[11]

The most interesting feature of the proton hyperfine spectrum of the PCQ anion radical is the lack of phenyl group splittings. This indicates an absence of conjugation of the phenyl group with the four-membered ring. The phenyl splittings must be small in comparison with the line width of the spectrum, which in DMSO solvent is only 0.35
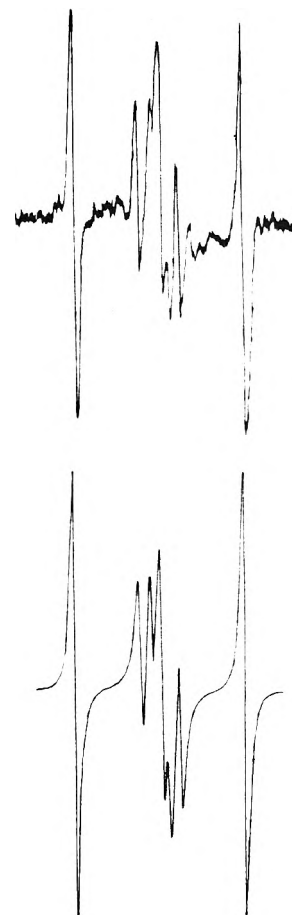
Figure 2. Experimental ESR spectrum of the phenylcyclobutadiene-quinone (PCQ) anion radical in DMSO after approximately 10–15 min of contact with a KTBO–DMSO solution. Lower portion represents the computer simulated spectrum.

G. The lack of phenyl conjugation in the anion radical is ascribed to a considerable twist of the phenyl group relative to the "cyclobutadiene" plane, and contrasts with the case of the parent PCQ molecule which is completely *planar* in the solid state.[12] The anion radical is thus a better model compound for the cyclobutadiene moiety.

We have performed Hückel MO (HMO) calculations of II in order to show that our "unconjugated" model of PCQ anion correlates well with the observed doublet proton splitting, the two ^{13}C splittings, the absence of phenyl

group proton splittings, and the magnitude of the line width. In addition we have made some computer experiments to search for a sensitivity of the calculated ESR results to the geometry of the four-membered ring. We have also performed a few INDO calculations of the spin distribution.

There are a large number of proposed sets of HMO parameters for carbonyl groups available in the literature.[13-15] The equations that describe these parameters are $\alpha_O = \alpha_C + h_O\beta_{CC}$ for the coulomb integral, and $\beta_{CO} = x_{CO}\beta_{CC}$ for the resonance integral. We have tried several sets of parameters and have correlated the calculated proton and ^{13}C coupling constants with the experimental results. The parameters which gave the best overall agreement for PCQ anion are $h_O = 1.0$ and $x_{CO} = 1.6$.

To model the twist of the phenyl group we performed a series of HMO calculations in which the parameter β_{45}/β_{CC} was varied from 0 to 1. All other nonzero values of β_{IJ} were kept equal to unity and the $\sigma-\pi$ parameter Q_{CH}^H was taken as -27.0 G.[16] The results are shown in Table II.

The completely conjugated model ($\beta_{45}/\beta_{CC} = 1.0$) gives poor agreement with experiment since it predicts 2-G phenyl-proton splittings and a ring-proton splitting of magnitude 7.5 G. As the value of β_{45}/β_{CC} is decreased, the magnitude of the ring splitting increases toward the experimental result. If the entire line width in the case of DMSO solvent (0.35 G) was ascribed to unresolved hyperfine splitting then the optimum agreement would be obtained using $0.2 < \beta_{45}/\beta_{CC} < 0.3$, and the predicted ring splitting would be -9.0 G, in fairly good agreement with experiment. This analysis sets an upper limit for β_{45}/β_{CC}. Using the relationship $\beta_{45} = \beta_{CC} \cos \theta$ we predict an approximate angle of twist of the phenyl group greater than $70°$.

To confirm these approximate results of HMO theory, INDO calculations were performed.[17] For a completely conjugated model, $a_3^H = -7.1$ G, $a_o^H = -2.4$ G, $a_m^H = +1.3$ G, and $a_p^H = -2.4$ G, in substantial agreement with the HMO results and in poor concordance with experiment. Using an unconjugated model, the magnitude of the ring-proton splitting increases to 7.8 G in conformity with the trend exhibited by the HMO calculations.

The intensity ratios of the ^{13}C to proton lines indicate that each of the ^{13}C splittings arises from two equivalent carbon-13 nuclei. Because of the very limited conjugation with the phenyl group these must be the four nuclei of the "cyclobutadiene" ring. Since this ring is substituted at the 4 position, the pairwise equivalence must be accidental and should be verified by calculation (see below). From Figure 1 it can be seen that the peak-to-peak heights of the ^{13}C lines are not the same. The height of the low-field line due to the 4.63-G splitting is greater than that of the peak due to the 8.26-G coupling constant; the ratio is 1.2. In agreement with this finding, the line width of the peak due to the 8.23-G coupling is larger than that due to the 4.63-G coupling; the ratio is 1.1. Line-width analysis of the ^{13}C hyperfine spectrum has been shown to be a powerful technique to distinguish between positions with different spin densities. Lines with larger width arise from positions with larger spin densities. As a consequence, the 8.23-G splitting will correspond to the ^{13}C nuclei at positions of higher π spin density. From the Hückel MO calculations and the experimental ring-proton splitting it follows that $0.3 < \rho_{3,4}^\pi < 0.4$, whereas $\rho_{1,2}^\pi \approx 0.07$. We therefore assign the 8.26-G splitting to the 3,4 positions and the 4.63-G splitting to the remaining 1,2 positions.

The calculations of the ^{13}C splittings were carried out using the HMO spin densities and the Karplus–Fraenkel equation with CC and CH $\sigma-\pi$ parameters as proposed by those authors.[18] The CO $\sigma-\pi$ parameters employed were those of Broze and Luz ($Q_{CO}^C = 24.3$ G and $Q_{OC}^C = -36.0$ G).[19] Use of the Das and Fraenkel[16] CO $\sigma-\pi$ parameters does not lead to significantly different results.

The first point to note from the calculated ^{13}C splittings in Table II is that, for small values of β_{45}/β_{CC}, the 3 and 4 position splittings differ from each other by less than the experimental line width (0.5 G). The same is true for the 1 and 2 position splittings. This calculation supports the conclusion drawn from measured intensities that the splittings arise from two "equivalent" pairs of carbon nuclei. This near equivalence is yet another indication of the absence of significant phenyl-group conjugation.

For small values of β_{45}/β_{CC}, the calculated splittings are $a_{3,4}^C \simeq +6.4$ G and $a_{1,2}^C = -5.7$ G. These differ from the experimental values by about 23% in both cases. Considering all the approximations and assumptions that go into this comparison, the agreement is fairly good. An INDO calculation[17] was performed using the unconjugated model of the PCQ anion. The results are qualitatively similar to those of HMO theory in that a larger positive value is predicted for the 3,4 splitting and a smaller negative splitting for the 1,2 positions. The INDO values are computed directly from carbon atom 2s orbital spin occupations, without any variation made in the usual parameters for the oxygen atom. They are $a_{3,4}^C = +14.2$ G and $a_{1,2}^C = -3.1$ G, in fair agreement with experiment.

There has been considerable interest in the influence of substituents on the geometry of the cyclobutadiene ring, specifically distortions from a square to a rectangle or a D_{2h} parallelogram.[1f,20] Although the HMO model used in this work is admittedly a very approximate one, we have used it to perform some calculations in which we have relaxed the assumption of a square geometry for the four-membered ring. Our purpose is to test whether the hyperfine couplings are sensitive to geometry and in particular whether a lower-symmetry geometry might lead to a significant improvement of the agreement between calculations and the ESR experiments. Using the unconjugated model, we made a series of HMO calculations in which β_{12}/β_{CC} was decreased, corresponding to the fact that this bond has the smallest bond order (ca. 0.2). As β_{12}/β_{CC} decreases the magnitude of a_3^H decreases and those of $a_{1,2}^C$ and $a_{3,4}^C$ become more similar in value, thus leading to worse overall agreement with experiment. Guided by the literature on 1,2-disubstituted cyclobutadienes, we have modeled the rectangular geometry through a decrease in β_{14}/β_{CC} and β_{23}/β_{CC}. This leads to an improvement in the agreement with measured ESR parameters. For example, using $\beta_{14} = \beta_{23} = 0.7\beta_{CC}$ and the unconjugated model we obtain $a_3^H = -10.43$ G, $a_{1,2}^C = -5.68$ G and $a_{3,4}^C = +7.54$ G. These values are closer to the experimental than those computed using the square geometry ($a_3^H = -9.26$ G; $a_{1,2}^H = -5.76$, $a_{3,4}^C = +6.40$ G). Because of the very approximate nature of the theory employed these results should not be taken as "proving" a rectangular geometry, but rather as suggesting that these EPR parameters may be sensitive to ring geometry and thus serve as a useful probe of geometry in future work on related systems.

As was noted above, the PCQ anion radical is reactive in solutions which are initially 0.02 M in PCQ. In agreement with this observation, Roberts et al.[2] have noted that the

TABLE II: Calculated Values of the Hyperfine Coupling Constants for the PCQ Anion Radical

β_{45}/β_{CC}	a_3^{H} [a]	a_o^{H}	a_m^{H}	a_p^{H}	a_1^{C} [b]	a_2^{C}	a_3^{C}	a_4^{C}
0	−9.26	0.00	0.00	0.00	−5.76	−5.76	+6.40	+6.40
0.1	−9.22	−0.04	0.00	−0.05	−5.69	−5.71	+6.37	+6.36
0.2	−9.10	−0.15	−0.01	−0.20	−5.64	−5.59	+6.30	+6.28
0.3	−8.92	−0.32	−0.03	−0.42	−5.56	−5.46	+6.18	+6.13
0.5	−8.46	−0.77	−0.06	−1.00	−5.28	−5.12	+5.92	+5.70
1.0	−7.45	−2.05	−0.11	−2.45	−4.31	−4.56	+4.04	+5.63

[a] All splittings are given in gauss. Spin densities were calculated using the HMO theory with $h_O = 1.0$ and $x_{CO} = 1.6$. Splittings were computed using the McConnell relation with $Q_{CH}^{H} = -27$ G. The experimental splitting ranges in magnitude from 10.7 to 12.3 G depending on solvent. [b] All ^{13}C splittings were computed using the Karplus–Fraenkel equation with parameters as given in ref 18 and 19. In the case of a_4^{C}, the value of Q_{CC}^{C} was chosen as 35.6 G. The experimental ^{13}C splittings are $|a_{3,4}^{C}| = 8.26$ G and $|a_{1,2}^{C}| = 4.63$ G.

polarographic reduction of PCQ does not follow a reversible pattern.

Two additional ESR signals are detected, a doublet of doublets ($a^{H} = 2.00, 0.88$ G) and a structureless line of width 5 G. Both have g values which are very similar to that of the PCQ anion radical thus indicating structural similarity. Both signals grow at the expense of that of the PCQ anion, with the former appearing first and then the latter totally replacing the PCQ anion spectrum after about 45 min (20 °C; DMSO solvent).

By analogy with previous work on similar systems[11] the most likely reaction course to explain these observations is anionic polymerization. The fact that in DMSO at the initial stages of the reaction a doublet of doublets with the same g value as the PCQ anion is detected suggests the formation of a dimer radical from the reaction of the PCQ anion with the excess PCQ present in solution. An ESR spectrum of such a paramagnetic dimer has previously been observed in the anionic polymerization of benzylidene malononitrile.[11d]

A possible structure for the dimer radical is suggested by the fact that PCQ is known to undergo nucleophilic substitution at position 3. In the reaction of alkoxy groups (RO⁻) with PCQ, intermediate III has been proposed.[2] Assuming

III   IV
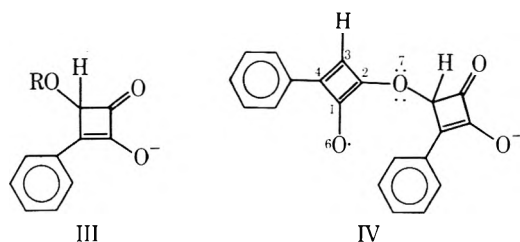
that in the present case the nucleophile is the PCQ anion radical, dimer radical IV may be formed.[21] Molecular models suggest that nucleophilic attack by oxygen atom 6 is prevented by steric repulsion of the phenyl groups. The spin density remains essentially localized on the attacking ring except for a small amount transmitted through the alkoxy oxygen atom 7.

We have made an HMO calculation to rationalize the large decrease of a_3^{H} from 10 G in the monomer anion to 2.0 or 0.9 G in the dimer. The dimer was modeled by the monomer anion structure in which the substituent at oxygen 7 was incorporated by changing the heteroatom parameters. The parameters used for oxygen atom 6 were the same as those which gave good agreement in the case of the monomer ($h_O = 1.0$, $x_{CO} = 1.6$) while for oxygen 7, parameters suggested for an alkoxy oxygen were employed ($h_O = 1.0$, $x_{CO} = 0.8$).[13] All values of β_{CC} were fixed at the stan-

dard value, except for $\beta_{45} = 0.3\beta_{CC}$. The calculated proton splitting is −0.99 G which is in quite good agreement with either of the two experimental possibilities (2.0, 0.9 G).[22] A range for the splitting due to the β proton of oxygen atom 7 can also be estimated. The Heller–McConnell relationship, $a_{\beta}^{H} = B\rho_O^{\pi} \cos^2 \theta$, is employed with $B = 20$ G, a value used to estimate the proton coupling constants of methoxy-substituted aromatic cation radicals.[23] From the HMO calculation described above, $\rho_O^{\pi} = 0.15$. Thus, since $0 < \theta < 90°$, we predict $0 < a_{\beta}^{H} < 3$ G, a range which is consistent with the experimental findings.

Further reaction of the dimer radical with more neutral PCQ leads finally to a polymer radical. As expected for a higher molecular weight species the reorientational correlation time is markedly slowed thus leading to spectral broadening. As a result, we see only a structureless resonance at about the same g value as the monomer anion. Similar structureless broad resonances have been observed previously in a variety of anionic polymerization systems.[11]

References and Notes

(1) (a) M. P. Cava and M. J. Mitchell, "Cyclobutadiene and Related Compounds", Academic Press, New York, N.Y., 1967; (b) O. L. Chapman, C. L. McIntosh, and J. Pacansky, *J. Am. Chem. Soc.*, **95**, 614 (1973); (c) O. L. Chapman, D. De La Cruz, R. Roth, and J. Pacansky, *ibid.*, **95**, 1337 (1973); (d) A. Krantz, C. Y. Lin, and M. D. Newton, *ibid.*, **95**, 2744 (1973); (e) G. Maier, *Angew. Chem., Int. Edit. Engl.*, **13**, 425 (1974); (f) L. T. J. Delbaere, M. N. G. James, N. Nakamura, and S. Masamune, *J. Am. Chem. Soc.*, **97**, 1973 (1975).

(2) (a) E. J. Smutny and J. D. Roberts, *J. Am. Chem. Soc.*, **77**, 3420 (1955); (b) E. J. Smutny, M. C. Caserio, and J. D. Roberts, *ibid.*, **82**, 1793 (1960); (c) M. P. Cava, D. R. Napier, and R. J. Pohl, *ibid.*, **85**, 2076 (1963).

(3) D. H. Geske and A. L. Balch, *J. Phys. Chem.*, **68**, 3423 (1964).

(4) G. A. Russell, G. R. Underwood, and D. C. Lini, *J. Am. Chem. Soc.*, **89**, 6636 (1967).

(5) J. R. Bolton and G. K. Fraenkel, *J. Chem. Phys.*, **40**, 3307 (1964).

(6) G. R. Stevenson and J. G. Concepcion, *J. Phys. Chem.*, **76**, 2176 (1972).

(7) D. H. Geske and A. H. Maki, *J. Am. Chem. Soc.*, **82**, 2671 (1960).

(8) J. G. Concepcion and G. Vincow, *J. Phys. Chem.*, **79**, 2037, 2042 (1975).

(9) The variation of a_3^{H} and the line width with solvent system is probably due in large measure to ion pairing interactions, which have been pre-

viously observed in many cases for semidiones (G. A. Russell, D. F. Lawson, H. L. Malkus, R. D. Stephens, G. R. Underwood, T. Takano, and V. Malatesta, *J. Am. Chem. Soc.*, **96**, 5830 (1974); G. A. Russell and J. L. Gerlock, *ibid.*, **96**, 5838 (1974)).

(10) We have considered another possible structure for this radical, namely, a cyclic aliphatic semidione such as 3-*R*-4-*R*-4-phenylcyclobutane-1,2-semidione. This structure was rejected because of the following experimental results: (a) ^{13}C splittings. Russell and co-workers (*J. Chem. Phys.*, **54**, 2164 (1971)) have reported ^{13}C splittings for a series of cyclic aliphatic semidiones such as cyclobutane-1,2-semidione. For this compound $a_{3,4}{}^{C} = 5.4$ G and $a_{1,2}{}^{C} = 1.4$ G. For a series of radicals modified at the 3,4 end of the ring, neither ^{13}C splitting varied from these values by more than ±1 G. Thus the spin distribution for such semidiones is quite constant. Our ^{13}C splittings are quite different in magnitude, namely, 8.23 and 4.63 G. Further we find experimentally that the 8.23-G splitting arises from a position of high spin density. In contrast, for the cyclobutane-1,2-semidione it is the smaller ^{13}C splitting (1.4 G) which arises from a high spin density position. (b) DMSO-d_6 results. Reduction of PCQ with KTBO in DMSO-d_6 afforded the *same* doublet spectrum as that observed when the reaction was conducted in DMSO. In contrast, Russell and co-workers have found that reduction in DMSO-d_6 generally yielded deuterium substitution at the 3,4 positions in such cyclic aliphatic semidiones.

(11) (a) H. P. Leftin and W. K. Hall, *J. Phys. Chem.*, **64**, 382 (1960); (b) K. Hirota and K. Kuwata, *J. Polym. Sci.*, **60**, S52 (1962); (c) M. Szwarc, "Carbanions, Living Polymers and Electron Transfer Processes", Wiley, New York, N.Y., 1968; (d) F. J. Smentowski and G. R. Stevenson, *J.*

Phys. Chem., **74**, 2525 (1970); (e) G. R. Stevenson, J. G. Concepcion, and J. Castillo, *ibid.*, **77**, 611 (1973).

(12) C. H. Wong, R. E. March, and V. Schomaker, *Acta Crystallogr.*, **17**, 131 (1964).
(13) A. Streitwiser, Jr., "Molecular Orbital Theory for Organic Chemists", Wiley, New York, N.Y., 1961, Chapter 2.
(14) N. L. Bauld, *J. Am. Chem. Soc.*, **87**, 4788 (1965).
(15) G. Vincow and G. K. Fraenkel, *J. Chem. Phys.*, **34**, 1333 (1961); ref 13.
(16) M. R. Das and G. K. Fraenkel, *J. Chem. Phys.*, **42**, 1350 (1965); W. M. Gulick, Jr., and D. H. Geske, *J. Am. Chem. Soc.*, **88**, 4119 (1966).
(17) INDO calculations were carried out at the University of Puerto Rico (Rio Piedras Campus). The bond-distance parameters employed were $r_{CC} = 1.397$ Å, $r_{CH} = 1.04$ Å, and $r_{CO} = 1.22$ Å.
(18) M. Karplus and G. K. Fraenkel, *J. Chem. Phys.*, **35**, 1312 (1961).
(19) M. Broze and Z. Luz, *J. Chem. Phys.*, **51**, 749 (1969).
(20) (a) P. Reeves, T. Devon, and R. Pettit, *J. Am. Chem. Soc.*, **91**, 5890 (1969); (b) R. Weiss and J. N. Murrell, *Tetrahedron*, **27**, 2877 (1971); (c) C. U. Pittman, Jr., K. L. Douglas, Q. Y. Ng, W. Hunter, D. Pace, and L. D. Kispert, *J. Org. Chem.*, **40**, 2121 (1975).
(21) We formulate the nucleophile with the negative charge localized on oxygen rather than on carbon atoms 3 or 4 since the oxygen atom is considerably more electronegative.
(22) If we interchange the oxygen atom parameters to model the dimer in which nucleophilic attack occurs at the 6 position, then the HMO calculation yields $a_3{}^{H} = -11.7$ G in very poor agreement with experiment.
(23) W. F. Forbes and P. D. Sullivan, *J. Chem. Phys.*, **48**, 1411 (1968), and references cited therein.

Equilibrium Studies by Electron Spin Resonance. XIV. Ion Pair Dissociation Constants by the Use of Time-Averaged Rate Constants

Gerald R. Stevenson,* Rosario Concepción, and Ignacio Ocasio

Department of Chemistry, University of Puerto Rico, Rio Piedras, Puerto Rico 00931 *(Received October 23, 1975)*

Publication costs assisted by the University of Puerto Rico

The addition of potassium iodide to solutions of the cyclooctatetraene (COT) anion radical in hexamethylphosphoramide (HMPA) results in a decrease in the rate of electron transfer between the anion radical and the COT dianion. This decrease is due to the formation of charged ion pairs (COT^{2-},K^{+}). The ion pair dissociation constant for this charged ion pair is algebraically related to the rate constant (k_{ex}) for the electron transfer process. Similarly, the addition of KI to solutions of the *p*-dinitrobenzene anion radical in HMPA yields a decrease in the rate of electron exchange between the anion radical and neutral molecule, and a similar algebraic relationship between this rate constant and the ion pair dissociation constant was found. By comparing the ion pair dissociation constants determined by this method with those using different techniques, it was found that the use of time-averaged kinetics gives values that are too large. This is attributed to the fact that the observed rate constants are sensitive to changes in the viscosity of the solution that are brought about by the addition of salt.

ESR spectroscopy has proven to be of particular value in the evaluation of certain kinetic and thermodynamic parameters that control processes and equilibria involving anion radicals. Some of the earliest work using this spectroscopic tool involves the determination of kinetic parameters for the electron exchange between an anion radical and neutral molecule[1]

$$R\cdot^{-} + R \rightleftarrows R + R\cdot^{-} \qquad (1)$$

Since this pioneering work by Weissman, the kinetic parameters controlling the electron exchange rates have been measured for a wide variety of anion radical and solvent metal systems. Further, electron exchange rates have been studied for systems involving both free radicals (eq 2)[2] and dianions (eq 3)[3].

$$R\cdot + R^{-} \rightleftarrows R^{-} + R\cdot \qquad (2)$$

$$R\cdot^{-} + R^{2-} \rightleftarrows R^{2-} + R\cdot^{-} \qquad (3)$$

One of the more significant observations brought out from these studies is that the second-order rate constant is highly dependent upon the state of solvation and the amount of ion pairing of the anionic species.[3,4] Chang and Johnson[4] have demonstrated that the rate of electron exchange (eq 1) for naphthalene systems is slower for the ion pair than it is for the free ion. This same effect has been observed for electron exchange involving dianions (eq 3).[3,5]

Since the degree of ion pairing is dependent upon the rate constant (k_2) for electron exchange, we were interested in developing an algebraic relationship between these rate constants and the equilibrium constant controlling the degree of ion pair dissociation for both an anion radical and a diamagnetic dianion. To accomplish this it is necessary that the anionic species are generated in a solvent where only free ions are formed so that the rate constant (k_{ex}^0) for the system free of ion pairing can be determined. However, for comparison of this rate constant with that obtained for the same system in the presence of ion pairing it is necessary that ion pairs can be readily generated upon the addition of alkali metal salt. The solvent of choice is hexamethylphosphoramide (HMPA).

It has been previously observed that anion radicals in hexamethylphosphoramide are virtually fully dissociated,[6] but the addition of alkali metal salts to these solutions of anion radicals in HMPA results in the formation of ion pairs.[7,8] In some cases these ion pairs can be observed simultaneously with the free ion.[9,10]

For the determination of the equilibrium constant for the dissociation of an ion pair (β) to form the free ion (α) and solvated cation (eq 4) a most useful expression has

$$\beta \rightleftharpoons \alpha + M^+ \qquad (4)$$

been utilized for cases where only the time-averaged species can be observed by ESR spectroscopy. This expression has been used routinely by NMR spectroscopists investigating hydrogen bonding,[11] and has recently been utilized in terms of ESR parameters (both g values and coupling constants) for the determination of ion pair dissociation constants.[7,12] After determination of the ESR parameter (Γ^0) for the free anion, a small amount of alkali metal salt can be added to the solution and the time-averaged spectroscopic parameter (Γ) will be observed. The ion pair dissociation constant (K_d) can then be determined by the use of eq 5 without direct measurement of the spectroscop-

$$1/(\Gamma - \Gamma^0) = K_d/(\Gamma' - \Gamma^0)(M^+) + 1/(\Gamma' - \Gamma^0) \qquad (5)$$

ic parameter (Γ') of the ion pair.[12] A simple plot of $1/(\Gamma - \Gamma^0)$ vs. $1/(M^+)$ yields a straight line with an intercept of $1/(\Gamma' - \Gamma^0)$ and a slope of $K_d/(\Gamma' - \Gamma^0)$.

Here we wish to describe the use of electron exchange rate constants in eq 5 for the determination of K_d for both an anion radical and a paramagnetic dianion. For the case of electron exchange between the anion radical and the neutral molecule the p-dinitrobenzene system was used. This anion radical can be generated free of ion pairing in HMPA by either sodium or potassium reduction.[13] For the case of electron exchange between the anion radical and the dianion the cyclooctatetraene (COT) system was chosen.

It is known that the reduction of COT by sodium metal in HMPA yields dianion and anion radical that are free of ion pairing.[14,15] Even after the addition of 0.3 M NaClO₃ no ion pairing between the sodium cation and dianion or anion radical could be detected.[14,15] However, reduction of COT with potassium metal results in a solution containing some singly ion paired dianions (charged ion pairs, R^{2-}, K^+). Even after the addition of 0.3 M KI this solution shows no ion pairing with the anion radical or the formation of neutral ion aggregates (R^{2-}, M^+_2).[14,15]

Results and Discussion

Electron Exchange for Dianion to Anion Radical. Re-

duction of COT with sodium metal in HMPA results in the formation of a solution yielding the typical nine-line ESR pattern for the COT anion radical. Due to the fact that the anionic species are free of ion pairing the electron exchange process is rapid when the dianion concentration is relatively large. Thus, the hyperfine components are quite broad. Addition of KI to this solution leads to the formation of charged ion pairs and dramatic line narrowing, Figure 1. This line narrowing is due to the inclusion of eq 6 along with eq 3 in the line broadening process.
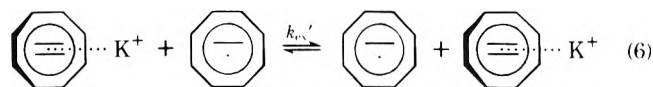
The rate constant for electron exchange between the free dianion and the anion radical was obtained by generating solutions containing various concentrations of dianion and plotting the observed line width (ΔW) for the central hyperfine component vs. the concentration of dianion according to (Figure 2)

$$k^0 = \sqrt{3}\pi(2.83 \times 10^6)(\Delta W - \Delta W^0)/(COT^{2-}) \qquad (7)$$

where ΔW is the line width (measured between the extrema in the first derivative spectrum) and ΔW^0 is the line width in the absence of exchange.[16]

The rate constant (k_{ex}^0) for the free dianion taken from Figure 2 is $(1.03 \pm 0.08) \times 10^8$ M⁻¹ s⁻¹, and the intercept (ΔW^0) is 0.083 ± 0.002 G.[17]

It is not possible to determine the observed rate constant (k_{obsd}) in this same manner with salt (KI) added to the solvent system, since the observed rate constant will be a function of the ratio of added salt to dianion. This problem can be resolved by maintaining the dianion concentration constant and varying the salt concentration. To do this a series of samples was prepared that were 0.04 M in dianion, a sample from each solution was taken and the line width determined, salt was then added to each solution, and another sample was taken for ESR analysis. Assuming that the intercept (ΔW^0) is the same for each concentration of added salt k_{obsd} was calculated.

By replacing Γ, Γ', and Γ^0 in eq 5 with k_{obsd}, k_{ex}', and k_{ex}^0, respectively, a plot of $1/(k_{obsd} - k_{ex}^0)$ vs. $1/(K^+)$ should be linear and have a slope of $K_d/(k_{ex}^0 - k_{ex}')$. Such a plot is linear (Figure 3), and K_d obtained from this plot is $(2.21 \pm 0.59) \times 10^{-3}$. This value is larger but still within experimental error with that obtained by an independent measurement.[15] The value for K_d obtained in this manner is expected to be larger than the true equilibrium constant for two reasons: (1) addition of KI to HMPA results in an increase in the viscosity of the solvent system, and this could cause the rate of electron exchange to fall off more rapidly than can be accounted for by the formation of ion pairs; (2) increasing the ionic strength of the media would also be expected to decrease the rate of eq 3.

Electron Exchange for Anion Radical to Neutral Molecule. Addition of a neutral molecule to a solution of the p-dinitrobenzene anion radical results in broadening of the ESR lines in the slow exchange limit. The rate constant for the electron transfer (eq 1) was calculated from the slope of the plot of line width vs. the concentration of added neutral molecule (N), Figure 4. Using the Lorentzian line shape, $k_{ex}^0 = 1.52 \times 10^7 (\Delta W - \Delta W^0)/(N)$.[18]

Successive additions of sodium chlorate to these HMPA solutions results in a gradual decrease in the rate constant for the electron exchange process. The observed rate con-
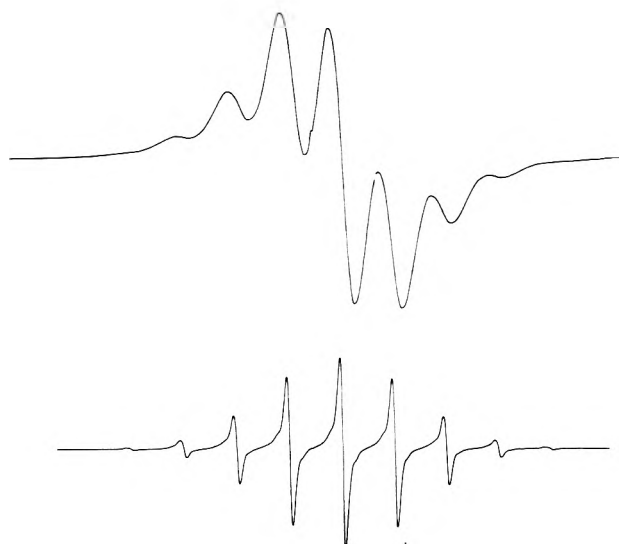
Figure 1. ESR spectra of the system COT–HMPA–Na. The lower spectrum was taken for the same anion radical solution but with added potassium iodide (0.1 M). Note the line narrowing upon addition of the salt.
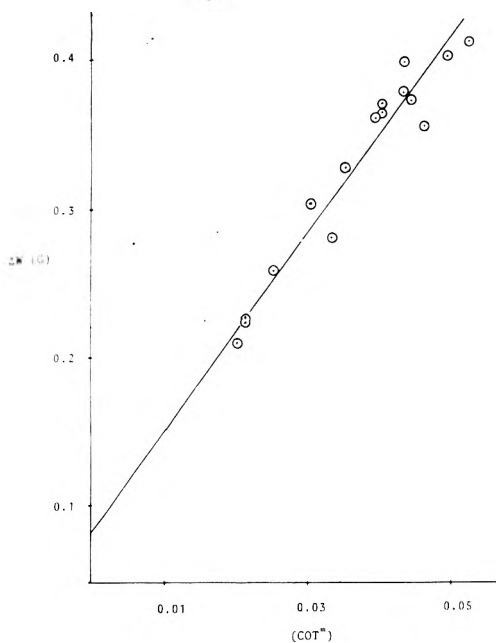
Figure 2. A Plot of the line width vs. the concentration (M) of the COT dianion for the system COT–HMPA–Na.
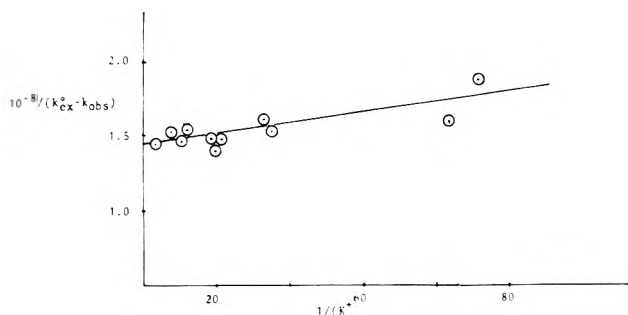
Figure 3. Plot of $10^{-8}/(k_{ex}^0 - k_{obsd})$ vs. one over the concentration of added KI for the system COT–HMPA–Na.
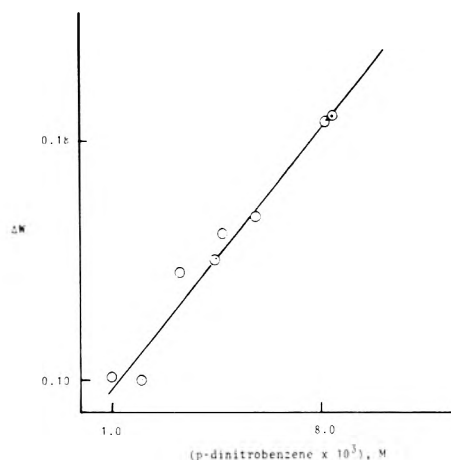
Figure 4. Plot of the line width vs. the concentration of neutral p-dinitrobenzene for the system p-dinitrobenzene–HMPA–Na at 23 °C.

stant must be a weighted average between the rate constant for the free ion (k_{ex}^0) and that for the ion pair (k_{ex}'). This relationship is given by

$$k_{obsd} = \{(\alpha)k_{ex}^0 + (\beta)k_{ex}'\}/\{(\alpha) + (\beta)\} \qquad (8)$$

The thermodynamic equilibrium constant for the ion pair dissociation is given by $K_{eq} = (\alpha)(Na^+)/(\beta)$, where (Na^+) represents the concentration of added salt, since the concentration of added salt is larger by more than two orders of magnitude than the anion radical concentration. Combining this expression with eq 8, we obtain eq 5 but in terms of rate constants.

K_d was obtained from the slope of a plot of $1/(k_{obsd} - k_{ex}^0)$ vs. $1/(Na^+)$ as shown in Figure 5. Typical data for a single experiment carried out at room temperature are shown in Table I.

It must be noted here that the addition of sodium chlorate to solutions of the p-dinitrobenzene anion radical in HMPA results in line broadening even in the absence of added neutral molecule. This is most likely due to a rapid exchange of the cation between the ion pair and the solvent (eq 4). This phenomenon has been previously observed,[19] and it shows that the rate of ion pair formation and dissociation is fast on the ESR time scale. This line broadening must be accounted for and subtracted from the total line broadening in the presence of neutral molecule in order to calculate the line broadening due to the electron transfer process, eq 1, from which the rate constant can be calculated. Since it was impractical to add identical concentrations of salt to several samples, a plot of the line width vs. the concentration of added salt (Figure 6) was made for each experiment before any neutral molecule was added (see Experimental Section). The intercept of the plot of ΔW vs. the concentration of added neutral molecule was then taken from this plot.

The fact that a single rate constant (k_{obsd}) was observed means that the mean time between electron transfer events is long compared to the mean time between association-dissociation events. If the reverse were true, simultaneous observation of the free ion and ion pair would be observed experimentally. That is, a superimposition of lines with different line widths would be observed, as was found by Chang and Johnson.[4]

The "real" values for k_{obsd} at each salt concentration are, of course, not known to the precision indicated in Table I. Once k_{ex}^0 was determined $(k_{ex}^0 = 1.9 \times 10^8)$ this value was
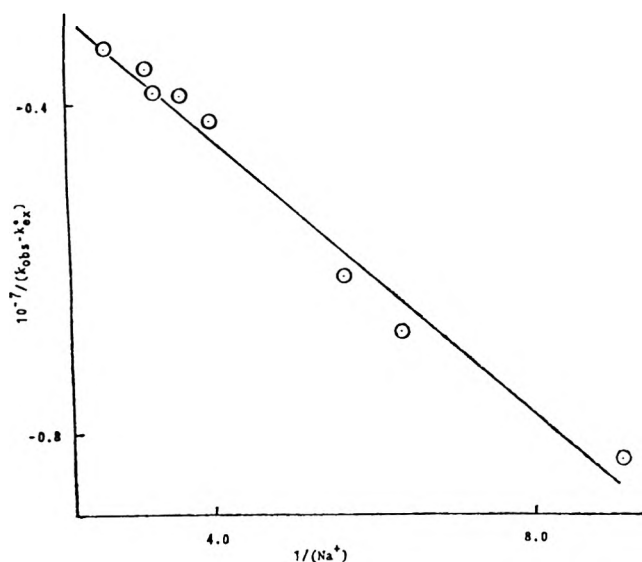
Figure 5. Plot of $10^{-7}/(k_{obsd} - k_{ex}{}^0)$ vs. one over the concentration of added salt. This plot was used to calculate K_d for the system p-dinitrobenzene–HMPA–Na.

TABLE I: Observed Rate Constant for the Electron Exchange Reaction with Added NaClO₃

(Na^+), M	k_{obsd}, M^{-1} s^{-1}
0	1.90×10^8 [a]
0.164	1.75×10^8
0.184	1.73×10^8
0.309	1.63×10^8
0.321	1.61×10^8
∞	0.9×10^8

[a] This value was obtained from Figure 4 and $k_{ex}{}^0$ was taken to be exactly 1.90×10^8 for each experiment. The other rate constants were obtained by comparing line widths with that for the sample without added salt.

then used as a standard value for each experiment. Thus for each experiment, samples were taken with no added salt and the rate constant was considered to be 1.9×10^8 M^{-1} s^{-1} exactly. Salt was then added to the solution and the rate constants for these samples were determined utilizing the sample taken without salt as a standard.

Deranleau[20] has recently pointed out that equilibrium constants for weak complexes are most reliable when they are based upon data that extend as much as possible into the region where the saturation factor (s) is between 0.2 and 0.8. For the kinetic experiment described here

$$s = (\beta)/\{(\alpha) + (\beta)\} = (k_{obsd} - k_{ex}{}^0)/(k_{ex}{}' - k_{ex}{}^0) \quad (9)$$

Calculated from eq 9 our saturation factor (s) varied from 0.15 to 0.33.

Equation 5 is particularly useful since it does not require an independent determination of Γ'. In our case, this means that $k_{ex}{}'$ (the rate constant for the ion pair) need not be determined independently. If, however, $k_{ex}{}'$ could be determined by some other means, the combination of $K_{eq} = (\alpha)(Na^+)/(\beta)$ with eq 8 will yield an expression simpler than eq 5 from which K_{eq} can be determined.

$$K_{eq} = (k_{ex}{}' - k_{obsd})(Na^+)/(k_{obsd} - k_{ex}{}^0) \quad (10)$$

This expression has the same form as that previously used for the determination of the equilibrium constant for
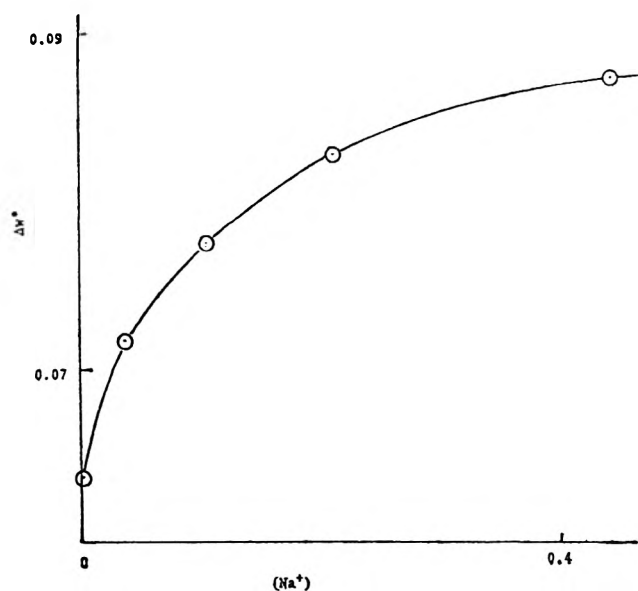
Figure 6. Plot of line width (ΔW_i^0) vs. the concentration of added salt for the systems not containing neutral molecule. This plot was used to obtain a numetical value for ΔW^0 to be usec to calculate k_{obsd} for the system p-dinitrobenzene–HMPA–Na–NaClO₃.

the hydrogen bond exchange reaction between the anion radical and the solvent.[21] From eq 10, a plot of $(k_{obsd} - k_{ex}{}^0)/(k_{ex}{}' - k_{obsd})$ vs. the concentration of added salt should yield a straight line with a slope equal to the reciprocal of the equilibrium constant for the ion pair dissociation (eq 4) and an intercept of 0,0. Utilizing 9×10^7 for $k_{ex}{}'$ (taken from Figure 5) such a plot is linear, and the K_{eq} determined from its slope (0.72) is in perfect agreement with that obtained from Figure 5 (see Table II). The equilibrium constant for the dissociation of the potassium p-dinitrobenzene anion radical ion pair was also determined in an identical manner. From a plot of $1/(k_{obsd} - k_{ex}{}^0)$ vs. $1/(K^+)$, Figure 7, K_{eq} was found to be 0.35 at 23 °C.

Potassium reduction of p-dinitrobenzene in HMPA results in a solution that yields a nine-line ESR pattern. The nine lines result from two equivalent nitrogens and four protons, which are almost equivalent to the two nitrogens. This radical has been shown to be the free anion radical.[13] Under high resolution conditions, however, some splitting of the central lines can be observed indicating that the nitrogen splitting is slightly larger than that for the protons ($A_N{}^0 = 1.155$ and $A_H{}^0 = 1.099$ G). Both $A_N{}^0$ and $A_H{}^0$ are independent of the temperature. The splitting observed in the second line of the nine-line pattern represents the difference in A_N and A_H (δ).

The addition of KI to this solution of the free p-dinitrobenzene anion radical results in an increase in the nitrogen coupling constant due to the formation of the ion pair. This increase in the nitrogen splitting is accompanied by a decrease in A_H, thus δ increases rapidly with increasing concentration of K^+. Since the two nitrogens remain equivalent after the addition of the K^+ (or Na^+) to the HMPA solution, there must be a rapid shift of ion pairing between the different NO_2 groups in solution.

Taking the value of δ as a weighted average between the ion paired anion radical and the free ion we can utilize eq 5 in terms of δ

$$1/(\delta - \delta^0) = K_{eq}/(Na^+)(\delta' - \delta^0) + 1/(\delta' - \delta^0) \quad (11)$$

TABLE II: Dissociation Constants for the Following Ion Pairs in HMPA at 23 °C

Ion pair	Method	K_d
PDNB$^-$,Na$^+$	Kinetic	0.74 ± 0.1
PDNB$^-$,K$^+$	Kinetic	0.35 ± 0.1
PDNB$^-$,K$^+$	Coupling constants	0.25 ± 0.1
COT^{2-},K$^+$	Kinetic	$(2.21 \pm 0.59) \times 10^{-3}$
COT^{2-},K$^+$	See ref 15	$(1.3 \pm 0.3) \times 10^{-3}$

TABLE III: Equilibrium Constant for the Dissociation of the Potassium p-Dinitrobenzeneide Ion Pair at Temperatures

K_{eq}	T, °C	K_{eq}	T, °C
0.316	-4	0.239	20
0.278	0	0.210	30
0.257	10	0.181	40
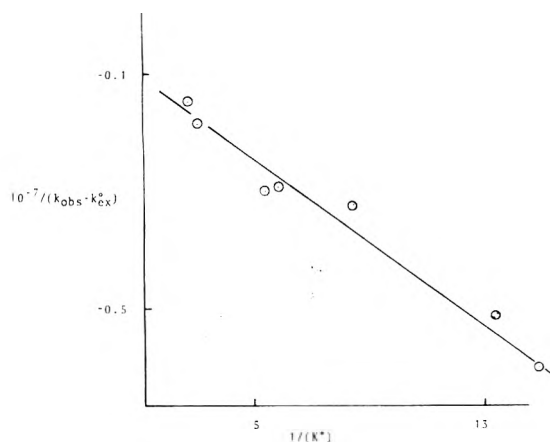
Figure 7. Plot of $10^{-7}/(k_{obsd} - k_{ex}{}^0)$ vs. one over the concentration of added KI to the system p-dinitrobenzene–HMPA–Na.

Figure 8. Plot of $1/(\delta - \delta^0)$ vs. one over the concentration of added KI to the system p-dinitrobenzene–HMPA–K.

where δ^0 and δ' represent the difference in A_N and A_H for the free ion and ion pair, respectively. A plot of $1/(\delta - \delta^0)$ vs. $1/(K^+)$ is linear, Figure 8, and yields the equilibrium constants given in Table III.

A vant'Hoff plot for this system, Figure 9, yields an enthalpy of -1.89 kcal/mol. This negative value indicates that the solvation of the cation is greater than that for the ion pair. It was experimentally impossible to determine K_{eq} for the sodium system from δ, since the addition of Na$^+$ resulted in considerable line broadening, and accurate coupling constants could not be measured.

It must be mentioned again that by no means are the rate constants in Table I accurate to the three significant figures given. However, the samples used for each determination of K_{eq} were all taken from the same bulk anion radical solution with different amounts of salt added. Thus, the change in k_{obsd} in going from one salt concentration to another is much more precise. Repeating the experiment results in significantly different values for k_{obsd}, but the equilibrium constant obtained from these values and Figure 4 will be the same. That is, the line in Figure 4 has a different slope and intercept for each determination of K_{eq}, but K_{eq} is constant from experiment to experiment.

A possible source of error in this type of determination may come from the fact the inorganic salts are not fully dissociated in HMPA. Recent conductivity data[22] imply that these salts are essentially fully dissociated in HMPA. An independent measurement of the ion association constant (K_a) for potassium iodide gave a value of about 4.[23] This small value for K_a does not lead to a correction large enough to be included in the equilibrium constants measured here.

Since the first attempt to study ion pair–free ion equilibria in 1960 by Atherton and Weissman,[24] this work, which is a continuation of a preliminary communication,[7b] repre-
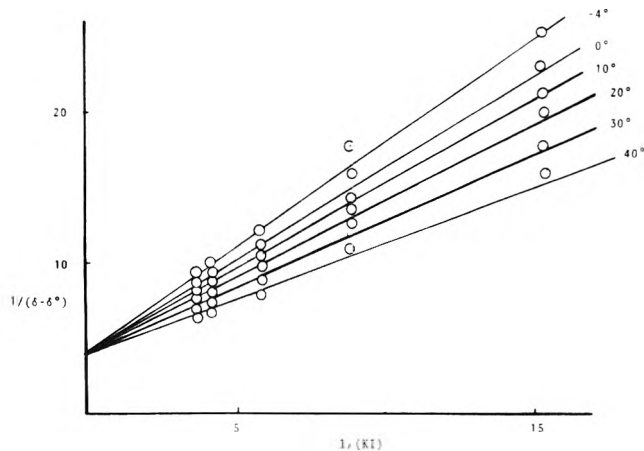
Figure 9. Plot of ln K_{eq} vs. $10^3/RT$ for the system p-dinitrobenzene–HMPA–K with added KI.

sents the first use of electron transfer kinetics for the determination of ion pair dissociation equilibrium constants.

Experimental Section

The p-dinitrobenzene was purchased from Aldrich Chemical Co. and recrystalized before use. Hexamethylphosphoramide (HMPA) was distilled from calcium hydride under reduced pressure and stored over Molecular Sieves 4A in a desiccator prior to use. The potassium iodide and the sodium chlorate were purchased from Alpha Inorganics and were stored in a vacuum oven for 48 h at 75 °C before use.

The ESR samples were prepared in the apparatus shown in Figure 10. About 75 ml of dry HMPA was placed in bulb
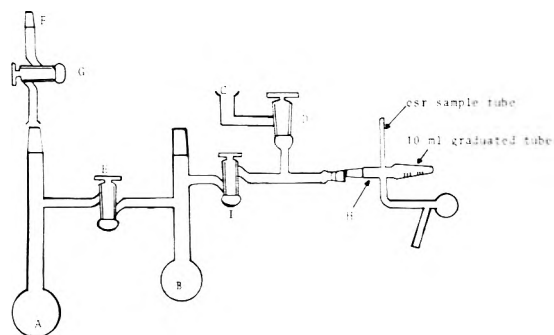
Figure 10. Apparatus used for the preparation of anion radical solutions used for the determination of K_{eq} for ion pair dissociation.

Figure 11. Apparatus used for the addition of KI to the COT–HMPA–Na system.

A with a small amount of potassium metal and about 10 mg of p-dinitrobenzene was placed in bulb B. The entire apparatus was then evacuated to 10^{-3} mm by connecting the apparatus to a vacuum line. While maintaining bulb B in a liquid nitrogen bath, the HMPA was distilled from bulb A to bulb B from the solvated electron. Stopcocks D and E were then shut and the entire apparatus was removed from the vacuum line. Bulb A was then opened and cleaned. After thorough clearing, a small amount of alkali metal was placed into bulb A, which was then reevacuated through F. Stopcock G was then shut and the apparatus was again removed from the vacuum line. The HMPA p-dinitrobenzene solution was allowed to pass into bulb A by opening E and inverting the apparatus. After the reduction was complete the anion radical solution was poured back into B. A known portion of this solution was placed into the 10-ml graduated tube, and this tube was subsequently sealed off at point H with a hand torch. The graduated tube was charged with salt before connecting it to the apparatus. After the sample was taken, stopcock I was shut, the exposed tube cleaned, a new graduated tube added, and this part of the system reevacuated through C and D. After sealing, the graduated tubes were shaken until all of the salt had dissolved. A portion of this solution was then placed into the extending ESR sample tube and the ESR spectrum recorded. A known portion of neutral molecule was then added to the bulk solution and the procedure repeated.

All rate constants were determined for the line broadening of the first hyperfine line. The correction in the rate constant for the difference in the lifetime of a particular anion radical and the residence time in a particular nuclear spin arrangement is 143/144 calculated in the manner described by Zandstra and Weissman.[17] Before any samples were taken with added neutral molecule for a given bulk solution of anion radical in bulb B, a series of samples were taken with various concentrations of added salt (either KI or $NaClO_3$). The line width (ΔW^0) was then plotted against the concentration of added salt. This plot was found to be different for each anion radical solution and represents the variance in the intercept of Figure 4 with added salt.

For the determination of the effect of added KI upon the rate of electron transfer between the dianion and anion of COT the apparatus shown in Figure 11 was used. Weighed portions of KI were placed in bulbs B, C, D, and E and a known quantity of Na^0 (enough to make the dianion 0.4 M) was placed in bulb A. The entire apparatus was then evacuated and a quantity of COT added via a break seal. HMPA (20 ml) was then distilled into the apparatus directly from a piece of potassium metal. The entire apparatus was then
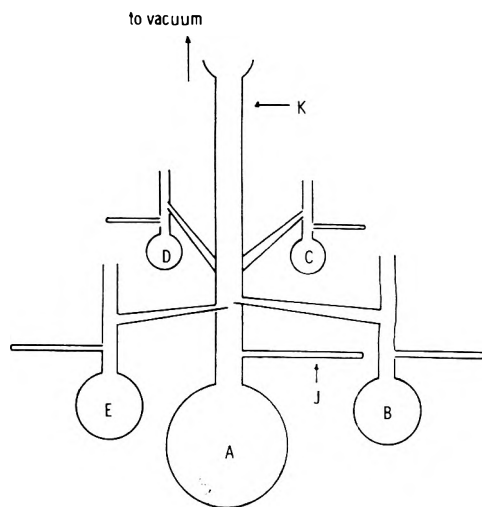
sealed from the vacuum line at point K. The solution was stirred until all of the sodium had dissolved whereupon a sample was taken in the ESR tube J. The remaining solution was then divided into four portions and transferred into bulbs B, C, D, and E. Each of these bulbs was then sealed from the apparatus. Each of the bulbs was weighed and shaken until all of the KI had dissolved into the HMPA solution. The ESR samples were then taken in the extending tubes. After the completion of the experiment each of the bulbs was emptied, cleaned, and reweighed.

All of the rate constants were determined from the line broadening of the center hyperfine line, where the statistical correction factor is 70/256.

X-band ESR spectra were recorded on a Varian E-9 ESR spectrometer.

References and Notes

(1) R. L. Ward and S. I. Weissman, J. Am. Chem. Soc., **79**, 2086 (1957).
(2) M. T. Jones and S. I. Weissman, J. Am. Chem. Soc., **84**, 4269 (1962).
(3) (a) T. J. Katz, J. Am. Chem. Soc., **82**, 3784, 3785 (1960); (b) F. J. Smentowski and G. R. Stecenson, ibid., **91**, 7401 (1969).
(4) R. Chang and C. S. Johnson, Jr., J. Am. Chem. Soc., **88**, 2338 (1966).
(5) G. R. Stevenson and J. G. Concepcion, J. Phys. Chem., **76**, 2176 (1972).
(6) A. Cserhegyi, E. Franta, J. Chardhuri, J. Jugar-Grodzinski, and M. Szwarc, J. Am. Chem. Soc., **89**, 7129 (1967).
(7) (a) A. E. Alegria, R. Concepcion, and G. R. Stevenson, J. Phys. Chem., **79**, 361 (1975); (b) G. R. Stevenson and R. Concepcion, J. Am. Chem. Soc., **96**, 4696 (1974).
(8) G. R. Stevenson and A. E. Alegria, J. Phys. Chem., **79**, 1042 (1975).
(9) G. R. Stevenson, L. Echegoyen, and L. R. Lizardi, J. Phys. Chem., **76**, 1439 (1972).
(10) (a) G. R. Stevenson and L. Echegoyen, J. Phys. Chem., **77**, 2339 (1973); (b) G. R. Stevenson and A. E. Alegria, ibid., **77**, 3100 (1973).
(11) G. R. Wiley and S. I. Miller, J. Am. Chem. Soc., **94**, 3287 (1972).
(12) G. R. Stevenson, A. E. Alegria, and A. McB. Block, J. Am. Chem. Soc., **97**, 4859 (1975).
(13) G. R. Stevenson and L. Echegoyen, J. Am. Chem. Soc., **96**, 3381 (1974).
(14) G. R. Stevenson and I. Ocasio, J. Phys. Chem., **79**, 1387 (1975).
(15) G. R. Stevenson and I. Ocasio, J. Am. Chem. Soc., **98**, 890 (1976).
(16) F. J. Smentowski and G. R. Stevenson, J. Am. Chem. Soc., **91**, 1701 (1969).
(17) The rate constant obtained from eq 7 was divided by the statistical correction factor of 70/256 as explained in P. J. Zandstra and S. I. Weissman, J. Chem. Phys., **35**, 757 (1961).
(18) The statistical correction factor for this system is 143/144.
(19) J. C. Bailey, P. R. Colau, and E. Warhurst, J. Chem. Soc., Faraday Trans. 1, **69**, 570 (1973).
(20) D. A. Deranleau, J. Am. Chem. Soc., **91**, 4044 (1969).
(21) G. R. Stevenson and H. Hidalgo, J. Phys. Chem., **77**, 1027 (1973).
(22) P. Bruno, M. D. Monica, and E. Righetti, J. Phys. Chem., **77**, 1258 (1973).
(23) G. R. Stevenson and A. E. Alegria, J. Am. Chem. Soc., **97**, 3869 (1975).
(24) N. M. Atherton and S. I. Weissman, J. Am. Chem. Soc., **83**, 1330 (1961).

An Electron Paramagnetic Resonance Study of Vanadyl(IV)–Serum Albumin Complexes

N. Dennis Chasteen* and Judy Francavilla

Department of Chemistry, University of New Hampshire, Durham, New Hampshire 03824 (Received November 12, 1975)

This study was undertaken to examine the usefulness of the vanadyl ion (VO^{2+}) spin probe as a technique for investigating multibinding site proteins in room-temperature solutions. Quantitative EPR signal intensity measurements were made with VO^{2+}–albumin solutions at pH 5 and 25 °C where both bound and free VO^{2+} signals could be observed. The spectrum reveals two types of binding sites. Scatchard and Hughes-Klotz plots reveal one "strong" binding site with a binding constant of $(2.6 \pm 0.3) \times 10^6$ M^{-1} and five essentially equivalent "weak" binding sites with a binding constant of $(2.5 \pm 0.1) \times 10^4$ M^{-1}. The "strong" site is probably the primary binding site for Cu^{2+}. The binding at the "weak" sites probably occurs with carboxyl groups as suggested by the EPR parameters. The room-temperature solution spectrum of VO^{2+} bound to albumin is very anisotropic, indicative of slow molecular tumbling. The spectrum of VO^{2+} coordinated at the "weak" binding sites is more rotationally averaged than at the "strong" site. This suggests that there is some local motion at the weakly coordinating sites with a correlation time short compared to that of the protein as a whole. The spectra of VO^{2+} doped powder albumin samples were also examined.

Introduction

Of all the oxidation states of vanadium, V(IV) as the vanadyl ion (VO^{2+}) is the easiest to study in biological systems because of its characteristic EPR spectrum. Recently vanadyl ion EPR has been successfully used to probe liquid crystals,[1] the hydrolysis of ATP,[2] anionic surfaces of acidic lipid bilayers from *H. Cutirubrum*,[3] micelles,[4] and the metal sites of a number of proteins.[5-9] Early work suggests that this ion might also serve as a probe of nucleic acids.[10] In their recent study of vanadium toxicity and molybdenum utilization in rats, Rajagopalan and co-workers[11] found vanadium as protein bound VO^{2+}, concentrated to about 10 ppm in the liver.

In light of the growing interest in the use of the vanadyl ion as a probe of biological systems, we have undertaken a room-temperature solution investigation of vanadyl serum albumin complexes. This multibinding site protein has often served as a model for NMR and EPR spin probe and metal ion investigations.[12-19] Here we report for serum albumin the number of vanadyl ion binding sites, their respective stability constants, and the relative motional freedom at these sites. The tentative identity of the coordinating ligands at these sites is inferred from the EPR parameters. The limitations of using EPR spectroscopy to obtain stability constant data are explored.

Albumin is a common protein in vertabrates, but where most common proteins are specific to one function, albumin has several.[12] In addition to transporting fatty acids and bilirubin, albumin apparently serves as a scavenger of heavy metals.[12] In the past three decades, a vast amount of research into the binding of various moieties by albumin has been conducted. The list of metal ions used is extensive; studies have been conducted on bovine or human serum albumin using Cu^{2+},[13-15] Zn^{2+},[16] Mn^{2+},[17] Co^{2+},[14] Ni^{2+},[14,15] Cd^{2+},[16c] Gd^{3+},[18] Tl^{3+},[19] and Hg^{2+},[19] among others. The binding properties are metal ion dependent. A vanadium study has never been reported.

Experimental Section

Bovine serum albumin, crystallized and lyophylized, was obtained from Sigma Chemical Co. (catalogue No. A4378).

To remove paramagnetic impurities, tentatively identified as copper and iron, 10^{-3} M solutions of the protein were dialyzed at 4 °C against 0.01 M o-phenanthroline, pH 6, for 12-16 h followed by several changes of distilled deionized water for 2 to 3 days or until all the orange color was removed. The albumin concentration was determined spectrophotometrically, ϵ 4.6 × 10^4 cm^{-1} M^{-1} at 279 nm.[20]

Procedures for handling the vanadyl ion and avoiding contaminating metal ions were as described previously.[5]

A 0.01 M lutidine–HNO_3 buffer, pH 5.01, was employed in the VO^{2+}–albumin binding studies. This buffer does not coordinate to the free vanadyl ion, thus avoiding corrections for buffer coordination in the stability constant determinations.

Polycrystalline samples were prepared by soaking 100 mg of BSA in 1 ml of 3 M ammonium sulfate and 5% EDTA solution for 24 h followed by washing with three 1-ml portions of 3 M $(NH_4)_2SO_4$. Then 1 ml of 3 M $(NH_4)_2SO_4$, pH 5.1 adjusted with NaOH, was added and the serum stoppered test tube purged with nitrogen before addition of an aliquot of vanadyl stock solution to give VO^{2+}: BSA mole ratios ranging from 1:1 to 20:1. After soaking the solid albumin for 24 h at 4 °C, the supernatant solution was removed and the pH measured. The solid was washed a minimum of three times with oxygen-free ammonium sulfate to remove any unbound VO^{2+} ion. The solid was then dried with a stream of nitrogen gas. In another procedure, solid samples were prepared in a similar fashion except 40% ethanol in water was used in place of 3 M $(NH_4)_2SO_4$.

Powder samples were analyzed for vanadium by EPR spectroscopy. After dissolving the wet sample in 1 ml of distilled deionized water, the protein concentration was determined spectrophotometrically. Then 50 μl of concentrated HCl and a few milligrams of ascorbic acid were added. The vanadium was determined by measuring the EPR signal height of the acid released $VO(H_2O)_5^{2+}$ as detailed elsewhere.[6]

Most EPR spectra were recorded on a Varian E-9 spectrometer operating at X-band frequency (9.5 gHz). Additional details of the experimental procedures can be found in ref 21.

N. D. Chasteen and J. Francavilla
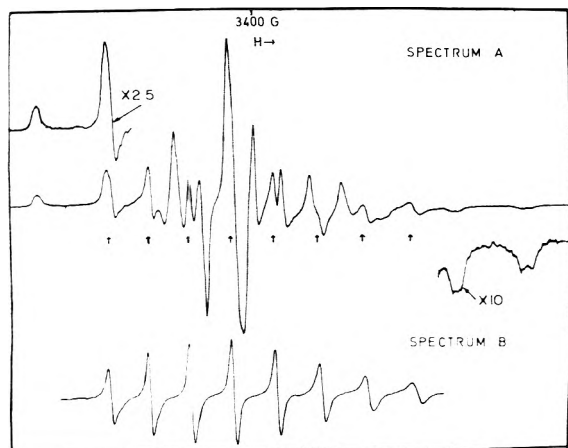
Figure 1. Spectrum A. First derivative EPR spectrum of 5.0×10^{-4} M serum albumin in 0.01 M lutidine–nitric acid buffer, pH 5.0, with 9.0 equiv of $VOSO_4$ added, 25 °C. The arrows indicate contributions from $VO(H_2O)_5^{2+}$. Spectrum B. First derivative EPR spectrum of $VO(H_2O)_5^{2+}$ at 4.42×10^{-4} M concentration, pH 4.87 adjusted with NaOH, 25 °C.
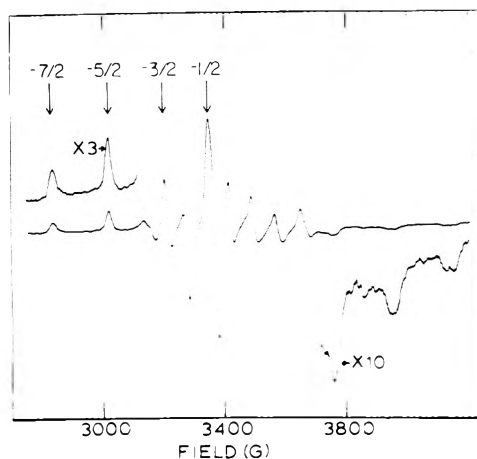
Figure 2. First derivative EPR spectrum of 4.9×10^{-4} M BSA with 10.0 equiv of $VOSO_4$ added, pH 5.8 adjusted with NaOH. The arrows denote the labeling of the four low-field "parallel" lines. The $M_I = -1/2$ line is actually a composite of parallel and perpendicular components. At this pH, the unbound VO^{2+} exists as a hydroxide which does not exhibit a room-temperature EPR spectrum.

Figure 3. EPR first derivative signal height divided by the instrument gain setting for 1:1 VO^{2+}–albumin, 7.6×10^{-4} M, as a function pH. Data for the $M_I = -7/2$ and $-5/2$ parallel lines of protein bound VO^{2+} are plotted.
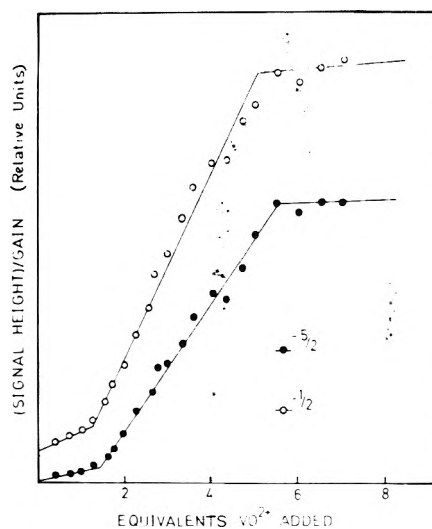
Figure 4. EPR first derivative signal height of protein bound VO^{2+} as a function of equivalents of $VOSO_4$ added. 5.0×10^{-4} M serum albumin, 0.01 M lutidine–nitric acid buffer, pH 5.0. Data for the $M_I = -5.2$ and $-1/2$ "parallel" lines are plotted.

Results and Discussion

Binding Constants. The room temperature spectrum of a pH 5 solution containing VO^{2+} albumin in a molar ratio of 9:1 is shown in Figure 1A. The spectrum consists of a superposition of resonances from free and bound VO^{2+}. The eight arrows in Figure 1A denote the eight resonances of unbound $VO(H_2O)_5^{2+}$ (Figure 1B). The remaining resonances constitute the spectrum of the protein bound vanadyl ion. Increasing the pH to 5.8 results in a loss of the $VO(H_2O)_5^{2+}$ lines due to formation of a $VO(OH)_2$ precipitate which exhibits no EPR spectrum at room temperature.[22] A room temperature solution spectrum of albumin bound VO^{2+} at pH 5.8 is shown in Figure 2. The spectrum displays parallel and perpendicular features characteristic of frozen solution or polycrystalline samples; upon binding the motion of the vanadyl ion becomes highly restricted and is largely governed by the slow tumbling of the albumin molecule.

In Figure 3 the first derivative intensities of the two low-

field "parallel" lines $M_I = -5/2$ and $-7/2$[23] (Figure 2) are shown as a function of pH for a 1:1 VO^{2+}–albumin complex. The first derivative intensities are proportional to the amount of VO^{2+} ion bound to the protein if no line width variation occurs over the pH range. This is the case here. Binding is seen to maximize and level off at about pH 4.7. Subsequent experiments were done at pH 5.0 which enabled us to measure the free VO^{2+} ion concentration. At a higher pH the $VO(H_2O)_5^{2+}$ spectrum could not be observed because of metal hydroxide formation as noted above. This is a limitation of the method.

By measuring the intensity of the EPR lines of the $VO(H_2O)_5^{2+}$ and VO^{2+}–albumin species as a function of the VO^{2+}/albumin mole ratio, one can determine the number of binding sites and their respective binding constants. Figure 4 displays the signal intensities of the $M_I = -5/2$ and $-1/2$ parallel lines (see Figure 2) as a function of the number of equivalents of VO^{2+} added to the protein at pH 5.01. Similar plots (not shown) are obtained with the other lines in the spectrum. The plots show a first break at an average value of 1.2 equiv and a second break at about 5.5
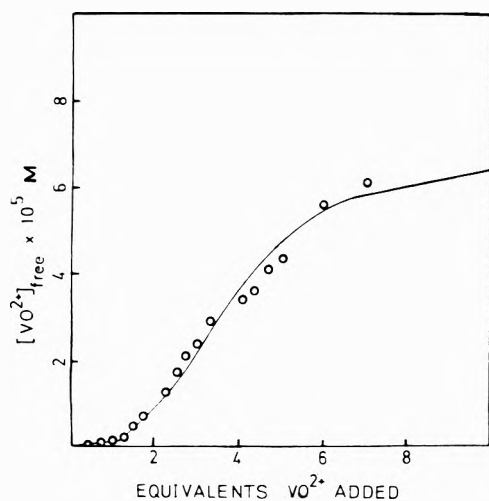
Figure 5. Concentration of $VO(H_2O)_5^{2+}$ as a function of equivalents of $VOSO_4$ added to the albumin solution described in Figure 4.

Figure 7. Scatchard plot after substracting from the data the effect of the binding at the first site. The deviation from the line at high $\bar{\nu}'$ values is due to vanadyl hydroxide formation. See text for definition of quantities.

Figure 6. Scatchard plot showing at least two classes of binding sites for the titration of albumin with VO^{2+}. See text for definition of quantities.

equiv; this indicates that chelation takes place at one "strong" binding site followed by four to five "weaker" binding sites. The abrupt change in slope at 1.2 equiv is a consequence of the different relaxation behavior of the VO^{2+} ion at the two types of sites. There appears to be greater motional freedom at the "weak" sites; this will be discussed in more detail later.

The concentration of free $VO(H_2O)_5^{2+}$, measured from its EPR first derivative intensity,[24] as a function of equivalents of VO^{2+} added is shown in Figure 5. The curve begins to roll over at high equivalent values due to the appearance of a $VO(OH)_2$ precipitate in the titration vessel.[24] In the absence of hydroxide precipitation, the curve in Figure 5 would climb steeply at high equivalent values.

In the binding of VO^{2+} ion to albumin it is apparent that multiple equilibria are involved. Data were treated by the method of Scatchard et al.[25] Plots of $\bar{\nu}/[VO^{2+}]_{free}$ vs. $\bar{\nu}$ were

made where $\bar{\nu}$ is the moles of VO^{2+} bound per mole of protein and $[VO^{2+}]_{free}$ is the $VO(H_2O)_5^{2+}$ concentration.

Ideally, one would like to measure the concentration of the vanadyl protein complex from its spectrum shown in Figure 2. Unfortunately, one does not know the proportionality constant relating the peak-to-peak signal intensity of the first-derivative curve to the concentration. Nor is it practical to perform a double integration because of the myriad of fine structure in the spectrum. Some of the problems of qualitative analysis by EPR spectroscopy are discussed in ref 6.

Instead, the concentration of VO^{2+} bound to the protein, $[VO^{2+}]_{bound}$, was determined from the relationship $[VO^{2+}]_{bound} = [VO^{2+}]_{added} - [VO^{2+}]_{free}$. This equation is valid only in the absence of vanadyl hydroxide formation, i.e., the early part of the titration of metal free albumin with VO^{2+}. $\bar{\nu}$ is given by $\bar{\nu} = [VO^{2+}]_{bound}/[albumin]$.

A Scatchard plot of the data (Figure 6) shows two straight line regions which indicates at least two classes of binding sites.[25] The intercept of the dashed curve with the abscissa yields a value of $n_1 = 1.25$ for the number of binding sites in the first class; correspondingly the slope, $-K_1$, gives the binding constant $K_1 = 2.3 \times 10^6$ M^{-1}. Other titration data not presented here confirm that there is only one binding site in the first class.[21] Hereafter we refer to this as the "strong" site, although the interaction is a relatively weak one.

The leveling of the curve to zero slope at high $\bar{\nu}$ values in Figure 6 is a consequence of the competition of OH^- with the protein for the available VO^{2+}. Data points are reliable only up to $\bar{\nu} \simeq 3$.

To determine the number of sites in the second class and their binding constant, we plot $\bar{\nu}'/[VO^{2+}]_{free}$ vs. $\bar{\nu}'$ where $\bar{\nu}' = \bar{\nu} - 1$ (Figure 7). This procedure substracts out the contribution of the "strong" site to the data. This is valid only when the two classes of sites are noninteracting, i.e., binding at one site does not affect binding at another. This seems to be the case here. From Figure 7 we obtain $n_2 = 5.0$ and $K_2 = 2.5 \times 10^4$ M^{-1} for the second class of sites, the "weak" sites. Again, the deviation of points above $\bar{\nu}' = 2$ is a consequence of the onset of hydroxide precipitation.

TABLE I: EPR Parameters of Frozen Solutions[a]

Site	$A_0(\pm 1.0)$[b,c]	$A_\parallel(\pm 0.5)$[c]	$A_\perp(\pm 1.0)$[c]	$g_0(\pm 0.002)$[d]	$g_\parallel(\pm 0.001)$	$g_\perp(\pm 0.002)$
Strong	100.3	172.8	64.0	1.966	1.939	1.979
Weak	102.8	177.1	65.6	1.965	1.938	1.979

[a] 0.01 M lutidine–HNO_3 buffer solution, pH 5.01. [b] Calculated from $A_0 = (A_\parallel + 2A_\perp)/3$. [c] Units of 10^{-4} cm^{-1}. [d] Calculated from $g_0 = (g_\parallel + 2g_\perp)/3$.

These data were also plotted according to the method of Hughes and Klotz[26] which yielded $n_1 = 1.3$ with $K_1 = 2.8 \times 10^6$ M^{-1} and $n_2 = 5.0$ with $K_2 = 2.5 \times 10^4$ M^{-1}. These values are in good agreement with the results from the Scatchard plots.

Nature of the Binding Sites. The primary site for copper binding is located on the amino terminal end of the protein[12,13] i.e., Asp-Thr-His-Lys. In this strong site, the α-amino nitrogen, the first two peptide nitrogens, and a nitrogen of the imidazole group of His-3 coordinate in a square-planar arrangement about the copper[13a,e,15] Ni^{2+} competes effectively with Cu^{2+} for the same binding site, apparently because Ni^{2+} readily forms square-planar complexes.[14,15]

We have conducted similar experiments with VO^{2+}–albumin and Ni^{2+}. (Competitive binding studies with VO^{2+} and Cu^{2+} were not undertaken because of the tendency of these ions to undergo a redox reaction with one another.) Varying amounts of Ni^{2+} were added to solutions of 4.4×10^{-4} M 1:1 VO^{2+}:albumin, 0.02 M lutidine, pH 5.0. After incubation for 0.5 h the EPR spectrum was recorded. The relative intensity of the free VO^{2+} spectrum increased from 1.0 to 1.8, 2.0, and 2.5 for 1, 2, and 3 equiv of Ni^{2+} added, respectively. Thus Ni^{2+} and VO^{2+} compete effectively for the same strong site which is probably the copper binding site.

The EPR parameters for the "strong" and "weak" sites as obtained from computer simulation[5] of frozen solution spectra are given in Table I. The parameters for the "weak" sites are very similar to those for VO^{2+} bound extraneously to single carboxyl groups in polycrystalline samples of bovine insulin[5] and carboxypeptidase A.[8] The "weak" sites are probably monodentate coordinating carboxyl groups of glutamyl or aspartyl amino acid residues.

If one assumes that Cu^{2+} and VO^{2+} bind at the same strong site, the question arises as to whether all four nitrogen ligands (α-amino, imidazole, and two amide) also coordinate to the vanadyl ion. The evidence is most consistent with only the imidazole group of His-3 binding in the first coordination sphere. The hyperfine splittings of the "strong" site are not greatly different from those of the "weak" site although the former values are smaller as expected for nitrogen vs. oxygen coordination (Table I). The similarities in the EPR parameters probably reflect the fact that most of the ligands for both sites are water molecules. Application of the rule of average environment for three water molecules and one aromatic nitrogen donor coordinated equatorially[5] leads to a predicted isotropic hyperfine splitting $A_0 = 101.8 \times 10^{-4}$ cm^{-1} which is not greatly different from the experimental value of $A_0 = 100.3 \times 10^{-4}$ cm^{-1} (Table I). Inclusion of other nitrogen donors in the first coordination sphere leads to lower A_0 values and considerably poorer agreement. Clearly, this procedure is not sufficiently reliable by itself to draw firm conclusions. However, the $pK_a \sim 6$ for imidazole is the closest of the nitrogen donors to the pH 5.0 used in these experiments and imidazole is known to coordinate to VO^{2+} in several other proteins.[5,7,8]

In addition, the vanadyl ion coordinates very weakly to α-amino groups. A formation constant of only 1.8 is observed for the formation of a bidentate 1:1 vanadyl–glycine complex from the ring closure of the monodentate oxygen coordinated complex.[27] The low affinity for amino groups is further amplified by the lack of reports in the literature of vanadyl complexes with aliphatic amines. The α-NH_2 group in serum albumin has a $pK_a = 7.8$.[28] Finally, ionization and coordination of peptide amide linkages is usually found only for copper.[29]

Molecular Motion. Except for small differences in line widths and hyperfine splittings, room-temperature EPR spectra of solutions of vanadyl labeled proteins are similar to spectra obtained with frozen solution or polycrystalline samples. For example, the values of $A_\parallel$ and $A_\perp$ are 195.7 and 71.0 G, respectively, from frozen solution spectra of the weak sites of albumin compared to 189.3 and 74.5 G at room temperature. These differences are due to partial rotational averaging of the anisotropic dipolar contribution to the hyperfine tensor in room-temperature solutions.

The dipolar contribution, A_p, to the hyperfine splitting is given by $A_p = (A_\parallel - A_0)/2$ where $A_0 = (A_\parallel + 2A_\perp)/3$.

We define an "order parameter" S as

$$S = A_p' A_0 / A_p A_0'$$

where the primed and unprimed symbols refer to the room-temperature and frozen solution values, respectively. The above definition is equivalent to that of Hubbell and McConnell for describing rapid anisotropic motion in membranes.[30] Here we use S as a starting point for discussion of motion in vanadyl proteins where the metal ion tumbling is primarily governed by the isotropic rotational correlation time, τ_r, of the protein as a whole. For rapid tumbling ($\tau_r < 10^{-10}$ s) A_p' is essentially averaged to zero and S is zero. Conversely in a completely "immobilized" spectrum ($\tau_r > 10^{-7}$ s) A_p' equals A_p and S is one. The factor A_0/A_0' is used to roughly correct for variations in spin density from solvent effects due freezing the sample.[30] For the vanadyl ion, this correction is generally near unity.

One expects S to vary monotonically with the correlation time for isotropic motion. The correlation time can be estimated from the Debye relationship,[31] $\tau_r = V\eta/kT$, in which the protein is treated as a sphere of volume V rotating in a fluid medium (H_2O) with a viscosity η at $T = 298$ K. k is the Boltzmann constant. We calculate an approximate molecular volume from the partial specific volume of 0.74 ml/g. Under these assumptions, the rotational correlation time is given by $\tau_r = 3.0 \times 10^{-13}$ W s, where W is the molecular weight (g/mol) of the protein.

Table II lists values of S and estimated τ_r for some vanadyl–protein complexes of different molecular weight. Although the values of S have an experimental uncertainty of about ± 0.01, they do show a definite increase with increasing molecular weight and estimated τ_r. It is clear, however,

TABLE II: Order Parameters (S) for Vanadyl–Protein Complexes

Protein	Molecular wt, g/mol	τ_r, 10^{-8} s	S
Serum albumin[a] (weak sites)	68 000		0.919
Carbonic anhydrase[b]	31 000	0.94	0.930
Carboxypepti- dase A[c]	35 000	1.1	0.936
Bovine serum albumin[a] (strong site)	68 000	2.1	0.952
Transferrin[d]	80 000	2.4	0.956

[a] This work. [b] Reference 7. [c] Reference 8. [d] J. C. Cannon and N. D. Chasteen, to be submitted for publication.

that S values (or other quantities such as $A_\parallel'/A_\parallel$[32]) based on experimental hyperfine splittings of room-temperature vanadyl protein solutions, are not sufficiently sensitive in the time domain $\tau_r \gtrsim 10^{-8}$.s to permit one to obtain accurate correlation times. For nitroxide spin labels, in which the hyperfine anisotropy is an order of magnitude smaller than for vanadyl, this limitation sets in at a larger correlation time, $\tau_r \gtrsim 10^{-7}$ s.[32]

The order parameter for the weak sites in vanadyl–albumin is significantly smaller than for the strong site, 0.919 vs. 0.952 (Table II), which suggests localized motion at the weak sites which is fast relative to the tumbling rate of the protein as a whole. This is reasonable in view of the small binding constant which probably reflects monodentate coordination to a single carboxyl group at these sites. The EPR parameters discussed earlier (Table I) are also consistent with this.[5]

Powdered Samples. Powdered samples of albumin were soaked in ammonium sulfate solution, pH 5, containing sufficient vanadyl sulfate to give a vanadium to protein molar ratios from 1:1 to 20:1 in the soaking solution (see Experimental Section). Powder samples removed from soaking solutions of molar ratios 1:1 to 5:1 exhibited spectra indicative of only one type of binding site with parameters $A_\parallel = 170.8 \times 10^{-4}$ cm^{-1}, $A_\perp = 63.1 \times 10^{-4}$ cm^{-1}, $g_\parallel = 1.936$ and $g_\perp = 1.978$. These parameters are similar to those of the strong site in frozen solutions of the protein (Table I). Metal analysis of a sample from 2:1 soaking solution gave 1.04 mol of vanadium per mole of albumin. Thus, powder and frozen solution samples appear to exhibit similar binding properties involving one "strong" site.

In contrast, the primary site in powder samples obtained from the ethanol–H_2O soaking procedure has quite different parameters ($A_\parallel = 166.3 \times 10^{-4}$ cm^{-1}, $A_\perp = 62.2 \times 10^{-4}$ cm^{-1}, $g_\parallel = 1.942$ and $g_\perp = 1.978$) from those of frozen solution samples or powder samples from the ammonium sulfate solution. Possibly the less polar alcohol solution effects the surface of the protein and induces a quite different mode of binding of the vanadium.

Spectra of powder samples obtained from the rather high molar soaking ratios of 10:1 and 20:1 of the ammonium sul-

fate procedure revealed additional resonance lines indicative of VO^{2+} binding in at least three different chemical environments. At these high molar ratios binding at various weakly coordinating sites in the solid state begins to occur.[21]

References and Notes

(1) J. P. Fackler, J. D. Levy, and J. A. Smith, *J. Am. Chem. Soc.*, **94**, 2436 (1972).
(2) G. M. Wolterman, R. A. Scott, and G. P. Haight, *J. Am. Chem. Soc.*, **96**, 7569 (1974).
(3) W. Z. Plachy, J. K. Lanyi, and M. Kates, *Biochemistry*, **13**, 4906 (1974).
(4) P. Stilbs and B. Lindman, *J. Colloid Interface Sci.*, **46**, 177 (1974).
(5) N. D. Chasteen, R. J. DeKoch, B. L. Rogers, and M. W. Hanna, *J. Am. Chem. Soc.*, **95**, 1301 (1973).
(6) J. J. Fitzgerald and N. D. Chasteen, *Anal. Biochem.*, **60**, 170 (1974).
(7) J. J. Fitzgerald and N. D. Chasteen, *Biochemistry*, **13**, 4338 (1974).
(8) R. J. DeKoch, D. J. West, J. C. Cannon, and N. D. Chasteen, *Biochemistry*, **13**, 4347 (1974), Corrections, *ibid.*, **14**, 196 (1974).
(9) J. C. Cannon and N. D. Chasteen, *Biochemistry*, **14**, 4573 (1975).
(10) W. Snipes and W. Gordy, *J. Chem. Phys.*, **41**, 3661 (1964).
(11) J. L. Johnson, H. J. Cohen, and K. V. Rajagopalan, *Biochem. Biophys. Res. Commun.*, **56**, 940 (1974)
(12) T. Peters, *Adv. Clin. Chem.*, **13**, 37 (1970).
(13) (a) W. T. Shearer, R. A. Bradshaw, F. R. N. Gurd, and T. Peters, *J. Biol. Chem.*, **242**, 5451 (1968); (b) F. H. Reynolds, R. K. Burhard, and D. D. Mueller, *Biochemistry*, **12**, 359 (1973); (c) J. C. Cassatt, *J. Biol. Chem.*, **248**, 6129 (1973); (d) B. Sarkar and Y. Wigfield, *Can. J. Biochem.*, **46**, 601 (1968); (e) S. J. Lau, T. P. A. Kruck, and B. Sarkar, *J. Biol. Chem.*, **249**, 5878 (1974), and references therein.
(14) I. M. Kolthoff and B. R. Willeford, *J. Am. Chem. Soc.*, **80**, 5673 (1958).
(15) T. Peters and F. A. Blumenstock, *J. Biol. Chem.*, **242**, 1574 (1967).
(16) (a) R. Osterberg, *Acta Chem. Scand.*, **25**, 3827 (1971); (b) E. L. Giroux, *Biochem. Biophys. Acta*, **273**, 64 (1972); (c) M. S. N. Rao and H. Lal, *J. Am. Chem. Soc.*, **80**, 3222 (1958).
(17) A. S. Mildvan and M. Cohn, *Biochemistry*, **2**, 910 (1963).
(18) J. Reuben, *Biochemistry*, **10**, 2834 (1971).
(19) J. L. Sudmeier and J. J. Pesek, *Anal. Biochem.*, **41**, 39 (1971).
(20) H. A. Soper and R. A. Harte, "Handbook of Biochemistry", Chemical Rubber Company Press, Cleveland, Ohio, 1973, p C71.
(21) J. Francavilla, M.S. Thesis, University of New Hampshire, Durham, N.H., 1974.
(22) J. Francavilla and N. D. Chasteen, *Inorg. Chem.*, **14**, 2860 (1975).
(23) This assignment assumes a negative vanadium nuclear hyperfine coupling constant. Nuclear spin, $I = 7/2$.
(24) For a discussion of the validity of this procedure, see ref 6. In the early stages of the titration, addition of a 10^{-2} M VOSO$_4$ stock solution with a microliter syringe produced a high localized concentration of vanadyl ion resulting in a VO(OH)$_2$ precipitate which dissolved upon gentle agitation. As the titration progressed, the precipitate dissolved more slowly until at 3 equiv of VO^{2+} added, it would not completely dissolve with limited stirring. Extensive agitation of the solution to affect complete dissolution was not possible because of protein denaturation from froathing. In principle, all the precipitate should dissolve since the VO(IV) ion is soluble to 1×10^{-4} M at pH 5; for VO(OH)$_2$, $K_{sp} = 1.08 \times 10^{-22}$.[22] The highest free VO^{2+} ion concentration achieved in these experiments was only 6×10^{-5} M.
(25) G. Scatchard, J. S. Coleman, and A. L. Shen, *J. Am. Chem. Soc.*, **79**, 12 (1957).
(26) T. R. Hughes and I. M. Klotz, *Methods Biochem. Anal.*, **3**, 265 (1956).
(27) H. Tomiyasu and G. Gordon, *J. Coord. Chem.*, **3**, 47 (1973).
(28) K. Linderstrom-Lang and S. O. Nielson, "Acid-Base Equilibria of Proteins" in "Electrophoresis: Theory, Methods, and Applications", M. Bier, Ed., Academic Press, London, 1959, p 49.
(29) J. Peisach, P. Aisen, and W. E. Blumberg, Ed., "The Biochemistry of Copper", Academic Press, New York, N.Y., 1966, pp 19 and 87.
(30) W. L. Hubbell and H. M. McConnell, *J. Am. Chem. Soc.*, **93**, 314 (1971).
(31) N. Bloembergen, E. M. Purcell, and R. V. Pound, *Phys. Rev.*, **73**, 679 (1948)
(32) R. P. Mason and J. H. Freed, *J. Phys. Chem.*, **78**, 1321 (1974).

Effect of Electron Transfer on Electron Spin–Lattice Relaxation Rates

C. P. Cheng and S. I. Weissman*

Department of Chemistry, Washington University, Saint Louis, Missouri 63130 (Received October 23, 1975)

Electron spin–lattice relaxation times (T_1) have been measured in solutions of potassium tetracyanoethylene containing neutral tetracyanoethylene. In the slow exchange limit, T_1 as measured by progressive saturation of individual lines, becomes shorter with increasing rate as does T_2. In the fast exchange limit, T_1 reverts to its value in the absence of exchange. The bearing of the results on existence of short-lived intermediates is discussed.

1. Introduction

The effect of chemical exchange between a radical ion and its neutral precursor on ESR line width is well understood.[1-3] If the rate of exchange is slow, every hyperfine line is broadened; if the rate of exchange is fast, the hyperfine pattern collapses into a single line. However, the effect of chemical exchange on spin–lattice relaxation time has received relatively little attention.[4-8] In those cases in which the line shape has been observed over the entire range between the well-resolved hyperfine spectrum and the single motionally narrowed line, there have been small but nagging discrepancies between calculated and observed shapes in the intermediate region. The calculations are exact solutions for the line shape under the assumptions that the electron transfer occurs instantaneously with no change in electron spin state, and that the rate is independent of nuclear spin states of the participating molecules.[9,10] In the hope that measurements of the spin–lattice relaxation rate might yield some symptom of intervention of nonsecular processes in the electron exchange, we have undertaken the measurements here described.

KTCNE (potassium tetracyanoethylene) was chosen as radical ion and DME (dimethoxyethane) as solvent. The ESR spectrum of dilute KTCNE in DME solution consists of nine lines with spacing of 1.56 ± 0.02 G.[11] The intensity ratio of the nine lines is $1:4:10:16:19:16:10:4:1$ expected for four equivalent ^{14}N ($I = 1$) nuclei. The line shape of the hyperfine lines is Lorentzian.[12] The solubility of TCNE (tetracyanoethylene) in DME is about 2 M at room temperature. Because of this high solubility one can carry out experiments both in the slow exchange limit and in the fast exchange limit.

The effect of chemical exchange on spin–lattice relaxation time is investigated theoretically using the Bloch equations[13] approach in section 2. In section 3 experimental method is described. In section 4 experimental results are presented and compared with the theoretical prediction.

2. Theory

The Bloch equation in the presence of chemical exchange can be written[14]

$$\frac{dM_{a+}}{dt} + \alpha_a M_{a+} = i\gamma H_1 M_{az} + \sum_b k_b M_{b+} - k_a M_{a+} \quad (1a)$$

$$\frac{M_{az}}{dt} = -\gamma H_1 \operatorname{Im} M_{a+} - \frac{M_{az} - M_{a0}}{T_{1a}} + \sum_b k_b M_{bz} - k_a M_{az}$$

$$(1b)$$

where the M's are the magnetization of electron, subscripts a and b refer to specific nuclear spin configuration of the radical ion

$$\alpha_a = i(\omega_{0a} - \omega) + 1/T_{2a}$$

and $\operatorname{Im} M_{a+}$ is the imaginary part of M_{a+}.

Suppose the electron transfer process is independent of initial and final magnetic environment, then $k_a = k = N k_b$, where N is the number of different nuclear spin configurations of the radical ion. If there are different nuclear configurations which have the same α_i and T_{1i} with fraction P_i, in steady state the system of linear eq 1a and 1b becomes

$$G = \sum_{a=1}^{N} M_{a+} = i\gamma H_1 N \frac{\sum_i P_i M_{iz} f_i}{1 - k \sum_i P_i f_i} \quad (2a)$$

$$M_{iz} = M_{i0} - \gamma H_i T_{1i} \operatorname{Im} M_{i+} + \sum_j k T_{1j} P_j M_{jz} - k T_{1i} M_{iz}$$

$$(2b)$$

where $f_i = (\alpha_i + k)^{-1}$. Simple solution for system of eq 2a and 2b can be obtained in two special cases. Both cases will be discussed below.

a. *Slow Exchange Limit Case.* In this limit where all the hyperfine lines are well separated from each other the following inequality holds:

$$|\omega_i - \omega_j| T_{2j}' \gg 1 \quad (3)$$

where ω_i and ω_j are the resonance frequencies of different hyperfine lines and $1/T_{2j}' = 1/T_{2j} + k$. When the radio frequency ω is close to ω_i, using inequality 3, from eq 2a, one obtains

$$G = i\gamma H_1 M_{i0} \frac{N P_i T_{2i}''}{1 + i(\omega - \omega_i) T_{2i}''} \frac{M_{iz}}{M_{i0}} \quad (4)$$

where T_{2i}'' is defined by

$$\frac{1}{T_{2i}''} = \frac{1}{T_{2i}} + k(1 - P_i) = \frac{1}{T_{2i}} + \frac{1 - P_i}{\tau} \quad (5)$$

If saturation is negligible, i.e., $M_{iz} = M_{i0} = M_0/N$, one obtains

$$M_y = \operatorname{Im} G = \frac{\gamma H_i M_0 P_i T_{2i}''}{1 + (\omega - \omega_i)^2 T_{2i}''^2} \quad (6)$$

This is identical with the result obtained by Piette and Anderson.[3] If saturation is not negligible, one makes the following assumption in order to simplify eq 2b and 4: when ω

$\simeq \omega_i$, only those M_{az}'s which are involved in the transition at ω_i deviate appreciably from their thermal equilibrium value, the other M_{bz}'s are assumed to have their thermal equilibrium value. Using this assumption, eq 2b becomes

$$M_{iz} = M_{i0} - \frac{\gamma H_1 T_{1i} \operatorname{Im} M_{i+}}{1 + kT_{1i}(1 - P_i)} \qquad (7)$$

Substituting eq 7 into eq 4 one obtains

$$M_y = \operatorname{Im} G = \gamma H_1 M_0 P_i T_{2i}'' \Big/ \left[1 + (\omega - \omega_i)^2 T_{2i}'' + \gamma^2 H_1^2 T_2'' \frac{T_{1i}}{1 + kT_{1i}(1 - P_i)} \right] \qquad (8)$$

From eq 8, one obtains the effective spin–lattice relaxation time T_{1i}'' given by

$$\frac{1}{T_{1i}''} = \frac{1}{T_{1i}} + \frac{1 - P_i}{\tau} \qquad (9)$$

In this limiting case, the effect of chemical exchange on T_1 is the same as on T_2. One can test these predictions by measuring $1/T_1$ and $1/T_2$ as a function of the concentration of the neutral precursor. One expects to find that $1/T_1$ and $1/T_2$ depend linearly on the concentration with the same slope.

b. *Fast Exchange Limit Case.* In this limit all hyperfine lines collapse into a single line, and the inequality

$$|\omega_i - \omega_j| T_{2j}' \ll 1 \qquad (10)$$

can be assumed to hold.

The following two assumptions are made in order to simplify eq 2a and 2b. (1) In the absence of chemical exchange, all hyperfine lines have the same T_2, i.e., $T_{2i} = T_{2j} = T_2$. (2) In the absence of chemical exchange, all hyperfine lines have the same T_1, i.e., $T_{1i} = T_{1j} = T_1$. From eq 2b, one obtains

$$M_{iz} = M_{i0} - \frac{\gamma H_1 T_1 \operatorname{Im} M_{i+}}{1 + kT_1} - \frac{\gamma H_1 T_1 (kT_1/N) \operatorname{Im} G}{1 + kT_1} \qquad (11)$$

Substitute eq 11 into eq 2a, one obtains

$$G = (i\gamma H_1 M_0 - i\gamma^2 H_1^2 T_1 \operatorname{Im} G) \cdot \frac{\displaystyle\sum_i \frac{P_i}{1 + \alpha_i \tau}}{\displaystyle\sum_i \frac{P_i \alpha_i}{1 + \alpha_i \tau}} \qquad (12)$$

In obtaining eq 12, one has made the approximation that

$$\sum_i \frac{NP_i \operatorname{Im} M_{i+}}{1 + \alpha_i \tau} = \operatorname{Im} G \times \left(\sum_i \frac{P_i}{1 + \alpha_i \tau} \right)$$

This is a good approximation, because eq 10 is true in this limiting case. The technique developed in ref 3 can be used to simplify the assumption in eq 12

$$\sum_i \frac{P_i}{1 + \alpha_i \tau} \Big/ \sum_i \frac{P_i \alpha_i}{1 + \alpha_i \tau} = \frac{1}{\dfrac{1}{T_2} + i(\omega - \langle \omega_j \rangle) + \nabla T_2'}$$

where ∇ is the second moment of the radical ion spectrum in the absence of chemical exchange, and $\langle \omega_j \rangle = \Sigma_j P_j \omega_j$. From eq 12, one obtains

$$M_y = \operatorname{Im} G = \frac{\gamma H_i M_0 T_2''}{1 + (\omega - \langle \omega_j \rangle)^2 T_2''^2 + \gamma^2 H_1^2 T_1 T_2''} \qquad (13)$$

where T_2'' is defined by

$$\frac{1}{T_2''} = \frac{1}{T_2} + \nabla T_2'$$

If the chemical exchange is the dominant mechanism which causes the hyperfine lines to collapse into a single line, then

$$\frac{1}{T_2''} = \frac{1}{T_2} + \nabla \tau \qquad (14)$$

From eq 13, one concludes that the effective spin–lattice relaxation time is T_1, the spin–lattice relaxation time of the radical ion in the absence of chemical exchange.

One can test the predictions by measuring $1/T_1$ and $1/T_2$ as a function of concentration of neutral precursor. One expects to find in the fast limit that $1/T_2$ depends linearly on the inverse of concentration and $1/T_1$ is independent of concentration.

3. Experimental Method

3.1. *Chemicals.* TCNE was obtained from Eastman. It was purified by sublimation under vacuum three times.

DME was obtained from Eastman. It was purified by distillation, then dried over a sodium–potassium alloy. After drying, it was stored in a solvent bottle which contained the sodium–potassium alloy.

KTCNE was prepared by allowing purified TCNE to react with pure potassium (supplied by MSA Research Corp.) under vacuum using DME as solvent. Excess TCNE was used in order to prevent the formation of the dinegative ion. After the reaction was completed, solvent was pumped away. The resulting substance was heated to 120 °C to sublime the unreacted TCNE. The prepared KTCNE was identified by its visible spectrum, and it was sent to Galbraith Laboratories for quantitative analysis. The observed percentage of elements is nitrogen 33.30%, carbon 42.95% and the calculated percentage is nitrogen 33.53%, carbon 43.11%.

3.2. *Sample Preparation.* Because there is the Heisenberg exchange effect in KTCNE solution, it is convenient to keep the KTCNE concentration the same for all samples.

All ESR sample tubes were Pyrex and have been selected so that they have the same inside and outside diameter. All glassware used in sample preparation has been carefully cleaned. All graduated tubes used in volume measurements were calibrated. A large volume of known KTCNE concentration (5×10^{-5} M) solution was prepared. Then a known amount of TCNE was introduced into the KTCNE solution through a breakseal. A small amount of this solution was introduced into an ESR sample tube which could be separated from the rest of the glass apparatus by a rotaflo stopcock. Then this tube was sealed off. More TCNE was dissolved in the KTCNE solution, and some solution was introduced into other ESR sample tubes and sealed off. This procedure was repeated again, until one prepared all the desired ESR sample tubes. All the above procedures were carried out under vacuum. The concentration of TCNE ranged from 1×10^{-3} to 6×10^{-2} M for the slow exchange limit experiment.

It is known[15] that there is a photoinduced radical ion formation of TCNE in DME solution. Samples prepared for the fast exchange limit experiment must be shielded against light. A large volume of known KTCNE concentration (1×10^{-4} M) solution was prepared. About 10 cm^3 of this solution was introduced into an ESR sample tube which consisted of a graduated tube, a breakseal containing

a weighed amount of TCNE, and an ESR probe tube. Then this tube was sealed off. These procedures were repeated until the desired amount of sample tubes were prepared. The breakseal was broken just before measuring the line width. The concentration of TCNE for the fast exchange limit experiments range from 0.5 to 1.8 M. All samples were stored in a freezer when not in use.

3.3. *Spectrometer.* All line widths were measured using a Varian E-3 X-band spectrometer with some modifications. A lockin amplifier HR-8, made by Princeton Applied Research Corp., was used to generate the modulation field and to detect the signal in order to avoid the effect of high modulation frequency. A 10 dB direction coupler was inserted in the E-3 waveguide network in order to measure the microwave power incident upon the cavity. The microwave power was measured by power meter Model 454A made by the General Microwave Corp. with Model 420 tfr power head. Temperature was controlled by a home-made temperature control which can control the temperature to within 0.5 °C. The loaded quality factor Q_L was measured by an Alfred sweep oscillator Model 650 and an Alfred sweep network analyzer Model 7051. In the slow exchange limit experiment all line widths measured never exceeded 500 mG in order to avoid the error originating from the interference between neighboring hyperfine lines.[16]

4. Result and Discussion

4.1. *Result for the Slow Exchange Limit Experiment.* Three lines have been studied in this experiment: the central line, the line next to the central line, and the second line away from the central line on the high-field side. The reasons that only three lines have been studied are as follows. (1) The lines on the wing of ESR spectrum are so weak that their width cannot be accurately measured and there are possible line shape distortions from the ^{13}C hyperfine splittings. (2) The corresponding lines on each side of the central line are expected to behave the same in this experiment. The line width of each line was measured three times at four different microwave powers and at four different temperatures for samples with different TCNE concentration. The consistency of the line width measurement is that the standard deviation is less than 5% of the average line width. The observed line width depends on radiation field amplitude H_1 as

$$\gamma \Delta H_{pp} = \frac{2}{\sqrt{3}} \frac{\sqrt{\gamma^2 H_1^2 T_1 T_2 + 1}}{T_2} \tag{15}$$

H_1 depends on the microwave power incident upon the microwave cavity as

$$\langle H_1^2 \rangle_s = K P_w Q_L \tag{16}$$

where P_w is the microwave power incident upon the cavity, Q_L is a loaded quality factor, K is a constant that depends on the filling factor, $\langle H_1^2 \rangle_s$ is the average H_1^2 over the sample inside the cavity. ΔH_{pp} is the true line width. The line width measured depends on the modulation amplitude H_m as[17,18]

$$\Delta H_{ppobsd} = \Delta H_{pp} \left(\frac{H_m}{\Delta H_{pp}} \right)^2 + 5 - 2 \left[\left(4 + \left(\frac{H_m}{\Delta H_{pp}} \right)^2 \right]^{1/2} \tag{17}$$

and the amplitude of the observed signal depends on the modulation amplitude as

TABLE I: K_{CE} Obtained from the Slow Exchange Limit Experiment

Temp, °C	k_{CE},[a] M^{-1} s^{-1}	k_{CE},[b] M^{-1} s^{-1}
−54.0	$(9.21 \pm 9.11) \times 10^6$	$(1.01 \pm 0.34) \times 10^7$
−33.5	$(2.49 \pm 0.27) \times 10^7$	$(2.34 \pm 0.39) \times 10^7$
−9.2	$(7.36 \pm 0.89) \times 10^7$	$(5.52 \pm 1.05) \times 10^7$
7.8	$(1.78 \pm 0.90) \times 10^8$	$(1.45 \pm 0.17) \times 10^8$

[a] Rate constant obtained from T_2 measurement. [b] Rate constant obtained from T_1 measurement.

$$A_{1pp} = \frac{C \left(\dfrac{H_m}{\Delta H_{pp}} \right)}{\left\{ 3 \left(\dfrac{H_m}{\Delta H_{pp}} \right)^2 + 8 + \left[\left(\dfrac{H_m}{H_{pp}} \right)^2 + 4 \right]^{3/2} \right\}^{1/2}} \tag{18}$$

where A_{1pp} is the peak-to-peak amplitude. From the above consideration one concludes that the parameters needed in calculating T_1 and T_2 are H_m, Q_L, and K.

The modulation amplitude is proportional to the voltage applied to the modulation coil. The line widths and amplitudes of a narrow ESR line were measured at five different voltages. A computer program was written to fit the experimental data to eq 17 and 18. The results are that the modulation amplitude used in this experiment is 33.4 mG from line width analysis and 34.6 mG was used in data analysis. The average value $H_m = 34.0$ mG was used in data analysis. Q_L's of all the samples prepared for this experiment were measured at the fixed coupling condition used in line width measurement at room temperature. They are constant within experimental error. The average Q_L is 2610 ± 160. The temperature dependence of Q_L for samples used in the fast exchange limit has been studied. The results indicated that Q_L is independent of temperature. Hence Q_L's will be regarded as constant in data analysis.

The parameter K was considered to be constant for all samples used in this experiment. It was determined by assuming $T_1 = T_2$ for dilute (5×10^{-5} M) KTCNE in DME solution. This assumption was verified later by measuring T_1 and T_2 of a 5.22×10^{-5} M KTCNE in DME solution using the pulse ESR technique at room temperature. The measurement[19] showed that $T_1 = 2.2$ μs and $T_2 = 2.2$ μs for the three lines studied in this experiment.

The T_1's and T_2's were calculated by the following procedures. First all line widths were corrected for modulation amplitude broadening by using eq 17. Then the line widths at four different microwave powers for a specific sample, a specific line at specific temperature, were put into the computer to fit them with the equation

$$\gamma \Delta H_{pp} = \frac{2}{\sqrt{3}} \frac{\sqrt{1 + P_\omega T_1 T_2}}{T_2}$$

The computer program used the algorithm of Marquardt[20] for the nonlinear least-squares fit. From the nonlinear least-squares fit one obtained T_2 and relative value of T_1. The absolute values of T_1's were obtained by setting $T_1 = T_2$ for samples without TCNE. After the T_1's and T_2's for one line at one temperature were calculated, $1/T_1$'s and $1/T_2$'s were fit linearly with respect to the TCNE concentration to obtain the chemical exchange rate $k = k_{CE}[TCNE]$. The temperature dependence of the TCNE concentration was corrected by using the DME density data determined by Carvajal, Tolle, Smid, and Szwarc.[21] The rate constants k_{CE} obtained after appropriate averaging are listed in Table I. Most of the chemical exchange rate constants k_{CE}

obtained from $1/T_1$ measurements are smaller than the corresponding rate constants obtained from T_2 measurements. This discrepancy will be considered now. In deriving eq 17, the assumption was made that when $\omega \simeq \omega_i$ only those M_{iz}'s involved in the transitions at resonance frequency ω_i deviate appreciably from their thermal equilibrium value; all the other M_{jz}'s are assumed to have their thermal equilibrium value. The discrepancy comes mainly from this assumption. If the assumption is neglected, then in the steady state one has to solve the following equations:

$$G = \frac{i\gamma H_i N \sum P_i M_{iz} f_i}{1 - k \sum_i P_i f_i} \quad (2a)$$

$$M_{iz}(1 + kT_{1i}(1 - P_i)) = M_{i0} - \gamma H_1 T_{1i} \operatorname{Im} M_i + kT_{1i} \sum_{j \neq i} P_j M_{jz} \quad (19)$$

$$M_{jz} = M_{j0} - \gamma H_1 T_{1j} \operatorname{Im} M_{j+} + kT_{ij} \sum_l P_l M_{lz} - kT_{1j} M_{jz} \quad (20)$$

The following assumptions will be made in order to simplify the solution of the above equation: (1) all T_{1i}'s and T_{2i}'s in the dilute radical ion solution are assumed to be the same, i.e., $T_{1i} = T_{1j} = T_1$; (2) when $\omega \simeq \omega_i$, the second term $\gamma H_1 T_{1j} \operatorname{Im} M_{j+}$ on the right-hand side of eq 20 will be assumed to be negligible; (3) when $\omega \simeq \omega_i$, all the M_{jz}'s except M_{iz}'s are assumed to be equal. This is perceivable because the only mechanism for M_{jz}'s to deviate from thermal equilibrium value comes from the chemical exchange. Using these assumptions, from eq 19 and 20, one obtains

$$M_{iz} = \frac{b}{a} M_{i0} - \frac{\gamma H_i T_i \operatorname{Im} M_{i+}}{a} \quad (21)$$

where

$$a = 1 + kT_i(1 - P_i) - \frac{k^2 T_1 P_i(1 - P_i)}{1 + kT_1 P_i}$$

$$b = 1 + \frac{kT_1(1 - P_i)}{1 + kT_1 P_i}$$

Substituting eq 21 for eq 2a and using the slow exchange limit condition, one obtains

$$M_y = \frac{(b/a)\gamma H_i M_0 P_i T_2''}{1 + (\omega - \omega_i)^2 T_{2i}'' + \gamma^2 H_i^2 (T_1/a) T_2''} \quad (22)$$

From this equation one draws the conclusion that the effective spin–lattice relaxation time T_1'' is

$$\frac{1}{T_1''} = \frac{1}{T_1} + \frac{1 - P_i}{\tau} - \frac{i^2 T_i(1 - P_i)}{1 + kT_1} \quad (23)$$

Comparing eq 23 with eq 9, one sees that the first two terms are identical. The last term makes a large contribution to $kT_1 \gtrsim 1$. Thus the discrepancy between k_{CE} measured from T_1 and T_2 can be explained. If the last term in eq 23 cannot be neglected, further increase in TCNE concentration will produce only slight increase in $1/T_1''$. This behavior has been observed experimentally. In Figure 1, $1/T_1$'s and $1/T_2$'s are plotted against the TCNE concentrations to illustrate eq 23.

4.2. *Result for the Fast Exchange Limit Experiment.* In this experiment, line widths have been measured three times for each sample at eight different microwave powers and at four different temperatures. The consistency of the
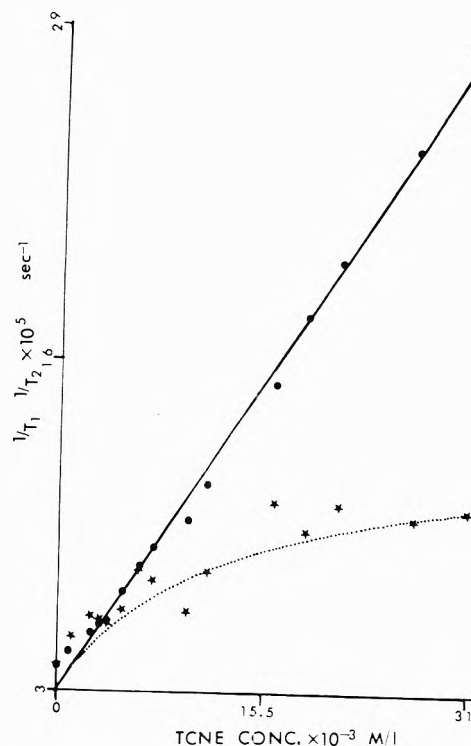
Figure 1. $1/T_1$ and $1/T_2$ of center line at -9.2 °C: circles, $1/T_2$; stars, $1/T_1$. The solid line is a linear least-squares fit of $1/T_2$ vs. [TCNE]. The dotted line is calculated from eq 22 using parameters obtained from the least-squares fit.

line width measurement is that the amplitude used in this experiment is either 32.6 or 82.9 mG depending on the signal-to-noise ratio. The loaded quality factors for all samples including the sample used in determining the parameter K have been measured at fixed coupling condition used in line width measurement at four different temperatures. The results are that at 30.9 °C $Q_L = 3840 \pm 110$, at 41.3 °C $Q_L = 3800 \pm 140$, at 49.0 °C $Q_L = 3780 \pm 200$, and at 59.5 °C $Q_L = 3920 \pm 100$. They are constant within experimental error. In determining the parameter K, a 7.0×10^{-2} M BDPA $(\alpha,\alpha,\gamma,\gamma\text{-bis(diphenylene)-}\beta\text{-phenylallyl})$ in DME solution was used. The T_1 of this sample has been measured by Brandle, Kruger, and Muller-Warmuth.[22] The method of computing T_1 and T_2 from the measured line widths and microwave powers is the same as in the slow exchange limit experiment. From the linear least-squares fit of $1/T_2$ vs. $1/[\text{TCNE}]$, one can calculate the chemical exchange rate constant k_{CE}. The Heisenberg exchange can be considered as a correlated chemical exchange. If one keeps the KTCNE concentration small compared to the TCNE concentration, the effective T_1 should be independent of the KTCNE concentration. This conclusion is verified in this experiment, two different concentrations of KTCNE, 3.38×10^{-4} and 3.75×10^{-4} M, were used in this experiment. The measured T_1's are constant within experimental error. They are listed along with the rate constant k_{CE} in Table II.

4.3. *Conclusion and Discussion.* The exchange rate constant k_{CE} depends on temperature as

$$k_{CE} = k_0 \exp[-(E_a/RT)]$$

If the k_{CE}'s calculated from $1/T_2$ measurements are fitted to the above equation, one obtains $\log k_0 = 12.49 \pm 0.13$ and $E_a = 5.54 \pm 0.16$ kcal/mol. These values agree very well

TABLE II: k_{CE} and T_1 Obtained from the Fast Exchange Limit Experiment

Temp, °C	k_{CE}, $M^{-1} s^{-1}$	T_1, s
30.9	$(3.60 \pm 0.14) \times 10^8$	$(1.76 \pm 0.43) \times 10^{-6}$
41.3	$(4.55 \pm 0.20) \times 10^8$	$(1.96 \pm 0.38) \times 10^{-6}$
49.0	$(4.89 \pm 0.20) \times 10^8$	$(2.14 \pm 0.17) \times 10^{-6}$
59.5	$(6.21 \pm 0.21) \times 10^8$	$(2.12 \pm 0.19) \times 10^{-6}$

with the data obtained by Watts, Lu, Chen, and Eastman.[23]

The conclusion that the chemical exchange effect on the spin–lattice relaxation time is that in the slow exchange limit $1/T_{1i}'' + (1 - F_i)/\tau$ and in the fast exchange limit T_1 is the intrinsic radical ion T_1 can be understood physically. The spin–lattice relaxation time is the time constant for the z component of magnetization approaching its thermal equilibrium value. In the slow exchange limit case chemical exchange provides another relaxation mechanism besides those present in the radical-ion solution. When the magnetization M_z at resonance frequency ω_i is saturated by a microwave field at frequency $\omega \simeq \omega_i$, the electrons will jump to other sites through chemical exchange. If one of them jumps to a site with a resonance frequency other than ω_i, the magnetization M_z loses part of its saturated M_{iz} and obtains other magnetization closer to its thermal equilibrium value. This kind of jump provides relaxation. If it jumps to a site with resonance frequency ω_i, this jump does not provide relaxation. This is why one has the $(1 - P_i)$ factor. In the fast exchange limit, the rate of jump is so fast that an electron can be considered as moving in an effective field produced by nuclear spins of the radical ion besides the field applied externally. One has to consider the total magnetization as a whole instead of dividing it into magnetizations at resonance frequencies ω_i, ω_j, etc., as in the slow exchange limit case. Hence the chemical exchange in this case cannot be considered as a relaxation mechanism. Nonsecular contributions of the exchange process could arise from excursions of short duration with large changes in the local magnetic field. One possible process of this could be an enhanced counterion hyperfine splitting during exchange. In the KTCNE–DME system, no potassium splitting characteristic of contact ion pairing was observed. Consequently, it may be supposed that this system involves essentially solvent-separated ion pairs. If the electron transfer reaction is accompanied by a counterion transfer through the formation of a sandwich structure in the transition state,[24] then in the transition state the electron will experience a hyperfine interaction due to the potassium nucleus (^{39}K, $I = 3/2$, natural abundance 93.10%). This hyperfine interaction contains terms such as I_+S_- and I_-S_+. These two terms contribute to the electron spin–lattice relaxation time in the transition state. The contribution from the hyperfine pulses can be approximated as[25]

$$\frac{1}{T_{1hf}} = \frac{\tau_2}{\tau} \frac{A^2 \tau_2}{1 + \omega_0^2 \tau_2^2} \tag{24}$$

where T_{1hf} is the electron spin–lattice relaxation time due to the hyperfine interaction in the transition state, A is the hyperfine coupling constant in the transition state, τ_2 is the average lifetime of the transition state, τ is the time between successive electron jumps which is equal to the inverse of k_{CE} times TCNE concentration, and ω_0 is electron Lamor frequency. If the contribution from the hyperfine pulses to total electron spin–lattice relaxation time is not

negligible, one would be able to observe this contribution in the fast exchange limit experiment.

In this research it is shown that in the fast exchange limit the observed electron spin–lattice relaxation time is the same as the intrinsic electron spin–lattice relaxation time of the radical ion. Consequently, it may be supposed that τ_2 is very short or there is no such kind of transition state at all in this system. One can give a rough estimate of τ_2 from eq 24, using the data that $1/\tau = 10^9$ s^{-1}, assuming that in transition state the hyperfine coupling constant A is the same as in atomic potassium, roughly 100 G and neglecting $\omega_0^2 \tau_0^2$ one obtains the following inequality:

$$\frac{1}{T_{1nf}} \simeq 4 \times 10^{27} \tau_2^2 \lesssim \frac{1}{T_1} \simeq 5 \times 10^5$$

From this inequality, τ_2 is approximately 10^{-11} s.

If there is a sandwich transition state, one may ask whether in the slow exchange limit the transition state affects the electron spin–lattice relaxation time? The answer is no. In the slow exchange limit, the chemical exchange process provides a path for the saturated electrons to jump to other nonresonant environments and simultaneously bring unsaturated electrons into the resonant environments to be saturated as explained before.

If the spin–lattice relaxation times had been measured by the method of Bloembergen and Wang[26] in which the recovery of the total magnetization *parallel* to the external field was recorded, no effect of chemical exchange would have been observed owing to the commutation of $\langle S_z \rangle_{total}$ with the exchange Hamiltonian. Pulse methods similar to those frequently used in nuclear magnetic resonance in which the temporal behavior of each part of the spectrum is observed would presumably have yielded results equivalent to those which we have found. Pulse methods are preferable but we mastered the necessary experimental methods too late.

References and Notes

(1) P. W. Anderson, *J. Phys. Soc. Jpn.*, **9**, 316 (1954).
(2) R. L. Ward and S. I. Weissman, *J. Am. Chem. Soc.*, **79**, 2086 (1957).
(3) L. H. Piette and W. A. Anderson, *J. Chem. Phys.*, **30**, 899 (1959).
(4) H. M. McConnell, *J. Chem. Phys.*, **28**, 430 (1958).
(5) T. J. Swift and R. E. Connick, *J. Chem. Phys.*, **37**, 307 (1962).
(6) D. E. O'Reilly and C. P. Poole, *J. Phys. Chem.*, **67**, 1762 (1963).
(7) J. Sohma, *J. Chem. Phys.*, **37**, 2151 (1962).
(8) J. H. Freed, *J. Phys. Chem.*, **71**, 38 (1967).
(9) N. Haran, Z. Luz, and M. Shporer, *J. Am. Chem. Soc.*, **96**, 4788 (1974).
(10) M. A. Komarynsky, Ph.D. Thesis, Washington University, 1969.
(11) W. D. Phillips, J. C. Rowell, and S. I. Weissman, *J. Chem. Phys.*, **33**, 626 (1960).
(12) M. P. Eastman, R. G. Kooser, M. R. Das, and J. H. Freed, *J. Chem. Phys.*, **51**, 2690 (1969).
(13) F. Bloch, *Phys. Rev.*, **70**, 460 (1946).
(14) P. D. Sullivan and J. R. Bolton, *Adv. Magn. Reson.*, **4**, 39 (1970).
(15) R. L. Ward, *J. Chem. Phys.*, **39**, 852 (1963).
(16) W. Plachy and D. Kivelson, *J. Chem. Phys.*, **47**, 3312 (1967).
(17) H. Wahguist, *J. Chem. Phys.*, **35**, 1780 (1961).
(18) R. Arndt, *J. Appl. Phys.*, **36**, 2522 (1965).
(19) D. J. Sloop and C. Cheng, unpublished result.
(20) P. R. Bevington, "Data Reduction and Error Analysis for the Physical Sciences", McGraw-Hill, New York, N.Y., 1969.
(21) C. Carvajal, K. J. Tolle, J. Smid, and M. Szwarc, *J. Am. Chem. Soc.*, **87**, 5548 (1965).
(22) R. Brandle, G. J. Kruger, and W. Muller-Warmuth, *Z. Naturforsh. A*, **25**, 1 (1970).
(23) M. T. Watts, M. L. Lu, R. C. Chen, and M. P. Eastman, *J. Phys. Chem.*, **77**, 2959 (1973).
(24) F. C. Adam and S. I. Weissman, *J. Am. Chem. Soc.*, **80**, 1518 (1958).
(25) N. Bloembergen, *J. Chem. Phys.*, **27**, 572 (1957).
(26) N. Bloembergen and S. Wang, *Phys. Rev.*, **93**, 72 (1954).

Quantum Mechanical Formalism for Computation of the Electronic Spectral Properties of Chlorophyll Aggregates[1]

Lester L. Shipman, James R. Norris, and Joseph J. Katz*

Chemistry Division, Argonne National Laboratory, Argonne, Illinois 60439 (Received October 23, 1975)

Publication costs assisted by Argonne National Laboratory

An improved exciton formalism is presented that permits more accurate evaluation of environmental (solvent and/or neighboring chlorophyll molecules) effects on the electronic transition energies of chlorophyll aggregates. This formalism, based on well-established exciton theory for molecular crystals, clearly shows that the environmental shifts and transition density–transition density shifts of the electronic transition energies of molecular aggregates are not additive (except in special cases) as has been generally assumed previously. Explicit equations have been derived for (a) the lower excited singlet state wave functions of chlorophyll dimer, and (b) transition energies and transition dipoles for the ground to lower excited singlet state transitions in chlorophyll dimer. The formalism is applied to a discussion of the nature of antenna chlorophyll and the electronic relationship between antenna chlorophyll and photoreaction trap chlorophyll. Much of the formalism in this paper is not restricted to chlorophyll aggregates and is applicable in general to aggregates containing a mixture of light-absorbing (chromophore) molecules and solvent molecules.

I. Introduction

Frenkel[2-4] was the first to introduce the concept of excitation waves (excitons) to explain the electromagnetic spectra of crystals. Later, the concept of excitons was developed in detail for molecular crystals by Davydov.[5] Much of the formalism[5-8] for excitons in crystals can also be applied directly to noncrystalline (i.e., nonperiodic) molecular aggregates. Our interest in exciton theory arose from our concern with the primary events of light collection and conversion in photosynthesis. These primary events are generally believed to occur within a photosynthetic unit[9-11] in which several hundred or more associated chlorophyll (Chl) molecules act cooperatively to absorb, transport, and convert light energy. In the photosynthetic unit light energy is absorbed by antenna Chl (which consists of the great majority of the Chl molecules present) where it is converted into electronic excitation energy. This excitation energy is then transferred very efficiently to a few special[12] chlorophyll molecules in a photoreaction center[13] where oxidizing and reducing capacity is generated.

Exciton theory has been used[14-20] to calculate the electronic spectral properties of Chl aggregates. Unfortunately, the formulations[18,21,22] applied in these previous studies[14-20] can be shown to be inapplicable either because the effects of the environment have been totally neglected, or because identical environmental transition energy shifts have been assumed for all chromophore molecules. In the present paper we present an improved exciton formalism for Chl aggregates that explicitly includes the effects of the environment. The formalism is not restricted to Chl aggregates, however, and is applicable in general to aggregates containing a mixture of light-absorbing (chromophore) molecules and solvent molecules. We are well aware that exciton states have been treated correctly for the case of molecular crystals,[5-8] and thus the basic physics of our formalism is not novel. However, previous applications of exciton theory to molecular aggregates have been subjected to simplifying assumptions regarding environmental effects, and these may seriously affect the validity of conclusions

drawn about the electronic structure of molecular aggregates. We believe that the formalism presented here is more appropriate than earlier ones for many problems of particular interest to chemists.

II. Chlorophyll Aggregates

Nuclear magnetic resonance[23-26] and infrared spectroscopic[23,24,27,28] studies have shown that the central magnesium atom of Chl is coordinatively unsaturated when assigned a coordination number of 4, as is the case in the structural formula as usually written (Figure 1). Thus, there is a strong tendency for one or both of the Mg axial positions to contain an electron donor group.[29] The donor ligand can be a typical Lewis base (e.g., a polar solvent such as acetone, pyridine, or diethyl ether that acts as a monofunctional donor), in which case monomeric Chl species, Chl·L_1 and Chl·L_2,[30] are formed. If the donor is a bifunctional ligand (e.g., dioxane, pyrazine), then cross-linked Chl species, which may be of colloidal dimensions, can be formed.[31,32] Water is a particularly important bifunctional ligand, for the oxygen atom can be coordinated to the Mg atom of one Chl molecule, and the two hydrogen atoms are then available for hydrogen bonding to one (or possibly two) other Chl molecules.[33,34] In the absence of other donors a Chl molecule can act as donor (via its keto C=O function at position 9 in ring V, Figure 1) to the Mg atom of another Chl.[35] The keto C=O···Mg self-aggregation can lead to the formation of dimers or oligomers,[36] depending upon conditions. Spectroscopic comparisons of in vivo Chl with various Chl species that can be prepared in vitro have led to the tentative identification of hydrated Chl dimer with photoreaction Chl,[37-43] and the Chl oligomer (Chl)$_n$ with antenna Chl.[44]

III. Electronic Spectral Properties of Molecular Aggregates

In this section we present a formalism for calculating the electronic spectral properties of chromophore-containing molecular aggregates of arbitrary structure and composi-
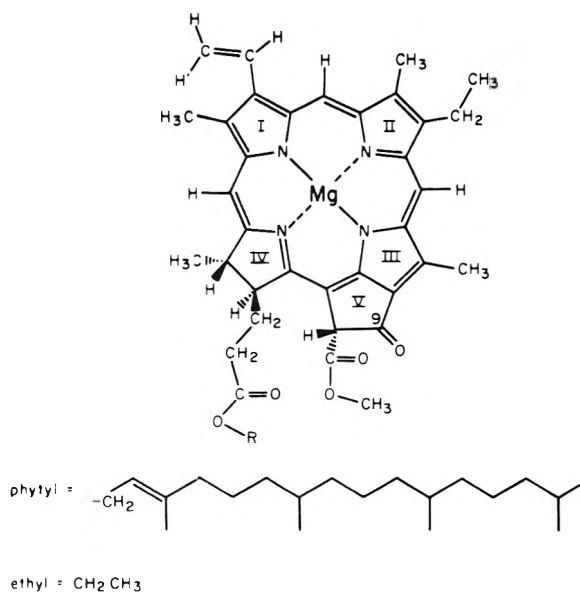
Figure 1. Molecular structures for chlorophyll a (Chl a) and ethyl chlorophyllide a: R = phytyl for chlorophyll a; R = ethyl for ethyl chlorophyllide a.

tion. In the present paper we will consider only the case where the Born–Oppenheimer approximation[45] holds for the aggregate.

Consider an aggregate of N molecules composed of one or more types of chromophore molecules along with some solvent molecules.[46] Let $\varphi_i{}^k$ denote the electronic wave function (under the Born–Oppenheimer approximation) for the kth electronic state of the ith molecule in the aggregate. If the overlap between the molecules is small,[47] the ground electronic state wave function, ψ^g, for the aggregate may be approximated by the (zeroth-order) wave function

$$\psi^g = \prod_i^N \varphi_i{}^0 \qquad (1)$$

where $\varphi_i{}^0$ is the ground state electronic wave function for the ith molecule when isolated. The Hamiltonian operator, $\hat{H}$, for the system contains electronic kinetic energy, electron–nuclear Coulombic interaction, electron–electron Coulombic interaction, and nuclear–nuclear Coulombic interaction terms and may be partitioned as follows:

$$\hat{H} = \sum_{i=1}^N \hat{H}_i + \sum_{i<j}^N \hat{H}_{ij} \qquad (2)$$

where $\hat{H}_i$ involves only electrons and nuclei on the ith molecule and $\hat{H}_{ij}$ contains electron–electron, nuclear–nuclear, and nuclear–electron Coulombic interaction terms between molecule i and molecule j. The energy (to first order[48]) of the ground state, E^g, of the aggregate may be written as

$$E^g = \langle \psi^g | \hat{H} | \psi^g \rangle \qquad (3)$$

$$= \sum_i^N E_i{}^0 + \sum_{i<j}^N \langle \varphi_i{}^0 \varphi_j{}^0 | \hat{H}_{ij} | \varphi_i{}^0 \varphi_j{}^0 \rangle \qquad (4)$$

where $E_i{}^0$ is the energy of the ith molecule in its ground state as an isolated molecule, and $\langle \varphi_i{}^0 \varphi_j{}^0 | \hat{H}_{ij} | \varphi_i{}^0 \varphi_j{}^0 \rangle$ is the Coulombic interaction energy between the ith molecule and jth molecule, both in their ground states.

Nonstationary excited electronic states may be formed in much the same way as the ground state wave function was formed, i.e., by taking products of the wave functions for

individual molecules with one or more of the molecules in excited states. For example

$$\phi_i = \left(\prod_{j=1}^{i-1} \varphi_j{}^0 \right) \varphi_i{}^1 \left(\prod_{j=i+1}^{N} \varphi_j{}^0 \right) \qquad (5)$$

is the (zeroth-order) wave function that represents the nonstationary excited state with the ith molecule excited to its first excited state with all other molecules remaining in their ground states. Additional ϕ_i's can be constructed that correspond (a) to just one molecule excited to a singlet state other than the first excited singlet state, (b) to two or more molecules excited, or (c) to charge transfer between molecules. Quasi-stationary electronic states are formed by taking linear combinations of the ϕ_i's; the linear coefficients are determined by minimizing the total energy with respect to the linear coefficients (variational method). The problem of determining the linear coefficients reduces to the problem of finding the unitary matrix, **U**, that diagonalizes the matrix, **H**, where

$$H_{ii} = \langle \phi_i | \hat{H} | \phi_i \rangle \qquad (6)$$

$$H_{ij} = H_{ji} = \langle \phi_i | \hat{H} | \phi_j \rangle \qquad (7)$$

and

$$\mathbf{U}^{\dagger} \mathbf{H} \mathbf{U} = \epsilon \qquad (8)$$

The quasi-stationary states, ψ_i, of energy ϵ_i (to first order[48]) are given by

$$(\psi_1, \psi_2, \ldots) = (\phi_1, \phi_2, \ldots) \mathbf{U} \qquad (9)$$

It should be pointed out that the states, ϕ_i, are nonstationary; if a single molecule is excited, the excitation energy will not remain localized on that molecule, but spreads in time to other molecules. The states, ψ_i, are called quasi-stationary here because they are purely electronic wave functions, and coupling to the nuclear motions would bring about a transfer of energy from electronic excitation energy to nuclear motions (i.e., heat).

Consider the lowest energy excited singlet state of the aggregate. We construct this state by taking a linear combination of the nonstationary states, ϕ_i, as defined in eq 5. The elements of **H** simplify to

$$H_{ii} = E_i{}^1 + \sum_{j \neq i}^N E_j{}^0 + \sum_{\substack{j<k \\ j \neq i \neq k}}^N \langle \varphi_j{}^0 \varphi_k{}^0 | \hat{H}_{jk} | \varphi_j{}^0 \varphi_k{}^0 \rangle$$
$$+ \sum_{j \neq i}^N \langle \varphi_i{}^1 \varphi_j{}^0 | \hat{H}_{ij} | \varphi_i{}^1 \varphi_j{}^0 \rangle \qquad (10)$$

and

$$H_{ij} = H_{ji} = \langle \varphi_i{}^0 \varphi_j{}^1 | \hat{H}_{ij} | \varphi_i{}^1 \varphi_j{}^0 \rangle \qquad (11)$$

where $\varphi_i{}^1$ is the wave function for the lowest excited singlet state of the ith molecule, $E_i{}^1$ is the energy of the lowest excited singlet state of the ith molecule, $E_j{}^0$ is the energy of the ground state of the jth molecule, $\langle \varphi_j{}^0 \varphi_k{}^0 | \hat{H}_{jk} | \varphi_j{}^0 \varphi_k{}^0 \rangle$ is the interaction energy between the jth molecule in its ground state, and the kth molecule in its ground state, $\langle \varphi_i{}^1 \varphi_j{}^0 | \hat{H}_{ij} | \varphi_i{}^1 \varphi_j{}^0 \rangle$ is the interaction energy between the ith molecule in its lowest excited singlet state and the jth molecule in its ground state, and $\langle \varphi_i{}^0 \varphi_j{}^1 | \hat{H}_{ij} | \varphi_i{}^1 \varphi_j{}^0 \rangle$ is the interaction energy between the transition density, $\varphi_i{}^1 \varphi_i{}^0$, on the ith molecule and the transition density, $\varphi_j{}^1 \varphi_j{}^0$, on the jth molecule.[49] If we modify the **H** to **H'** by subtracting the ground state energy (eq 4) of the aggregate from each H_{ii}, the same unitary matrix, **U**, that diagonalizes **H** will

also diagonalize $\mathbf{H}'$; thus, the eigenvectors will be unchanged but the eigenvalues, ϵ_i, will now be transition energies from the ground state.

$$H_{ii}' = E_i^1 - E_i^0 + \sum_{j \neq i}^{N} \langle \varphi_i^1 \varphi_j^0 | \hat{\mathcal{H}}_{ij} | \varphi_i^1 \varphi_j^0 \rangle -$$

$$\sum_{j \neq i}^{N} \langle \varphi_i^0 \varphi_j^0 | \hat{\mathcal{H}}_{ij} | \varphi_i^0 \varphi_j^0 \rangle \quad (12)$$

and

$$H_{ij}' = H_{ji}' = \langle \varphi_i^0 \varphi_j^1 | \hat{H}_{ij} | \varphi_i^1 \varphi_j^0 \rangle \quad (13)$$

Consider an aggregate composed of M chromophore molecules (not necessarily identical) with comparable ground to first excited singlet state transition energies and $N - M$ solvent molecules.[46] It follows from nondegenerate perturbation theory that the solvent molecules will affect the energy of the aggregate only through the ground state of the solvent molecules interacting differentially with the ground and first excited states of the chromophore molecules. Thus, if we are only interested in the N lowest excited singlet states of the aggregate, the solvent effects may be retained in the chromophore diagonal elements of $\mathbf{H}'$, and the matrix, $\mathbf{H}'$, to be diagonalized may be reduced from an $N \times N$ to an $M \times M$ matrix, $\mathbf{H}''$. The $\mathbf{H}''$ matrix then contains isolated molecule transition energies plus the environmental shifts (due to solvent molecules and chromophore molecules in their ground states) on the diagonal and the transition density–transition density interaction energies between chromophore molecules on the off-diagonal.

IV. Application of the Formalism

We now consider the kinds of information needed for practical implementation of the formalism to chemical problems. If the molecules in the aggregate under study have permanent dipole moments, and if each chromophore molecule has a significant change in its dipole moment in going from the ground state to the first excited singlet state, then the *minimum* information about isolated molecules needed to apply the exciton formalism presented in this paper is (a) the ground state to first excited singlet state transition energies of the chromophore molecules; (b) the ground state permanent dipole moment vectors for all molecules in the aggregate; (c) the first excited singlet state dipole moment vectors (or alternatively, the vector difference, $\vec{\mu}_e - \vec{\mu}_g$, between the first excited singlet state dipole moment and the ground state dipole moment) for all the chromophore molecules; and (d) the transition dipole moment vector for the ground to first excited singlet state transition of the chromophore molecules.

The quantities a–d are used to construct an approximate H'' matrix in the following way. The off-diagonal matrix element, H_{ij}'', is the dipole–dipole interaction energy between the transition dipole on chromophore i and the transition dipole on chromophore j. The diagonal element, H_{ii}'', is the ground to first excited singlet state transition energy for an isolated chromophore molecule i plus the pairwise sum of the dipole–dipole interaction energies between the difference dipole, $\vec{\mu}_e - \vec{\mu}_g$, on chromophore molecule i and the ground state dipole moment vectors on all the other molecules in the aggregate.

The electronic transition energy (quantity a) and the length of the transition dipole (quantity d) are readily obtainable from electronic absorption spectroscopy. The other quantities are, in principle, obtainable from experiment, although the availability of such data in the literature varies greatly for chromophore molecules of interest. All of the quantities required for practical applications of the formalism are in principle calculable by molecular quantum mechanical techniques. In practice, it is not always possible to calculate the required quantities by currently available theoretical computational techniques at a reasonable cost and with sufficient accuracy. For the particular case of the chlorophylls, we are attempting to compute quantities a–d by an ab initio molecular orbital approach. It still remains to be seen whether these parameters can be computed with sufficient accuracy, but we consider this a promising approach.

For the special case of a one-, two-, or three-dimensional crystal with one molecule per unit cell, the transition density–transition density shift and the environmental shift are additive. Thus, if the crystal structure, transition dipole moment vector, and the total shift (from electronic absorption spectroscopy) are known, then the environmental shift can be computed without detailed knowledge of quantities b and c. We use this approach in section VII to compute the environmental shift for a hydrated monolayer of ethyl chlorophyllide a.

V. Chromophore Dimers

The formalism of the previous section can be used to derive explicit formulas for dimers of interacting chromophore molecules (e.g., $(Chl\ a)_2$, Chl a·Chl b) with comparable ground state to first excited state transition energies. The case of the chromophore dimer with two not necessarily identical molecules has been correctly treated by Förster.[50] In this section we treat the more general case of a chromophore dimer embedded in a molecular aggregate containing solvent[46] molecules. Let Δ_1 and Δ_2 be the ground state to first excited singlet state transition energies of the isolated chromophores.

$$\Delta_1 = \langle \varphi_1^1 | \hat{\mathcal{H}}_1 | \varphi_1^1 \rangle - \langle \varphi_1^0 | \hat{\mathcal{H}}_1 | \varphi_1^0 \rangle \quad (14)$$

$$\Delta_2 = \langle \varphi_2^1 | \hat{\mathcal{H}}_2 | \varphi_2^1 \rangle - \langle \varphi_2^0 | \hat{\mathcal{H}}_2 | \varphi_2^0 \rangle \quad (15)$$

Let σ_1 and σ_2 denote the aggregate environmental shift of the ground to first excited singlet state transition energies

$$\sigma_1 = \sum_{i \neq 1}^{N} \langle \varphi_1^1 \varphi_i^0 | \hat{\mathcal{H}}_{1i} | \varphi_1^1 \varphi_i^0 \rangle -$$

$$\sum_{i \neq 1}^{N} \langle \varphi_1^0 \varphi_i^0 | \hat{\mathcal{H}}_{1i} | \varphi_1^0 \varphi_i^0 \rangle \quad (16)$$

$$\sigma_2 = \sum_{i \neq 2}^{N} \langle \varphi_2^1 \varphi_i^0 | \hat{\mathcal{H}}_{2i} | \varphi_2^1 \varphi_i^0 \rangle -$$

$$\sum_{i \neq 2}^{N} \langle \varphi_2^0 \varphi_i^0 | \hat{\mathcal{H}}_{2i} | \varphi_2^0 \varphi_i^0 \rangle \quad (17)$$

where the sums range over the two chromophore molecules (molecules 1 and 2) and the $N - 2$ solvent molecules[46] in the aggregate. Let T denote the transition density–transition density interaction energy between chromophore molecules 1 and 2:

$$T = \langle \varphi_1^0 \varphi_2^1 | \hat{\mathcal{H}}_{12} | \varphi_1^1 \varphi_2^0 \rangle \quad (18)$$

The lowest quasi-stationary excited singlet states for the dimer (ψ_+ and ψ_-) and the corresponding transition energies (ϵ_+ and ϵ_-) are obtained by diagonalizing the H'' matrix as follows:

$$\mathbf{U}^+ \begin{vmatrix} \Delta_1 + \sigma_1 & T \\ T & \Delta_2 + \sigma_2 \end{vmatrix} \mathbf{U} = \begin{vmatrix} \epsilon_+ & 0 \\ 0 & \epsilon_- \end{vmatrix} \quad (19)$$

The resulting transition energies are

$$\epsilon_{\pm} = \frac{\Delta_1 + \sigma_1 + \Delta_2 + c_2}{2} \pm$$

$$\tfrac{1}{2}[(\Delta_1 + \sigma_1 - \Delta_2 - \sigma_2)^2 + 4T^2]^{1/2} \quad (20)$$

corresponding to the quasi-stationary states

$$\psi_+ = 2^{-1/2} \left[1 + \frac{\Delta_1 + \sigma_1 - \Delta_2 - \sigma_2}{[(\Delta_1 + \sigma_1 - \Delta_2 - \sigma_2)^2 + 4T^2]^{1/2}} \right]^{1/2} \varphi_1^1 \varphi_2^0 +$$

$$2^{-1/2} \left[1 - \frac{\Delta_1 + \sigma_1 - \Delta_2 - \sigma_2}{[(\Delta_1 + \sigma_1 - \Delta_2 - \sigma_2)^2 + 4T^2]^{1/2}} \right]^{1/2} \varphi_1^0 \varphi_2^1 \quad (21)$$

$$\psi_- = 2^{-1/2} \left[1 - \frac{\Delta_1 + \sigma_1 - \Delta_2 - \sigma_2}{[(\Delta_1 + \sigma_1 - \Delta_2 - \sigma_2)^2 + 4T^2]^{1/2}} \right]^{1/2} \varphi_1^1 \varphi_2^0 -$$

$$2^{-1/2} \left[1 + \frac{\Delta_1 + \sigma_1 - \Delta_2 - \sigma_2}{[(\Delta_1 + \sigma_1 - \Delta_2 - \sigma_2)^2 + 4T^2]^{1/2}} \right]^{1/2} \varphi_1^0 \varphi_2^1 \quad (22)$$

Similarly, the transition dipoles for the transitions from the ground state are

$$\vec{\mu}_+ = 2^{-1/2} \left[1 + \frac{\Delta_1 + \sigma_1 - \Delta_2 - \sigma_2}{[(\Delta_1 + \sigma_1 - \Delta_2 - \sigma_2)^2 + 4T^2]^{1/2}} \right]^{1/2} \vec{\mu}_1 +$$

$$2^{-1/2} \left[1 - \frac{\Delta_1 + \sigma_1 - \Delta_2 - \sigma_2}{[(\Delta_1 - \sigma_1 - \Delta_2 - \sigma_2)^2 + 4T^2]^{1/2}} \right]^{1/2} \vec{\mu}_2 \quad (23)$$

$$\vec{\mu}_- = 2^{-1/2} \left[1 - \frac{\Delta_1 + \sigma_1 - \Delta_2 - \sigma_2}{[(\Delta_1 + \sigma_1 - \Delta_2 - \sigma_2)^2 + 4T^2]^{1/2}} \right]^{1/2} \vec{\mu}_1 -$$

$$2^{-1/2} \left[1 + \frac{\Delta_1 + \sigma_1 - \Delta_2 - \sigma_2}{[(\Delta_1 + \sigma_1 - \Delta_2 - \sigma_2)^2 + 4T^2]^{1/2}} \right]^{1/2} \vec{\mu}_2 \quad (24)$$

where $\vec{\mu}_1$ and $\vec{\mu}_2$ are the transition dipoles for isolated chromophore molecules 1 and 2, respectively.

$$\vec{\mu}_1 = \langle \varphi_1^1 | \vec{r} | \varphi_1^0 \rangle \quad (25)$$

$$\vec{\mu}_2 = \langle \varphi_2^1 | \vec{r} | \varphi_2^0 \rangle \quad (26)$$

It can be clearly seen from eq 20–24 that the contribution from transition density–transition density splitting, $2T$, is *not* mathematically additive to the contribution from environmental splitting, $c_1 - \sigma_2$ (except for special cases), for any of the exciton properties presented here. This is an important point that has not been sufficiently appreciated in past studies of excitons in Chl aggregates.

VI. Effects of Nuclear Degrees of Freedom on the Electronic Spectrum

Intramolecular and intermolecular degrees of freedom can significantly affect the electronic spectrum of molecular aggregates. The electronic transitions can be coupled to intramolecular vibrations which then split the electronic transition peak into a series of vibronic peaks. Also, intramolecular degrees of freedom allow for conformational equilibria with each conformation having a characteristic electronic spectrum. Aggregates of the same molecular composition may sometimes be found in more than one geometric arrangement of component molecules and each of these geometric arrangements has its own characteristic electronic spectrum.

The ground electronic state to first excited singlet state transition of Chl a monomer is significantly coupled to at least one intramolecular vibration; a (0,0) peak is found at approximately 660 nm and a (0,1) peak is found at approximately 613 nm. Typically in Chl a aggregates, formed with keto C=O···Mg interactions, the energy separation between the (0,0) and (0,1) bands in the monomer spectrum is

larger than the width of the (0,0) band in the aggregate spectrum. Under these conditions, the formalism of this paper may be applied to the behavior of the (0,0) band in aggregates, with the modification that the off-diagonal H matrix elements are scaled down by the product of vibrational wave function overlap factors (Franck–Condon) as follows:

$$H_{ij} = \langle \varphi_i^0 \varphi_j^1 | \hat{\mathcal{H}}_{ij} | \varphi_i^1 \varphi_j^0 \rangle \langle \chi_i^0(0) | \chi_i^1(0) \rangle \times$$

$$\langle \chi_j^0(0) | \chi_j^1(0) \rangle \quad (27)$$

where $\chi_i^0(0)$ and $\chi_i^1(0)$ are the ground vibrational wave functions (for the vibration coupled to the electronic transition) in the ground and first excited singlet electron states, respectively, of the ith molecule. It should be noted that the behavior of the (0,1) peak is much more complicated than the behavior of the (0,0) band; in particular, an aggregate of N Chl molecules can have as many as N individual peaks in the (0,0) band and as many as N^2 peaks in the (0,1) band.

VII. Importance of Environmental Effects in Chlorophyll Aggregates

One contribution to the environmental shifting of the transition energy of a Chl molecule in an aggregate is the difference between the Coulombic interaction of the excited state and ground state with the environment of the molecule in the aggregate. Recent ab initio calculations[51] on ethyl chlorophyllide a monohydrate indicate that Chl a monohydrate has a substantial dipole moment ($\sim$5.6 D) and that the difference, $\vec{\mu}_e - \vec{\mu}_g$, between the first excited singlet state dipole moment, $\vec{\mu}_e$, and ground state dipole moment, $\vec{\mu}_g$, may be as large as 6.4 D. These two results taken together strongly indicate that Coulombic environmental shifting should be important for aggregates of Chl a.

Experimental evidence for the importance of environmental effects in Chl aggregates comes from the absorption spectrum of methyl chlorophyllide a hydrated monolayers for which the (0,0) absorption peak is at 735 nm.[52] The red shift from monomer ($\sim$660 nm) to hydrated monolayer ($\sim$735 nm) is approximately 1547 cm^{-1}. We can make the reasonable assumption that the structure of the hydrated monolayer of methyl chlorophyllide a is isomorphous to the structure of a hydrated monolayer (ab crystal plane) from the Strouse x-ray crystal structure[19] of ethyl chlorophyllide a dihydrate with the same lattice constant ($a = b = 8.852$ Å[19]). There is only one molecule per unit cell in this monolayer, and it can be shown for the case of one molecule per unit cell the transition density shift and environmental shift are additive. We approximate the transition density–transition density interaction energy between a pair of molecules as the interaction energy between two point transition dipoles of length 4.87 D[20] directed along the N(I)–N(III) direction (Figure 1). The total transition density–transition density interaction energy was computed by first picking a molecule in the sheet and then summing the energies for pairwise interaction of its transition dipole with the transition dipoles of all other molecules in the sheet. Using this procedure, we computed a transition density–transition density shift of 869 cm^{-1} and by subtraction (1547 cm^{-1} − 869 cm^{-1}) we compute the environmental shift to be approximately 678 cm^{-1}. Thus, for this important case, the environmental shift is of comparable magnitude to the transition density shift, and cannot be ignored.

VIII. Energy Trapping in Photosynthesis

The formalism presented in this paper has strong implications about the electronic relationship between the antenna and the trap in the photosynthetic unit. Differences in diagonal elements, H_{ii}, in the interaction energy matrix due to differences in local environment will tend to reduce the amount of mixing of the nonstationary states (i.e., the excited states localized on single molecules) in the formation of quasi-stationary states. Thus, differences in monomer environments within an aggregate tend to localize excited electronic states. For example, in (Chl)$_2$, if the local environmental splitting, $\sigma_1 - \sigma_2$, is equal to or greater than the transition density–transition density splitting, $2T$, then from eq 21-22 the two quasi-stationary states will be at least 85% pure locally excited states. Thus, if the trap is characterized by a local environment that stabilizes the first excited singlet state more than the ground state, there will be quasi-stationary states that are highly localized in the region of the trap but which contain small contributions from antenna Chl molecules. The antenna quasi-stationary states would be expected to be much more delocalized and to contain small contributions from trap Chl molecules. The energy separation ($\sim$420 cm^{-1}) between the antenna ($\sim$680 nm) and the trap ($\sim$700 nm) of green plants should be sufficiently great to cause localization of the trap quasi-stationary states.

IX. The Nature of Antenna Chlorophyll

A question of current interest is whether the Chl in the antenna of the photosynthetic unit occurs as (a) Chl aggregates formed through self-interactions (as proposed by Katz et al.[44]), (b) hydrated Chl aggregates formed through interactions involving the bifunctional ligand water (as proposed first by Fischer et al.[53] and later by Strouse[19,20]), (c) Chl–protein complexes, or, (d) some combination of a, b, c. In vivo and in vitro experimental evidence exists that bears on the choice of (a) or (b) as the better model and we will briefly review this evidence here.[54] The Chl a in the antenna of green plants absorbs with a broad peak at approximately 680 nm.[44] There is direct in vitro experimental evidence[44] that anhydrous Chl a aggregates (formed through self-interactions involving keto C=O···Mg interactions) in nonpolar solvents absorb at 680 nm much the same as does the Chl a in the in vivo antenna. On the other hand, no hydrated Chl a aggregates (formed through Chl–H$_2$O···Chl interactions) that have been prepared in the laboratory have their absorption maximum in the 680-nm region of the spectrum; the absorption of hydrated Chl aggregates is strongly red-shifted to the 700–740-nm region. Thus, the available experimental evidence by visible absorption spectroscopy on Chl aggregation in the antenna supports the anhydrous Chl aggregate model for antenna Chl and is not consistent with a hydrated Chl aggregate model. Strouse[19,20] had carried out theoretical exciton calculations in support of a hydrated Chl oligomer model for antenna Chl, and his computed peak positions match well with the peak positions from deconvoluted antenna Chl spectra.[55] Unfortunately, the Strouse exciton calculations were made with the complete neglect of environmental shifts and, as we have shown in this paper, these shifts are important for hydrated Chl aggregates. Correction of the Strouse calculations on chlorophyll–water adducts by inclusion of the environmental shifts results in additional substantial red shifts of the peak positions and the match of the calculated with the observed in vivo antenna data disappears. The

Strouse calculations in our view therefore cannot be accepted as valid evidence for a hydrated oligomer model for antenna Chl.

The formalism developed here has been used to analyze the lower-energy bands in the electronic spectra of Chl a and (Chl a)$_2$, and these results will be reported elsewhere.

References and Notes

(1) This work was performed under the auspices of the U.S. Energy Research and Development Administration.
(2) J. I. Frenkel, *Phys. Rev.*, **37**, 1276 (1931).
(3) J. I. Frenkel, *Zh. Eksp. Teor. Fiz.*, **6**, 647 (1936).
(4) J. I. Frenkel, *Phys. Rev.*, **37**, 17 (1937).
(5) A. S. Davydov, "Theory of Molecular Excitons", Translated by M. Kasha and M. Oppenheimer, Jr., McGraw-Hill, New York, N.Y., 1962.
(6) D. P. Craig and S. H. Walmsley, "Excitons in Molecular Crystals", W. A. Benjamin, New York, N.Y., 1968.
(7) R. S. Knox, "Theory of Excitons", Solid State Physics, Supplement 5, Academic Press, New York, N.Y., 1963.
(8) D. L. Dexter and R. S. Knox, "Excitons", Interscience, New York, N.Y., 1965.
(9) R. Emerson and W. Arnold, *J. Gen. Physiol.*, **15**, 391 (1931–1932).
(10) R. Emerson and W. Arnold, *J. Gen. Physiol.*, **16**, 191 (1932–1933).
(11) R. K. Clayton, *Adv. Chem. Phys.*, **19**, 353 (1971).
(12) J. J. Katz and J. R. Norris, *Curr. Top. Bioenerg.*, **5**, 41 (1973).
(13) R. K. Clayton, *Ann. Rev. Biophys. Bioeng.*, **2**, 131 (1973).
(14) K. Sauer, J. R. Lindsay Smith, and A. F. Schultz, *J. Am. Chem. Soc.*, **88**, 2681 (1966).
(15) E. A. Dratz, A. J. Schultz, and K. Sauer, *Brookhaven Symp. Biol.*, **19**, 303 (1966).
(16) E. A. Dratz, Ph.D. Dissertation, University of California, Berkeley, Calif., 1966.
(17) C. Housier and K. Sauer, *J. Am. Chem. Soc.*, **92**, 779 (1970).
(18) J. C.-E. Chang, Ph.D. Dissertation, University of Rochester, 1972.
(19) H.-C. Chow, R. Serlin, and C. E. Strouse, *J. Am. Chem. Soc.*, **97**, 7230 (1975).
(20) C. E. Strouse, *Prog. Inorg. Chem.*, in press.
(21) I. Tinoco, *Radiat. Res.*, **20**, 133 (1963).
(22) M. Kasha, H. R. Rawls, and M. Ashraf El-Bayoumi, *Pure Appl. Chem.*, **11**, 371 (1965).
(23) G. L. Closs, J. J. Katz, F. C. Pennington, M. R. Thomas, and H. H. Strain, *J. Am. Chem. Soc.*, **85**, 3809 (1963).
(24) J. J. Katz, R. C. Dougherty, and L. J. Boucher in "The Chlorophylls", L. P. Vernon and G. R. Seely, Ed., Academic Press, New York, N.Y., 1966, Chapter 7, pp 185–251.
(25) J. J. Katz and T. R. Janson, *Ann. N.Y. Acad. Sci.*, **206**, 579 (1973).
(26) S. G. Boxer, G. L. Closs, and J. J. Katz, *J. Am. Chem. Soc.*, **96**, 7058 (1974).
(27) A. F. H. Anderson and M. Calvin, *Arch. Biochem. Biophys.*, **107**, 251 (1964).
(28) M. Henry and J.-P. Leicknam, *Colloq. Int. C.N.R.S.*, **No. 191**, 317 (1970).
(29) J. J. Katz, *Dev. Appl. Spectrosc.*, **6**, 201 (1968).
(30) J. J. Katz, H. H. Strain, D. L. Leussing, and R. C. Dougherty, *J. Am. Chem. Soc.*, **90**, 784 (1968).
(31) T. M. Cotton and J. J. Katz, unpublished results.
(32) J. J. Katz in "Inorganic Biochemistry", Vol. II, G. L. Eichhorn, Ed., Elsevier, Amsterdam, 1973, pp 1022–1066.
(33) J. J. Katz and K. Ballschmiter, *Angew. Chem., Int. Ed. Engl.*, **7**, 286 (1968).
(34) K. Ballschmiter and J. J. Katz, *J. Am. Chem. Soc.*, **91**, 2661 (1969).
(35) L. L. Shipman, T. R. Janson, J. J. Katz, and G. J. Ray, *Proc. Natl. Acad. Sci. U.S.A.*, **72**, 2873 (1975).
(36) K. Ballschmiter, K. Truesdell, and J. J. Katz, *Biochim. Biophys. Acta*, **184**, 604 (1969).
(37) J. J. Katz, K. Ballschmiter, M. Garcia-Morin, H. H. Strain, and R. A. Uphaus, *Proc. Natl. Acad. Sci. U.S.A.*, **60**, 100 (1968).
(38) M. Garcia-Morin, R. A. Uphaus, J. R. Norris, and J. J. Katz, *J. Phys. Chem.*, **73**, 1066 (1969).
(39) J. R. Norris, R. A. Uphaus, H. L. Crespi, and J. J. Katz, *Proc. Natl. Acad. Sci. U.S.A.*, **68**, 625 (1971).
(40) J. J. Katz and J. R. Norris, *Curr. Top. Bioenerg.*, **5**, 41–75 (1973).
(41) J. R. Norris, H. Scheer, and J. J. Katz, *Ann. N.Y. Acad. Sci.*, **244**, 260 (1975).
(42) M. Thurnauer, J. R. Norris, and J. J. Katz, *Proc. Natl. Acad. Sci. U.S.A.*, **72**, 3270 (1975).

(43) J. J. Katz, W. Oettmeier, and J. R. Norris, *Proc. R. Soc.*, in press.
(44) T. M. Cotton, A. D. Trifunac, K. Ballschmiter, and J. J. Katz, *Biochim. Biophys. Acta*, **368**, 181 (1974).
(45) M. Born and J. R. Oppenheimer, *Ann. Phys.*, **84**, 457 (1927).
(46) Here we take the term "solvent molecules" to include any compounds in the aggregate whose ground state to first excited singlet state transition energies are significantly greater than the corresponding transition energies for the chromophore molecules.
(47) By taking the overlap between molecules to be small and choosing the form of the wave function in eq 1 we are, in effect, neglecting intermolecular exchange energy. Therefore, caution should be exercised when applying this formalism to a system where there may be reason to suppose that the overlap between molecules may not be small.
(48) We wish to caution the reader that the possibly important dispersion energy and induction energy (permanent moment–induced moment and induced moment–induced moment interactions) terms are not included in the first-order energy.
(49) $\langle \varphi_i{}^0 \varphi_j{}^1 | \mathcal{H}_{ij} | \varphi_i{}^1 \varphi_j{}^0 \rangle$ is usually approximated by the interaction between a transition dipole, $\langle \varphi_i{}^0 | \vec{\mu} | \varphi_i{}^1 \rangle$, on chromophore molecule i and a transition dipole, $\langle \varphi_j{}^0 | \vec{\mu} | \varphi_j{}^1 \rangle$ on chromophore molecule j.
(50) Th. Forster in "Modern Quantum Chemistry", Part 3, O. Sinanoglu, Ed., Academic Press, New York, N.Y., p 93.
(51) L. L. Shipman, unpublished.
(52) G. L. Gaines, W. D. Bellamy, and A. G. Tweet, *J. Chem. Phys.*, **41**, 2572 (1964).
(53) M. S. Fischer, D. H. Templeton, A. Zalkin, and M. Calvin, *J. Am. Chem. Soc.*, **94**, 3613 (1972).
(54) It should be noted that the evidence discussed here does not bear on the question of whether antenna Chl could be a Chl–protein complex and therefore does not rule out this possibility.
(55) C. S. French, J. S. Brown, and M. C. Lawrence, *Plant Physiol.*, **49**, 421 (1972).

Contribution of Vibrational Excitation to the Rate of Carbon Dioxide Dissociation in Electrical Discharges

Pio Capezzuto, Francesco Cramarossa,* Riccardo d'Agostino, and Ettore Molinari

Centro di Studio per la Chimica dei Plasmi del C.N.R., Istituto di Chimica Generale ed Inorganica, Università di Bari, Bari, Italy (Received June 4, 1975; Revised Manuscript Received January 23, 1976)

Rates of dissociation of carbon dioxide have been measured in radio-frequency discharges operated at 1–10 cal cm^{-3} s^{-1}, 5–40 Torr, and gas flow rates between 0.1 and 17 l. (STP) min^{-1}. A comparison has been made of the experimental rate constants with those calculated from electron energy distribution functions and the excitation cross section with threshold at 7 eV. Evidence is presented that a mechanism of dissociation involving vibrationally excited molecules makes a significant contribution to the observed rates and become the dominant one at pressures above $\simeq$20 Torr. At 40 Torr up to 60% of the energy pumped into the vibrational system of CO_2 is utilized for dissociation.

Introduction

In a previous study[1] on the dissociation of molecular hydrogen in radio-frequency discharges operated at power densities between 1 and 10 cal cm^{-3} s^{-1}, and at pressures of 5–40 Torr, evidence has been presented for the existence of a mechanism of dissociation involving vibrationally excited molecules. The contribution of a mechanism of this type has been shown to increase, with increasing pressure, with respect to dissociation by direct electron impact, which represents the prevailing mechanism at pressures below about 2 Torr.[2] The fact that vibrational excited states can play an important role in the process of dissociation under plasma conditions is expected on theoretical grounds[3] for systems characterized by a strong nonequilibrium situation, with the electronic temperature T_e, the vibrational temperature T_v, the rotational temperature T_r, and the translational temperature T_g all different from each other ($T_e > T_v \geq T_r > T_g$),[4] and has been utilized to rationalize the results of earlier work from this laboratory.[5] In the present paper the dissociation of carbon dioxide has been investigated under similar discharge conditions, and it will be shown that the conclusions arrived at for molecular hydrogen are confirmed and can be put on a more quantitative basis for this system.

This is largely the consequence of the detailed information on electron energy distributions in CO_2 presently available from studies in the field of molecular gas lasers.[6-9]

Experimental Section

The discharge reactor is a vertical quartz tube (internal radius r_T = 1.75 cm), surrounded by a water jacket utilized for calorimetric measurements, capacitively coupled to a radio-frequency generator (35 MHz, 10 kW) by means of two external annular electrodes of copper, 3.5 cm high, set at a fixed separation of L = 18 cm including electrode height. Experimental details and discharge characteristics are similar to those described in ref 1 and 5. In particular, the following points should be stressed. (1) Calorimetric measurements performed with a water jacket subdivided into sectors yields results entirely similar to those reported in Figures 4 and 5 of ref 1, which indicate that power dissipation is axially constant within the discharge region including the electrodes. (2) Calorimetric measurements also show that the total power transferred to the plasma is W_T = (0.96 ± 0.03) $V_p I_p/2$ in strict analogy with the results of Figure 3 of ref 1; V_p and I_p are the dc plate voltage and current intensity, respectively. (3) Visual and photographic observation of the discharge show that, at pressures above 5 Torr, the plasma column is essentially uniform within the

electrodes, with small fringes extending beyond them, in full agreement with the calorimetric results quoted in (1) above. These results indicate that the effective discharge length can be taken, as a good approximation, to coincide with the electrode separation L.

The axial uniformity of power dissipation, including the electrode regions (1), the good coupling of the discharge to the generator (96%) (2), and the confinement of the discharge within the distance L (3) are characteristics of the generator used and allow therefore equating, within a few percent, the effective electric field E (V cm^{-1}) to $V_p/L\sqrt{2}$.

The extent of CO_2 dissociation, β, has been determined at different axial positions l (cm), as measured from the upper edge of the upper electrode in the downward direction of the gas flow (this selection of the origin of the scale of l is justified by the above discussion), at pressures between 5 and 40 Torr, gas flow rates, Φ, from 0.1 to 17 l. (STP) min^{-1}, and power densities, $\langle W \rangle = W_T/\pi r_T^2 L$, of 0.5–6.0 cal cm^{-3} s^{-1}. The reacted gas was sampled at different axial positions by means of thin probes and analyzed gas chromatographically. Two different types of probes have been utilized: "L" shaped quartz probes which can be positioned with their tips lapping either the border of the contracted plasma column or the reactor's wall; and thin probes of alumina set along the reactor axis. Figure 1 illustrates the results of sampling with the different probe arrangements, at various values of l, inside and outside of the discharge zone. Values of β obtained using the quartz probe lapping the contracted plasma column are the highest. The presence of limited radial profiles is indicated by the lower β values obtained when the tip is lapping the reactor's wall.

The results obtained with the alumina probe positioned along the reactor axis are more complex and are characterized by the lowest values of β. These probes, when fully immersed in the discharge, are heated to temperatures which increase with increasing power and decreasing l, up to white heat. Values of β obtained with these probes can be accounted for on the assumption of a temperature dependent catalytic recombination of carbon monoxide and oxygen taking place within the probes.

It can now be questioned whether the data collected with the quartz probes accurately reflect the gas composition at the sampling point. Any recombination process leading to CO_2, and taking place within the probe, would in fact give values of β lower than at the probe inlet, as in the case of the Al_2O_3 tip. The results of Figures 1–4, with values of β which can be as high as 93%, with very marked axial profiles, indicate that recombination processes of this kind, if present, would alter the probe composition at the probe inlet by a few percent only (see also below).

Values of β obtained with the quartz probe lapping the contracted plasma column can therefore be taken as reasonably representative of the gas composition of the discharge and will be utilized hereafter.

Results

Axial profiles of β at 20 Torr are shown in Figure 2 for different gas flow rates and power densities. Maxima of β are to be found $\simeq 1$ cm below the lower edge of the lower electrode ($l \simeq 19$ cm) for all flow rates except 0.1 l. min^{-1}. At this low flow rate a stationary state is reached at $l \leq L/2$ and the values of β measured at $l \simeq 14$ cm will be taken as representative of the composition corresponding to this stationary state. Figure 2 shows that, in all cases, a constant composition is reached at $l \geq 35$ cm. Values of β at
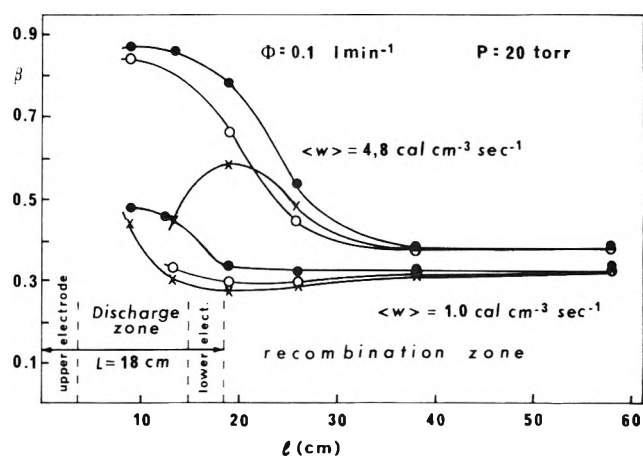
Figure 1. Degree of CO_2 decomposition β as a function of the axial coordinate l, for different sampling conditions: (X) alumina probe along the reactor axis; (O) L-shaped probe of quartz with tip toward the reactor wall; (●) the same probe with tip lapping the border of the luminous plasma column.
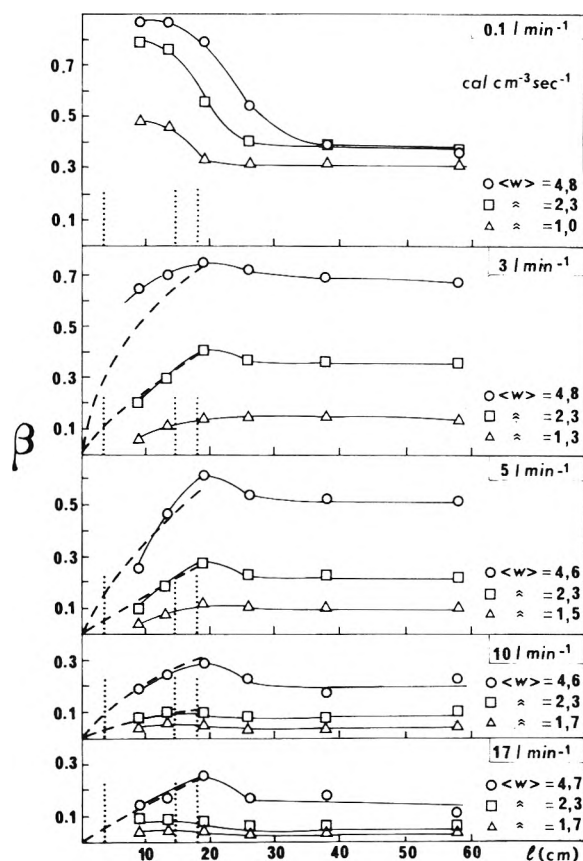
Figure 2. Axial profiles of β at different power densities $\langle W \rangle$ and for various gas flow rates (20 Torr). Dotted lines are values calculated from eq 1 (see text).

the reactor end ($l = 60$ cm) will be taken as representative of the limiting composition reached in the recombination region.

The dependence of β_{19} and of β_{60} on power density $\langle W \rangle$ at 5, 10, 20, and 40 Torr is illustrated in Figure 3a and b, for different flow rates. Experimental points marked X (20 Torr, 0.1 l. min^{-1}) have been obtained using a stoichiometric $CO-O_2$ mixture, and are seen to coincide with the points
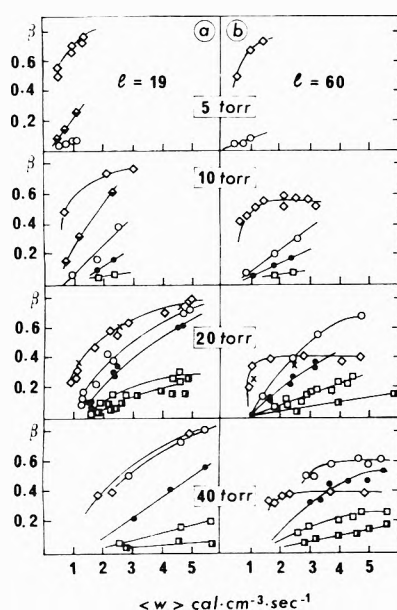
Figure 3. Dependence of β_{19} (a) and of β_{60} (b) on power density $\langle W \rangle$ at different pressures and various gas flow rates. ◊, ◆, ○, ●, □, ▣, Φ = 0.1, 1, 3, 5, 10, 17 l. (STP) min^{-1}, respectively; $\times$ refers to values obtained from CO/O_2 = 2/1 mixtures, p = 20 Torr.
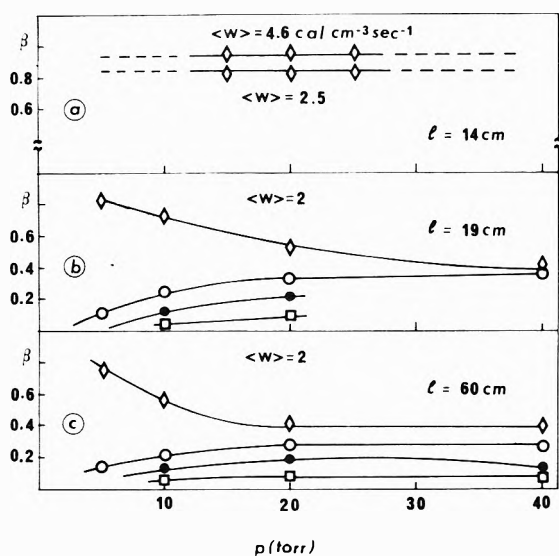
Figure 4. Pressure dependence of β at constant $\langle W \rangle$: (a) Φ = 0.1 l. (STP) min^{-1}, l = 14 cm. $\langle W \rangle$ = 4.6 (cal cm^{-3} s^{-1}), $\langle W \rangle$ = 2.5; (b) l = 19 cm, $\langle W \rangle$ = 2.0, ◊, ○, ●, □, Φ = 0.1, 3, 5, 10 l. (STP) min^{-1}, respectively; (c) same as b, l = 60 cm.

obtained with pure CO_2. A common stationary state can therefore be reached at 0.1 l. min^{-1} and $l \leq L/2$ (Figure 2) starting from both sides of the reaction.

The dependence on pressure, at a fixed $\langle W \rangle$, for β_{14} (0.1 l. min^{-1}), β_{19}, and β_{60} (all flows) is illustrated in Figure 4.

The data of Figures 1 and 2 clearly show that the discharge region is followed by a recombination region. The difference between β_{19} or β_{14} at 0.1 l. min^{-1} and β_{60} measures the extent of back reaction leading to CO_2. The decrease of β in this region follows from the two reactions

$$CO + O + M \rightarrow CO_2 + M \qquad \text{(a)}$$

$$CO + S\text{-}O \rightarrow CO_2 + S \qquad \text{(a')}$$
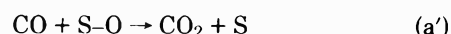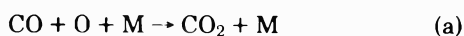
where S is a surface site of the wall. These reactions compete for O atoms with

$$O + O + M \rightarrow O_2 + M \qquad \text{(b)}$$

$$O + S\text{-}O \rightarrow O_2 + S \qquad \text{(b')}$$

A selection of rate constants for the above reactions can be found in ref 10. Under conditions where $v_a + v_{a'} \gg v_b + v_{b'}$, where $v_{a,a',b,b'}$ are the rates of reactions a, a', b, and b', a decrease of β is expected equal to the concentration of O atoms at l_{max}. No variation of β between l_{max} and l = 60 should be observed under $v_a + v_{a'} \ll v_b + v_{b'}$. A comparison of the values of β at 0.1 l. min^{-1} measured at l = 14, 19, and 60 cm, as given in Figures 4a–c, shows that both conditions can be observed: $v_a + v_{a'} \ll v_b + v_{b'}$ at $p \leq 5$ Torr; $v_a + v_{a'} \gg v_b + v_{b'}$ at $p \geq 20$ Torr. An estimate of the degree of oxygen dissociation, α, is therefore possible above 20 Torr. The maximum estimated α at 0.1 l. min^{-1} and 20 Torr is 0.5, and this value decreases with decreasing $\langle W \rangle$. and increasing Φ. From the rate constants of ref 10 and the expression for heterogeneous reaction utilized in ref 1, it is possible to estimate $v_{a,a',b,b'}$ as a function of pressure and of O atoms concentration, and one finds that an "inversion" point, corresponding to $v_a + v_{a'} = v_b + v_{b'}$, can in fact be predicted at p = 12–15 Torr. It should be appreciated, from the data of Figure 4, that while the values of β_{14} at 0.1 l. min^{-1}, which correspond to the *stationary state* reached at $l \leq L/2$, do not depend on pressure (Figure 4a); the corresponding values of β_{19} and β_{60} decrease with increasing pressure (Figures 4b,c) for the reason illustrated above. As already pointed out in ref 10 the stationary state values of β reached at 0.1 l. min^{-1} should not be confused with thermodynamic equilibrium values. Gas temperatures in excess of 4000 K would in fact be necessary to obtain thermodynamic equilibrium values corresponding to the observed β's, while estimated values of T_g are those of Figure 7a. At flow rates higher than 1 l. min^{-1} both β_{19} and β_{60} increase with pressure. These data reflect the *kinetic* situation to be described below. It should be emphasized at this point that the possibility of probing without significant alteration of the gas composition at the probe inlet, in the region of the reactor where O atoms are present, is connected with the condition $v_b + v_{b'} \gg v_a + v_{a'}$. This condition is apparently verified in our quartz probes, as previously mentioned. It can be shown that within the probes, a' and b' heterogeneous processes predominate and, furthermore, $v_{b'} > v_{a'}$.

The kinetic equation for the isothermal *first-order* decomposition $CO_2 \rightarrow CO + \frac{1}{2}O_2$, with a volume variation of $(1 + \frac{1}{2}\beta)$, due to the decomposition process, can be written in terms of β, according to ref 11 and 12, as

$$\frac{l}{\Phi} = \frac{1}{k_{expt}} \frac{RT_g}{P} \frac{1}{\pi r_T^2} A[-0.5 - 1.5 \ln(1 - \beta)] \qquad (1)$$

where A is a conversion factor. In this equation the volume variation due to oxygen dissociation and the recombination processes leading to CO_2 have been neglected, in that they represent minor corrections only, as discussed above. Values of β_{19} at 20 Torr and different $\langle W \rangle$ have been fitted by this equation for $\Phi > 1$ l. min^{-1}, as shown in Figure 5. Similar results have been obtained at 10 and 40 Torr. The validity of eq 1 for the present conditions is justified by the low values of the oxygen atoms concentration present at $\Phi \geq 3$ l. min^{-1}. This can be appreciated from the data reported in Figure 2 for $\Phi \geq 3$ l. min^{-1}, which show that the extent of back reaction at $l > 19$ cm is relatively small.

The slopes of the straight lines of Figure 5 can be utilized in eq 1 to calculate the dependence of β on the axial coordinate l at constant Φ and different $\langle W \rangle$. The dotted lines of Figure 2 show that the calculated dependence fits the experimental points rather satisfactorily. Equation 1 gives therefore consistent results which can be utilized to calculate first-order rate constant k_{expt}, once the gas temperature is known.

Discussion

The rate constant of CO_2 dissociation can be calculated as a function of the reduced average electron energy $\bar{u}_r$ according to

$$k_e = (2/m_e)^{1/2} \int_0^\infty u \, \sigma(u) \, f(u) \, du \qquad (2)$$

where m_e is the electron mass, $f(u)$ the electron energy distribution function, defined so that $\int_0^\infty u^{1/2} f(u) \, du = 1$ and $\bar{u}_r = \frac{2}{3} \int_0^\infty u^{3/2} f(u) \, du$ ($\bar{u}_r = kT_e$ for a Maxwellian distribution), $\sigma(u)$ is the appropriate cross section for the process leading to dissociation by electron impact. The cross section with threshold at 7 eV, derived in ref 13, corresponds, according to ref 6 and 14, to a process of dissociative electronic excitation of the type

$$CO_2 + e \rightarrow CO_2{}^* + e \rightarrow CO + O + e \qquad (3)$$
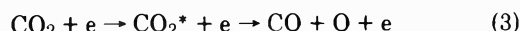
where $CO_2{}^*$ is a carbon dioxide molecule electronically excited to a state 7 eV above ground state. This is the cross section which should be utilized in eq 2. In fact, dissociative attachment, of the type

$$CO_2 + e \rightarrow CO + O^- \qquad (4)$$
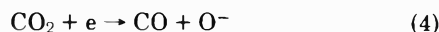
represents, according to ref 3, 15, and 16 a minor contribution only.

The electron energy distribution functions utilized for the present calculations are those of ref 6. These functions are highly non-Maxwellian and their use, under our experimental conditions, is justified by the low values of the fractional ionization, i.e., $n_e/N < 10^{-6}$, where n_e and N are the electron and neutral densities, respectively. Under these conditions the thermalizing effect of electron–electron collisions has been found[17] to be negligible. The data of ref 6 also allow the reduced average energy $\bar{u}_r$ to be determined as a function of the reduced electric field, E/p_0 (V cm^{-1} Torr^{-1}) or E/N (V cm^2). These values of $\bar{u}_r(E/N)$ are in satisfactory agreement with the experimental ones reported in ref 13. In Figure 6 calculated values of k_e have been plotted as a function of $\bar{u}_r$ and E/N.

In order to compare the experimental values of rate constants, k_{expt}, derived from eq 1, with the corresponding values of k_e, an at least approximate knowledge of T_g is necessary, and this is a complex problem for this type of discharges.[5,9] The temperatures utilized in the present calculation have been reproduced in Figure 7a, as a function of $\langle W \rangle$ and for different pressures. The temperatures at 5 Torr have been derived from values measured in ref 10. These temperatures have been found to coincide with those evaluated for H_2 in ref 1 for similar discharge conditions. The dependence of T_g on pressure, which cannot be derived from ref 10 for pressures above 5 Torr, has been assumed to be the same as in ref 1.

From the temperature data reported in Figure 7a one can calculate $N = p/kT_g$ (cm^{-3}) and with the values of the electric field evaluated as specified in the Experimental
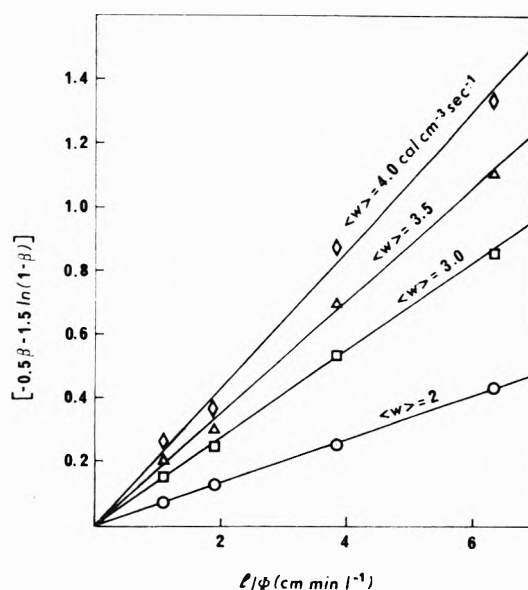
Figure 5. Plots of β_{19} against l/Φ ($l = 19$ cm) according to eq 1 at different power densities $\langle W \rangle$ (20 Torr).
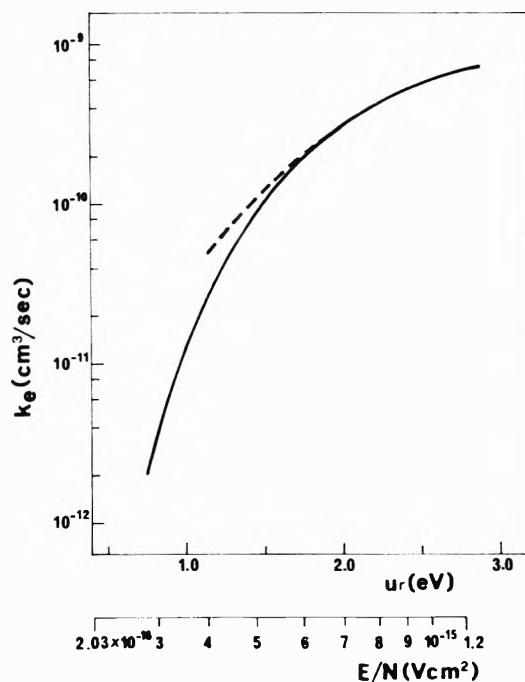
Figure 6. Plots of calculated rate constants for dissociation by direct electron impact, k_e, against the reduced average energy, $\bar{u}_r$, or the reduced electric field, E/N. Solid line represents calculation under the assumption of no oscillation of the electron energy with the applied radio-frequency field. Dotted line represents under the assumption of maximum oscillation of the electron energy with the applied radio-frequency field (see text (c)).

Section, values of the reduced field E/N as a function of $\langle W \rangle$ have been determined and reported in Figure 7b.

Values of k_{expt} determined under various discharge conditions from the plots of Figure 5 and with the gas temperatures of Figure 7a have been collected in Figure 8.

The rate of reaction 3 should be written as

$$v_e(E/N) = -dN_{CO_2}/dt = k_e n_e N_{CO_2} \qquad (5)$$
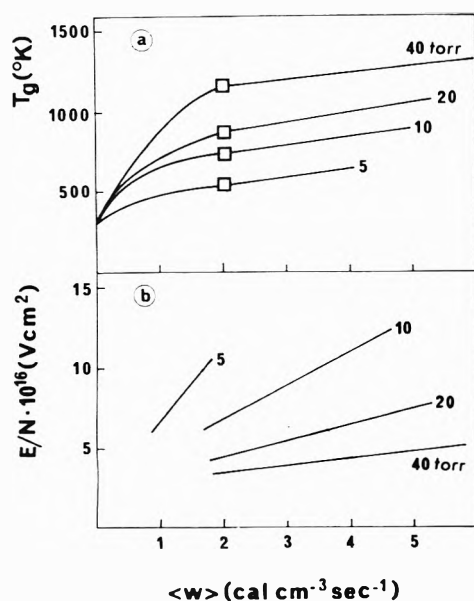
Figure 7. (a) Values of the gas temperatures T_g utilized in the calculations as a function of $\langle W \rangle$, at various pressures: ($\square$) from ref 1. (b) Values of the reduced electric field E/N (V cm^2) as a function of $\langle W \rangle$, at different pressures.
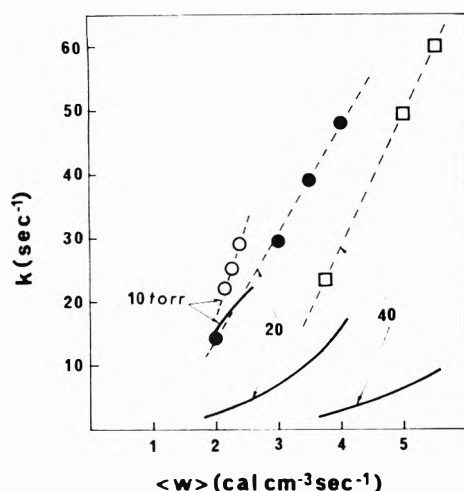
Figure 8. First-order rate constants as a function of power density $\langle W \rangle$. $\square$, $\bullet$, O, k_{expt} at 40, 20, 10 Torr, respectively. Full curves represent calculated values of $k_e n_e$ at 40, 20, and 10 Torr.

The electron density (cm^{-3}) can be evaluated according to the expression

$$\langle W \rangle = \frac{n_e E^2 e^2}{m_e} \left(\frac{\nu_m}{\nu_m^2 + \omega^2} \right) \qquad (6)$$

where ν_m is the frequency of elastic collisions of the electrons and ω the frequency of the applied field.

An alternative way for evaluating $k_e n_e$, without an explicit knowledge of either n_e or of N, is the following: in Figure 9 of ref 6 the *fractional* power transferred to the process of dissociative electronic excitation (reaction 3) has been given, *for pure* CO_2, as a function of E/N or $\bar{u}_r$. For weakly ionized plasmas this fractional power is found to be independent of both electrons and heavy particle density. The dissociation rate can therefore be calculated as follows:

$$v_e(E/N) = \frac{f_e(E/N)\langle W \rangle}{1.61 \times 10^5} \qquad (7)$$

where $f_e(E/N)$ is the fractional power transferred to dissociative electronic excitation at a given E/N and 1.61×10^5 (cal mol^{-1}) is the threshold energy corresponding to 7 eV. Values of $k_e n_e$ evaluated according the two methods have been found to be in very good agreement and have been compared with k_{expt} in Figure 8 (solid lines).

In Figure 9 values of k_e calculated from eq 2 as a function of $\bar{u}_r$ have been compared with the corresponding experimental values derived from the measurements in ref 15 at pressures between 0.3 and 3 Torr.

The ratio $k_e n_e/k_{expt}$ has been plotted as a function of $\bar{u}_r$ in Figure 10 for the points at 10, 20, and 40 Torr. A corresponding plot of k_e(calcd)/k_e(obsd), derived from Figure 9, has also been included (dotted line).

The results presented in Figures 8–10 deserve some comments.

(a) *Influence of Gas Composition on* $k_e n_e$. According to ref 6, the electron energy distribution function and the value of $\bar{u}_r$, at a given E/N, strongly depend on the CO_2/CO ratio (no influence of oxygen is expected). The result is that values of k_e calculated for pure CO_2 are higher than for mixtures of CO_2-CO at the same E/N. On the other hand, the electron density n_e, at a given E/N, increases with increasing CO concentration; this follows from eq 6 in that the frequency of elastic collisions of the electrons, ν_m, increases from pure CO_2 to CO-O_2 mixtures.[13] Values of k_e, n_e, and $k_e n_e$, calculated for pure CO_2 and pure CO at 20 Torr and for the extreme experimental values of $\langle W \rangle$, have been collected in Table I. One appreciates that the rate constant of reaction 3, $k_e n_e$, will decrease from pure CO_2 to pure CO. Values of $k_e n_e$ reported in Figure 8 refer to pure CO_2 and represent therefore *upper* limits to these quantities under the present experimental conditions which comprise a wide range of CO_2/CO compositions. The same is true for the $k_e n_e/k_{expt}$ ratios of Figure 10. The situation of Figure 9 is different in that experimental rate constants refer to *initial* rates, i.e., to rates determined in essentially pure CO_2, and are therefore directly comparable with the theoretical values.

(b) *Influence of Gas Temperature on* k_{expt} *and* $k_e n_e$. As already mentioned the gas temperature T_g influences both the values of k_{expt} derived from eq 1 and the values of E/N for a given experimental value of E: e.g., a temperature increase will cause an increase of both k_{expt} and E/N, and hence of $k_e(E/N)$. The $k_e n_e/k_{expt}$ ratios of Figure 10 will therefore depend on T_g. A reasonable error in the estimated values of T_g of Figure 7a is ±150 K. The two points marked by crosses in Figure 10 have been calculated assuming a ±150 K variation for the highest ($k_e n_e/k_{expt}$, $\bar{u}_r$) point reported at 20 Torr. One appreciates that the uncertainty in T_g does not alter significantly the reported trends.

The following observation adds weight to the values of T_g reported in Figure 7a. Inspection of Figure 3a and b shows that the β vs. $\langle W \rangle$ curves extrapolate at $\beta = 0$ at values of $\langle W \rangle$ which increase with increasing pressure. From Figure 7b one calculates the corresponding E/N and, according to ref 6, values of $\bar{u}_r$ which fall between 0.4 and 0.5 eV. This result is in very good agreement with the experimental curve of Figure 9,[15] which also extrapolate to zero for $0.4 \leqslant \bar{u}_r \leqslant 0.5$ eV.

(c) *Influence of the Radio-Frequency Field.* When the electric field is calculated from $V_p/L\sqrt{2}$ and the value of k_e at a given E/N is derived from Figure 6, an implicit assumption is made, namely, that the electron energy distribution function does not follow in time the applied radio-
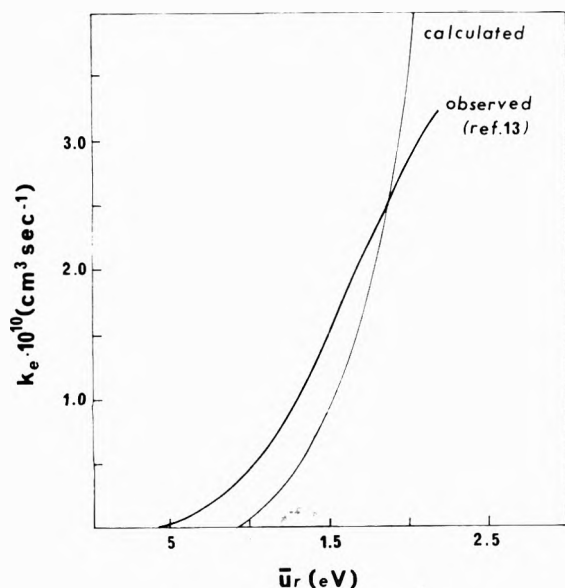
Figure 9. Observed (ref 15) and calculated values of k_e as a function of the reduced average electron energy $\bar{u}_r$ ($0.3 \leq p \leq 3$ Torr).
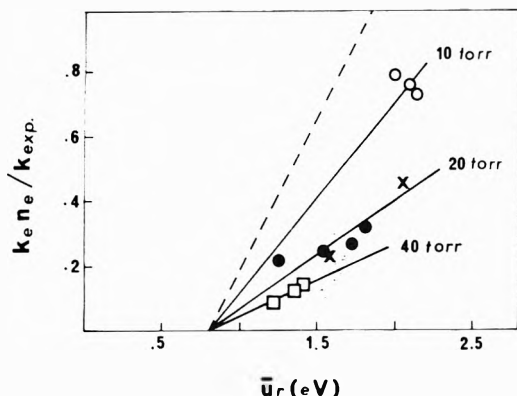
Figure 10. $k_e n_e / k_{expt}$ as a function of $\bar{u}_r$ at different pressures. Dotted line shows values calculated from Figure 9, (X) variation of the highest experimental point reported at 20 Torr when a ±150 K variation is assumed for T_g.

TABLE I: Values of k_e, n_e, and $k_e n_e$ calculated, at 20 Torr, for the Extreme Experimental Power Densities and for the Limiting Values of the CO₂–CO Mixtures

	$E/N = 4.5 \times 10^{-16}$ V cm²; $\langle W \rangle = 2.0$ cal cm⁻³ s⁻¹			$E/N = 6.5 \times 10^{-16}$ V cm²; $\langle W \rangle = 4.0$ cal cm⁻³ s⁻¹		
	k_e, cm³ s⁻¹	$10^{-10} n_e$, cm⁻³	$k_e n_e$, s⁻¹	k_e, cm³ s⁻¹	$10^{-10} n_e$, cm⁻³	$k_e n_e$, s⁻¹
Pure CO₂	5.7×10^{-11}	5.5	3.1	2.1×10^{-10}	8.6	18
Pure CO	4.3×10^{-12}	9.2	0.4	2.3×10^{-11}	11	2.5

frequency field and so is appropriately referred to the "effective" field $V_p/L\sqrt{2}$. The situation is however more complex and can be examined by referring to the analysis reported in ref 18.

Two limiting conditions can be expected, depending on whether the quantity $k\nu_m/2\omega$ is $\gg 1$ or $\ll 1$, with k equal to the average fraction of electronic energy lost per collision.

TABLE II: Fraction of Energy Pumped into Vibrational System of CO₂ Utilized for the Dissociation Processes $\langle W_{vd} \rangle / \langle W_v \rangle$, at Different Pressures and Power Densities

p, Torr	$\langle W \rangle$, cal cm⁻³ s⁻¹	$\langle W_{vd} \rangle / \langle W_v \rangle$
40	3.75–5.5	0.54–0.59
20	2.0 –4.0	0.28–0.42
10	2.14–2.38	0.03–0.06

For $k\nu_m/2\omega \gg 1$ the electron energy follows the field with a 100% oscillation around its mean value, for $k\nu_m/2\omega \ll 1$ the electron energy oscillates about the mean value with a small ripple of magnitude $k\nu_m/2\omega$. The latter case does therefore correspond to the implicit assumption made in the present calculations.

The value of $k\nu_m/2\omega$ can be estimated from the data of ref 6, for our experimental conditions. One finds that $k\nu_m/2\omega$ is < 1 and the electron energy oscillates by more than 90% about its mean value, i.e., follows the field in time: the assumption made is therefore not correct. During one cycle the electron energy rises, therefore, from zero to its maximum value corresponding to the *peak* value of the electric field V_p/L. From the data of Figure 6 it is possible to calculate how k_e oscillates during one cycle and to derive the corresponding average value. Average values determined at different E/N have been compared in Figure 6 (dotted line) with those previously utilized in the calculations. This comparison shows that differences between the two sets of values become significant at the lowest values of E/N only. In view of the uncertainties discussed under (a) and (b) this will not alter the general conclusions which can be drawn from the results reported in Figures 8–10.

Conclusions

The results of Figures 8–10 clearly show that reaction 3 cannot represent the unique mechanism of carbon dioxide dissociation, even at the low pressures of Figure 9 (0.3–3 Torr). A different mechanism must therefore contribute to the observed rates of dissociation and is likely to involve the participation of vibrationally excited molecules, as previously suggested.[1,5] The fractional power transferred to dissociative electronic excitation and to the excitation of different vibrational modes of CO₂ is a unique function of $\bar{u}_r$ (or E/N) (Figure 9 of ref 6). In the range of $\bar{u}_r$ of the experiments these excitation processes make up 90–100% of the power transferred by the field to the discharge. The meaning of Figure 10 is that, with increasing pressure, an increasing fraction of the power transferred to the vibrational modes of CO₂ should actually be utilized for the process of dissociation. This fraction can be calculated from the following equations:

$$\langle W \rangle = \langle W_v \rangle + \langle W_e \rangle \tag{8}$$

$$\langle W_e \rangle = 1.61 \times 10^5 v_e \tag{9}$$

$$\langle W_{vd} \rangle = 1.27 \times 10^5 (v_{expt} - v_e) \tag{10}$$

from which

$$\frac{\langle W_{vd} \rangle}{\langle W_v \rangle} = \frac{1.27 \times 10^5 (v_{expt} - v_e)}{\langle W \rangle - 1.61 \times 10^5 v_e} \tag{11}$$

where $\langle W \rangle$ is the power density transferred to vibrational modes, $\langle W_e \rangle$ the power density utilized for dissociative electronic excitation, and $\langle W_{vd} \rangle$ the power density utilized for the dissociation of CO₂ by processes other than reaction

3. 1.27×10^5 cal mol^{-1} is the dissociation energy of CO_2. Values of $\langle W_{vd}\rangle/\langle W_v\rangle$ at different pressures and different $\langle W \rangle$ have been collected in Table II. One appreciates that, at 40 Torr, a fraction of about 60% of the energy pumped into the vibrational system of CO_2 is utilized for the process of dissociation. This fraction decreases with decreasing pressure and power density $\langle W \rangle$.

The observation that in discharges operated at moderate pressures the average electron energy is too low for a mechanism of dissociation by direct electron impact to be important, and that the gas temperature is also too low for a mechanism of thermal dissociation, led to the suggestion,[1,5] confirmed by spectroscopic measurements,[4] that the vibro-rotational temperature T_ξ should be sufficiently high to warrant the contribution of a mechanism of dissociation involving vibrationally excited molecules. An approximate rate expression has been derived in ref 1 and 5 for this type of process, which can be written, for CO_2 dissociation, as

$$v_v = v_{\text{expt}} - v_e = k_0 N N_{CO_2}\left(\frac{1}{T_\xi - T_g + RT_\xi T_g B}\right)$$
$$\times \exp(1.27 \times 10^5 B) \exp\left(\frac{-1.27 \times 10^5}{RT_\xi}\right) \quad (12)$$

where B is a constant accounting for the dependence of the crude collisional preexponential factor, k_0, on the vibrational quantum number.

The observed dependence of the experimental results on pressure and power density can be accounted for, at least qualitatively, on the basis of eq 12. Spectroscopic measurements of T_ξ are actually in progress.

A very similar mechanism of molecular dissociation involving vibrationally excited states has been recently suggested in ref 19 to account for the observed rates of N_2 dissociation in glow discharges in the pressure range 2–10 Torr.

References and Notes

(1) P. Capezzuto, F. Cramarossa, R. d'Agostino, and E. Molinari, *J. Phys. Chem.*, **79**, 1487 (1975).
(2) A. T. Bell, *Ind. Eng. Chem., Fundam.*, **11**, 209 (1972).
(3) L. S. Polak, *Pure Appl. Chem.*, **39**, 307 (1974).
(4) F. Cramarossa and G. Ferraro, *J. Quant. Spectrosc. Radiat. Transfer*, **14**, 159 (1974); F. Cramarossa, G. Ferraro, and E. Molinari, *ibid.*, **14**, 419 (1974).
(5) P. Capezzuto, F. Cramarossa, G. Ferraro, P. Maione, and E. Molinari, *Gazz. Chim. Ital.*, **103**, 1153 (1973); P. Capezzuto, F. Cramarossa, R. d'Agostino, and E. Molinari, *ibid.*, **103**, 1169 (1973); P. Capezzuto, F. Cramarossa, P. Maione, and E. Molinari, *ibid.*, **103**, 891 (1973); **104**, 1109 (1974) (all in english). For a review see E. Molinari, *Pure Appl. Chem.*, **39**, 343 (1974).
(6) N. L. Nigham, *Phys. Rev. A*, **2**, 1989 (1970); *Proc. Int. Conf. Ioniz. Phenom. Gases, 11th, 1973*, 267 (1974).
(7) J. J. Lowke, A. V. Phelps, and B. W. Irvin, *J. Appl. Phys.*, **44**, 4664 (1973).
(8) M. J. W. Boness and G. J. Schultz, *Phys. Rev. A*, **9**, 1969 (1974).
(9) M. Z. Novgorodov and N. N. Sobolev, *Proc. Int. Conf. Ioniz. Phenom. Gases, 11th, 1973*, 215 (1974).
(10) L. C. Brown and A. T. Bell, *Ind. Eng. Chem., Fundam.*, **13**, 203, 210 (1974).
(11) S. M. Smith, "Chemical Engineering Kinetics", McGraw-Hill, New York, N.Y., 1970.
(12) O. A. Hougen and K. M. Watson, "Chemical Process Principles", Wiley, New York, N.Y., 1949.
(13) R. D. Hake and A. V. Phelps, *Phys. Rev.*, **158**, 70 (1967).
(14) W. J. Wiegand, M. C. Fowler, and J. A. Benda, *Appl. Phys. Lett.*, **16**, 237 (1970).
(15) K. Kutsegi Corvin and S. J. B. Corrigan, *J. Chem. Phys.*, **50**, 2570 (1969).
(16) M. J. Barton and A. Von Engel, *Phys. Lett. A*, **32**, 173 (1970).
(17) S. Rockwood, *J. Appl. Phys.*, **45**, 5229 (1974).
(18) D. L. Flamm, E. R. Gilliland, and R. F. Baddour, *Ind. Eng. Chem., Fundam.*, **12**, 276 (1973).
(19) L. S. Polak, P. A. Sergeev, D. J. Slovetsky, and R. D. Todesaite, *Proc. Int. Conf. Ioniz. Phenom. Gases, 12th, I 2A*, 65 (1975).

Diffusion Relationships in the Binary System Benzene–Perdeuteriobenzene at 25 °C

R. Mills

Diffusion Research Unit, Research School of Physical Sciences, Australian National University, Canberra, A.C.T. 2600, Australia
(Received December 3, 1975)

Measurements are reported at 25 °C of the self-diffusion coefficient of perdeuteriobenzene and the tracer-diffusion coefficients of both the components of benzene–perdeuteriobenzene mixtures. It is shown that the ratio of self-diffusion coefficients of benzene and perdeuteriobenzene is approximately equal to the inverse square root of their respective masses and the small deviation that remains can be explained in terms of the intermolecular forces involved. For tracer diffusion a volume effect is found, which is in accordance with theoretical equations formulated by Bearman for this case.

The system benzene–perdeuteriobenzene is a very interesting one in which to study interrelationships among the various diffusion coefficients. The main interest stems from the fact that since the two components differ only in isotopic composition, the system can be regarded as a "regular" one in which the molecules have similar size, shape, and interaction potentials. For such systems Bearman[1] has derived equations which relate the mutual diffusion coefficient with the two tracer- (or intra-) diffusion coefficients and also the latter coefficients with the molecular volumes. Another point of interest is that the self-diffusion coefficients for pure normal benzene and for pure perdeuteriobenzene can be compared. For two such closely similar liquids the inverse square root mass dependence which is

predicted by several theories should apply. There are virtually no precise data of this type available with the exception of the analogous coefficients reported by Mills[2] for H_2O and D_2O. Some NMR self-diffusion measurements in pure isotopically related liquids have been made but, with errors ranging from 2 to 5%, data of this type are of little use for testing the theoretical mass dependence.

It should be noted that in this paper we restrict the use of the term self-diffusion to that measured in a pure one-component liquid. In a binary system of two bulk components there are two diffusion coefficients (which can be defined in terms of the velocity autocorrelation function for each component) as well as the mutual diffusion coefficient. The former coefficients can be termed intradiffusion coefficients as defined by Albright and Mills[3] but here are approximated by the respective tracer-diffusion coefficients. Some workers use the term "self-diffusion" to describe these coefficients.

Experimental Section

Perdeuteriobenzene (99.5% D) was obtained from Merck Sharpe and Dohme, Canada and from CEA, France (99.8% D). Tracers used were C_6H_5T and C_6D_5T (D = deuterium, T = tritium); their preparation has been outlined in a previous paper.[4] The diffusion method was the magnetically stirred diaphragm cell as described by Mills and Woolf.[5]

Results and Discussion

The self- and tracer-diffusion results obtained in this study are given in Table I.

As indicated in the introductory paragraphs self-diffusion in the pure liquids and tracer diffusion in the mixtures fall into separate categories. We shall treat the self-diffusion case first.

Self-Diffusion

For self-diffusion in one-component liquids there have been several formulations which incorporate the effect of mass explicitly among which are derivations by Longuet-Higgins and Pople,[6] Rowlinson,[7] Brown and March,[8] and Friedman.[9] In these approaches a simplified picture is assumed; either that the molecules are hard spheres or that molecular interactions between species differing only in mass are the same. In all the derivations D_s is found to be proportional to $m^{-1/2}$. Friedman[9] made a more detailed study of the effect of isotopic substitution distinguishing between fully and partially substituted molecules. He suggested that in the latter case moments of inertia are changed and therefore rotational motions might be affected which in turn could cause deviations from the simple proportionality.

Results for self-diffusion in C_6H_6 and in C_6D_6 are shown in Table II together with our previous results[2] for H_2O and D_2O and some relevant viscosity data.[10]

It will be seen that the viscosity and self-diffusion ratios are practically identical both for the water and benzene isotopic pairs. However, the transport ratios are in both cases higher than the respective mass ratios and in the water case the difference is quite large. In view of the assumptions made in the theoretical approaches the simple mass law can only be expected to apply to monatomic liquids. Deviations from it as shown by more complex liquids must be attributed to such factors as correlated motions, coupling between rotational and translational motions, and differences in intermolecular potentials. For the water case, McLaugh-

TABLE I: Tracer Diffusion in C_6H_6–C_6D_6 Mixtures

x C_6D_6	Tracer	$10^9 D_T$, $m^2 s^{-1}$
0	C_6H_5T	2.203 ± 0.004
	C_6D_5T	2.207 ± 0.007
25	C_6H_5T	2.172
50	C_6H_5T	2.142 ± 0.005
	C_6D_5T	2.153 ± 0.005
100	C_6D_5T	2.090 ± 0.001

TABLE II: Self-Diffusion in Benzene and Water

Temp, °C	$(m(D_2O)/m(H_2O))^{1/2}$	$D_s(H_2O)/D_s(D_2O)$	$\eta(D_2O)/\eta(H_2O)$
5	1.054	1.29	1.31
25	1.054	1.23	1.23
45	1.054	1.20	1.20

	$(m(C_6D_6)/m(C_6H_6))^{1/2}$	$D_s(C_6H_6)/D_s(C_6D_6)$	$\eta(C_6D_6)/\eta(C_6H_6)$
25	1.038	1.057	1.063^a

^{a} Viscosity ratio as derived from data of Dixon and Schiessler.[10]

lin[11] has attributed the high viscosity ratio to the moment of inertia difference between H_2O and D_2O. These moment ratios vary from 1.3 to 1.4 and might be expected to affect the viscosity through rotational–translational coupling. From the equality of the transport ratios in Table II it would appear that in water the diffusion process is similarly affected which leads to the corollary that rotational–translational coupling is similar for both transport processes. It is noteworthy that the viscosity ratio for the pair $H_2^{18}O/H_2^{16}O$ at 25 °C as measured by Kudish, Wolf, and Steckel[12] is 1.054 in exact agreement with the square-root mass law. Since the center of mass of the water molecule is only slightly displaced from the oxygen atom, the moments of inertia for this pair will change very little upon isotopic substitution. For the benzene case it will be seen from Table II that both transport ratios are ~2% higher than the mass ratio. The square root of the moment of inertia ratio $(I_D/I_H)^{1/2}$ between C_6H_6 and C_6D_6 can be calculated to be 1.024 for all three axes. (This assumes the center of molecule to carbon distance to be 1.30 Å and both the C–H and C–D distances to be 1.08 Å.) It would seem unlikely therefore that rotational effects are causing the higher transport ratios in this case.

An alternative explanation of the higher ratio for C_6H_6/C_6D_6 is available which does not involve moment of inertia changes. Steele[12] in a study of isotopically substituted classical fluids has given expressions for the differences in their transport properties in terms of a corresponding states treatment. These equations incorporate the changes in the potential parameters ϵ and σ and so reflect the difference in intermolecular potentials (which are assumed to be conformal) between normal and deuterated molecules. It may be noted also that these expressions contain the inverse square root mass relation so that one can test directly the difference between the ratios in Table II. Values of $\delta\epsilon$ and $\delta\sigma$ for the benzene case have been given by Steele and values of $(\partial \ln D/\partial P)_T$ and $(\partial \ln D/\partial T)_P$ were calculated from the data of McCool, Collings, and Woolf,[14] and Collings and Mills.[15] The value for $D_{C_6H_6}/D_{C_6D_6}$ calculated from
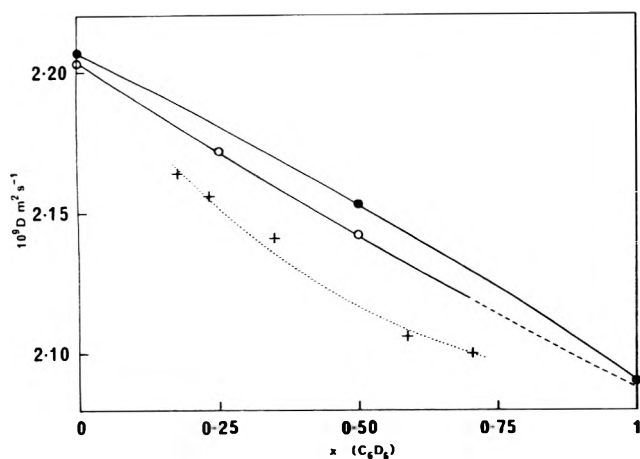
Figure 1. Diffusion coefficients for the C_6H_6–C_6D_6 system at various compositions: (●) tracer-diffusion coefficient for C_6D_5T; (○) tracer-diffusion coefficient for C_6H_5T; (+) mutual diffusion data of Shankland and Dunlop.[16]

TABLE III: Comparison of Tracer-Diffusion Data with Eq 1

Solvent	D_D/D_H	$v_H/v_D{}^a$
C_6H_6	1.002	1.003
50% C_6H_6–C_6D_6	1.005	1.003
C_6H_{12}	1.004	1.003

^{a} Molar volume data from Dixon and Schiessler.[17]

Steele's equations is 1.057 in excellent agreement with the experimental ratio. The correlation is not successful for water.

Tracer Diffusion

Tracer-diffusion data from Table I for tritiated benzene and perdeuteriobenzene in mixtures of the bulk components are shown in Figure 1. Mutual diffusion data for the same system as reported by Shankland and Dunlop[16] are shown also.

For regular systems of this type, Bearman,[1] from statistical mechanical considerations, has derived relations between tracer and mutual diffusion coefficients. He has analyzed also the older diffusion equations and shown that with suitable restrictions they give essentially these same results. His equations are

$$D_1/D_2 = v_2/v_1 \tag{1}$$

$$D = D_1 \frac{\partial \ln a_1}{\partial \ln c_1} \tag{2}$$

$$= [D_1 x_2 + D_2 x_1] \frac{\partial \ln a_1}{\partial \ln x_1} \tag{3}$$

where D is the mutual diffusion coefficient, and D_i, v_i, a_i, c_i, and x_i are the tracer (or intradiffusion) coefficient, molecular volume, activity, concentration, and mole fraction of component i, respectively. Unfortunately there are no published data for the thermodynamic activities of the benzene–perdeuteriobenzene system so eq 2 and 3 cannot be tested at this time. However, inspection of Table I and Figure 1 shows that there is a small but apparently real difference in the tracer-diffusion coefficients of the tracer species C_6H_5T and C_6D_5T in 50 mol % mixtures. Friedman[9] has made a theroetical study of isotopic mass effects in "solute" diffusion of this kind and his equations predict that the inverse square-root mass law ought not to apply. This prediction has in general been borne out by recent experiments.[4] In the present case, the difference between the two tracers is also obviously not a normal mass effect as the heavier tracer diffuses faster than the lighter one. It may be noted that closer examination of our previous results[4] for tracer diffusion in pure benzene and pure cyclohexane shows the same small effect. It is known that the molar volume of deuterated compounds is smaller than their hydrogenated analogues and one might therefore suspect that the difference is due to a volume effect. As indicated above, Bearman has derived eq 1 which predicts that tracer-diffusion coefficients in regular mixtures should be inversely proportional to the molecular volumes. In Table III, we compare eq 1 with our results for the diffusion of the two tracers in 50 mol % C_6H_6–C_6D_6, pure C_6H_6, and pure C_6H_{12}. The subscripts H and D represent the hydrogenated and deuterated tracer species, respectively.

It is evident that there is a correlation between the tracer-diffusion mobilities and molecular volumes of the tracer species. It will be realized that due to the similar volumes of the two isotopically related species the test is not as definitive as, for example, a system such as krypton and argon. Nevertheless the agreement in three different systems is good evidence that eq 1 is valid for this type of diffusion.

References and Notes

(1) R. J. Bearman, *J. Phys. Chem.*, **65**, 1961 (1961).
(2) R. Mills, *J. Phys. Chem.*, **77**, 685 (1973).
(3) J. G. Albright and R. Mills, *J. Phys. Chem.*, **69**, 120 (1965).
(4) R. Mills, *J. Phys. Chem.*, **79**, 852 (1975).
(5) R. Mills and L. A. Woolf, "The Diaphragm Cell", ANU Press, Canberra, 1968.
(6) H. C. Longuet-Higgins and J. A. Pople, *J. Chem. Phys.*, **25**, 884 (1956).
(7) J. S. Rowlinson, *Physica*, **19**, 303 (1953).
(8) R. C. Brown and N. M. March, *Phys. Chem. Liquids*, **1**, 141 (1969).
(9) H. L. Friedman, "Molecular Motions in Liquids", J. Lascombe, Ed., D. Reidel, Dordrecht, Holland, 1974, p 87.
(10) J. A. Dixon and R. W. Schiessler, *J. Phys. Chem.*, **58**, 430 (1953).
(11) E. McLaughlin, *Physica*, **26**, 650 (1960).
(12) W. A. Steele, *J. Chem. Phys.*, **33**, 1619 (1960).
(13) A. J. Kudish, D. Wolf, and F. Steckel, *J. Chem. Soc., Faraday Trans. 1*, **68**, 2041 (1972).
(14) M. A. McCool, A. F. Collings, and L. A. Woolf, *J. Chem. Soc., Faraday Trans. 1*, **68**, 1489 (1972).
(15) A. F. Collings and R. Mills, *Trans. Faraday Soc.*, **66**, 2761 (1970).
(16) I. R. Shankland and P. J. Dunlop, *J. Phys. Chem.*, **79**, 1319 (1975).
(17) J. A. Dixon and R. W. Schiessler, *J. Am. Chem. Soc.*, **76**, 2197 (1954).

Contact Charge-Transfer Bands of Some Alkyl Halide–Iodine Systems

Hiroshi Morita[1] and Milton Tamres*

Department of Chemistry, University of Michigan, Ann Arbor, Michigan 48104 (Received December 11, 1975)

Publication costs assisted by the National Science Foundation

Absorption spectra were measured at room temperature of iodine (I_2) and some alkyl (methyl, ethyl, n-propyl, and isopropyl) iodides, n-propyl bromide, and n-propyl chloride in n-heptane solution. All alkyl iodide–I_2 systems have a complex spectrum in the region 240–340 nm, whereas n-propyl bromide–I_2 and n-propyl chloride–I_2 show simple spectra with peaks at 242.5 and 220.7 nm, respectively. The broad alkyl iodide–I_2 spectrum was resolved into component bands which are attributed to two contact charge transfer bands and a blue-shifted $n \rightarrow \sigma^*$ transition of the alkyl iodide. Correlation of band maxima with the ionization potentials of the alkyl halides clearly suggests the charge-transfer character of the bands, and the linear dependence of absorbance on either the iodine or alkyl halide concentration is consistent with the view that the spectra arise from contacts. The concentration of contacts, equilibrium constant, molar extinction coefficient, and oscillator strength were calculated based on collision theory, and these are discussed.

Introduction

Contacts, or electron donor–acceptor pairs which persist during a collision[2a,b] (or encounter[2c]), have attracted much attention as a limiting case of charge-transfer (CT) interaction. Several spectroscopic studies with molecular iodine (I_2) and very weak electron donors such as the saturated hydrocarbons[3] have been made in an attempt to characterize contact charge-transfer (CCT) bands, both in solution[4-6] and in the vapor phase.[7-9] The reported characteristics of the saturated hydrocarbon–I_2 CCT bands in solution cannot be taken as correct because of the problem of choosing a reference solvent to subtract the free iodine contribution to the absorbance.[6,8] In the vapor phase, too, these bands have not as yet been fully characterized owing to the fact that they extend into the vacuum ultraviolet region.[8,9]

Thermodynamic and spectroscopic studies of alkyl halide–I_2 pairs are few and show that association is quite weak.[4,10] They can be placed in the category of contacts (as will be discussed). In one solution study[4] a well-defined CCT band for alkyl bromide–I_2 pairs is reported, as well as a single CCT band maximum for alkyl iodide–I_2 pairs. A CCT band maximum also has been found for the n-heptyl bromide–I_2 system in the vapor phase.[7]

Much more attention has been given to the transient species formed between alkyl halides and atomic iodine (I) as the acceptor (generated by flash photolysis[3,11-15] and pulse radiolysis[16-18] techniques). These bands appear in the visible and near-uv regions.[11] Recently, methyl iodide (MeI)–I, ethyl iodide (EtI)–I, n-propyl iodide (n-PrI)–I, and isopropyl iodide (i-PrI)–I, all in the vapor phase,[15,19] were reported to have two CCT bands in the visible region. These bands have been attributed to there being two rather close ionization potentials for the donor;[20-22] the ionization is from the nonbonding electrons of the iodine atom in the alkyl iodides and is split through spin–orbiting coupling. Usually only the CCT band positions have been given, although the equilibrium constant has been estimated[13] for EtI–I and EtBr–I.

In this study, we undertook to measure quantitatively the characteristics of the CCT bands of some alkyl halides–I_2 in n-heptane solution, and with the aid of collision theory to estimate such physical quantities as the concentration of contacts, the equilibrium constant (K), and band intensity. The alkyl halides used in the present work are MeI, EtI, i-PrI, n-PrI, n-propyl bromide (n-PrBr), and n-propyl chloride (n-PrCl).

Experimental Section

Materials. Iodine (J. T. Baker) was purified as described previously.[23] n-Heptane (Eastman spectro grade) was used without further purification. Methyl iodide (Matheson Coleman and Bell), ethyl iodide (Fisher Scientific), n-propyl and isopropyl iodides (Aldrich Chemical), and n-propyl bromide and chloride (Aldrich Chemical) were dried over molecular sieves, type 3 Å, and purified by fractional distillation under nitrogen gas. To prevent the photodecomposition of the alkyl iodides, the pure liquids were stored in the dark under nitrogen gas in a desiccator.

Measurements. Spectra were measured at room temperature ($\sim$24 ± 1 °C) in the uv region with a Cary 14 recording spectrophotometer. Matched cells of 1.04 and 1.03 mm path length were used. These were determined by comparing the absorbance of a 9.45×10^{-3} M iodine solution in n-heptane in these cells with the absorbance of the above solution diluted (by weight) by a factor of 10 in a 0.991-cm cell. The latter cell path was determined using a Wild cathetometer and the value obtained agreed well with that based on the extinction coefficient of iodine in n-heptane usually reported ($\sim$900 M^{-1} cm^{-1}).[24,25] In the region of interest, several species have appreciable absorbance besides the RX–I_2 contacts, namely, n-heptane–I_2 contacts,[4-6] I_2–I_2 interaction (or I_4 complex),[26,27] and RX local excitation.[28-30] The maximum concentration of donor and acceptor of each RX–I_2 system was limited to below that which would cause the slit width of the spectrophotometer to open to its maximum (3.0 mm). Fresh solution was used in each measurement to avoid the effect of photodecomposition of the alkyl halides.

The sample cell contained an n-heptane solution of an alkyl halide–iodine mixture of known composition and the reference cell contained the same concentration of the corresponding alkyl halide (or sometimes the iodine). The difference spectrum so obtained was then corrected for the absorbance of an n-heptane solution of iodine (or some-
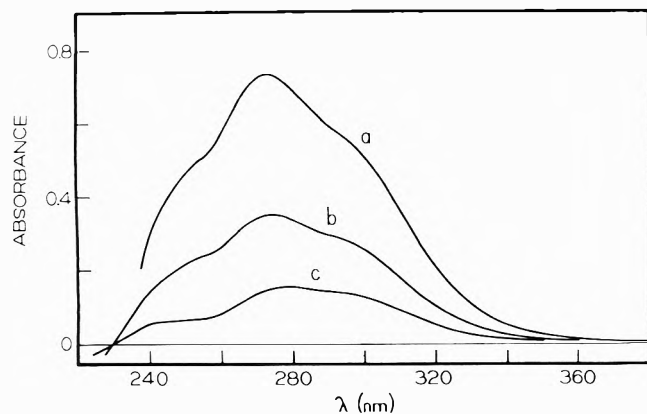
Figure 1. Contact CT spectra of methyl iodode (MeI)–I_2 in n-heptane solution at room temperature in a 1.04-mm cell. Concentrations are (a) I_2 = 7.82 × 10^{-3} M, MeI = 8.48 × 10^{-2} M, (b) I_2 = 3.91 × 10^{-3} M, MeI = 8.47 × 10^{-2} M, (c) I_2 = 1.96 × 10^{-3} M, MeI = 8.46 × 10^{-2} M.

Figure 2. Contact CT spectra of ethyl iodide (EtI)–I_2 in n-heptane solution at room temperature in a 1.04-mm cell. Concentrations are (a) I_2 = 7.82 × 10^{-3} M, EtI = 7.01 × 10^{-2} M, (b) I_2 = 3.90 × 10^{-3} M, EtI = 7.02 × 10^{-2} M, (c) I_2 = 1.95 × 10^{-3} M, EtI = 7.01 × 10^{-2} M.

times the alkyl halide) of the same concentration as in the mixture to give the spectrum attributed to RX–I_2 alone. The concentrations were made up by weighing, and they matched in the sample and reference cells to less than 0.5%.

Results and Discussion

The spectra of the RX–I_2 contacts in n-heptane solution are shown in Figures 1–6. As is clearly seen, a distinct maximum is observed in each case. The peak position and the maximum absorbance for the most concentrated sample (sample a in Figures 1–6) are listed in Table I, together with the absorbance normalized to the same concentration as that in n-PrI–I_2 assuming a linear dependence of absorbance on the concentration of each solute species. The observed band maxima of EtI–I_2, i-PrI–I_2, n-PrBr–I_2, and n-PrCl–I_2 (274.5, 278.5, 242.5, and 220.7 nm, respectively) are at slightly shorter wavelengths than those previously reported (280, 280, 244, and 224 nm, respectively).[4]

At the low wavelength side in Figures 1–6, not only is there a crossing of the curves of different concentration but the absorbance even becomes negative. This must be due to an "overcorrection" in this region (a) for the contribution of the strong RX absorption, and (b) for the strong n-heptane–I_2 CCT absorption which starts at ~260 nm at the high I_2 concentrations used. The correction in absorbance in terms of total iodine and total alkyl halide concentrations, rather than the "free" concentrations (total minus contacts),[31] is too large. Thus the band shapes are probably better resolved on the high wavelength side than on the low.

The CCT bands for I_2 with n-PrCl and n-PrBr seem simple (in agreement with a literature report for the latter as donor).[4] However, they are more complex for the RI donors. There is an appearance of a shoulder on both the high wavelength side (~295–310 nm) and the low wavelength side (~240–255 nm), which implies the presence of multiple bands. This is suggested also by the data on the CCT band half-widths ($\Delta\nu_{1/2}$) in Table I, i.e., the $\Delta\nu_{1/2}$ values are about twice as large for the RI donors compared to those for RBr and RCl. The presence of multiple bands parallels the finding in the study of the alkyl iodide–atomic iodine system where distinct multiple bands (actually two) have been observed.[15,16,19]

Resolution of the RI–I_2 bands was made using a comput-
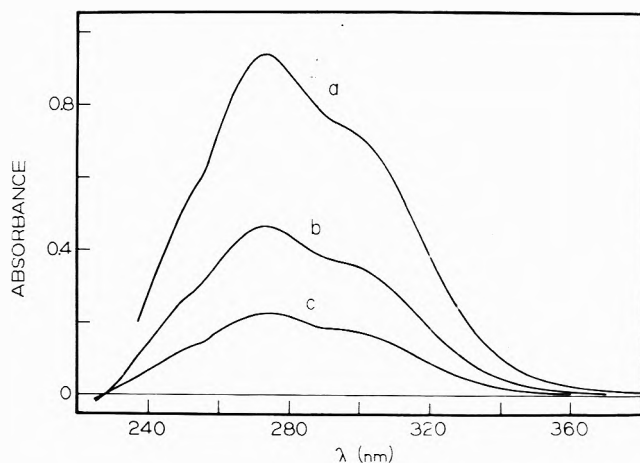
Figure 3. Contact CT spectra of n-propyl iodide (n-PrI)–I_2 in n-heptane solution at room temperature in a 1.04-mm cell. Concentrations are (a) I_2 = 7.81 × 10^{-3} M, n-PrI = 6.45 × 10^{-2} M, (b) I_2 = 3.91 × 10^{-3} M, n-PrI = 6.44 × 10^{-2} M, (c) I_2 = 1.96 × 10^{-3} M, n-PrI = 6.42 × 10^{-2} M.
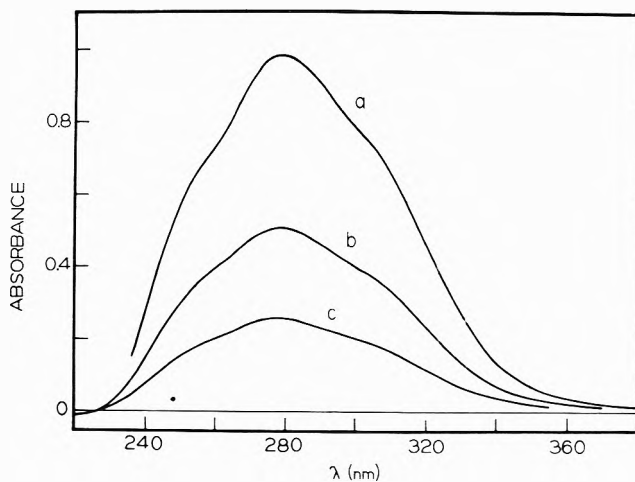
Figure 4. Contact CT spectra of isopropyl iodide (i-PrI)–I_2 in n-heptane solution at room temperature in a 1.04-mm cell. Concentrations are (a) I_2 = 7.83 × 10^{-3} M, i-PrI = 5.76 × 10^{-2} M, (b) I_2 = 3.91 × 10^{-3} M, i-PrI = 5.77 × 10^{-2} M, (c) I_2 = 1.95 × 10^{-3} M, i-PrI = 5.77 × 10^{-2} M.

TABLE I: Wavelengths (λ_{max}), Half-Maximum Band Widths ($\Delta\nu_{1/2}$), and Absorbance Maxima Observed for Alkyl Halide–I_2 Contacts in n-Heptane

Donor	λ_{max}		$\Delta\nu_{1/2}$, cm^{-1}	Absorbance[a]	
	nm	eV		Sample a[b]	Normalized[c]
MeI	295~310[d]	4.00~4.20[d]			
	272.5 ± 0.5	4.550	8910	0.733	0.557
	240~255[d]	4.86~5.17[d]			
EtI	295~310[d]	4.00~4.20[d]			
	274.5 ± 0.5	4.516	8850	0.861	0.790
	240~255[d]	4.86~5.17[d]			
n-PrI	295~310[d]	4.00~4.20[d]			
	273.3 ± 0.5	4.536	8650	0.937	0.937
	240~255[d]	4.86~5.17[d]			
i-PrI	295~310[d]	4.00~4.20[d]			
	278.5 ± 0.5	4.452	9130	0.983	1.099
	240~255[d]	4.86~5.17[d]			
n-PrBr	242.5 ± 0.3	5.113	4430	0.536	0.413
n-PrCl	220.7 ± 0.3	5.617	4010	0.942	0.130

[a] Measured in a 1.04-mm cell. [b] Most concentrated sample in each of Figures 1–6. [c] Calculated absorbance where the concentrations of donor and I_2 are normalized to those of n-PrI–I_2. [d] Shoulder.
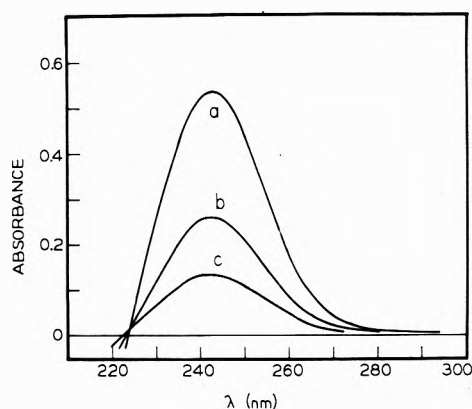
Figure 5. Contact CT spectra of n-propyl bromide (n-PrBr)–I_2 in n-heptane solution at room temperature in a 1.04-mm cell. Concentrations are (a) I_2 = 3.91 × 10^{-3} M, n-PrBr = 1.67 × 10^{-1} M, (b) I_2 = 1.95 × 10^{-3} M, n-PrBr = 1.67 × 10^{-1} M, (c) I_2 = 9.74 × 10^{-4} M, n-PrBr = 1.68 × 10^{-1} M.
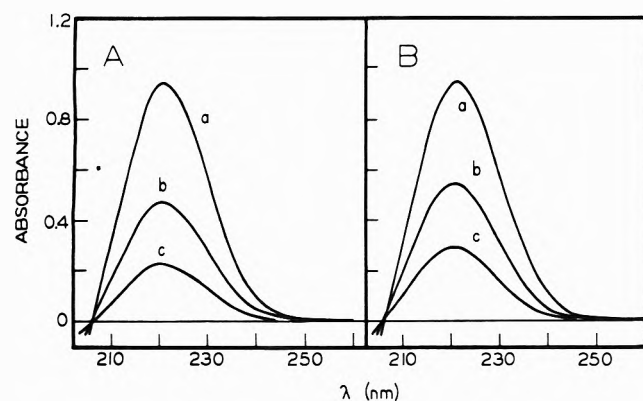
Figure 6. Contact CT spectra of n-propyl chloride (n-PrCl)–I_2 in n-heptane solution at room temperature in a 1.04-mm cell. Concentrations are (A): n-PrCl = 1.86 M and (a) I_2 = 1.96 × 10^{-3} M, (b) I_2 = 9.79 × 10^{-4} M, (c) I_2 = 4.89 × 10^{-4} M; and (B): I_2 = 1.96 × 10^{-3} M and (a) n-PrCl = 1.86 M, (b) n-PrCl = 0.928 M, (c) n-PrCl = 0.463 M.

erized curve-fitting program assuming Gaussian shapes of the component bands. Analysis was carried out in two ways. In the first procedure, the spectrum in the region 275–360 nm was resolved into two bands. This was based on the assumption that the third band below 255 nm has a negligible contribution in this region. By subtracting the sum of the contributions of the two resolved bands from the observed RI–I_2 spectrum in the region below 275 nm then gave the third band. This is illustrated for the EtI–I_2 system in Figure 7A (the results for the other RI–I_2 systems are quite similar). In the second procedure, the RI–I_2 spectrum over the entire 240–360-nm region was resolved into three Gaussian bands as shown in Figure 7B, also for EtI–I_2 (the fit for the other RI–I_2 systems being equally good). As may be seen, the latter method enhances the contribution of band 3 (at the lowest wavelength) at the expense of the middle band. A comparison of the results from both procedures is given in Table II. There is a small difference in the band maxima obtained by the two procedures, but the relative trends among the several RI–I_2 contacts are quite similar and either set of data leads to the same conclusion when compared with theory. We have chosen to compare the results obtained in the first procedure because (1) the region of band 3 is one where there is possibly greater uncertainty in absorbance corrections, (2) $\Delta\nu_{1/2}$ is more comparable for bands 1 and 2, and (3) the interpretation of the origin of band 3 (to be discussed) suggests a smaller expected intensity of band 3 compared to bands 1 and 2.

One possibility to account for the third band at the low wavelength side is to attribute it to an electron transfer from I_2 to RI (a back CCT band). The ionization potentials of molecular iodine (9.311 and 9.953 eV)[32] are almost the same as those of EtI. The normal and back CCT bands could appear in the same region provided the electron affinities of I_2 and RI are comparable, and assuming similar solvent effects. Acceptor properties of RI do not seem to have been determined, and the back CCT band concept must be taken as highly speculative. A more plausible explanation for the third band is that it is due to a blue shift of the locally excited n → σ^* transition in the RI molecule with greatly enhanced intensity. Such a shift with enhancement has been observed in other systems. For example,

TABLE II: Spectral Characteristics of Alkyl Iodide–Iodine Systems

	MeI	EtI	n-PrI	i-PrI
First $I_D{}^V$, eV	9.50[a]	9.34[b]	9.27[b]	9.19[c]
Second $I_D{}^V$,[b] eV	10.13	9.93	9.82	9.75
λ_{max}, nm (free donor)[d]	257.5	258.2	257.6	262.5
Resolved bands of RI–I_2[e]				
Band 1 λ_{max}, nm	297.6	303.0	304.7	307.9
	(294.7)	(298.3)	(298.9)	(302.0)
$\Delta\nu_{1/2}$, cm^{-1}	4440	4230	4130	4320
	(4850)	(4880)	(4890)	(4930)
Absorbance	0.461	0.518	0.549	0.512
	(0.504)	(0.596)	(0.674)	(0.675)
Band 2 λ_{max}, nm	269.0	271.5	270.5	275.0
	(269.6)	(271.0)	(271.8)	(275.5)
$\Delta\nu_{1/2}$, cm^{-1}	4000	4300	4800	5000
	(3500)	(3620)	(3400)	(3710)
Absorbance	0.640	0.795	0.900	0.915
	(0.512)	(0.638)	(0.577)	(0.661)
Band 3 λ_{max}, nm	245.5	247.5	245.0	248.7
	(247.5)	(249.4)	(252.2)	(252.7)
$\Delta\nu_{1/2}$, cm^{-1}	3240	3370	3220	3510
	(3920)	(3750)	(4840)	(4200)
Absorbance	0.337	0.350	0.253	0.369
	(0.396)	(0.431)	(0.461)	(0.551)

[a] Reference 20. [b] Reference 22. [c] Reference 21. [d] In n-heptane, ref 28. [e] Upper data are from the two-Gaussian curve resolution, and the lower data (in parentheses) are from the three-Gaussian curve resolution (see text for details).
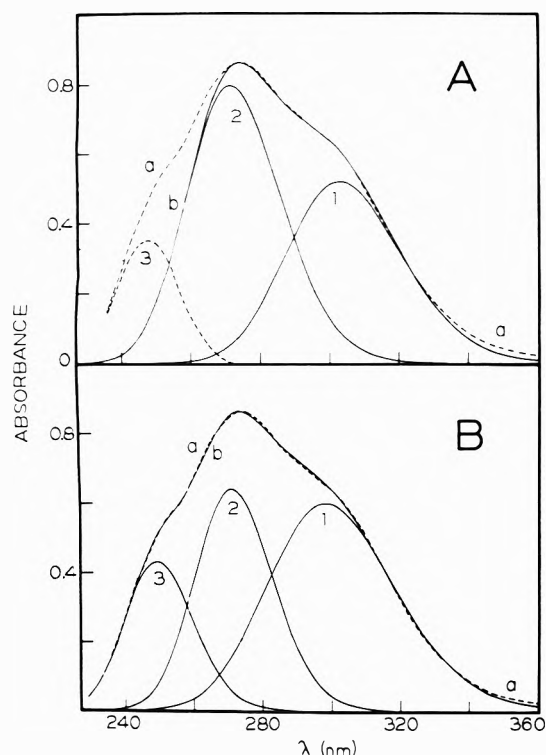
Figure 7. Resolution of the ethyl iodide–I_2 spectrum: (A) a two-Gaussian curve fit over the region 275–360 nm and (B) a three-Gaussian curve fit over the region 240–360 nm (see text for details). The dashed curve (a) is the observed spectrum and the solid curve (b) is calculated from the sum of the resolved bands.

with complexes of thioacetamide–I_2 it is reported that the n → π^* transition of the thioacetamide is blue shifted and, since this band is very near a CT band, it is proposed that the intensity is very much increased due possibly to mixing with the highly intense CT band.[33a]

Together with the band resolution results, Table II includes data on the ionization potentials and the band position of the n → σ^* transition of the "free" donor. The first and second ionization potentials of the donor are correlated with the data of the first and second bands, respectively. The third band is at a lower wavelength, in each case, than that of the corresponding "free" donor, and is consistent with the view that the third band corresponds to a blue shifted n → σ^* transition. The magnitude of this blue shift for MeI, EtI, n-Pr-I, and i-Pr-I is, respectively (in eV), 0.24, 0.21, 0.25, and 0.26. It would be expected that the iodine would undergo a blue shift as well. Voigt[33b] has made a systematic study of the blue-shifted iodine visible band as a function of the type of donor solvent and its ionization potential. The visible band maximum of iodine is at 520 nm in n-heptane (taken to be an "inert" solvent, and comparable to a gas phase value). In MeI, EtI, n-Pr-I, and i-Pr-I the iodine band maximum was found to be at 481, 478, 478.5, and 473 nm, respectively. In terms of an iodine blue shift (in eV) this corresponds to 0.19, 0.21, 0.21, and 0.24, which are comparable to the donor shifts.

This assignment also would account for the absence of a similar shoulder in the RBr–I_2 and RCl–I_2 systems. In n-PrBr and n-PrCl, the n → σ^* transitions are at quite low wavelengths (~197 and <190 nm, respectively)[34] compared to the CCT band positions (Table I), and it is understandable that the spectra for iodine contacts do not have the same complexity (Figures 5 and 6).

According to theory,[3,35,36] the position of the CCT band in the vapor phase is approximated by the equation

$$h\nu_{CCT} \simeq I_D{}^V - E_A{}^V - (e^2/d_{12}) \tag{1}$$

where $I_D{}^V$ is the vertical ionization potential of the donor, $E_A{}^V$ is the vertical electron affinity of the acceptor, e is the electron charge, and d_{12} is the diameter of the donor–acceptor pair. It is known that CT band positions are altered by solvents.[36] There is evidence that the shift for weak

complexes in going from the vapor phase to solution is toward longer wavelength, with a larger shift the weaker the complex.[3] Therefore, in comparing the present solution results with theory, a correction to shorter wavelengths estimated at ~0.5 eV should be made for the solvent effect on the system in the vapor phase.

A plot of $h\nu_{CCT}$ vs. I_D for the n-PrX–I_2 contacts is shown in Figure 8. Here both bands for n-PrI–I_2, corresponding to the first and second I_D of n-PrI, are included. Since it was not possible to resolve the CCT spectrum of n-PrBr–I_2, the average value of the first and second I_D of n-PrBr (10.18 and 10.50 eV)[22] was used. The good linear agreement lends strong support for the CCT character of the bands. The slope of the line is ~ 1.0 which would seem in accord with eq 1 provided d_{12} does not vary greatly for the series. (An estimate of d_{12} is made later.) However, a systematic solvent influence on the slope cannot be discounted.

A similar plot for both CCT bands of all the RI–I_2 contacts is shown in Figure 9. It appears that the data are best decribed by two lines, each of slope much less than 1.0. The reason for this is not clear. It may be noted that, here, the range of $h\nu_{CCT}$ and I_D for each series is relatively narrow compared to that in Figure 8, so that any small systematic effect could change the slope appreciably. Contributing factors may be the interaction of the CCT bands with the n–σ^* band of RI, the approximations made in resolving the bands (e.g., assuming Gaussian shapes of the bands[37]), and the possible dependence of the solvent shifts on the bulkiness of the alkyl group. Error limits of ± 1.5 nm have been added to show how large the effect would be on the points in Figure 9.

A further correlation is shown in Figure 10 between the present solution results for the CCT bands of alkyl iodides with molecular iodine and the vapor phase results for the same donors with atomic iodine. The CCT bands for the latter have been reported as follows: MeI–I at 416 and 349 nm (2.98 and 3.55 eV),[15,19] EtI–I at 426 and 359 nm (2.91 and 3.45 eV),[15,19] n-PrI–I at 429 and 361 nm (2.89 and 3.43 eV),[19] and i-PrI–I at 436 and 368 nm (2.84 and 3.37 eV).[19] A rather good correlation is obtained for the set of CCT bands of lower energy. Extrapolation of the line passes reasonably well through the CCT bands of higher energy, but the possibility of two different slopes cannot be ruled out. The difference of ~0.6 eV between the first and second I_D of the above alkyl iodides is of comparable magnitude to the difference of ~0.5 eV between the two CCT bands for either the RI–I_2 or RI–I contacts. For the same RI, the difference in $h\nu_{CCT}$ for the solution results with molecular iodine and the vapor phase results with atomic iodine is ~1.1–1.2 eV for both the first and second CCT bands. If the solvent effect is considered, this difference would be even larger, possibly ~1.6–1.7 eV. From eq 1

$$\Delta h\nu_{CCT} \simeq \left[-E_A{}^V - \frac{e^2}{d_{12}}\right]_{I_2} - \left[-E_A{}^V - \frac{e^2}{d_{12}}\right]_I \qquad (2)$$

The difference in electron affinity of the iodine atom (3.063 eV)[38] and the iodine molecule (2.58 eV)[39] is only 0.48 eV. Therefore the larger part of the difference is attributable to the e^2/d_{12} terms, and leads to the conclusion that d_{12} for RI–I_2 is larger than that for RI–I.

In the Person rearrangement[40] of the Benesi–Hildebrand equation,[41] where $D_0 \gg A_0$ (and $A_0 > C$), the absorbance is given by

$$\text{absorbance} = \frac{D_0 A_0 b K \epsilon'}{1 + K D_0} \qquad (3)$$
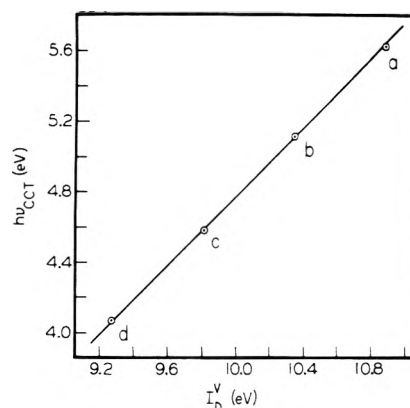
Figure 8. Dependence of the CCT band maximum (eV) of n-propyl halide–I_2 upon the ionization potential, $I_D{}^V$ (eV), of the donor (a) n-PrCl–I_2, (b) n-PrBr–I_2, (c) n-PrI–I_2 (higher energy band), and (d) n-PrI–I_2 (lower energy band).
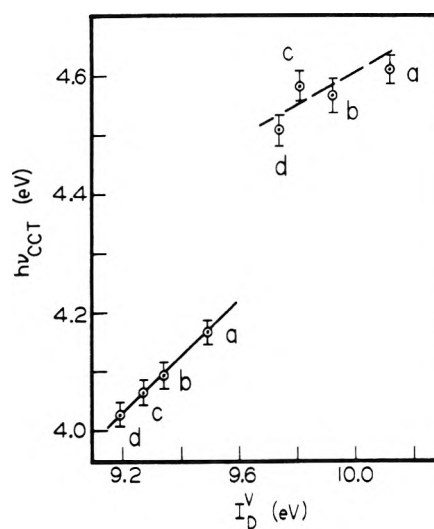
Figure 9. Dependence of the CCT band maximum (eV) of alkyl iodide–I_2 upon the first and second ionization potentials, $I_D{}^V$ (eV), of the donor (a) MeI–I_2, (b) EtI–I_2, (c) n-PrI–I_2, and (d) i-PrI–I_2.
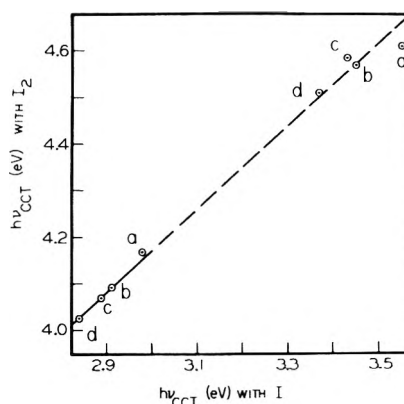
Figure 10. Relation between the maxima for the first and second CCT bands (eV) of molecular iodine and atomic iodine acceptors with the donors (a) MeI, (b) EtI, (c) n-PrI, and (d) i-PrI.

where D_0 and A_0 are the initial concentrations of donor and acceptor, b is the cell path length, ϵ' is a corrected extinction coefficient (extinction coefficient of the complex minus those of the donor and the acceptor at the wave-
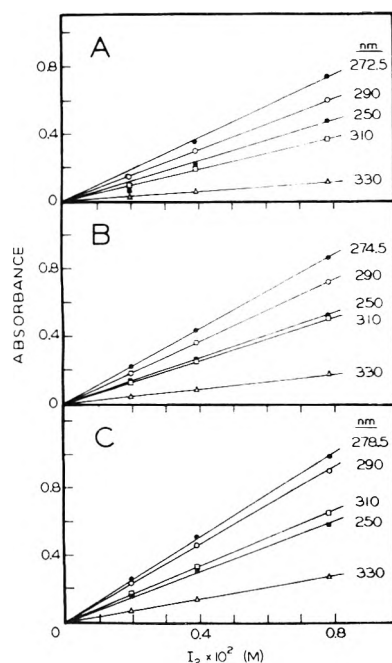
Figure 11. Dependence of the CCT band absorbance of RI–I$_2$ at several wavelengths upon the I$_2$ concentration with fixed RI concentration in a 1.04-mm cell at room temperature: (A) [MeI] = 8.47 × 10^{-2} M; (B) [EtI] = 7.01 × 10^{-2} M; and (C) [i-PrI] = 5.77 × 10^{-2} M.

length λ), and K is the formation constant. For weak complexes in the region of low donor concentration

$$\text{absorbance} \simeq D_0 A_0 b K \epsilon' \qquad (4)$$

This equation applies, of course, to contacts as a limiting case of weak complexes. According to eq 4 there is a linear dependence of absorbance on either the donor or the acceptor concentration.

A similar conclusion is reached from gas phase collision theory.[42] The concentration of contacts n_c (molarity) is given by[8]

$$n_c = 37.84 \times 10^{-4} n_D n_A d_{12}{}^2 \Delta d \qquad (5)$$

where n_D and n_A are the initial concentrations (molarity) of donor and acceptor, respectively, d_{12} is the mean molecular diameter (Å) of the pair, and Δd is the distance (Å) between the pair within which electron transfer can occur. The absorbance from contacts is

$$\text{absorbance} = b\epsilon' n_c = (37.84 \times 10^{-4} d_{12}{}^2 \Delta d) n_D n_A b \epsilon' \qquad (6)$$

In Figure 11, the absorbance of the CCT bands of MeI, EtI, and i-PrI for fixed alkyl halide concentration is plotted at several wavelengths against the iodine concentration. As is seen, there is excellent linearity in all cases, with the line going through the origin, except for one point, i.e., at the lowest concentration of the MeI–I$_2$ system.[43] The dependence of the CCT absorbance on both the concentration of iodine at fixed alkyl halide concentration and of the alkyl halide at fixed iodine concentration was measured in the case of n-PrI–I$_2$, n-PrBr–I$_2$, and n-PrCl–I$_2$. For the first two systems excellent linearity again is observed (Figures 12 and 13). In fact, the spectral curves in general were the same whether the iodine concentration was altered or the donor concentration was altered, as long as the factor was the same. Only in the case of n-PrCl–I$_2$ was this not true. Here, the absorbance showed linearity when the n-
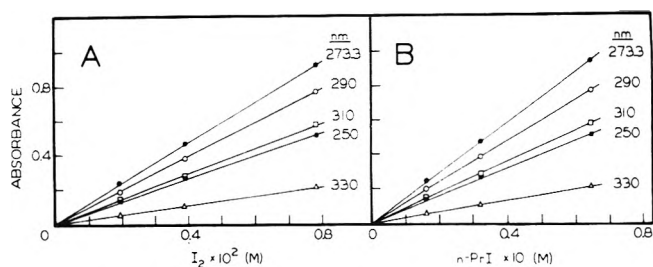
Figure 12. Dependence of the CCT band absorbance of n-PrI–I$_2$ at several wavelengths in a 1.04-mm cell at room temperature upon (A) the I$_2$ concentration with fixed n-PrI concentration (6.44 × 10^{-2} M) and (B) the n-PrI concentration with fixed I$_2$ concentration (7.81 × 10^{-3} M).
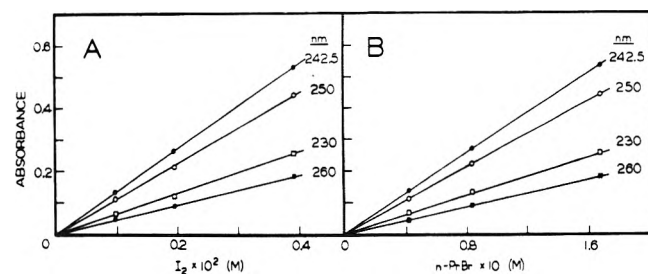
Figure 13. Dependence of the CCT band absorbance of n-PrBr–I$_2$ at several wavelengths in a 1.04-mm cell at room temperature upon (A) the I$_2$ concentration with fixed n-PrBr concentration (1.67 × 10^{-1} M) and (B) the n-PrBr concentration with fixed I$_2$ concentration (3.91 × 10^{-3} M).
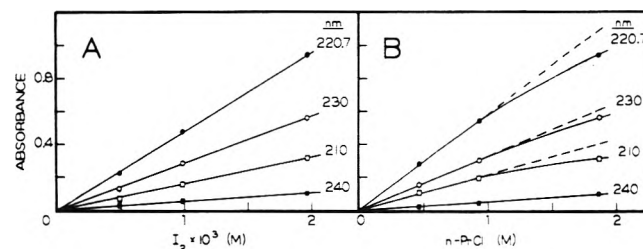
Figure 14. Dependence of the CCT band absorbance of n-PrCl–I$_2$ at several wavelengths in a 1.04-mm cell at room temperature upon (A) the I$_2$ concentration with fixed n-PrCl concentration (1.862 M) and (B) the n-PrCl concentration with fixed I$_2$ concentration (1.96 × 10^{-3} M).

PrCl concentration was held constant but there was definite curvature when the iodine concentration was held constant (Figure 14). This can be attributed to the absorption intensity of the n-PrCl–I$_2$ contacts being lower than that of any of the other contacts in the series studied. Consequently, a quite high range of donor concentrations had to be used, and change by a factor of 2 undoubtedly had appreciable effect on the dielectric property of the medium, which could affect ϵ.[44] This difference in dependence of absorbance with regard to acceptor and donor concentrations for n-PrCl–I$_2$ is apparent also in Figure 6A and 6B.

Equating (4) and (6), the equilibrium constant for contacts (M^{-1}) is

$$K \simeq 37.84 \times 10^{-4} d_{12}{}^2 \Delta d \qquad (7)$$

A somewhat improved K can be calculated from

$$K = \frac{n_c}{(n_D - n_c)(n_A - n_c)} \qquad (8)$$

After correcting $h\nu_{CCT}$ for solvent shift, the vapor phase

TABLE III: Estimated Values of Contact Pair Size (d_{12}), Equilibrium Constant (K), Maximum Molar Extinction Coefficient (ϵ_{max}), and Oscillator Strength (f) of Alkyl Halide–Iodine Contacts

	MeI	EtI	n-PrI	i-PrI	n-PrBr	n-PrCl
$h\nu_{CCT}$,[a] eV	4.166	4.092	4.069	4.027	5.113^b	5.617
I_D^V, eV	9.50	9.34	9.27	9.19	10.34^c	10.88
d_{12},[d] Å	6.39	6.64	6.79	6.91	6.71	6.60
$n_D(RX)$, M	0.0848	0.0701	0.0645	0.0576	0.167_0	1.86_0
$n_A(I_2)$, M × 10³	7.82	7.82	7.81	7.83	3.91	1.96
$\Delta d = 1.0$ Å						
n_c, M	1.02×10^{-4}	$0.91_4 \times 10^{-4}$	$0.87_8 \times 10^{-4}$	$0.81_5 \times 10^{-4}$	1.11×10^{-4}	6.00×10^{-4}
K, M⁻¹	0.15_7	0.16_9	0.17_7	0.18_3	0.17_5	0.23_7
ϵ_{max},[e,f] M⁻¹ cm⁻¹	4.33×10^4	5.44×10^4	6.01×10^4	6.04×10^4	4.64×10^4	1.51×10^4
f[f,g]	0.83_0	0.99_4	1.07	1.13	0.88_8	0.26_2
$\Delta d = 2.0$ Å						
n_c, M	2.04×10^{-4}	1.83×10^{-4}	1.76×10^{-4}	1.63×10^{-4}	2.22×10^{-4}	12.0×10^{-4}
K, M⁻¹	0.31_8	0.34_3	0.35_8	0.37_0	0.36_1	0.85_0
ϵ_{max},[e,f] M⁻¹ cm⁻¹	2.16×10^4	2.72×10^4	3.00×10^4	3.02×10^4	2.32×10^4	$0.75_4 \times 10^4$
f[f,g]	0.41_5	0.49_7	0.53_6	0.56_3	0.44_4	0.13_1
$\Delta d = 4.0$ Å						
n_c, M	4.10×10^{-4}	3.66×10^{-4}	3.51×10^{-4}	3.26×10^{-4}	4.45×10^{-4}	$(> n_A)$
K, M⁻¹	0.65_4	0.70_4	0.73_4	0.75_9	0.76_9	
ϵ_{max},[e,f] M⁻¹ cm⁻¹	1.08×10^4	1.36×10^4	1.50×10^4	1.51×10^4	1.16×10^4	
f[f,g]	0.20_8	0.24_9	0.26_8	0.28_2	0.22_2	

[a] Solution result. [b] Composite band. [c] Average I_D. [d] Constant value of 0.5 eV added to $h\nu_{CCT}$ as the shift from solution to the vapor phase in calculating d_{12} from eq 1. [e] Calculated for RI–I₂ from absorbance data in Table II, and for n-PrBr–I₂ and n-PrCl–I₂ from absorbance data in Table I; cell path length = 0.104 cm. [f] These values pertain to solution because the absorbances were measured in n-heptane solvent. [g] $f \simeq 4.32 \times 10^{-9}\epsilon_{max}\Delta\nu_{1/2}$ (ref 36).

value for d_{12} can be calculated from eq 1 since all other terms are known. The equation is applicable to both the first and second CCT bands. Selection of a value for Δd then permits calculation of n_c, K, the molar extinction coefficient at the band maximum (ϵ_{max}), and the oscillator strength (f).

These calculations were made for the RX–I₂ contacts for several values of Δd (1.0, 2.0, and 4.0 Å) and the results are given in Table III. For the case of RI–I₂, only data for the lower energy CCT band were used. The reasons for this choice are (1) there should be less error on the high wavelength side in correcting for free donor and free acceptor contributions to the absorbance, (2) the generally better correlation with theory involving band positions (Figures 9 and 10), and (3) the fairly constant value for $\Delta\nu_{1/2}$, ~4100–4400 cm⁻¹ for the RI–I₂ series (Table II), which is of a magnitude quite common for CT bands.[45] Further, calculations based on the second CCT band give results which differ only by approximately 15% from the other,[46] and would not change the order of magnitude of the results.

The values for d_{12} are somewhat larger than the van der Waals distance, as proposed by Mulliken.[2a] The trend in contact "size" is reasonable in part, but quantitative comparison of d_{12} really is dubious because of the assumption of a constant correction for the solvent shift of $h\nu_{CCT}$. The values of n_c and K should apply to the vapor phase, and perhaps to solution, but those of ϵ_{max} and f are for solution because the absorbance was measured in n-heptane and the solvent effect on ϵ has not yet been determined.

Values of Δd of the order 1~2 Å are expected.[8,47] The maximum value is likely to be below 4 Å, in the present estimation, because the concentration of contacts for n-PrCl–I₂ then exceeds 100% of the initial iodine concentration for the conditions used (Table III). It is interesting to note that the derived magnitude of K and ϵ when Δd is of the order 1~2 Å is typical of those reported for contacts. For example, Keefer and Andrews[10] report the following K

values in n-heptane solution for MeI–I₂, EtI–I₂, and i-PrI–I₂: 0.23, 0.36, and 0.43 M⁻¹, respectively. Further, Hastings et al.[4] determined the K and ϵ_{max} values for n-butyl bromide–I₂ in n-heptane to be 0.339 M⁻¹ and 23 400 M⁻¹ cm⁻¹. Even if, according to Scott,[48] the equilibrium constant obtained by the Benesi–Hildebrand procedure corresponds to an association in excess of random collisions, the latter appears to be at least an equally important contributor. Such comparison is somewhat complicated by the fact that the experimental determination of K and ϵ is difficult to achieve for weak complexes (although the $K\epsilon$ product can be obtained precisely).[3]

Besides determining K, Keefer and Andrews[10] also obtained values for ϵ in the spectral region 330–360 nm, which is the tail region of the band, and they estimated that ϵ_{max} at lower wavelengths may be of the order 3×10^4 M⁻¹ cm⁻¹. Using their values of ϵ and the resolved band shapes in the present study, ϵ_{max} was calculated for the lower energy CCT band; $\sim2.8 \times 10^4$ for MeI–I₂, $\sim2.6 \times 10^4$ for EtI–I₂, and $\sim2.3 \times 10^4$ for i-PrI–I₂. The results agree with the estimate of Keefer and Andrews. There is reasonably good correlation also with ϵ_{max} in Table III for the case $\Delta d \simeq 2$ Å.

The value listed in Table III for the oscillator strength of MeI–I₂ is a little smaller than that of n-PrBr–I₂. However, the f value for the contact with iodine actually is larger for MeI than for n-PrBr if one considers the fact that with MeI only a single CCT band is involved whereas with n-PrBr there is a composite band. Thus the absorption intensities for contacts with iodine increase in the order n-PrCl < n-PrBr < MeI < EtI < n-PrI < i-PrI, which is the order of decreasing donor ionization potential.

References and Notes

(1) On leave of absence from the Institute for Solid State Physics, The University of Tokyo, Roppongi, Minato, Tokyo, Japan.

(2) (a) R. S. Mulliken, Recl. Trav. Chim. Pays-Bas, **75**, 845 (1956); (b) L. E. Orgel and R. S. Mulliken, J. Am. Chem. Soc., **79**, 4839 (1957). (c) A term suggested by Mulliken to emphasize that violent impact is not necessary.

(3) M. Tamres in "Molecular Complexes", R. Foster, Ed., Crane, Russak and Co., New York, N.Y., 1974, Chapter 2.

(4) S. H. Hastings, J. L. Franklin, J. C. Schiller, and F. A. Matsen, J. Am. Chem. Soc., **75**, 2900 (1953).

(5) D. F. Evans, J. Chem. Phys., **23**, 1424 (1955); J. Chem. Soc., 4229 (1957).

(6) L. M. Julien and W. B. Person, J. Phys. Chem., **72**, 3059 (1968).

(7) C. N. R. Rao, G. C. Chaturvedi, and S. N. Bhat, J. Mol. Spectrosc., **33**, 554 (1970).

(8) M. Tamres and J. Grundnes, J. Am. Chem. Soc., **93**, 801 (1971).

(9) S. N. Bhat, M. Tamres, and M. S. Rahaman, J. Phys. Chem., **77**, 2756 (1973).

(10) R. M. Keefer and L. J. Andrews, J. Am. Chem. Soc., **74**, 1891 (1952).

(11) R. E. Bühler, J. Phys. Chem., **76**, 3220 (1972); Radiat. Res. Rev., **4**, 233 (1972).

(12) R. L. Strong, S. J. Rand, and J. A. Britt, J. Am. Chem. Soc., **82**, 5053 (1960).

(13) T. A. Gover and G. Porter, Proc. R. Soc. London, Ser. A, **262**, 476 (1961).

(14) D. Timm, Acta Chem. Scand., **16**, 1455 (1962); **20**, 2219 (1966).

(15) V. A. Brosseau, J. R. Basila, J. F. Smalley, and R. L. Strong, J. Am. Chem. Soc., **94**, 716 (1972).

(16) J. K. Thomas, J. Phys. Chem., **71**, 1919 (1967).

(17) J. P. Mittal and W. H. Hamill, J. Am. Chem. Soc., **89**, 5749 (1967).

(18) C. Capellos and A. J. Swallow, J. Phys. Chem., **73**, 1077 (1969).

(19) R. L. Strong, private communication.

(20) (a) J. L. Ragle, I. A. Stenhouse, D. C. Frost, and C. A. McDowell, J. Chem. Phys., **53**, 178 (1970). (b) An b^v of 9.533 ± 0.001 recently has been reported: B. P. Tsai, T. Baer, A. S. Werner, and S. F. Lin, J. Phys. Chem., **79**, 570 (1975).

(21) F. Brogli and E. Heilbronner, Helv. Chim. Acta, **54**, 1423 (1971).

(22) K. Kimura, S. Katsumata, Y. Achiba, H. Matsumoto, and S. Nagakura, Bull. Chem. Soc. Jpn., **46**, 373 (1973).

(23) M. Brandon, M. Tamres, and S. Searles, J. Am. Chem. Soc., **82**, 2129 (1960).

(24) H. Tsubomura and R. P. Lang, J. Am. Chem. Soc., **83**, 2085 (1961).

(25) J. D. Childs, Ph.D. Thesis, University of Oklahoma, Norman, Okla., 1971.

(26) M. M. de Maine, P. A. D. de Maine, and G. E. McAlonie, J. Mol. Spectrosc., **4**, 271 (1960).

(27) R. M. Keefer and T. L. Allen, J. Chem. Phys., **25**, 1059 (1956).

(28) K. Kimura and S. Nagakura, Spectrochim. Acta, **17**, 166 (1961).

(29) H. Ito, P. C. Huang, and E. M. Kosower, Trans. Faraday Soc., **57**, 1662 (1961).

(30) R. A. Toschi and D. R. Salahub, Mol. Phys., **24**, 289 (1972).

(31) There is also a contribution of the iodine dimer (I_4) in the sample and reference cells but the difference is not considered to be significant [for references see M. Tamres, W. K. Duerksen, and J. M. Goodenow, J. Phys. Chem., **72**, 966 (1968)].

(32) (a) D. C. Frost, C. A. McDowell, and D. A. Vroom, J. Chem. Phys., **46**, 4255 (1967); A. B. Cornford, D. C. Frost, C. A. McDowell, J. L. Ragle, and I. A. Stenhouse, ibid., **54**, 2651 (1971); (b) B. R. Higginson, D. R. Lloyd, and P. J. Roberts, Chem. Phys. Lett., **19**, 480 (1973).

(33) (a) A. F. Grand and M. Tamres, J. Phys. Chem., **74**, 208 (1970); (b) E. M. Voigt, ibid., **72**, 3300 (1968).

(34) This work.

(35) R. S. Mulliken, J. Am. Chem. Soc., **74**, 811 (1952).

(36) R. S. Mulliken and W. B. Person, "Molecular Complexes: A Lecture and Reprint Volume", Wiley, New York, N.Y., 1969.

(37) Charge-transfer bands often are skewed. G. Briegleb, "Elektronen-Donator-Acceptor-Komplexe", Springer-Verlag, Berlin, 1961, p 46.

(38) R. S. Berry and C. W. Reimann, J. Chem. Phys., **38**, 1540 (1963); R. S. Berry, Chem. Rev., **69**, 533 (1969).

(39) W. A. Chupka, J. Berkowitz, and D. Gutman, J. Chem. Phys., **55**, 2724 (1971).

(40) W. B. Person, J. Am. Chem. Soc., **87**, 167 (1965).

(41) H. A. Benesi and J. H. Hildebrand, J. Am. Chem. Soc., **71**, 2703 (1949).

(42) W. J. Moore, "Physical Chemistry", 4th ed, Prentice-Hall, Englewood Cliffs, N.J., p 149.

(43) This experiment was repeated in our laboratory by Dr. K. Fuke with essentially the same result.

(44) Reference 36, p 97.

(45) Reference 3, Table 2.

(46) For example for MeI-I_2, d_{12} = 5.90 Å, n_c = 0.873 × 10^{-4} M, and K = 0.133 M^{-1} when Δd = 1.0 Å.

(47) J. E. Prue, J. Chem. Soc., 7534 (1965).

(48) R. L. Scott, J. Phys. Chem., **75**, 3843 (1971).

Nanosecond Fluorescence Decay Studies of 2-Hydroxy-1-naphthaleneacetic Acid. Excited-State Proton Transfer[1a]

Ari Gafni,[1b] Robert L. Modlin, and Ludwig Brand*[1c]

Biology Department and McCollum-Pratt Institute, The Johns Hopkins University, Baltimore, Maryland 21218

(Received November 6, 1975)

Excited-state reactions involved in the fluorescence of 2-hydroxy-1-naphthaleneacetic acid have been investigated in aqueous solution in the absence and presence of sodium acetate. Measurements of steady-state fluorescence, nanosecond fluorescence decay, and nanosecond time-resolved emission spectra showed that at least two absorbing species exist in the ground state. Emission is observed from at least three excited-state species (two singly ionized and one doubly ionized). The complex decay kinetics of 2-hydroxy-1-naphthaleneacetic acid are discussed in detail and compared to those of 2-naphthol. This study demonstrates the advantage of nanosecond fluorometry over steady-state measurements for investigations of excited-state reactions.

Introduction

It is well known that aromatic hydroxyl derivatives are stronger acids in the first excited singlet state than in the ground state.[2a] Weller[2b] showed that in the case of salicylic acid, intramolecular proton transfer from the hydroxyl group to the carboxylate ion can occur during the lifetime of the excited state. This process is facilitated since the carboxylate becomes a stronger base in the excited state while the hydroxyl becomes a stronger acid. Schulman and his co-workers[3-5] have used absorption and steady-state fluorescence measurements to investigate ionization sequences in the ground and excited states of salicylic acid, hydroxynaphthoic acids, and other similar aromatic acids.

Loken et al.[6] have used fluorescence decay measure-

ments to investigate excited-state proton transfer with 2-naphthol and have shown that nanosecond time-resolved emission spectroscopy is capable of providing detailed information about these systems. 2-Naphthol undergoes a two-state excited-state reaction (proton transfer) which can be reversible or irreversible depending on the pH. It was shown by these authors that 2-naphthol follows the general reaction mechanisms[2a] shown in Scheme I. When

Scheme I
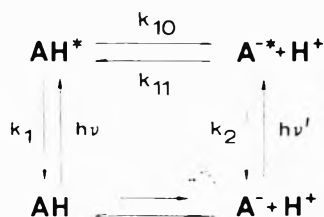
the pH is well below the ground-state pK only the neutral species, AH, will be present in the ground state. Excited-state proton transfer will take place to an extent determined by the rate constants k_{11} and k_{10} as well as by the pH of the solution and k_1, the combined rate constant for all processes which compete with the proton transfer for depopulating the excited singlet state AH*. These include both radiative and nonradiative mechanisms.

Around neutral pH the rate of reprotonation in the excited state is negligible compared with the competing processes (denoted by k_2), due to the small H$^+$ concentration (k_2 is usually of the order of 10^8 s^{-1} while even if reprotonation is diffusion controlled, i.e., $k_{11} \sim 10^{11}$, the product $k_{11}[\text{H}^+]$ will be only 10^4 s^{-1}). For 2-naphthol (pK = 9.46, pK^* = 2.8[2a]), excited-state proton transfer at neutral pH will thus be irreversible and the concentrations of neutral and ionized species will change with time according to

$$[\text{AH*}] = [\text{AH*}]_0 e^{-t/\tau_1} \qquad (1a)$$

$$[\text{A}^{-*}] = \frac{[\text{AH*}]_0 k_{10}}{k_1 + k_{10} - k_2} [e^{-t/\tau_2} - e^{-t/\tau_1}] \qquad (1b)$$

$$\tau_1 = 1/(k_1 + k_{10}) \qquad (1c)$$

$$\tau_2 = 1/k_2 \qquad (1d)$$

At neutral pH the 2-naphthol fluorescence thus decays as a single exponential. The fluorescence due to the naphtholate anion formed in the excited state follows a double exponential decay law with the two preexponential terms equal in absolute value but opposite in sign. Note that τ_1 is dependent upon k_{10}, the deprotonation rate constant, and will become shorter when the latter process is facilitated.

In the present study, excited-state reactions involving a related molecule, 2-hydroxy-1-naphthaleneacetic acid, were examined using steady-state fluorescence, nanosecond fluorescence decay measurements, and time-resolved emission spectroscopy. It is shown that this molecule, whose steady-state emission spectrum resembles that of 2-naphthol, actually follows very different, and more complex, reaction mechanisms. Nanosecond fluorescence techniques thus allow one to obtain a deeper insight into molecular kinetics in the excited state.

Experimental Section

2-Hydroxy-1-naphthaleneacetic acid, obtained from the Aldrich Chemical Co. (Milwaukee, Wisc.), was treated twice with activated charcoal, recrystallized from ethanol–water (10:90, v:v), and dried for 5 days under vacuum over silica gel in the dark. To prevent decomposition, it was

stored in the dark at about −20 °C. It migrated as a single spot on silica-gel thin layer chromatography with a solvent of benzene–dioxane–acetic acid (90:25:4, v:v:v). Absorbance measurements were made with a Beckman DU or a Cary 14 spectrophotometer. Steady-state fluorescence spectra were obtained with a Perkin-Elmer MPF-4 spectrophotofluorometer (uncorrected) or with an instrument constructed in the laboratory (corrected). The latter instrument collects spectra by the photon counting method. These data are stored in a multichannel analyzer operating in the multichannel scaling mode, then transferred to a Hewlett-Packard 2100 minicomputer, and required corrections are made under software control. In all the fluorescence measurements the dye concentrations were ~5 × 10^{-5} M.

Fluorescence decay curves and nanosecond time-resolved emission spectra were obtained with a monophoton counting fluorescence decay instrument.[7,8] The lamp profile and the decay curve were collected semisimultaneously in order to compensate for timing drift or change in shape of the lamp profile. This was achieved by mounting the sample and scattering cuvettes on a turntable. A computer controls the turntable position so that each cuvette can alternately be positioned in the light path. The computer also controls the emission wavelength and the function of the multichannel analyzer (MCA). During data collection, the computer first positions the fluorescence sample in the light path and sets the monochromator to the desired emission wavelength. The MCA is directed to store in the first half of memory and start collecting data in the accumulation mode. After a designated dwell time (typically 5–10 min) the data collection is stopped. The turntable is then positioned so that the scattering solution (Ludox) is in the light path and the emission monochromator is set to the exciting wavelength. The MCA is directed to route to the second half of memory and data collection is started in the accumulation mode. After a specified lamp dwell time (typically 2 to 3 min) the data collection is stopped. The sequence is repeated until the desired total number of counts has been obtained and the lamp and sample data are then transferred to computer memory.

The sample was excited by an air flash lamp through a Ditric 313-nm interference filter. The sample holder was thermostated at 20 °C. The emission was observed at right angles through a Bausch and Lomb 0.5-m monochromator with slits giving a 6.6 nm half-band width. The lifetime instrumentation has been described in more detail elsewhere.[8]

Deconvolution and analysis for a sum of exponential terms was achieved by the method of Laplace transforms[9] and/or by the method of nonlinear least squares.[10] The fitting function that was used to model the experimental decay data is defined in terms of the convolution integral

$$F(\lambda, t) = \int_0^t E(x - Q)\, \mu(x - Q)\, f(\lambda, t - x)\, dx \qquad (2)$$

where $\mu(t)$ is the unit step function. Q is the energy-dependent time shift of the detector.[9] This is determined independently with the use of single-lifetime reference dyes. The impulse model, $f(\lambda, t)$, is given by a sum of exponentials.

$$f(\lambda, t) = \sum_{j=1}^{p} a_j e^{-t/\tau_j} \qquad (3)$$

The fit between the experimental and theoretical decay curves was evaluated by convolving the experimental lamp flash with the impulse response obtained by analysis and

A. Gafni, R. L. Modlin, and L. Brand

by inspection of the reduced χ^2, the weighted residuals, and the autocorrelation function of the residuals.

Deconvolved time-resolved emission spectra were obtained by analysis of the decay curves for each wavelength to three or four exponential terms. The decay curves at the different wavelengths are collected for varying periods of time. The impulse responses, $f(\lambda,t)$, must therefore be normalized to a constant excitation light flux intensity. The equivalent procedure used here was to normalize the impulse responses to the steady-state emission spectrum of the sample which was obtained under the same instrumental conditions as the decay curves.

Results

The absorption and steady-state fluorescence spectra of 2-hydroxy-1-naphthaleneacetic acid are in general similar to those found with 2-naphthol. The expected shift to longer wavelength is observed as the hydroxyl group becomes ionized. The pK_a for this ionization was determined spectrophotometrically at 360 nm and was found to be 10.5. This is about one pK unit above the corresponding pK_a for 2-naphthol,[2a] reflecting the influence of the ionized carboxyl group on the ease of proton release by the hydroxyl group.

The steady-state fluorescence spectra of 2-hydroxy-1-naphthaleneacetic acid at acid, neutral, and alkaline pH are shown in Figure 1. The emission maximum at acid pH is very close to that observed for 2-naphthol, indicating that the neutral carboxyl group has little effect on the emission energy. In basic solution the emission maximum is at 436 nm as compared to 425 nm for 2-naphthol. The excited-state pK_a (pK_a^*) of 2-hydroxy-1-naphthaleneacetic acid was determined from the spectral data by use of the Förster cycle[11] and found to be equal to 3.3. In view of the values for the ground-state and excited-state pK_a it is clear that at neutral pH only the singly ionized species (ionized carboxyl and protonated hydroxyl) will be present in the ground state. The long wavelength shoulder in the emission spectrum at neutral pH (Figure 1b) may thus be attributed to excited-state proton transfer.

The effect of increasing concentrations of acetate ion on the steady-state fluorescence spectra of 2-hydroxy-1-naphthaleneacetic acid is shown in Figure 2. Acetate, having a pK_a well above the pK_a^* of the hydroxyl group, may serve as a proton acceptor and thus facilitate excited-state proton transfer.[2a] As expected, proton transfer increases with increasing acetate concentration. An apparent isoemissive point is observed at 399 nm which might be taken to indicate that only two emitting species are present. Based only on steady-state fluorescence spectra, 2-hydroxy-1-naphthaleneacetic acid might appear to follow Scheme I, i.e., to be a two-state system like 2-naphthol.

This simple picture is totally altered when the results of nanosecond fluorescence decay measurements are considered. Figure 3 shows the decay curve of 2-hydroxy-1-naphthaleneacetic acid at 450 nm obtained in aqueous solution at neutral pH. The experimental lamp flash is also shown. Figure 3a shows the best fit for a two-component exponential decay while Figure 3b indicates the best fit for a three-component exponential decay law. The analyses were carried out by the method of nonlinear least squares.[10] The fit for a two exponential decay law is seen to be poor while that for three exponential components is excellent. The negative amplitude associated with the short lifetime component clearly indicates that an excited-state reaction is
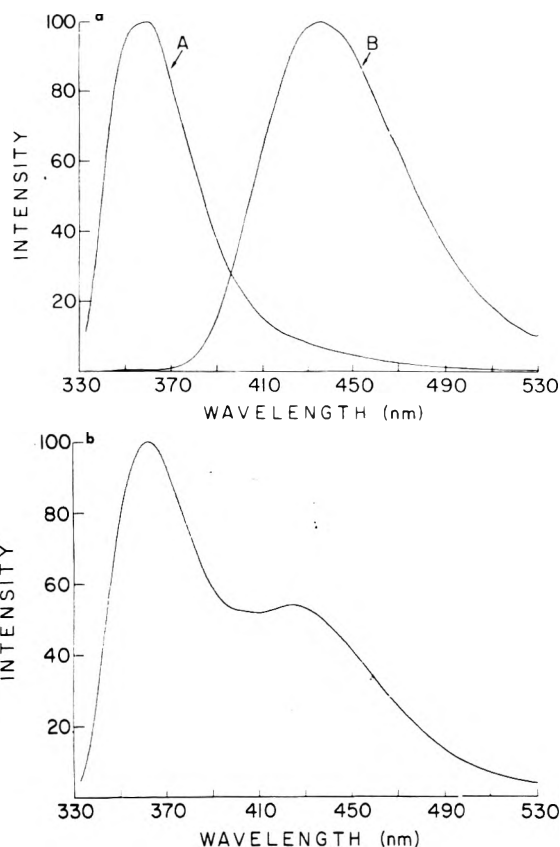
Figure 1. Corrected steady-state emission spectra of 2-hydroxy-1-naphthaleneacetic acid. The excitation wavelength was 313 nm; emission half-bandwidth was 6.6 nm; $T = 20$ °C. (a) Emission in aqueous 0.1 N HCl (A) and 0.1 N NaOH (B) normalized to the same height at the peaks. (b) Emission in aqueous 0.001 M phosphate buffer, pH 7.2.
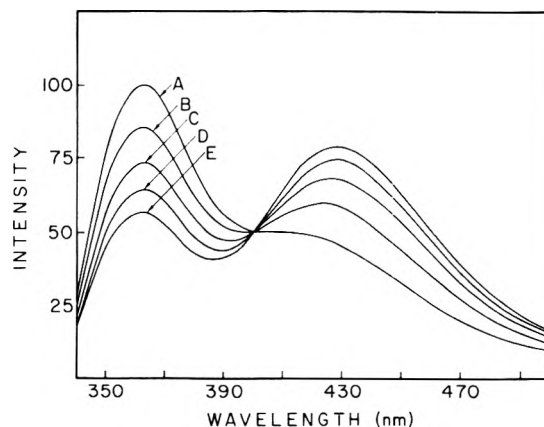
Figure 2. Emission spectra of 2-hydroxy-1-naphthaleneacetic acid in neutral aqueous solution in the presence of different concentrations of sodium acetate: (A) no acetate, (B) 0.025 M acetate, (C) 0.05 M acetate, (D) 0.075 M acetate, (E) 0.1 M acetate. Excitation wavelength 330 nm, room temperature (~23 °C).

taking place. However, in contrast with the prediction of eq 1b, the sum of the two positive amplitudes is appreciably higher than that of the negative one; the reasons for this will be discussed later. The two exponential terms associated with positive amplitudes indicate that 2-hydroxy-1-naphthaleneacetic acid deviates from the simple two-state mechanism shown in Scheme I. As will be shown, these two decay constants represent two emitting species.

The deviation between the decay mechanism of the mol-
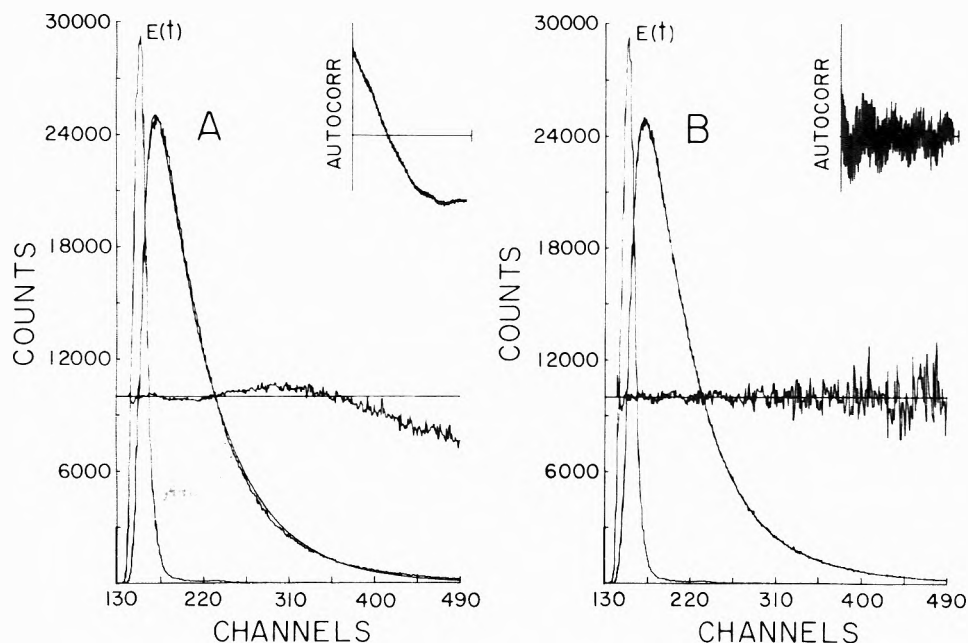
Figure 3. Experimental and computed fluorescence decay curves of 2-hydroxy-1-naphthaleneacetic acid in aqueous 0.001 M phosphate buffer, pH 7.2. The lamp flash used for excitation, $E(t)$, as well as the weighted residuals and the autocorrelation function of the residuals are also shown. The excitation wavelength was 313 nm; emission wavelength 450 nm; $T = 20$ °C; timing calibration 0.204 ns/channel. (a) Decay curve analyzed for two components. Parameters obtained: $\tau_1 = 1.6$ ns, $\alpha_1 = -0.13$, $\tau_2 = 11.6$ ns, $\alpha_2 = 0.38$, $\chi^2 = 14.8$. (b) Decay curve analyzed for three components. Parameters obtained: $\tau_1 = 4.2$ ns, $\alpha_1 = -0.43$, $\tau_2 = 7.1$ ns, $\alpha_2 = 0.60$, $\tau_3 = 17.0$ ns, $\alpha_3 = 0.10$, $\chi^2 = 1.53$.

ecule under study and Scheme I becomes more dramatic when decay curves obtained at different emission wavelengths are examined. The results of such a study are summarized in Table I. It is seen that even in the short wavelength region of emission, where the singly ionized species emits, the decay laws are multiexponential, while Scheme I predicts a single decay constant in this part of the spectrum (which is the case for 2-naphthol at neutral pH). Moreover, a definite negative amplitude, associated with a very short decay time, indicates that emitting species in this spectral range as well are, to some extent, generated in an excited-state reaction. This is pictorially represented in Figure 4 which shows the impulse responses at a number of wavelengths. Since the impulse responses describe the fluorescence intensity changes following an infinitely short flash of exciting light, they are free of convolution distortions and the rise in intensity at short times is a manifestation of one or more excited-state reactions.

The fluorescence decay of 2-hydroxy-1-naphthaleneacetic acid was also obtained in 1 N HCl at 360-nm emission and in 0.1 N NaOH at 450-nm emission. In base both the hydroxyl and the carboxyl groups are expected to be ionized. The decay curves obtained both in acid and in base gave a good analysis for single exponentials. The decay time in acid was 6.1 ns and the decay time in base was 16.7 ns.

The results obtained at neutral pH will be described with reference to the tentative reaction mechanism shown in Scheme II. As is indicated in Table I, the fluorescence decay at neutral pH can be analyzed according to a three exponential decay law. In the long-wavelength region (406–520 nm) an exponential component is obtained with a decay time, τ_3, of 16–20 ns. The variation of the exact value of this decay component as a function of wavelength is attributed, at least in part, to analysis error. Simulation experiments have shown that a long lifetime component with a low relative amplitude tends to be given a somewhat

Scheme II
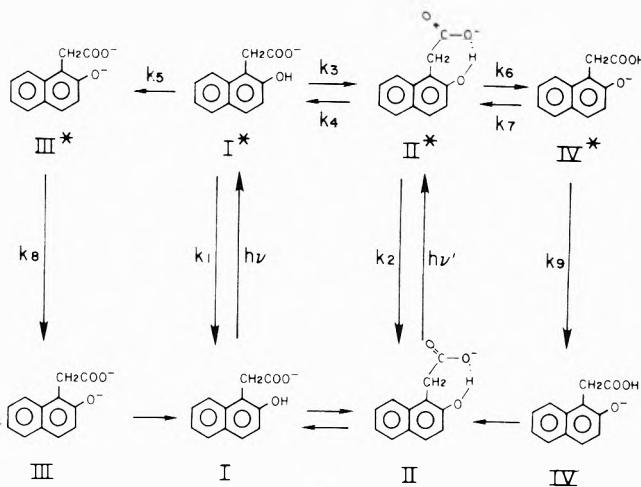
longer decay time by the non-linear least-squares algorithm.

It is reasonable to assign the 16–20-ns decay component (τ_3) to emission from the doubly ionized species (III* in Scheme II). This is done by analogy with the 16.7-ns decay obtained as a single exponential in base where only the dianion can exist.

The fluorescence across the long-wavelength emission band is assumed to arise mainly from species with an ionized hydroxyl (designated as III* and IV* in Scheme II). A short decay time, τ_1, with a value of about 4.5 ns and a *negative* preexponent is observed across this emission band. It is postulated that this is a kinetic component associated with the lifetime of I* which generates the species III* and IV* whose emission is observed in this wavelength region.

The third decay time observed in this wavelength region is designated as τ_2 and has a value of 7–8 ns. By the process of elimination it is assigned to the decay of IV*. Additional experimental evidence to support this assignment has been

TABLE I: Decay Parameters, at Various Wavelengths, of 2-Hydroxy-1-naphthaleneacetic Acid in Aqueous 0.001 M Phosphate Buffer (pH 7.2, T = 20 °C)[a]

λ, nm	Fractional amplitude	Decay time, ns	χ^2
340	$\alpha_1 = -41$	$\tau_1 = 0.5$	1.18
	$\alpha_2 = +47$	$\tau_2 = 4.5$	
	$\alpha_3 = +12$	$\tau_3 = 6.9$	
352	$\alpha_1 = -17$	$\tau_1 = 0.2$	1.19
	$\alpha_2 = +63$	$\tau_2 = 4.6$	
	$\alpha_3 = +19$	$\tau_3 = 6.3$	
370	$\alpha_1 = -22$	$\tau_1 = 0.2$	1.10
	$\alpha_2 = +66$	$\tau_2 = 4.7$	
	$\alpha_3 = +13$	$\tau_3 = 6.7$	
406	$\alpha_1 = -5$	$\tau_1 = 4.5$	1.16
	$\alpha_2 = +90$	$\tau_2 = 7.3$	
	$\alpha_3 = +5$	$\tau_3 = 20.6$	
435	$\alpha_1 = -38$	$\tau_1 = 4.4$	1.31
	$\alpha_2 = +54$	$\tau_2 = 7.0$	
	$\alpha_3 = +8$	$\tau_3 = 17.1$	
460	$\alpha_1 = -39$	$\tau_1 = 4.4$	1.18
	$\alpha_2 = +52$	$\tau_2 = 7.2$	
	$\alpha_3 = +9$	$\tau_3 = 17.3$	
490	$\alpha_1 = -38$	$\tau_1 = 4.0$	1.40
	$\alpha_2 = +51$	$\tau_2 = 7.9$	
	$\alpha_3 = +11$	$\tau_3 = 18.0$	
520	$\alpha_1 = -44$	$\tau_1 = 4.5$	1.81
	$\alpha_2 = +47$	$\tau_2 = 6.2$	
	$\alpha_3 = +9$	$\tau_3 = 16.3$	

[a] The lifetimes are numbered, at each wavelength, according to increasing values and are not necessarily equivalent to the corresponding ones in the theoretical equations.
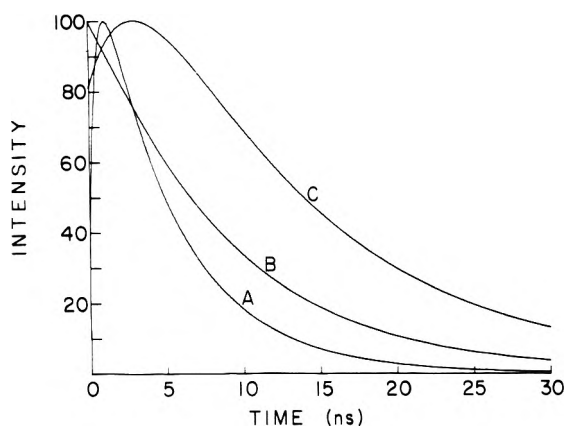
Figure 4. Normalized fluorescence impulse response functions generated from the decay parameters for different wavelengths: (A) 340 nm, (B) 410 nm, (C) 510 nm.

obtained both by acetate competition experiments and by means of time-resolved emission spectroscopy. Since acetate ions can serve as proton acceptors, they are expected to compete with *intramolecular* proton transfer. This would cause the fraction of the doubly ionized, III*, to increase at the expense of the singly ionized, IV*. The results given in Table II show that this is indeed the case. As the rate of proton transfer is enhanced by acetate, τ_1, the lifetime assigned to the proton donor (I*) becomes shorter as predicted by eq 1c. The amplitude associated with τ_3 increases relative to that associated with τ_2, while the two decay times do not change significantly. It is of interest that as α_3 becomes larger, τ_3 approaches the decay time ob-

TABLE II: Decay Parameters Obtained for 2-Hydroxy-1-naphthaleneacetic Acid in Aqueous Solution in the Presence of Different Concentrations of Sodium Acetate[a]

Acetate concn, M	τ_1	α_1	τ_2	α_2	τ_3	α_3	χ^2
0	4.2	-38	7.1	53	17.0	9	1.53
0.025	3.4	-36	7.6	38	17.3	26	1.56
0.05	3.2	-38	6.3	28	16.9	34	1.48
0.10	2.5	-38	6.1	17	16.9	45	1.33
0.20	1.7	-39	6.4	8	16.9	53	1.42

[a] The pH was 7.2 for all the solutions, T = 20 °C. The excitation wavelength was 313 nm, fluorescence decays were followed at 450 nm.

tained in 0.1 N NaOH in accord with the comment made above regarding analysis errors. A plot of $1/\tau_1$ vs. acetate concentration gave a straight line, yielding a value of 1.7 X 10^9 M^{-1} s^{-1} for the bimolecular acetate quenching constant. The acetate experiments provide support for the assignments for τ_1, τ_2, and τ_3 made above.

Additional evidence for the existence of the intramolecular proton transfer product (species IV*) has been obtained by means of time-resolved emission spectroscopy. The rationale for this experiment was as follows. Comparison of the steady-state fluorescence spectra of 2-naphthol[2a,12] and 2-hydroxy-1-naphthaleneacetic acid indicates that the protonated carboxyl group has little effect on the emission maximum of the neutral molecule while the ionized carboxylate anion has a significant effect on those of both the protonated and ionized hydroxyl forms. It follows that species IV* which has a protonated carboxyl might be expected to have an emission maximum near 425 nm (like the 2-naphtholate ion) in contrast to the emission maximum of 436 nm of the doubly ionized species, III*. The emission attributed to IV* has a greater amplitude but shorter decay time than that due to III*. Thus emission from IV* should dominate the longer wavelength band emission spectra obtained at early times while emission from III* should dominate the emission spectra obtained at late times during the decay.

Deconvolved nanosecond time-resolved emission spectra (fluorescence spectra at different times during the decay) were obtained according to the procedure described here and elsewhere.[8] Fluorescence decay curves in neutral aqueous solution were collected between 335 and 480 nm in 3–5-nm intervals and between 480 and 520 nm in 10-nm intervals. The decay parameters were then obtained by analysis of the data and the emission spectra at discrete times after excitation were constructed. Figure 5 shows the emission spectra of 2-hydroxy-1-naphthaleneacetic acid at 0.4, 12, 24, and 48 ns normalized to the same height at 398 nm.[13] Since these were constructed using deconvolved decay data, distortion due to convolution was eliminated.

In order to compare the long wavelength region of the different spectra, the contribution due to the 360-nm band was eliminated as follows. The spectrum at 0.4 ns and the spectrum to be analyzed for peak wavelength were normalized to the same area between 355 and 365 nm. The 0.4-ns spectrum, so normalized, was then subtracted from the spectrum to be analyzed, yielding a spectrum practically free from distortions by the 360-nm band. The resulting "corrected" spectra were normalized to the same height at the peak to allow easy visual check of peak shifts. Two of these spectra, after 12 and after 60 ns, are shown in Figure
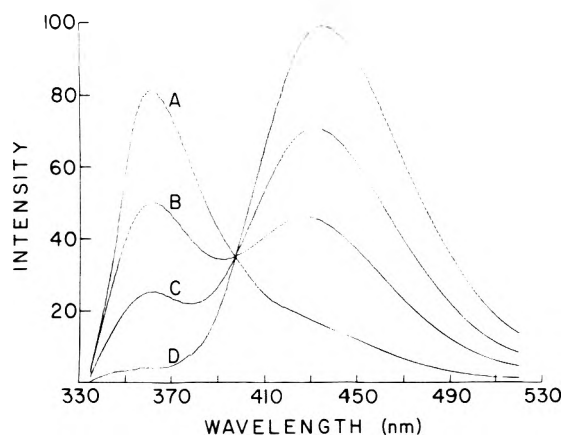
Figure 5. Deconvolved nanosecond time-resolved emission spectra of 2-hydroxy-1-naphthaleneacetic acid in aqueous 0.001 M phosphate buffer, pH 7.2, $T = 20$ °C: (A) 0.4 ns, (B) 12 ns, (C) 24 ns, (D) 48 ns after photoexcitation. The spectra were normalized to the same height at 398 nm.

Figure 6. Time-resolved emission spectra (A) after 12 ns and (B) after 60 ns, from which the 360-nm band has been subtracted (see text for details). The spectra were normalized at the peaks.

6, and a shift to longer wavelength is clearly seen to take place with time. The species decaying with a lifetime of about 6–7 ns does resemble 2-naphthol in its emission and is very likely to be the product of intramolecular proton transfer (IV*). It is of interest to note that no shift with time was observed when time-resolved emission spectra of 2-naphthol were treated in the manner described above,[12] providing a control for this experiment.

Analysis of decay curves obtained through the long wavelength emission band (Table I) indicates that the sum of the positive amplitudes is appreciably greater than the absolute value of the negative amplitude. Two possible explanations for this discrepancy are: (1) that the emitting species is partially created directly by the exciting light or by a very fast excited-state reaction, or (2) that the difference in amplitudes is caused by "spectral contamination" from the parent compound[12] (AH* in Scheme I), if its emission spectrum overlaps that of the product. Equation 1b then becomes

$$[A^{-*}] = \frac{[AH^*]_0 k_{10}}{k_1 + k_{10} - k_2} [e^{-t/\tau_2} - e^{-t/\tau_1}] + ce^{-t/\tau_1} \qquad (4)$$

c is the factor which determines the contribution of emission due to the parent compound at the wavelength of interest. At a wavelength near the isoemissive point, where the parent and product species emit with comparable intensities, c will be large and the resultant amplitude associated with τ_1 will be small. This is clearly the case at 406 nm (Table I). In contrast, errors due to spectral contamination cannot account for the constant high ratio of ~1.5 found between the sum of the positive and the negative amplitudes in the 430–520-nm region. It is thus reasonable to assume that a significant fraction of the emission in the 430–520-nm spectral region is due to molecules in which the hydroxyl group is ionized rapidly following excitation. Support for this proposal is found in the time-resolved emission spectra obtained at early times. The 0.4-ns emission spectrum (Figure 5) shows a shoulder above 400 nm. No such shoulder appears in the emission spectrum at acid pH (Figure 1) or in the 0.4-ns time-resolved emission spectrum of 2-naphthol.[12] The *difference* between the positive and negative amplitudes observed with 2-naphthol is either absent or very small.[12] A possible explanation for this finding is that the shoulder near 400 nm represents emission from the hydrogen bond species designated as II* in Scheme II. It is not unreasonable to suggest that a small
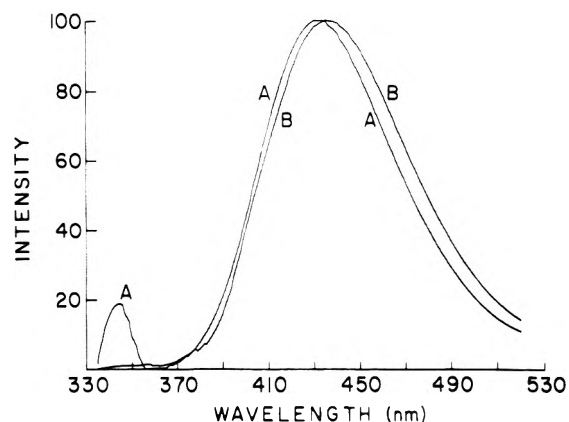
fraction of the molecules may exist in a hydrogen bonded form (II) in the ground state. Direct conversion of II to II* as indicated in Scheme II would explain the burst of proton transfer invoked above on the basis of the inequality of the positive and negative amplitudes.

Discussion

The complex excited-state kinetics proposed here for 2-hydroxy-1-naphthaleneacetic acid are summarized in Scheme II. Two species, I and II, may exist in equilibrium in the ground state. Direct excitation by light leads to I* and possibly II* which emit light but also form III* and IV* which then contribute to the fluorescence. Thus three or possibly four species emit light at neutral pH. Of these only I* emits at the short wavelength band around 360 nm. Species IV* and III* emit with maxima at about 425 and 435 nm, respectively. Species II* may make a small contribution to the emission in the 400-nm region. It is present in small concentration due to its high reactivity.

One observation which deserves clarification is the isoemissive point obtained in the acetate titration (see Figure 2). In the absence of acetate, mainly species IV* is generated, as seen in Table II. Acetate ions cause increasing concentrations of species III* to appear and a shift of the isoemissive point to longer wavelength might have been anticipated. The absence of such a shift suggests that the two isoemissive points are very close to each other. This may be due to the fact that species III*, in addition to its longer wavelength of emission, also has a higher quantum yield (recall that it has the longer lifetime). The decay data presented here are inconsistent with a model based on only two emitting species. The use of isoemissive points as criteria for two-state systems should be exercised with caution.

The experimental decay times and amplitudes obtained in this study can best be understood if they are considered in relation to the theoretical rate equations describing Scheme II. These are derived with the reasonable assumption that at neutral pH the H^+ concentration is too low for any appreciable reprotonation of species III* prior to emission. In addition species IV* will not ionize directly to form III* since, if the pK_a of the carboxyl group is near 4 and even if its protonation is diffusion controlled, the ionization rate of IV* will be slow compared to the rate of light emission.

The differential rate equations describing fluorescence emission from the excited species shown in Scheme II are given as follows

$$d[I^*]/dt = k_4[II^*] - (k_1 + k_3 + k_5)[I^*] \quad (5a)$$

$$d[II^*]/dt = k_3[I^*] + k_7[IV^*] - (k_2 + k_4 + k_6)[II^*] \quad (5b)$$

$$d[III^*]/dt = k_5[I^*] - k_8[III^*] \quad (5c)$$

$$d[IV^*]/dt = k_6[II^*] - (k_7 + k_9)[IV^*] \quad (5d)$$

By denoting

$$K_1 = k_1 + k_3 + k_5$$
$$K_2 = k_2 + k_4 + k_6$$
$$K_3 = k_7 + k_9$$

it can be shown that the decays of both I* and IV* can be described by the same expression

$$\frac{d^3[Y^*]}{dt^3} + (K_1 + K_2 + K_3)\frac{d^2[Y^*]}{dt^2}$$
$$+ (K_1K_2 + K_1K_3 + K_2K_3 - k_3k_4 - k_6k_7)\frac{d[Y^*]}{dt}$$
$$+ (K_1K_2K_3 - k_3k_4K_3 - k_6k_7K_1)[Y^*] = 0 \quad (6)$$

where Y* represents I* or IV*.

Thus the differential equations describing the decay of these two species are identical. As a consequence, the three decay constants obtained as the three real roots of the cubic auxiliary equation will be identical so that

$$[I^*] = a_1e^{-t/\tau_1} + a_2e^{-t/\tau_2} + a_3e^{-t/\tau_3} \quad (7a)$$

$$[IV^*] = b_1e^{-t/\tau_1} + b_2e^{-t/\tau_2} + b_3e^{-t/\tau_3} \quad (7b)$$

The decay times as obtained from emission in the short wavelength band are (Table I) $\tau_1 \sim 0.2$ ns, $\tau_2 \sim 4.5$ ns, and $\tau_3 \sim 6.5$–7 ns.

The amplitudes in eq 7a are different than those in eq 7b since the boundary conditions for I* and IV* differ. I* is to a large extent created directly by the exciting light pulse and its concentration at zero time will be finite ($a_1 + a_2 + a_3 > 0$). In contrast IV* is generated totally in the excited state and its concentration is zero at zero time ($b_1 + b_2 + b_3 = 0$). The amplitudes a_1 and b_1 which are associated with the short decay time, τ_1, are negative and represent the excited-state generation of I* and IV* from II*. The amplitudes a_3 and b_3 have to be positive since they are associated with the longest decay time for the two corresponding species. If this were not the case, the concentrations of the emitting species would become negative at long times.

It is important to emphasize that the emission in the short wavelength region is essentially all due to I*, and thus the analyses given in Table I for 340–370 nm represent the parameters of eq 7a. In contrast the fluorescence at long wavelengths contains contributions due to emission from IV*, III*, and possibly to a smaller extent from II*.

The time-dependent concentration of species III* is found by substituting the expression for I* from eq 7a into eq 5c and solving the differential equation thus obtained. This yields

$$[III^*] = c_1e^{-t/\tau_1} + c_2e^{-t/\tau_2} + c_3e^{-t/\tau_3} + c_4e^{-t/\tau_4} \quad (8)$$

where

$$c_1 = \frac{k_5a_1}{\frac{1}{\tau_4} - \frac{1}{\tau_1}}; \quad c_2 = \frac{k_5a_2}{\frac{1}{\tau_4} - \frac{1}{\tau_2}}; \quad c_3 = \frac{k_5a_3}{\frac{1}{\tau_4} - \frac{1}{\tau_3}};$$

$$c_4 = c_1 + c_2 + c_3; \quad \tau_4 = \frac{1}{k_8}$$

τ_4 is the decay constant of the doubly ionized species and is the longest lifetime associated with III* (~17 ns). c_4 is

therefore positive. Of the other three amplitudes c_1 is positive (since $a_1 < 0$) while c_2 and c_3 are negative.

Since the suggested species II* serves as an intermediate between I* and IV*, it will decay with the same decay constants as these two species. All three amplitudes associated with it will be positive. The emission maximum of II* could not be identified in the steady-state or time-resolved emission spectra due to its low relative intensity but it is reasonable to assume that it would contribute to the longer wavelength emission band.

Since the longer wavelength emission band contains a contribution from III*, it should show all four lifetimes τ_1 to τ_4. The amplitude associated with τ_1 is probably very small since the negative amplitude it has in the expression for [IV*] tends to be cancelled by the two positive amplitudes associated with τ_1 in [III*] and [II*]. This, combined with its very short lifetime, results in the masking of τ_1 by τ_2 which is also associated with a negative amplitude in this spectral region. τ_3 will be associated with a net positive amplitude since the negative amplitude it has in the expression for [III*] is reversed by the much larger positive amplitude it has in the expression for [IV*], which is the dominant emitting species in the long wavelength band at neutral pH.

Conclusion

Advances in instrumental techniques and procedures for data analysis have made nanosecond fluorometry a powerful tool for investigation of excited-state reactions. The development of nanosecond time-resolved emission spectroscopy makes it possible to identify spectral intermediates which are not easily seen in steady-state spectra. 2-Hydroxy-1-naphthaleneacetic acid differs from the hydroxynaphthoic acids in that the carboxyl is separated from the aromatic ring by a methylene group and thus its ionization does not have a large effect on the fluorescence spectra. While steady-state fluorescence measurements might suggest that this is a two-state system similar to 2-naphthol, nanosecond fluorometry provides strong evidence for emission from three distinct species (I*, III*, and IV* in Scheme II) and tentative evidence for a small contribution by a fourth species to the fluorescence emission.

References and Notes

(1) (a) Supported by NIH Grant No. GM11632. This is publication No. 851 from the McCollum-Pratt Institute. (b) Supported by a U.S.A. State Department grant. (c) Supported by NIH Career Award Development Grant No. GM10245.
(2) (a) A. Weller, *Prog. React. Kinet.*, 1, 189 (1961); (b) *Z. Elektrochem.*, 60, 1144 (1956).
(3) P. J. Kovi, C. L. Miller, and S. G. Schulman, *Anal. Chim. Acta*, 61, 7 (1972).
(4) P. J. Kovi and S. G. Schulman, *Anal. Chem.*, 45, 989 (1973).
(5) S. G. Schulman and A. C. Capomaccia, *J. Phys. Chem.*, 79, 1337 (1975).
(6) M. R. Loken, J. W. Hayes, J. R. Gohlke, and L. Brand, *Biochemistry*, 11, 4779 (1972).
(7) W. R. Ware in "Creation and Detection of the Excited State", A. A. Lamola, Ed., Vol. Ia, Marcel Dekker, New York, N.Y., 1971.
(8) J. H. Easter, R. P. DeToma, and L. Brand, *Biophys. J.*, in press.
(9) A. Gafni, R. L. Modlin, and L. Brand, *Biophys. J.*, 15, 263 (1975).
(10) A. Grinvald and I. Z. Steinberg, *Anal. Biochem.*, 59, 583 (1974).
(11) H. H. Jaffe and H. L. Jones, *J. Org. Chem.*, 30, 964 (1965).
(12) W. Laws and L. Brand, manuscript in preparation.
(13) This normalization is arbitrary and is not to be confused with the isoemissive point observed in steady-state spectra at this wavelength.

SUPER SERVICE

Now your J.T. Baker distributor can also ship you things he <u>doesn't</u> have!

How can your Baker distributor ship you things he doesn't have? Easy. He now can immediately contact the Baker Super Service Center and—in almost every instance—have the desired item shipped directly to you within 24 hours. *It's as though your J. T. Baker distributor has just added the largest reagent warehouse in the world to his backyard to serve you.* (To super-serve you.)

Now depend on your nearest Baker distributor for *all* of your laboratory reagent needs.

And do you have our new 428-page Catalog 750 featuring thousands of Baker quality laboratory chemicals? If not, please write. Thanks.

And, of course, J. T. Baker's Super Service is also available for...

NEW ULTRAPURES:

Ammonium Hydroxide, "metal-free" solvent, ultrapure metals, metal oxides, and products for fiber optic research.

The J. T. Baker ULTREX® line is an ever-expanding listing of the ultimate ultrapures. For example: ULTREX Ammonium Hydroxide, ULTREX Methyl iso-Butyl Ketone, ULTREX Silicon Dioxide, etc., etc. Plus dozens of previously-introduced ULTREX products.

J.T.Baker

J. T. Baker Chemical Co., 222 Red School Lane, Phillipsburg, N.J. 08865   201 859-5411

29.图.2519